Investigation of the Nucleation and Growth of Colloidal Indium Phosphide: from Molecular Precursors to Semiconductor Nanocrystals through $In_{37}P_{20}(O_2CR)_{51}$ as a Magic-Size Intermediate

Dylan C. Gary

A dissertation

submitted in partial fulfillment of the

requirements for the degree of

Doctor of Philosophy

University of Washington

2016

Reading Committee:

Brandi M. Cossairt, Chair

Daniel R. Gamelin

Dennis M. Heinekey

David S. Ginger

Hugh Hillhouse

Program Authorized to Offer Degree:

Chemistry

University of Washington

Abstract

Investigation of the Nucleation and Growth of Colloidal Indium Phosphide: from Molecular Precursors to Semiconductor Nanocrystals through $In_{37}P_{20}(O_2CR)_{51}$ as a Magic-Size Intermediate

Dylan C. Gary

Chair of the Supervisory Committee:

Professor Brandi M. Cossairt

Department of Chemistry

Semiconductor nanocrystals have drawn a considerable amount of interest in recent decades from both academia and industry. These crystallites possess a unique property in which the energy of electromagnetic radiation absorbed and/or emitted by the crystallites is inversely correlated with the particle's size. This phenomenon (dubbed the quantum confinement effect) is immediately integrable with current downconversion technology employed in LCD displays. Substitution of the traditional yttrium aluminum garnet (YAG) phosphors, employed in such displays, with red and green emitting nanocrystals offers superior energy efficiency and a wider color palette. In order to attain such enhancements, the nanocrystals employed require minimal size disparity.

Cadmium selenide (CdSe) nanocrystals are the preferred choice for such displays as their syntheses have matured to afford nearly monodisperse samples across a wide range of sizes. The toxicity of cadmium, however, poses a serious health and environmental risk as well as a barrier to

further commercialization. Indium phosphide (InP) stands as the ideal candidate to replace current cadmium based nanocrystals since indium is relatively benign and InP possesses a bulk bandgap that would enable tuning across a wide region of the electromagnetic spectrum through the quantum confinement effect. Attempts to adapt the synthetic techniques which have been proven successful for cadmium based nanocrystal have failed to produce an InP sample with size distributions narrow enough to be competitive. This thesis discusses insights into the nucleation and growth of InP nanocrystals which should prove a valuable resource in rationally designing syntheses of InP with more narrow size distributions.

After a brief introduction on the topic, chapter 2 discusses the protonolysis of the P^{3-} precursor, $P(Si(CH_3)_3)_3$, along with the impact this reaction has on the nucleation and growth of InP. Chapter 3 investigates the effect of precursor conversion kinetics on the final particle size and size distribution. In chapter 4, a magic-size cluster is implicated in the inherent difficulty of temporally separating nucleation and growth. The physical structure and electronic properties of the cluster identified in chapter 4 are discussed in chapter 5 as determined by X-ray crystallography and DFT calculations. Finally, chapter 6 investigates the role of primary amines on surface chemistry and thermal stability of magic-size clusters in an attempt to consolidate conflicting literature reports on the effect of primary amines on precursor conversion kinetics.

TABLE OF CONTENTS

List of Figures

List of Schemes

List of Tables

Acknowledgments

My graduate studies at the University of Washington mark the longest period of enrollment at an academic institution that I have ever experienced, and almost certainly will ever experience in my lifetime. While this statement, at first glance, may appear as an exclamation of conquest over drudgery (and it would be palpably dishonest to claim that graduate school does not often entail endeavors that are just that), upon reflection I view this moment in my life with a mixture of euphoric enthusiasm for a promising future and with bittersweet nostalgia for a rewarding chapter of my life coming to an end. The talents and knowledge I have acquired in graduate school are indispensable in furthering my career as a scientist. I owe an immense debt of gratitude to my advisor, my colleagues, the faculty of the University of Washington, and my friends and family for their expertise and unwavering support.

I cannot imagine a superior advisor for my graduate research than Brandi Cossairt. While I tend to personify the stereotypical absent-minded professor in my approach to science, Brandi has regularly acted as my ballast by bringing my inspirations back into the context of a more organized and rational approach to scientific inquiry. Brandi has given me a deep understanding of the efficiency of such methods and I am certain that continuing to develop these skills is an absolute necessity for my continued improvement as a scientist. If the previous statements have painted Brandi in a harsh light, nothing could be further from the truth. Brandi has been nothing but an incredibly patient mentor and good friend. I will never forget the various outings of Cossairt lab: a scavenger hunt, snow shoeing, barbeques, and the many times Brandi has treated us to lunch. Thank you Brandi, for always being a wise mentor and a true friend.

Being Brandi's first graduate student has offered me a rare perspective where I have been privileged to witness the Cossairt lab rapidly grow and flourish each year with the influx of remarkable new talent: Benjamin Glassy, Danielle Henckel, Betsy Flowers, Coleman Schwartz, Jenny Stein, Mike Norris, Michael Enright, David Ung, Beth Mundy, and Andrew Ritchhart are all exemplary scientists

and valuable coworkers. I am certain that the most influential discoveries from the Cossairt lab will be the product of the hard work and creativity of these next generations, and I am only disappointed that I will not be here to see it firsthand.

My first experience in graduate research at the University of Washington was with the Mayer lab. I am incredibly fortunate to have had Jim Mayer for my advisor and Joel Schrauben for my mentor during my first quarter of research. Their patience, insight, and enthusiasm sparked a desire to learn more about synthetic inorganic chemistry. I would also like to thank my dear friend Tom Porter from the Mayer lab who went out of his way to befriend the me when I was the last graduate student to join a lab from my year. I am grateful to David Lao for his valiant (albeit futile) attempts to teach me how to properly shotgun a beer.

The faculty and staff at the University of Washington's chemistry department have proven themselves to be top notch. I would like to thank Daniel Gamelin and Mike Heinekey for taking time to help me interpret my data, suggest important follow up experiments, and even proofread my manuscripts prior to publication. Adrienne Roehrich, Paul Miller, and Rajan Paranji have trained me more times than I can recall on various techniques for NMR. Scott Braswell, Ellen Lavoie, Alec Pakhomov, and Liam Bradshaw have all helped in training me to use the transmission electron microscope and X-ray diffractometer and interpret the data.

One of the greatest pleasures to moving to Seattle has been my newfound friendship with John Schaub. From encouraging me to learn how to scuba dive to hanging out at the movies John has been a true friend throughout my graduate school career.

Finally, I would like to thank my family for their unwavering love and support. To Marcus and Danica, I know that being the oldest sibling tends to set a precedence for being a role model, but I wouldn't be surprised to find that I look to both of you for inspiration more than the other way

around. To my parents, Clive and Terry, thank you for encouraging me to pursue my passions and instilling in me an insatiable curiosity.

Dedication

To my parents Clive and Terry

for their endless love and support and their unshakeable belief in me

Chapter 1: Interpreting Nucleation and Growth through a LaMer Model to Rationally Design Syntheses Targeting Monodisperse Indium Phosphide Quantum Dots

1.1 Discovery and Applications of Colloidal Semiconductor Nanocrystals

Colloidal, semiconductor nanocrystals (quantum dots[1]) have attracted a great deal of interest over the past thirty-three years since their discovery as evident by over 14,000 journal articles published on the topic as well as their commercial success as downconverters for wide color gamut display technologies.[2,3] Quantum dots were first recognized to have discrete energy levels in glass matrices by Alexey Ekimov in 1981.[4] The first colloidal syntheses of semiconductor nanoparticles was reported by Louis E. Brus in 1983.[5] Since these landmark discoveries, it has been shown that it is possible to tailor the band structure as well as the ligand set of semiconductor nanocrystals to meet a wide range of demands such as narrow, tunable absorption and emission, high carrier mobility, solution processability, and size and shape manipulation. The versatility of nanocrystals holds great promise for a wide range of applications, including photovoltaics,[6–9] *in vivo* biological imaging,[10–14] and light emitting devices.[15–18] A colloidal approach is particularly attractive for industrial applications as it is inexpensive, scalable, and compatible with solution processing techniques, such as roll-to-roll printing. The first widespread commercial application of colloidal quantum dots was as downconverters for liquid crystal displays.[19] By exploiting, the narrow, tunable emission profiles of nanocrystals, these displays were able to provide a wider color gamut than those which incorporated the traditional cerium-doped yttrium aluminum garnet phosphor. In order for a quantum dot sample to emit light with a high degree of color purity, the sample must have minimal dispersion in particle size and shape. These criteria can be accounted for by the quantum confinement effect.

1.2 Brief Description of the Quantum Confinement Effect

While a macroscopic semiconductor is characterized by a band structure in which the density of states is continuous for both the valence band and the conduction band, this paradigm begins to break down in the size regime of ~1 to 100 nm. Crystalline semiconductors in this size regime possess inherent, discrete mid-gap states. These states explain the narrow absorbance and emission linewidths achievable by quantum dots since a specific energy would be associated with these transitions, analogous to molecular electronic transitions.

An instructive analogy often given for quantum dots is the model of a particle in a box. In a bulk semiconductor, when an incident photon excites an electron from the valance band into the conduction band a Columbic attraction will arise from the negatively charge electron and the positively charged hole. If a dimension of the semiconductor in which the exciton was formed is less than the Bohr radius of either the electron or the hole, then the semiconductor is said to be confined in that dimension. Semiconductors can be confined in zero (bulk material, three dimensional), one (nanosheets, two dimensional), two (nanorods, one dimensional), or all three spatial dimensions (quantum dots, zero dimensional). The greater the quantum confinement effect (the smaller the box) the greater the energy required to generate the electron-hole pair for a given material (Figure 1.1).

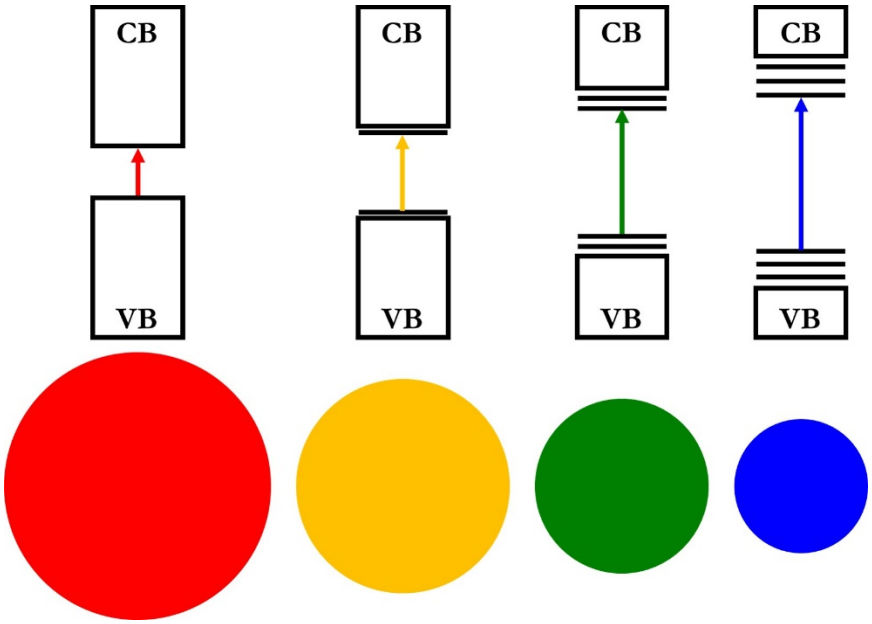

Figure 1.1 Cartoon depiction of the band structure of a zero dimensional semiconductor nanocrystal as a function of particle size. As particle size decreases, energy states emerge between the valance band (VB) and the conduction band (CB) giving rise to discrete energy transitions. The number of these mid-gap states and the difference in energy between them increases with a decrease in particle size.

1.3 Indium Phosphide: a Promising Alternative to Cadmium-based Nanocrystals

Current state of the art nanocrystal luminophores in both industry and academia contain cadmium. While the synthesis of cadmium-based nanocrystals has matured to enable the synthesis of samples with narrow spectral linewidths across the visible region of the electromagnetic spectrum,[20] cadmium possess a significant health and environmental hazard as well as a barrier to global commercialization. Cadmium is currently ranked seventh priority in the Priority Substance List by the Agency for Toxic Substances and Disease Registry in the United States.[21] Cadmium is a nephrotoxin

responsible for one of the Four Big Pollution Diseases of Japan, the itai-itai disease (lit. it hurts-it hurts disease).[22–24] Inhalation of cadmium fumes is the main safety concern for cadmium in the workplace. The Occupational Safety and Health Administration has set the permissible exposure limit of cadmium in the workplace at 5 $\mu g/m^3$.[23]

Indium phosphide (InP) stands as the ideal candidate to replace current cadmium based nanocrystals as indium is relatively benign and InP has a bulk bandgap of 1.35 eV[25] and a exciton Bohr radius of 15 nm[26] which should allow for narrow emission across the visible region of the electromagnetic spectrum. The direct bandgap of III-V semiconductors allows these materials to absorb and emit light with greater efficiency than indirect bandgap semiconductors such as silicon.[27,28] III-V materials also have higher carrier mobilities than other direct bandgap semiconductors such as cadmium selenide and lead sulfide.[28–30] For these reasons, III-V semiconductors with bandgaps in the visible region, such as gallium arsenide (GaAs) and indium phosphide (InP), are being developed for high-performance transistors, optoelectronics, and photovoltaics.[28,30–32]

In order to compare and contrast the toxicity of InP nanocrystals to cadmium selenide (CdSe) nanocrystals, Brunetti et al. measured the extent of release of the metal cation for two analogous core/shell nanocrystal samples in aqueous media.[33] Indium phosphide was found to retain the metal cation in the core of the nanocrystal while cadmium constantly leached from the CdSe nanocrystal under prolonged exposure to simulated lysosomal conditions. The resistance to hydrolysis for InP was attributed to the covalent nature of the III-V bond. Unfortunately, these materials are currently unable to compete with the CdSe because of the broad emission profiles that result from the poor particle size dispersity afforded by current synthetic methods. In order to compete with existing CdSe nanocrystals, the intrinsic linewidth of InP nanocrystals must be similar to CdSe. A recent report by Cui et al. was able to demonstrate that spectral linewidth in InP samples was a product of sample inhomogeneity and confirmed that the intrinsic linewidth of InP was nearly identical to CdSe.[34]

1.4 Conceptualizing Colloidal Nucleation and Growth of Nanocrystals through the LaMer Model

In order to rationally design a superior colloidal synthesis of InP nanocrystals, one must first understand the current models used to interpret the reaction scheme from molecular precursors to nanocrystals. The fundamental steps for the nucleation and growth for a sample of colloidal particles was outlined by LaMer et al. in 1950 (Figure 1.2).[35] While this model may be an oversimplification for the nucleation and growth of InP quantum dots, the fundamental steps will still be the same and serve as a guide for the criteria a synthesis targeting a sample with a narrow size distribution should satisfy.

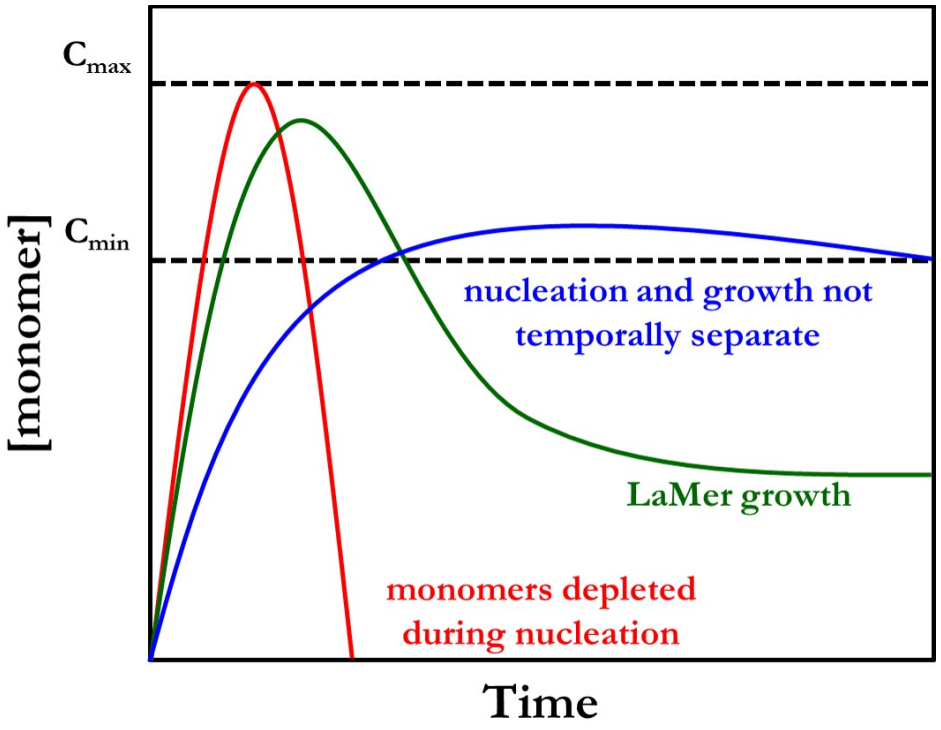

Figure 1.2 LaMer diagram for the three stages of colloidal nucleation and growth. Three distinct scenarios are represented. In the growth profile depicted by the red curve, all monomers are consumed during the nucleation event precluding monomer reserves required for a size-focusing growth stage. The blue curve portrays a scenario in which the chemical potential of monomers in solution never reached a maximum value conducive to rapid nucleation and nucleation occurs throughout the course of the reaction. The green curve portrays the desired reaction profile. In this scenario, both burst-like nucleation and subsequent growth exclusively from newly formed or leftover monomers has been accomplished.

In the LaMer model, a colloidal synthesis from molecular precursors proceeds through three main stages. During the first stage of the reaction, the chemical potential of a soluble form of the desired colloid (called the monomer) is rapidly increased. In a typical quantum dot synthesis, this is achieved through increasing the monomer concertation via the *in situ* generation of the monomer

species from the conversion of one or more molecular precursors. In the second stage of the reaction, the chemical potential of the monomer reaches a critical limit and precipitates from the solution. Ideally, this critical limit achieved by the monomer should be well above the supersaturation level of the solution so that nucleation occurs nearly instantaneously to bring the solution below supersaturation. This criterion is crucial as temporal separation of nucleation and growth is necessary to avoid differences in particle growth history which will invariably lead to an increase in particle size distribution. The final stage of the LaMer model is the growth of the newly formed particles either from adsorption of the remaining monomer species left over in the solution or from newly generated monomers from continued precursor conversion. During this stage of the reaction, a size-focusing kinetic regime can be obtained.[36,37] At a sufficiently high monomer concentration, particle growth will be favored over dissolution back into monomers. Remaining monomers will preferentially adsorb onto smaller particles considering a smaller particle would have fewer bonds on average for surface bound atoms than atoms on the surface of a larger particle. This scenario will result in a decrease in size distributions with time. If monomer concentrations are too low during the growth stage, then particle dissolution back to monomers will be favored over monomer adsorption and growth will proceed via an Ostwald ripening mechanism with an overall increase in size distribution.

With this model in mind, an ideal synthesis of nanocrystals should target a temporally separate nucleation and growth stage while maintaining sufficiently high monomer concentrations during particle growth. In line with these criteria, a typical technique employed to obtain a monodisperse sample of nanocrystals is the hot-injection method.[36,38,39] The hot-injection method rapidly introduces a room temperature solution of one or more reactants to a separate solution of the remaining reactants at an elevated temperature. In this way, there is an initial spike in the number of monomers in the solution due to rapid precursor conversion kinetics at the initial temperature and precursor concentrations. Shortly after injection, the temperature has equilibrated and a significant fraction of

potential monomers have been consumed via nucleation, effectively retarding precursor conversion kinetics in order to maintain a steady monomer supply for the subsequent size-focusing growth stage.

1.5 Brief Outline of Future Chapters

Herein, recent developments in the understanding of the nucleation and growth of indium phosphide nanocrystals will be discussed. The protonolysis of $P(Si(CH_3)_3)_3$, a typical P^{3-} source employed in InP syntheses, was found to precede In−P bond formation. Control experiments were performed with the secondary phosphine, $HP(Si(CH_3)_3)_2$, as well as aprotic carboxylate ligands to assess the effects of silylphosphine protonolysis on the nucleation and growth of InP nanocrystals. A new class of triarylsilylphosphines ($P(Si(C_6H_4X)_3)_3$ (where X = H, CH_3, Cl, or CF_3) was synthesized, and the precursor conversion kinetics of these phosphines were analyzed. Silylphosphines with disparate precursor conversion kinetics were employed in a tandem injection ($P(Si(CH_3)_3)_3$ and $P(Si(C_6H_5)_3)_3$) as a novel method to tune nucleation and growth through stoichiometry. Magic-size clusters of InP were implicated as key intermediates in the growth profile of InP, explaining deviations from LaMer-like behavior. The core structure, and thermal stability of magic-size clusters was found to be dependent on the choice of ligand set. A LaMer growth profile was accomplished by employing clusters as single source precursors to InP nanocrystals. A magic-size cluster was identified as $In_{37}P_{20}(O_2CCH_2C_6H_5)_{51}$ by X-ray crystallography, revealing a nonstoichiometric, charged core structure, with a metal-rich and highly passivated surface. Insight into the electronic structure of $In_{37}P_{20}(O_2CCH_2C_6H_5)_{51}$ was obtained through TDDFT calculations which agree well with low temperature UV-Vis absorbance spectra. Finally, $In_{37}P_{20}(O_2CR)_{51}$ was used as a model system to better understand the reaction of primary amines with the surface of carboxylate ligated clusters and propose a reaction scheme in which amine removes surface bound In from $In_{37}P_{20}(O_2CR)_{51}$.

1.6 References

(1) Reed, M.; Randall, J.; Aggarwal, R.; Matyi, R.; Moore, T.; Wetsel, A. *Physical Review Letters* **1988**, *60* (6), 535–537.

(2) Kim, J. Y.; Voznyy, O.; Zhitomirsky, D.; Sargent, E. H. *Advanced Materials* **2013**, *25* (36), 4986–5010.

(3) Coe-Sullivan, S.; Liu, W.; Allen, P.; Steckel, J. S. *ECS Journal of Solid State Science and Technology* **2012**, *2* (2), R3026–R3030.

(4) Ekimov, A. I.; Onushchencko A. A. *Journal of Experimental and Theoretical Physics Letters* **1981**, 34 (6), 345-349.

(5) Brus, L. E. *The Journal of Chemical Physics* **1983**, *79* (11), 5566–5571.

(6) Nozik, A. . *Physica E: Low-dimensional Systems and Nanostructures* **2002**, *14* (1–2), 115–120.

(7) Kamat, P. V. *The Journal of Physical Chemistry C* **2008**, *112* (48), 18737–18753.

(8) Kongkanand, A.; Tvrdy, K.; Takechi, K.; Kuno, M.; Kamat, P. V. *Journal of the American Chemical Society* **2008**, *130* (12), 4007–4015.

(9) Robel, I.; Subramanian, V.; Kuno, M.; Kamat, P. V. *Journal of the American Chemical Society* **2006**, *128* (7), 2385–2393.

(10) Chan, W. C. *Science* **1998**, *281* (5385), 2016–2018.

(11) Alivisatos, A. P.; Gu, W.; Larabell, C. *Annual Review of Biomedical Engineering* **2005**, *7* (1), 55–76.

(12) Chan, W. C. .; Maxwell, D. J.; Gao, X.; Bailey, R. E.; Han, M.; Nie, S. *Current Opinion in Biotechnology* **2002**, *13* (1), 40–46.

(13) Jaiswal, J. K.; Mattoussi, H.; Mauro, J. M.; Simon, S. M. *Nature Biotechnology* **2002**, *21* (1), 47–51.

(14) Medintz, I. L.; Uyeda, H. T.; Goldman, E. R.; Mattoussi, H. *Nature Materials* **2005**, *4* (6), 435–446.

(15) Talapin, D. V.; Steckel, J. *MRS Bulletin* **2013**, *38* (9), 685–691.

(16) Shirasaki, Y.; Supran, G. J.; Bawendi, M. G.; Bulović, V. *Nature Photonics* **2012**, *7* (1), 13–23.

(17) Wood, V.; Bulović, V. *Nano Reviews* **2010**.

(18) Tessler, N. *Science* **2002**, *295* (5559), 1506–1508.

(19) Steckel, J. S.; Ho, J.; Hamilton, C.; Xi, J.; Breen, C.; Liu, W.; Allen, P.; Coe-Sullivan, S. *Journal of the Society for Information Display* **2015**, *23* (7), 294–305.

(20) Chen, O.; Zhao, J.; Chauhan, V. P.; Cui, J.; Wong, C.; Harris, D. K.; Wei, H.; Han, H.-S.; Fukumura, D.; Jain, R. K.; Bawendi, M. G. *Nat Mater* **2013**, *12* (5), 445–451.

(21) Priority List of Hazardous Substances | ATSDR http://www.atsdr.cdc.gov/spl/ (accessed May 9, 2016).

(22) Inaba, T.; Kobayashi, E.; Suwazono, Y.; Uetani, M.; Oishi, M.; Nakagawa, H.; Nogawa, K. *Toxicology Letters* **2005**, *159* (2), 192–201.

(23) Cadmium (Cd) Toxicity: What Are the U.S. Standards for Cadmium Exposure? | ATSDR - Environmental Medicine & Environmental Health Education - CSEM http://www.atsdr.cdc.gov/csem/csem.asp?csem=6&po=7 (accessed May 9, 2016).

(24) Godt, J.; Scheidig, F.; Grosse-Siestrup, C.; Esche, V.; Brandenburg, P.; Reich, A.; Groneberg, D. *J Occup Med Toxicol* **2006**, *1* (1), 1–6.

(25) Li, L.; Reiss, P. *Journal of the American Chemical Society* **2008**, *130* (35), 11588–11589.

(26) Guzelian, A. A.; Katari, J. E. B.; Kadavanich, A. V.; Banin, U.; Hamad, K.; Juban, E.; Alivisatos, A. P.; Wolters, R. H.; Arnold, C. C.; Heath, J. R. *The Journal of Physical Chemistry* **1996**, *100* (17), 7212–7219.

(27) Vurgaftman, I.; Meyer, J. R.; Ram-Mohan, L. R. *Journal of Applied Physics* **2001**, *89* (11), 5815–5875.

(28) Adachi, S. *Properties of Group-IV, III-V and II-VI Semiconductors: Adachi/Properties of Group-IV, III-V and II-VI Semiconductors*; John Wiley & Sons, Ltd: Chichester, UK, 2005.

(29) Gupta, S.; Whitaker, J. F.; Mourou, G. A. *IEEE Journal of Quantum Electronics* **1992**, *28* (10), 2464–2472.

(30) Schubert, E. F. *Doping in III–V Semiconductors*; Cambridge University Press: Cambridge, 1993.

(31) Craig Casey. *Devices for Integrated Circuits: Silicon and III-V Compound Semiconductors*; Wiley: New York, 1998.

(32) Tingkai Li; Michael Mastro; ArminutesDadgar. *III–V Compound Semiconductors: Integration with Silicon-Based Microelectronics*; CRC Press: Boca Raton, FL, 2011.

(33) Brunetti, V.; Chibli, H.; Fiammengo, R.; Galeone, A.; Malvindi, M. A.; Vecchio, G.; Cingolani, R.; Nadeau, J. L.; Pompa, P. P. *Nanoscale* **2013**, *5* (1), 307–317.

(34) Cui, J.; Beyler, A. P.; Marshall, L. F.; Chen, O.; Harris, D. K.; Wanger, D. D.; Brokmann, X.; Bawendi, M. G. *Nat Chem* **2013**, *5* (7), 602–606.

(35) LaMer, V. K.; Dinegar, R. H. *Journal of the American Chemical Society* **1950**, *72* (11), 4847–4854.

(36) Peng, X.; Wickham, J.; Alivisatos, A. P. *Journal of the American Chemical Society* **1998**, *120* (21), 5343–5344.

(37) Yin, Y.; Alivisatos, A. P. *Nature* **2005**, *437* (7059), 664–670.

(38) Park, J.; Joo, J.; Kwon, S. G.; Jang, Y.; Hyeon, T. *Angewandte Chemie International Edition* **2007**, *46* (25), 4630–4660.

(39) Murray, C. B.; Norris, D. J.; Bawendi, M. G. *Journal of the American Chemical Society* **1993**, *115* (19), 8706–8715.

Chapter 2: Alkylsilylphosphine Speciation is Observed Prior to In−P Bond Formation in Syntheses that Employ Silyl Phosphine and Indium Carboxylate Precursors

2.1 Introduction

Although hot-injection methods have been highly successful for other systems, such as CdSe, the reactivities of currently employed phosphorus precursors for InP, such as tris(trimethylsilyl)phoshphine ($P(Si(CH_3)_3)_3$),[1–5] result in full consumption of the phosphorus precursor during nucleation. Without an InP monomer reservoir supplied by steady precursor conversion, InP nanoparticles must grow by a ripening process which increases particle size distributions. As the synthesis of InP nanocrystals typically employ a source of P^{3-} or P^0 (to react with In^{3+} or In^0, respectively), there are a limited number of feasible phosphorus precursors which will avoid unnecessary redox steps. Notable alternatives to $P(Si(CH_3)_3)_3$ include phosphine gas (PH_3),[6–8] white phosphorus (P_4),[9,10] and more recently, tris(trimethylgermyl)phosphine, $P(Ge(CH_3)_3)_3$). [11]

To improve upon current InP syntheses and rationally design better systems, the roles of each of the precursors need to be considered with respect to the formation of the soluble semiconductor species. A previous investigation into the formation of colloidal InP quantum dots (QDs) from $P(Si(CH_3)_3)_3$ and indium myristate ($In(O_2C(CH_2)_{12}CH_3)_3$) has led to the proposal of an amine-inhibited charge-dispersion S_N2 transition state for the initial formation of an In–P bond.[12] We have observed that rapid protonolysis of $P(Si(CH_3)_3)_3$ proceeds at 20 °C in the presence of myristic acid, which is typically present in excess in current hot-injection strategies using $P(Si(CH_3)_3)_3$.[1–5] On the basis of this observation, we propose a competing, acid catalyzed, pathway to InP QDs from $P(Si(CH_3)_3)_3$ and $In(O_2C(CH_2)_{12}CH_3)_3$, as depicted in Scheme 2.1. This pathway depicts only a single protonolysis event,

forming the secondary phosphine, for simplicity. The full mechanistic picture including all potential protonolysis products, $H_{3-n}P(Si(CH_3)_3)_n$ can be seen in Scheme 2.2. This acid-dependent pathway bears close analogy with the mechanism proposed by Theopold and Douglas for the formation of small InP clusters in solution using the molecular precursors RR'In–$P(Si(CH_3)_3)_2$) in the presence of methanol (R = Cp*, R' = Cl; R, R' = $(H_3C)_3SiCH2$; R = $(H_3C)_3SiCH_2$, R' = Cl; and R, R' = $(H_3C)_3CCH_2$).[13]

It is known that $P(Si(CH_3)_3)_3$ can be used to prepare $HP(Si(CH_3)_3)_3$ when treated with 1 equivalent of methanol or 0.5 equivalents of water.[14,15] The corresponding primary phosphine and PH_3 can also be prepared analogously.[8,14] Typical conditions for InP nanocrystal preparation involve the *in situ* generation of $In(O_2C(CH_2)_{12}CH_3)_3$ from mixing 4 equivalents of myristic acid and $In(O_2CCH_3)_3$ in octadecene at 100 °C under vacuum for 1 hour.[1,2,16–20] These conditions are assumed to fully convert indium acetate to indium myristate and acetic acid and to remove any water or acetic acid from the reaction mixture. The use of excess myristic acid to fully convert the indium acetate means that a protic species remains in the reaction mixture even if all of the acetic acid and water are removed. Combined with observations that carboxylic acid concentration greatly affects QD growth,[1,8] this information suggests that under typical nanocrystal growth conditions, $P(Si(CH_3)_3)_3$ may be converted to $H_{3-n}P(Si(CH_3)_3)_n$, leading to competing nucleation pathways.

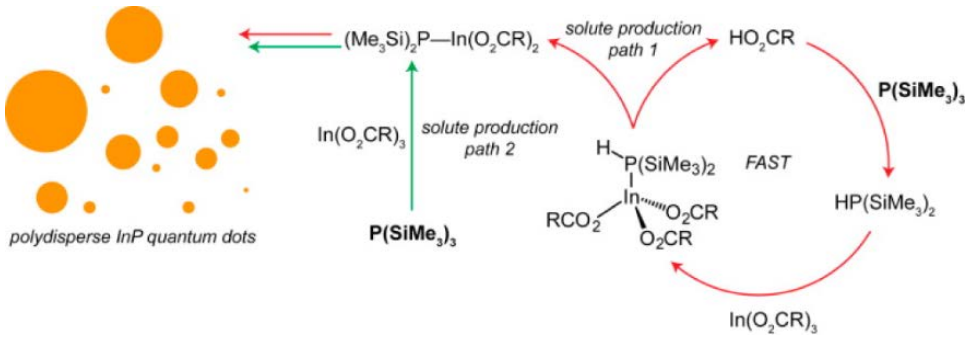

Scheme 2.1 Simplified reaction scheme depicting the effect of protonolysis of $P(Si(CH_3)_3)_3$ on precursor conversion reactions prior to nucleation and growth of colloidal indium phosphide nanocrystals. See Scheme 2.2 for a more a more complete description of the proteolysis pathways depicted in the red outlined circle.

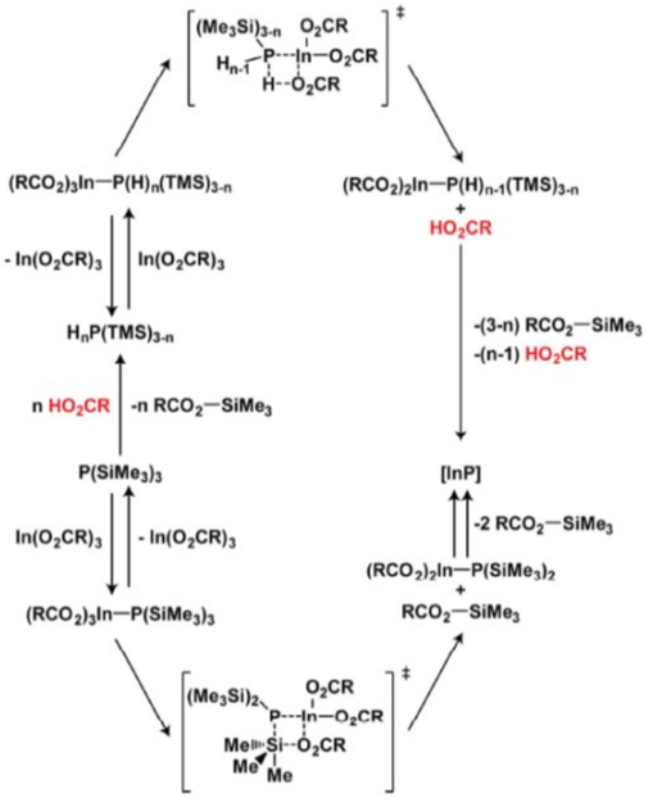

Scheme 2.2 Complete reaction scheme for the formation of [InP] (where [InP] is some soluble form of InP that retains no carboxylate or silane functional groups from the original molecular precursors) from $P(Si(CH_3)_3)_3$ and $In(O_2CR)_3$. Note that the bottom reaction pathway is identical to the reaction scheme proposed by Allen et al. in the absence of primary amines.[2]

2.2 Results and Discussion

2.2.1 Speciation of $P(Si(CH_3)_3)$ to $H_{3-n}P(Si(CH_3)_3)_n$ by H_2O, $HOCH_3$, HO_2CCF_3, HCl, and $HO_2C(CH_2)_{12}CH_3$

We have taken a three-pronged approach to investigating the role of acid on $P(Si(CH_3)_3)_3$ speciation and thus InP QD formation. First, control experiments have been performed to assess the

ability of various proton sources including water, methanol, trifluoroacetic acid, myristic acid, and HCl, to generate $H_{3-n}P(Si(CH_3)_3)_n$. These experiments were carried out in rigorously dried hydrocarbon solvent at 20 and 240 °C and analyzed by proton-coupled ^{31}P NMR spectroscopy. Representative data revealing the speciation of $P(Si(CH_3)_3)_3$ in the presence of 1 equivalent of trifluoroacetic acid at 20 °C are shown in Figure 2.1.

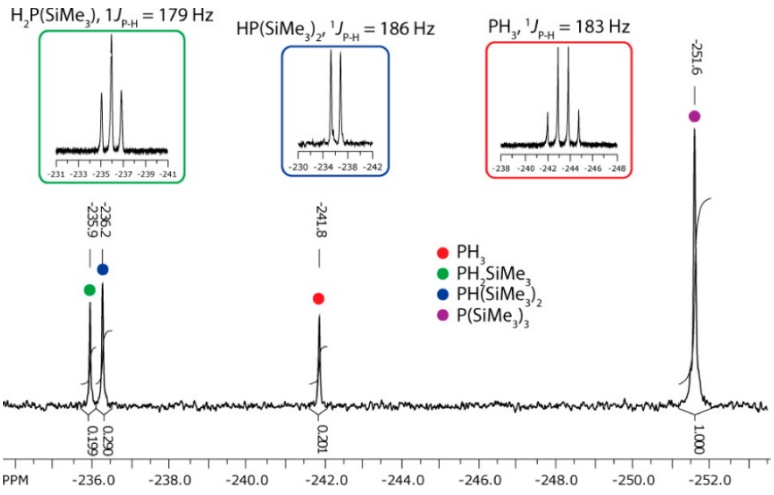

Figure 2.1 $^{31}P\{^1H\}$ NMR spectrum obtained upon mixing $P(Si(CH_3)_3)_3$ with HO_2CCF_3 at 20 °C. ^1H-coupled spectra are shown in the insets.

At 20 °C, one equivalent of methanol was found to slowly and selectively produce $HP(Si(CH_3)_3)_2$, whereas 0.5 equivalents of water, one equivalent of carboxylic acid, and one equivalent of HCl all showed nonselective formation of a mixture of $HP(Si(CH_3)_3)_2$, $H_2P(Si(CH_3)_3)$, and PH_3. (Figure 2.2) InP syntheses performed at room temperature showed similar results (Figure 2.3). These results suggest that even at room temperature, $P(Si(CH_3)_3)_3$ is readily converted to $H_{3-n}P(Si(CH_3)_3)_n$ by H_2OCR, a fact with important mechanistic implications for the controlled synthesis of phosphide materials using this P^{3-} source.

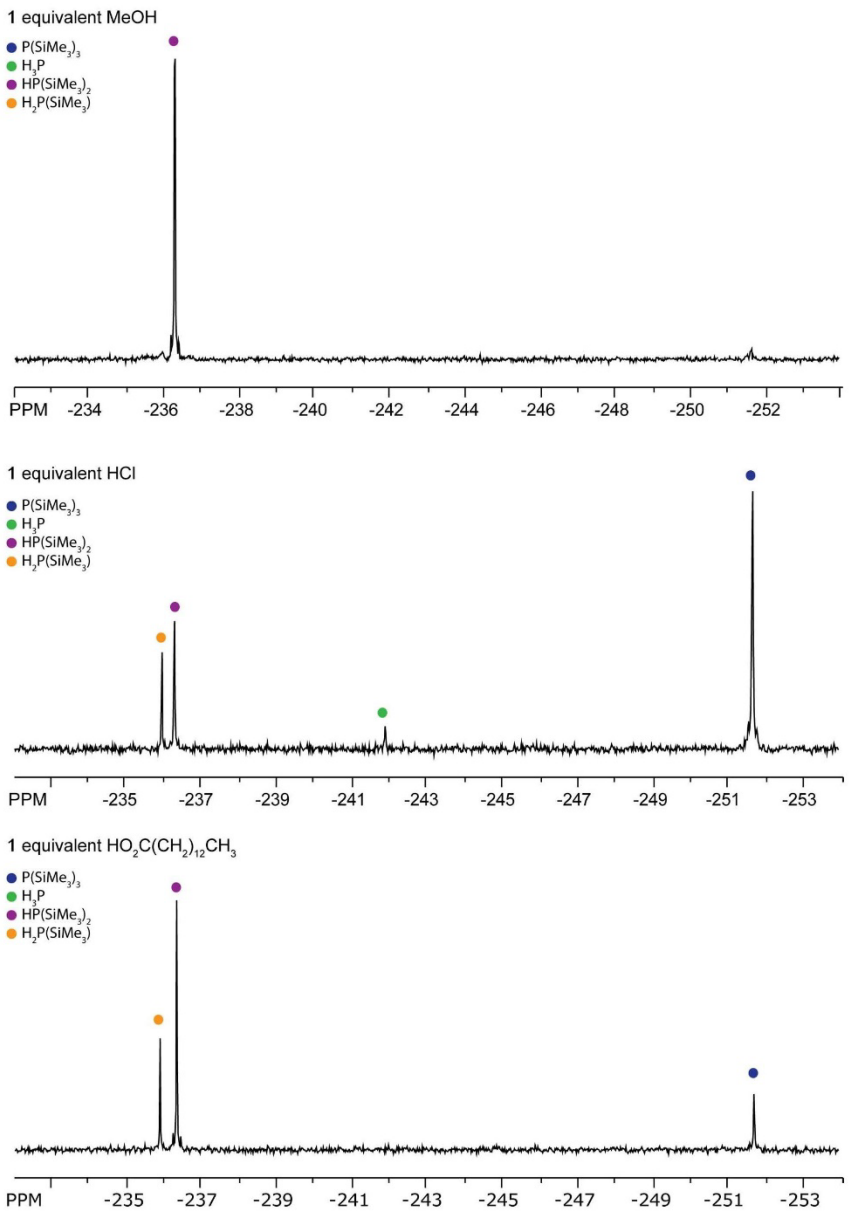

Figure 2.2 $^{31}P\{^{1}H\}$ NMR spectra of reactions resulting from addition of CH_3OH (top), HCl (middle), and $HO_2C(CH_2)_{12}CH_3$ (bottom) to $P(Si(CH_3)_3)_3$ in C_6D_6. Reactions were allowed to proceed to completion, requiring approximately 10 hours for CH_3OH, and only 10 minutes for the stronger acids.

2.2.2 Controls to Determine if Speciation of $P(Si(CH_3)_3)_3$ to $H_{3-n}P(Si(CH_3)_3)_n$ Precedes In−P Bond Formation

We have analyzed $P(Si(CH_3)_3)_3$ speciation during InP QD synthesis using optimized procedures adapted from Peng and co-workers.[1] Specifically, 0.4 mmol of $In(O_2CCH_3)_3$ was combined with 3.6 equivalents of myristic acid in 4 grams of dried and distilled octadecene and was heated under vacuum (20 mTorr) at 100 °C for 16 hours. Freshly distilled $P(Si(CH_3)_3)_3$ (0.2 to 0.8 mmol) was dissolved in 2 grams of dried and distilled octadecene in an inert atmosphere glovebox and loaded into the injection syringe. Spectra of aliquots taken within 5 seconds of phosphine injection at 20 °C and at 315 °C in the presence of a 2-fold excess of the phosphine precursor show phosphine speciation comparable with that observed in the control experiments discussed above (Figure 2.3). Prior to conversion of the phosphine precursor into nanocrystals, $P(Si(CH_3)_3)_3$ protonolysis has occurred. Such speciation was not observed in the earlier mechanistic work.[2] This may be due to the presence of primary amine in the experiments performed by Allen and coworkers.

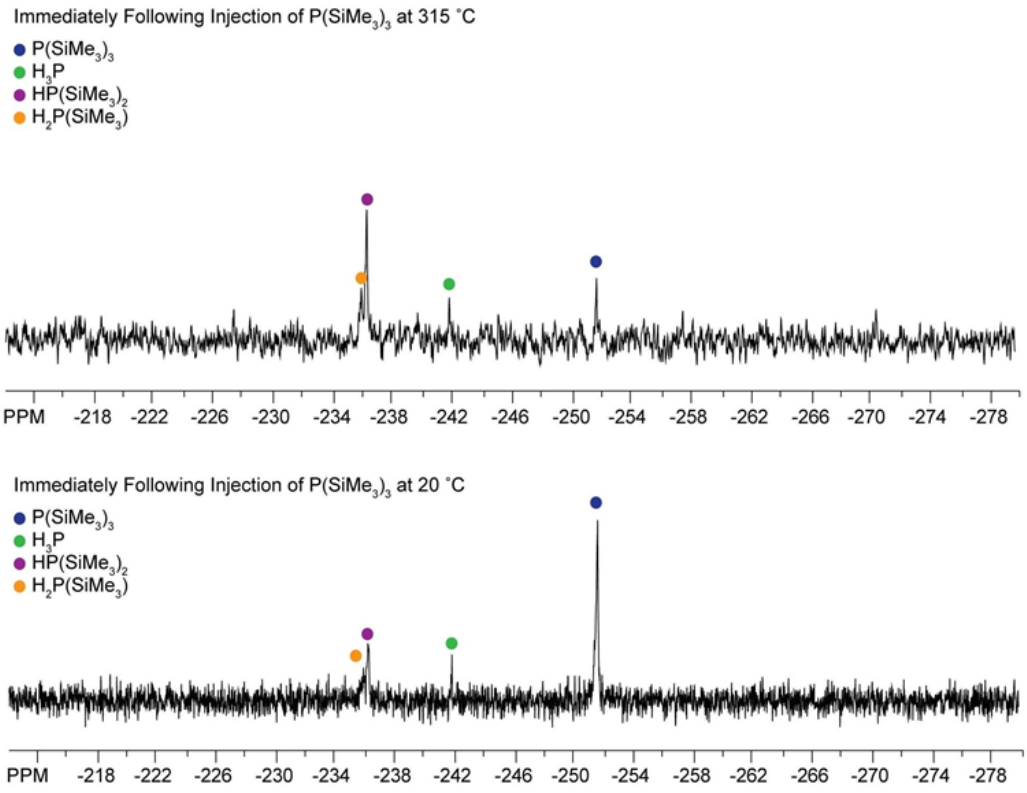

Figure 2.3 $^{31}P\{^{1}H\}$ NMR spectra of InP reaction mixture aliquots obtained immediately (within 10 seconds) after injection of $P(Si(CH_3)_3)_3$ at 315 °C (top) and 20 °C (bottom). In both cases, protonolysis of $P(Si(CH_3)_3)_3$ to $H_{3-n}P(Si(CH_3)_3)_n$ is observed suggestive that protonolysis of $P(Si(CH_3)_3)_3$ is rapid enough to precede In−P bond formation.

Allen et al. used primary amines to slow the reaction kinetics by since amine binding to indium is likely to impede In−P bond formation. One possible alternative role of primary amines is to deprotonate carboxylic acid (or water), generating alkylammonium carboxylate. Control experiments run with $P(Si(CH_3)_3)_3$ in the presence of octylammonium myristate indeed show significant variation in the phosphine protonolysis profile, with a shift toward the starting tertiary phosphine with analogous reaction times (Figure 2.4). This is likely a thermodynamic effect resulting from the higher

pKa of octylammonium myristate relative to myristic acid. The inhibitory effect of amine on In−P bond formation could also be due to modulation of the acid-catalyzed pathway.

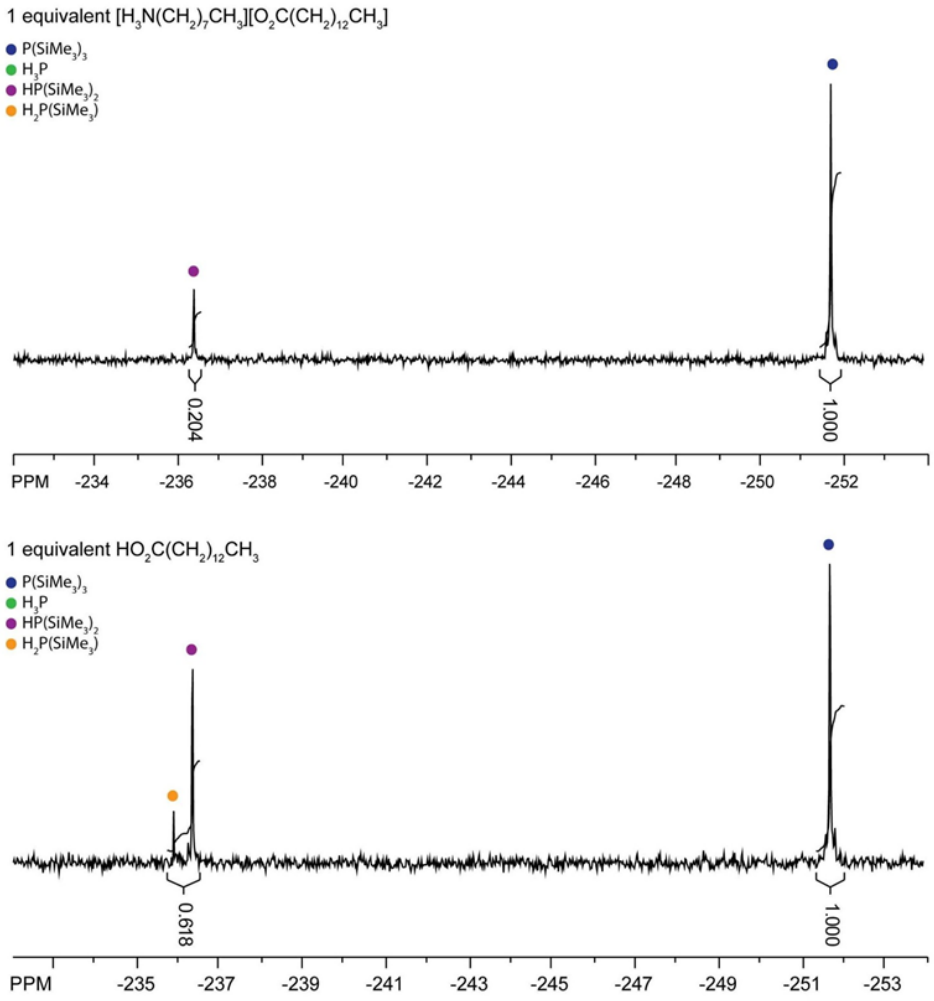

Figure 2.4 ^{31}P $\{^{1}H\}$ NMR spectra of reactions resulting from addition of $[H_3N(CH_2)_7CH_3][O_2C(CH_2)_{12}CH_3]$ (top) and $HO_2C(CH_2)_{12}CH_3$ (bottom) to $P(Si(CH_3)_3)_3$ in C_6D_6. Spectra were obtained approximately 10 minutes after mixing at room temperature and showed no further changes with time.

2.2.3 Comparison of $P(Si(CH_3)_3)_3$ and $HP(Si(CH_3)_3)_2$ as P^{3-} Sources in InP Nanocrystal Synthesis with Varying H_2OCR Concentrations

The above data suggest that protonolysis occurs prior to In−P bond formation, and therefore the secondary phosphine should also yield InP nanocrystals if isolated and used as a P^{3-} source. To test this hypothesis, we have prepared InP nanocrystals directly from $HP(Si(CH_3)_3)_2$. Growth profiles of the syntheses using both the tertiary and the secondary phosphines have been compared using UV-Vis absorption spectroscopy (Figure 2.5). The lowest energy electronic transitions (LEET) were fit to Gaussian curves to allow quantitative comparison of the peak widths (indicative of polydispersity), amplitudes (indicative of particle concentration), and energies (indicative of particle size). Absorbance was also monitored at 310 nm, where the extinction coefficient is expected to be relatively independent of particle size and therefore a qualitative measure of total InP concentration.[11,21] In all experiments the precursors were prepared as described above, the phosphine injection temperature was 315 °C, and the growth temperature was maintained at 285 °C. Two types of experiments were run for each phosphine. One set employed three equivalents of myristic acid relative to $In(O_2CCH_3)_3$ (stoichiometric amount needed to generate indium myristate and found empirically to be optimal for $HP(Si(CH_3)_3)_2$ and one set used 3.6 equivalents of myristic acid relative to $In(O_2CCH_3)_3$ (empirically determined to be optimal for $P(Si(CH_3)_3)_3$. These data are summarized in Figure 2.6 and Figure 2.7.

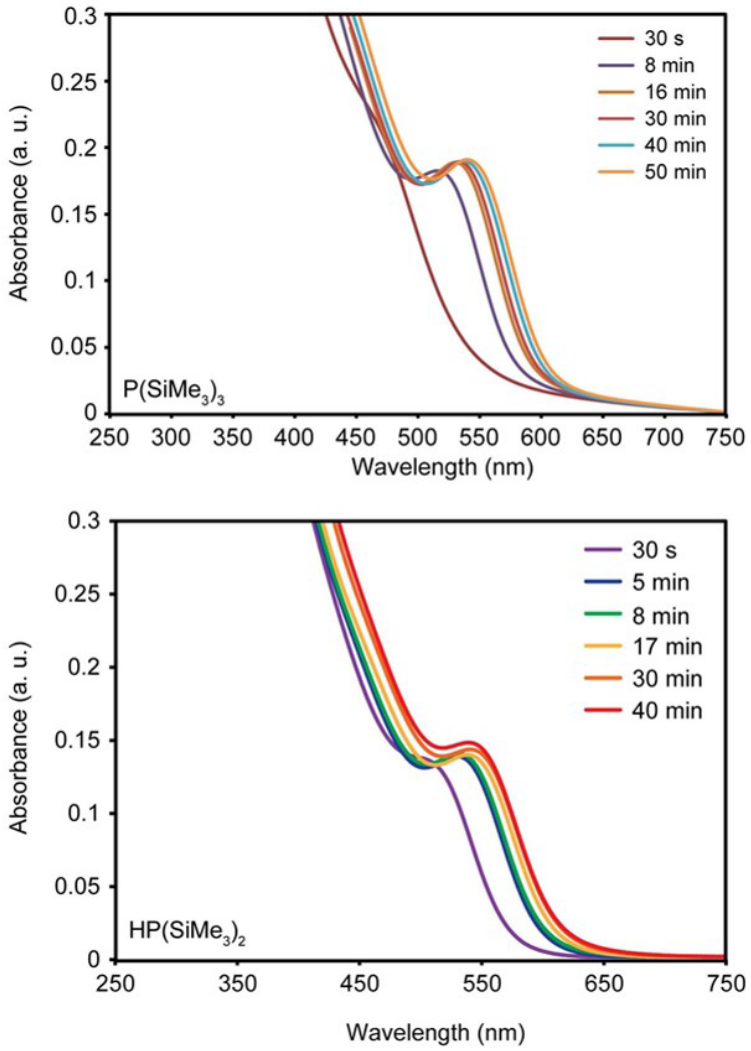

Figure 2.5 UV-Vis spectra of timed aliquots from syntheses using $P(Si(CH_3)_3)_3$ and $HP(Si(CH_3)_3)_2$ as P^{3-} precursors. (top) 0.40 mmol $In(O_2CCH_3)_3$, 1.45 mmol myristic acid, 0.20 mmol $P(Si(CH_3)_3)_3$, 315 °C inject, 285 °C grow. (bottom) 0.40 mmol $In(O_2CCH_3)_3$, 1.20 mmol myristic, 0.20 mmol $HP(Si(CH_3)_3)_2$ 315 °C inject, 285 °C grow. The synthesis that incorporated $P(Si(CH_3)_3)_3$ and ~1 equivalent of myristic acid in excess of that needed to form $In(O_2C(CH_2)_{12}CH_3)_3$ exhibits similar final particle size, size distribution, and nucleation and growth rates as the synthesis that incorporated $HP(Si(CH_3)_3)_2$ and stoichiometric myristic acid.

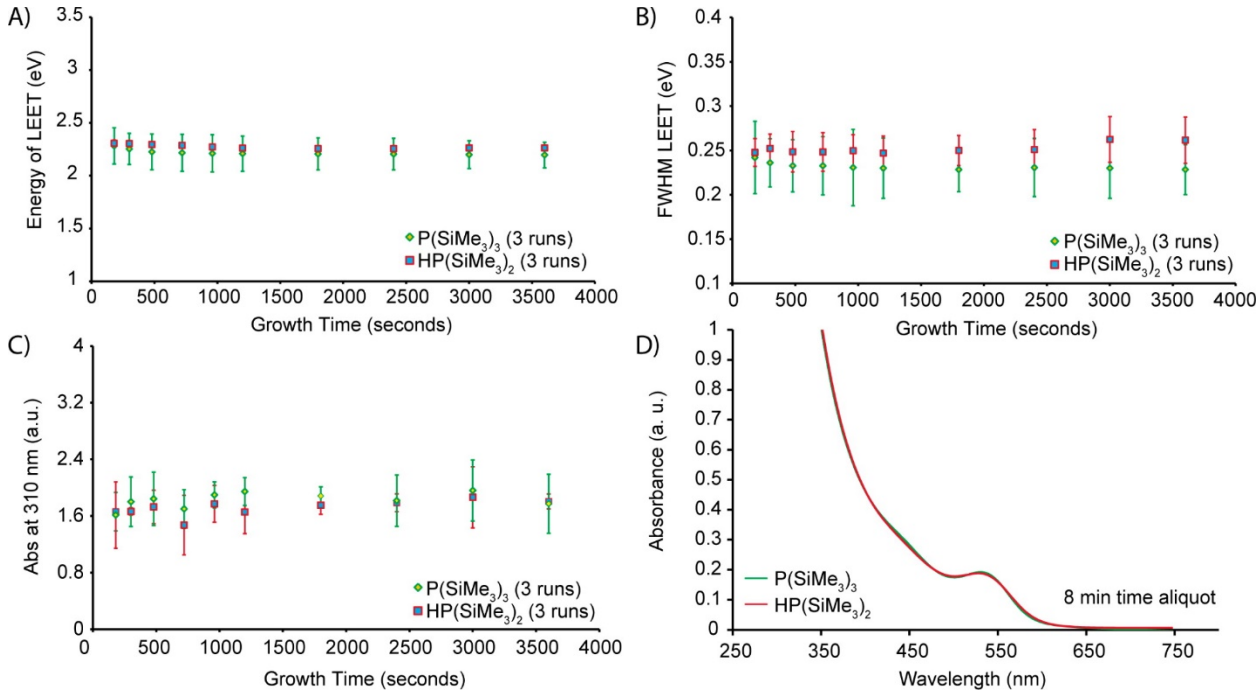

Figure 2.6 Data extracted from Gaussian fitting of the UV-Vis spectra of aliquots taken at different times during InP nanocrystal growth using $P(Si(CH_3)_3)_3$ and $HP(Si(CH_3)_3)_2$ precursors. Data points represent averages from three separate experiments with error bars at a 95% confidence interval. (A) Energy of LEET versus time (indicative of particle size); (B) Full width at half-maximum of LEET versus time (indicative of particle size dispersity); (C) Absorbance at the peak maximum of the LEET versus time (indicative of concentration); (D) Representative UV-Vis traces for 8 minute aliquots for $P(Si(CH_3)_3)_3$ and $HP(Si(CH_3)_3)_2$ reactions.

The data in Figure 2.6 reveal that the InP QD sizes, size distributions, and concentrations are very similar in reactions run with the two phosphines under optimal conditions. This result suggests that in experiments with $P(Si(CH_3)_3)_3$, the added 0.6 equivalents (1.2 equivalents relative to $P(Si(CH_3)_3)_3$) of acid may serve to generate $HP(Si(CH_3)_3)_2$. This interpretation is corroborated by the data shown in Figure 2.7, which compares the full width at half maximum (FWHM) of the absorption spectra for particles grown with $P(Si(CH_3)_3)_3$ and $HP(Si(CH_3)_3)_2$, both with 3 and 3.6 equivalents of

myristic acid relative to $In(O_2CCH_3)$. These data show that, on average, QD polydispersity is optimal when $P(Si(CH_3)_3)_3$ is used in conjunction with an extra 0.6 equivalents of acid, as observed above, but when $HP(Si(CH_3)_3)_2$ is used, optimal QD polydispersity is obtained with stoichiometric acid (3 equivalents). The observation that reactions using the tertiary phosphine require an excess of acid to give narrowest size distribution demonstrates the significance of the acid-catalyzed pathway shown in Scheme 2.1.

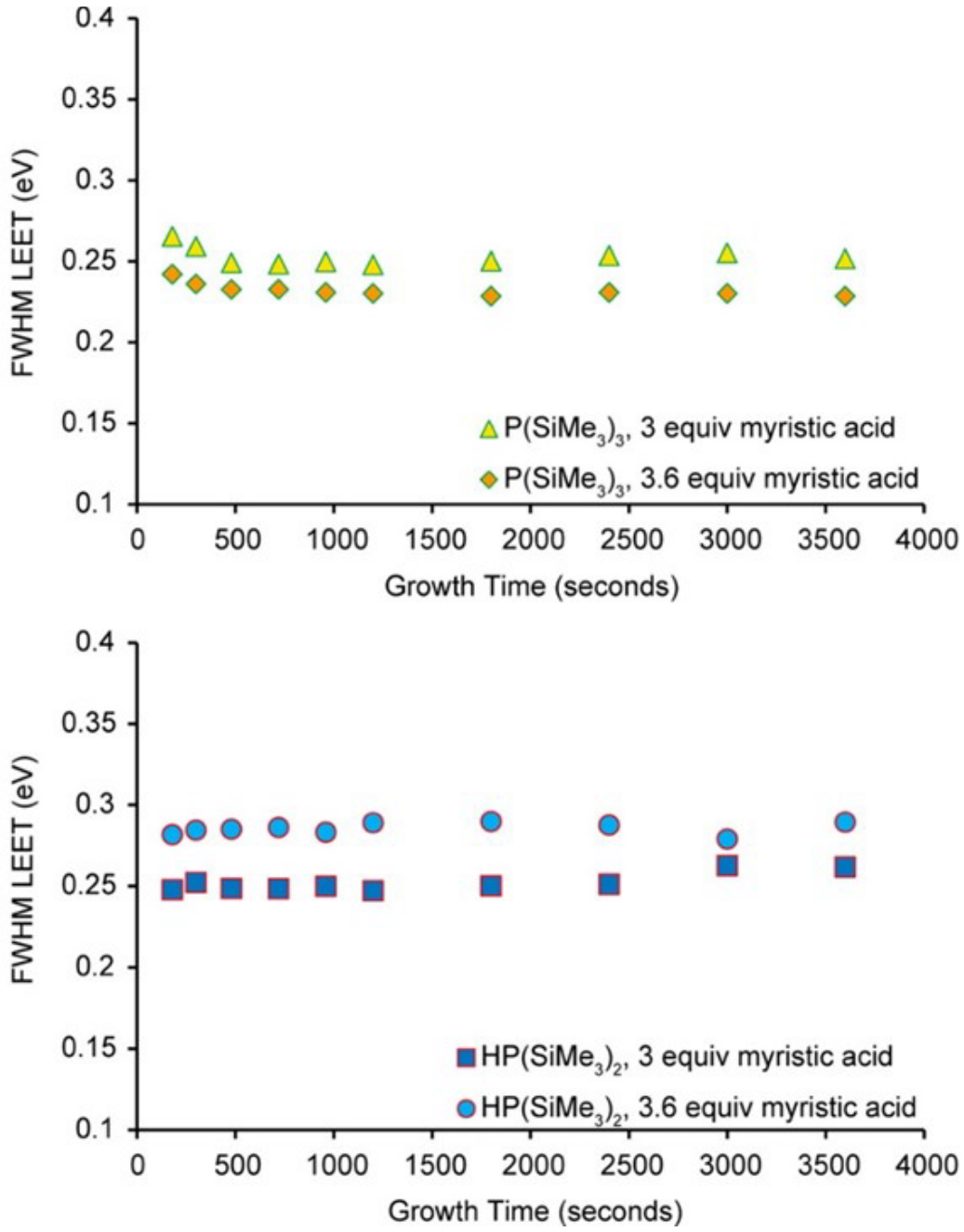

Figure 2.7 Data extracted from Gaussian fitting of UV-Vis time aliquots of InP growth from $P(Si(CH_3)_3)_3$ (top) and $HP(Si(CH_3)_3)_2$ (bottom) with 3 and 3.6 equivalents of myristic acid. Data points represent averages from three separate experiments.

One convoluting effect of $HP(Si(CH_3)_3)_2$ being involved on the path to InP QD formation is its ability to generate 1 equivalent of myristic acid on reaction with indium myristate. This reaction appears unfeasible upon examination of the relative pKa's of PH_3 (~27)[22] and myristic acid (~7.9).[23] Xie et al. have performed high temperature ab initio molecular dynamics simulations of InP formation from PH_3 and indium acetate $In(O_2CCH_3)_3$.[24] These calculations predicted that InP formation proceeds through four distinct stages: formation of an $[In(O_2CCH_3)_3]_6$ complex, binding of PH_3 to the indium carboxylate hexamer, dissociation of three P−H bonds accompanied by formation of four In-P bonds, and finally structural rearrangement to give a nearly tetrahedral geometry about phosphorus in the final $In_6P(O_2CCH_3)_{18}$ complex. During the third stage of this reaction, P−H bond cleavage is facilitated by the adjacent acetate ligands in the PH_3*$[In(O_2CCH_3)_3]_6$ adduct. The bond dissociation energies for this reaction (four In−P bonds = 4 * 197.9 ± 8.4 kJ mol^{-1}, three H-O(O)CR = 3 * 468.6 ± 12.6 kJ mol^{-1}, three H−PH_2 = 3 * 351.0 ± 2.1 kJ mol^{-1}, and three In−O = 3 * 320 ± 21 kJ mol^{-1}) gives $\Delta H_{reaction}^{\circ}$ = 184.4 ± 161.7 kJ mol^{-1}, suggesting that indeed this reaction is enthalpically unfavorable. [25] However, one thing we must bear in mind when considering this type of chemistry is the extreme temperatures at which these reactions are being carried out, which can lead to large negative entropy terms and hence favorable reaction thermodynamics.

2.2.4 Decoupling the Roles of HO_2CR as Free Ligand and Acid in the Speciation of $P(Si(CH_3)_3)_3$ to $H_{3-n}P(Si(CH_3)_3)_n$ by Employing Tetrabutylammonium Salts

Myristic acid not only leads to P–Si bond cleavage, as discussed extensively above, but it also serves as a passivating agent for the QD surface in both its protonated form and as the myristate anion.[26–29] Studies have shown that the concentration of surfactant has a dramatic effect on the growth profiles of nanomaterials, influencing size,[30,31] shape,[32] and particle dispersity.[1] To isolate the roles of

myristic acid as an agent in P–Si bond rupture and as a QD ligand, we have conducted a series of experiments in which $In(O_2C(CH_2)_{12}CH_3)_3$ is preformed and 0.6 equivalents of tetrabutylammonium myristate, $[N((CH_2)_3CH_3)_4][O_2C(CH_2)_{12}CH_3]$, is added as an aprotic myristate anion source. Notably, when this experiment is performed using $P(Si(CH_3)_3)_3$ as the phosphorus source, QD polydispersity shows a slight improvement over that obtained with 3.6 equivalents of myristic acid (0.01 eV lower average FWHM), suggesting that it is the myristate anion that is necessary for maintaining particle dispersity (Figure 2.8 and Figure 2.9).When the analogous experiment is run with $HP(Si(CH_3)_3)_2$ as the phosphorus source, QD dispersity suffers and is again analogous to experiments run with 3.6 equivalents of myristic acid. The reaction of $HP(Si(CH_3)_3)_2$ with indium myristate results in myristic acid formation during the course of the experiment suggesting that the protons are indeed responsible for the higher polydispersity as a result of the acid-catalyzed pathway.

One caveat to these experiments is the increased thermal sensitivity of tetrabutylammonium myristate precursor solutions over myristic acid precursor solutions. Solutions containing tetrabutylammonium myristate undergo a visible thermal decomposition near 315 °C,[20] the optimal injection temperature for our InP QDs. To prevent thermal decomposition, injections can be performed between 305 and 310 °C, which results in lower reaction temperature immediately following injection of the phosphine precursor and typically a poorer QD size dispersity. If InP QD syntheses using $P(Si(CH_3)_3)_3$ are directly compared at 310 °C injection temperatures using 0.6 equivalents of tetrabutylammonium myristate versus 0.6 equivalents of myristic acid, significant improvements (0.05 eV average lower FWHM, Figure 2.8) are observed using tetrabutylammonium myristate, further reinforcing the detrimental effects of protons in these syntheses.

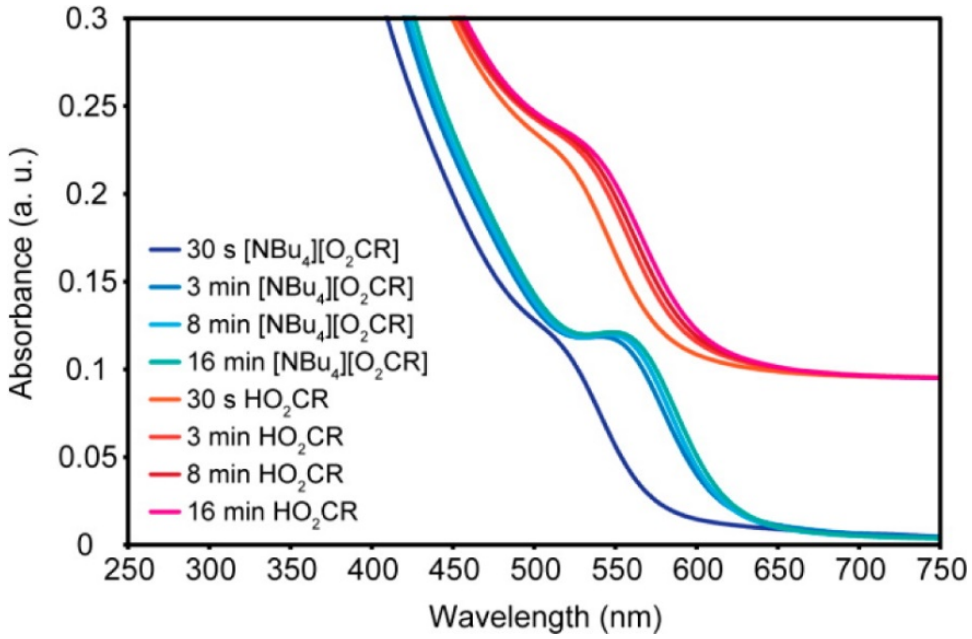

Figure 2.8 Representative UV-Vis data obtained from timed aliquots during InP QD synthesis from $In(O_2C(CH_2)_{12}CH_3)_3$, 0.6 equivalents of $[N((CH_2)_3CH_3)_4][O_2C(CH_2)_{12}CH_3]$, and $P(Si(CH_3)_3)_3$ (blue traces) and $In(O_2C(CH_2)_{12}CH_3)_3$, 0.6 equivalents of $HO_2C(CH_2)_{12}CH_3$, and $P(Si(CH_3)_3)_3$ (red traces). All injections were performed at 310 °C to avoid possible precursor decomposition effects. R = $(CH_2)_{12}CH_3$.

In order to assess the nucleation and growth of InP nanocrystals in the absence of free carboxylic acids, but with the presence of excess myristate anions, a synthesis was performed where $[N((CH_2)_3CH_3)_4][O_2C(CH_2)_{12}CH_3]$ was added to the $In(O_2C(CH_2)_{12}CH_3)_3$ at room temperature, degassed. Finally, the flask was rapidly heated to the injection temperature followed by immediately by the injection of $P(Si(CH_3)_3)_3$ to avoid thermal decomposition (Figure 2.9).Analysis of representative growth profiles obtained from experiments using $In(O_2C(CH_2)_{12}CH_3)_3$, 0.6 equivalents of $[N((CH_2)_3CH_3)_4][O_2C(CH_2)_{12}CH_3]$, and $P(Si(CH_3)_3)_3$ under ideal injection conditions (315 °C injection temperature) show that in the absence of the acid-catalyzed speciation pathway, precursor conversion,

nucleation, and crystal growth are still too rapid and occur nearly simultaneously. This observation underlines the need for further development of new molecular precursors to allow for effective separation of nucleation and growth in the synthesis of InP QDs.

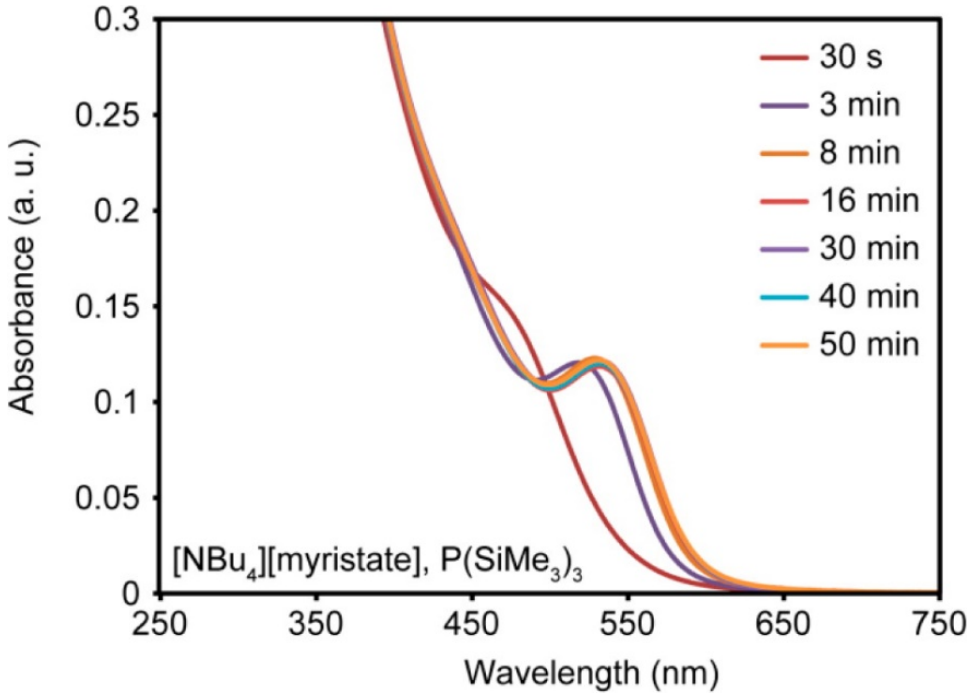

Figure 2.9 Representative UV-Vis data obtained from timed aliquots during InP QD synthesis from $In(O_2C(CH_2)_{12}CH_3)_3$, 0.6 equivalents of $[N((CH_2)_3CH_3)_4][O_2C(CH_2)_{12}CH_3]$, and 0.5 equivalents of $P(Si(CH_3)_3)_3$. Injection temperature 315 °C, growth 285 °C. Tetrabutylammonium myristate was synthesized separately, added to the indium myristate flask, and degassed prior to rapidly ramping to the injection temperature to avoid thermal decomposition.

2.3 Conclusions

These results have important general implications for the synthesis of colloidal III-V semiconductor nanocrystals. The solution phase synthesis of colloidal III-V semiconductors has

greatly lagged behind those of their II-VI and IV-VI counterparts in terms of process reproducibility and particle quality.[2,11,33] For II-VI QDs, the ability to effectively separate crystal nucleation and growth is enabled by precursor conversion being single-mechanism and rate limiting. The results presented here show that the presence of protic reagents in the synthesis of phosphide materials, namely InP, opens up a competing acid-catalyzed reaction pathway, preventing molecular precursors from providing a constant solute supply and hence inhibiting reproducibility and QD quality. Additionally, efforts to synthesize rate-limiting phosphine precursors must consider the rate of protonolysis of such precursors in the presence of free carboxylic acids as protonated phosphines will convert to InP at a rate comparable to $P(Si(CH_3)_3)_3$.Isolating the dual roles of myristic acid as a proton source and a source of myristate anion, a necessary component of the QD surface, has allowed us to identify criteria for ideal InP size dispersity using $P(Si(CH_3)_3)_3$, namely, elimination of acidic protons.

While we have specifically focused on the fact that phosphine protonolysis is detrimental to InP QD formation, studies performed by Chaudret et al. have shown in a related study that the high temperature injection of $P(Si(CH_3)_3)_3$ coincides with ketonic decarboxylation of the carboxylic acids used in traditional syntheses, producing water as a byproduct.[20] The water so generated can oxidize the quantum surface, generating an $InPO_x$ shell around the core, inhibiting growth. Our work demonstrates that water present in the reaction mixture has the additional disadvantage of causing phosphine speciation. Taken together, these studies demonstrate the need for improved phosphorus precursor development and the exploration of surface-passivating ligands that do not contain acidic protons to bypass such pathways. Recently, Franke et al. have shown for silylphosphines and germylphosphines that a decrease in precursor conversion rates actually coincided with a significant increase in particle size distribution.[34] They hypothesized that reaction pathways with impurities, such as water or acid, could be the cause of polydispersity. One explanation for this result would be that a slow protonolysis rate of these phosphines leads to multiple distinct steps in the synthesis as InP

would be formed primarily from P–H bond cleavage. A reaction scheme with multiple, long-lived intermediates is not conducive for a synthesis targeting a slow, steady release of monomer into the solution during the growth stage.

This discovery parallels important advances in our understanding of II-VI nanocrystal syntheses with respect to the roles of impurities such as phosphonic acids,[35–37] and the roles of secondary phosphines in trioctylphosphine-chalcogenide-based syntheses of II-VI and IV-VI QDs.[38–40] All of these studies underline the fact that understanding the molecular reactions involved in precursor conversion to QD nuclei is critical to the development of synthetic methods that adequately control colloidal QD synthesis. Although the chemistries of III-V nanocrystal syntheses are not as mature as those of their II-VI and IV-VI counterparts, the results presented here illustrate that a concrete understanding of the roles of protons in InP precursor conversion results in improved control over InP nanocrystal synthesis.

2.4 Experimental Section

2.4.1 General Considerations

All glassware was dried in a 160 °C oven overnight prior to use. All reactions, unless otherwise noted were run under an inert atmosphere of dry nitrogen using a Vacuum Atmospheres OMNI glovebox or using standard Schlenk technique under an inert atmosphere of dry nitrogen or argon. Celite and 4 Å molecular sieves (Sigma-Aldrich) were dried under reduced pressure at 200 °C for 16 hours prior to use. 1-Octadecene (Sigma-Aldrich, 90%) and 1,2-dimethoxyethane (Sigma-Aldrich, ≥99%) were dried over calcium hydride, distilled, and stored over 4 Å molecular sieves in a nitrogen-filled glovebox. Indium acetate (Sigma-Aldrich, 99.99%), myristic acid (Sigma-Aldrich, ≥99%), red phosphorus (Sigma-Aldrich, ≥99.99%), and trimethylsilylchloride (Sigma-Aldrich, ≥99%) were used

as received. Sodium metal (Sigma-Aldrich) and potassium metal (Sigma-Aldrich, 98%) were washed with hexane and had fresh surfaces cut prior to use. Methanol (Sigma-Aldrich, ≥99.9%) was sparged with nitrogen for 10 minutes prior to use. UV-Vis spectra were acquired on a Cary 5000 UV-Vis-NIR spectrophotometer. NMR Spectroscopy: NMR spectra were obtained using 300 or 499 MHz Bruker Avance spectrometers. In ^{31}P NMR experiments requiring integration, a single pulse was used to allow quantitative comparison. ^{31}P NMR spectra were referenced externally with 85% H_3PO_4. All NMR data was collected in a deuterated solvent (C_6D_6, Cambridge Isotope Laboratories) that was dried with CaH_2, distilled, and stored over 4 Å molecular sieves prior to use. TEM images were acquired on an FEI Tecnai G2 F20 transmission electron microscope.

2.4.2 Synthesis of $P(Si(CH_3)_3)_3$[14]

Caution! Sodium potassium alloy is pyrophoric and will spontaneously ignite in air and will react violently with water. $P(Si(CH_3)_3)_3$ is pyrophoric and will spontaneously ignite in air.

In a typical synthesis of $P(Si(CH_3)_3)_3$ targeting 11 grams, 2.25 grams (57.5 mmol, 1.3 equivalents) of potassium and 1.80 grams (78.3 mmol, 1.8 equivalents) of sodium were weighed out in scintillation vials in a nitrogen filled glovebox. The sodium and potassium were combined in a 250 mL three-neck round-bottom flask along with a football-shaped magnetic stir bar. Approximately 100 mL of 1,2-dimethoxyethane was added to the three-neck flask. One of the side necks of the flask was fitted with a 24/40 Schlenk line gas flow adapter that had been greased with H grease. Two 24/40 septa were then used to stopper the remaining two necks of the flask. A 1.35-gram portion (43.6 mmol of P, 1 equivalent) of red phosphorus was placed into a solid addition funnel in the glovebox. The solid addition funnel was greased with silicone grease and stoppered with a 100 mL round-bottom flask in the glovebox.

The three-neck flask and solid addition funnel were taken out of the glovebox. After cycling the Schlenk line with nitrogen/vacuum three times, the three-neck flask was placed under nitrogen, and the flask was outfitted with a reflux condenser under a counter flow of N_2. The three-neck flask was suspended in a silicone oil bath and heated to a gentle reflux with vigorous stirring for 2 hours. During this time period, the solution changed colors from a vibrant blue to a dull green. The apparatus was then raised from the silicone oil bath, and the bath was removed to allow the solution to come to room temperature while maintaining stirring, returning the deep blue color.

Under a counter flow of nitrogen, the remaining septum was exchanged for the solid addition funnel. The solid addition funnel was rotated to deliver the red phosphorus to the sodium/potassium alloy suspension. The apparatus was once again suspended in the silicone oil bath and heated to a gentle reflux with vigorous stirring for a 24-hour period; during which a deep black suspension was produced.

After 24 hours, the solution was allowed to come to room temperature. The reflux condenser was replaced with a 100 mL dropping funnel under a counter flow of nitrogen. Twenty milliliters of 1,2-dimethoxyethane was cannula transferred from a Schlenk flask to the dropping funnel. Two 9 mL aliquots of chlorotrimethylsilane (15.4 grams, 141.8 mmol, 3.2 equivalents) were drawn from an air-free container and injected into the dropping funnel.

The chlorotrimethylsilane solution was added dropwise to the sodium/potassium phosphide suspension at a rate of about 1 drop a second. After the addition of the chlorotrimethylsilane solution, the dropping funnel was exchanged for a Teflon stopper against a counter flow of nitrogen. Electrical tape was wrapped several times around the three-neck flask and each of the Teflon stoppers as well as the air-free flow control gas adapter. The three-neck flask was carefully brought into the glovebox with fifteen rapid cycles of partial vacuum.

The product solution was filtered through a pad of Celite to remove the salts formed during the reaction. The filter pad was washed with pentane, and the colorless to pale yellow solution was concentrated to a total volume of 30 mL. The solution was transferred to a 100 mL 14/20 neck Schlenk flask equipped with a small football-shaped magnetic stir bar and was removed from the glovebox for distillation using a vacuum-jacketed short-path distillation apparatus.

A first fraction containing solvent and any unreacted chlorotrimethylsilane was removed under full vacuum with heating at 30 °C. The second distillation fraction, which contained the desired product in pure form, was collected under full vacuum (20 mTorr) at approximately 45 °C. The collected $P(Si(CH_3)_3)_3$ was stored in the glovebox in the dark. Mass of distilled product: 8.94 grams (35.7 mmol, 82% yield).

2.4.3 Synthesis of $HP(Si(CH_3)_3)_2$

$HP(Si(CH_3)_3)_2$ was prepared in pure form following a procedure adapted from Buhro and co-workers.[15] Tetrahydrofuran was substituted for diethyl ether.

$HP(Si(CH_3)_3)_2$ was prepared *in situ* according to the following procedures: In a typical synthesis, 5.00 grams of 1-octadecene was weighed out into a 250 mL 24/40 neck Schlenk flask in a nitrogen filled glovebox to which was added 145 μL (0.50 mmol) of $P(Si(CH_3)_3)_3$. The flask was outfitted with a 24/40 septum.

The flask was brought out of the glovebox and placed under nitrogen after cycling the Schlenk line with nitrogen/vacuum three times. A scintillation vial was filled with methanol and stoppered with a rubber septum that was secured with electrical tape to ensure an airtight seal. The methanol was sparged with nitrogen for 10 minutes, and then 20 μL (0.50 mmol) of the sparged methanol was

delivered to the Schenk flask with vigorous stirring. The solution was allowed to stir for approximately 10 hours.

An NMR tube was stoppered with a septum in the glovebox, and the septum was secured with electrical tape. The NMR tube was brought out of the glovebox, and a 0.4 mL aliquot of the octadecene solution was injected into the NMR tube using a long metal needle and a 1 mL disposable syringe. A small piece of Parafilm was wrapped around the top of the NMR tube to ensure the seal. A $^{31}P\{^{1}H\}$ NMR spectrum was taken of the sample to confirm protonolysis of $P(Si(CH_3)_3)_3$ to $HP(Si(CH_3)_3)_2$. If the spectrum confirmed at least 85% conversion (typically near 100%) to the desired product, then the Schlenk flask solution was used as a stock solution for the indium phosphide nanoparticle synthesis.

2.4.4 Synthesis of $[N((CH_2)_3CH_3)_4][O_2C(CH_2)_{12}CH_3]$

In a typical synthesis targeting 5 grams, 6.90 grams (106 mmol) of a 40% by weight aqueous solution of tetra-n-butylammonium hydroxide and 2.43 grams (106 mmol) of myristic acid were added to a 250 mL, 3-neck round-bottom flask. Approximately 100 mL of acetonitrile was added to the flask. The flask was outfitted with a reflux condenser and connected to the Schlenk line. After stoppering the remaining two necks with Teflon stoppers, the flask was placed under a flow of nitrogen. The flask was suspended in a silicone oil bath and carefully heated to reflux. Reflux was maintained for 2 hours. Solvent was removed with a rotary evaporator, and conversion to the desired product was confirmed by ^{1}H NMR spectroscopy (Figure 2.10).

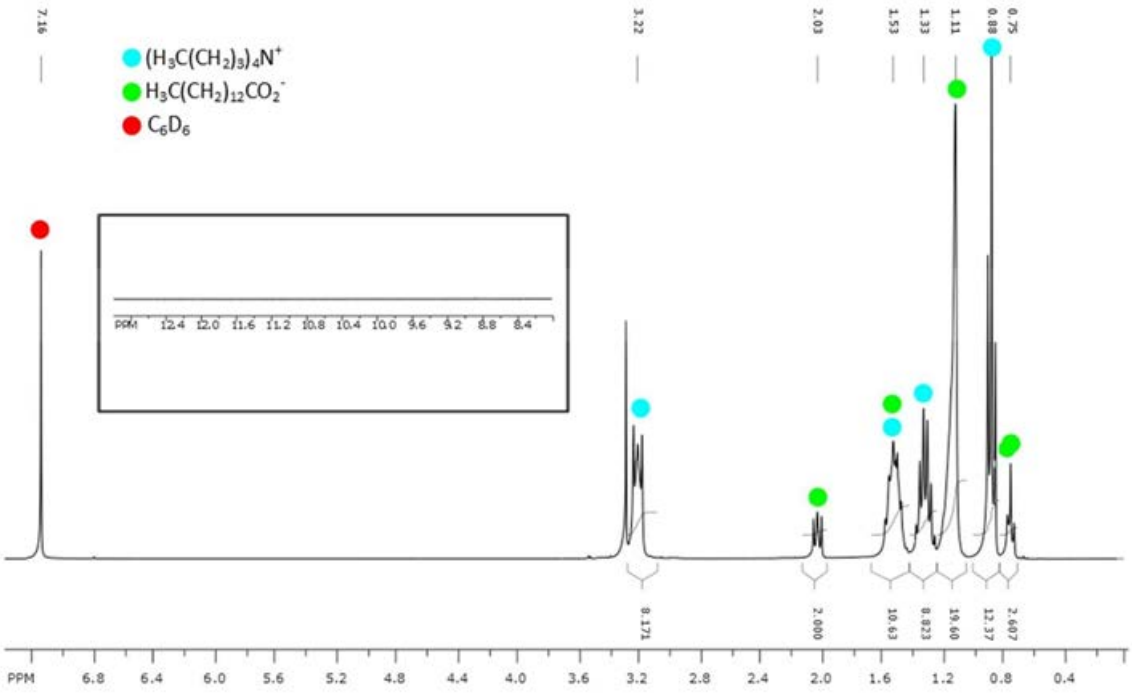

Figure 2.10 ^{1}H NMR of $[N((CH_2)_3CH_3)_4][O_2C(CH_2)_{12}CH_3]$. Spectrum exhibits same peaks as starting material, but with the lack of the peak from the OH^{-1} counterion of tetrabutylammonium hydroxide and the peak for the carboxylic acid OH proton (inset).

2.4.5 Synthesis of InP QDs from $P(Si(CH_3)_3)_3$ and $In(O_2C(CH_2)_{12}CH_3)_3$

In a typical synthesis, 0.117 grams (0.40 mmol) of indium acetate, and 0.331 grams (1.45 mmol), or 0.274 grams (1.20 mmol) for the stoichiometric studies, of myristic acid were weighed out into a 25 mL, 14/20 3-neck round-bottom flask with a small football-shaped magnetic stir bar. The three neck flask was secured with a claw clamp over a stir plate. A 14/20 thermocouple probe adapter

and a 14/20 reflux condenser were greased with H grease. The reflux condenser was inserted into the middle neck of the round-bottom flask and the thermocouple probe adapter was inserted into one of the side necks of the three-neck flask. A 14/20 hose adapter was greased with silicone grease and inserted into the reflux condenser. A 4.00-gram portion of 1-octadecene was weighed out into a scintillation vial in the glovebox, and the scintillation vial was capped. The scintillation vial was removed from the glovebox, and the 1-octadecene was delivered to the 3-neck flask with a glass pipet. The remaining neck of the 3-neck flask was stoppered with a 14/20 Suba seal septum.

The hose adapter was connected to the Schlenk line, and the apparatus was evacuated with vigorous stirring. The Schlenk flask was then lowered into a heating mantle and wrapped with glass wool for insulation. A temperature probe was inserted into the thermocouple probe adapter, and both the heating mantle and the temperature probe were plugged into a temperature controller. The temperature controller was set to 100 °C. The solution was allowed to off-gas acetic acid to generate the indium myristate solution for approximately 12 hours at 100 °C. The apparatus was then placed under nitrogen and raised to 316 °C using the temperature controller.

A 2.00-gram portion of 1-octadecene was weighed out into a scintillation vial in the glovebox. Fifty-eight microliters of $P(Si(CH_3)_3)_3$ was injected into this solution using a 100 μL syringe. This solution was drawn into a 6 mL disposable syringe outfitted with 21G needle and then the needle was inserted into the end of a 14/20 septum to seal off the $P(Si(CH_3)_3)_3$ solution. The syringe was brought out of the glovebox and injected into the indium myristate solution when the temperature controller read 315 °C as the temperature of the solution was falling, after adjusting the temperature to 285 °C, the QD growth temperature.

In experiments run using tetrabutylammonium myristate, a solution of tetrabutylammonium myristate in octadecene was injected after the overnight degassing step, and the total amount of octadecene was kept the same as described above. To ensure quantitative transfer, the

tetrabutylammonium myristate solution was added by injection with a glass syringe after heating the solution to 100 °C to melt the ammonium salt.

2.4.6 Synthesis of InP QDs from $HP(Si(CH_3)_3)_2$ and $In(O_2C(CH_2)_{12}CH_3)_3$

In a typical synthesis, the indium myristate solution was prepared in the same manner as that employed for the synthesis of indium phosphide nanoparticles from $P(Si(CH_3)_3)_3$ and indium myristate. The solution of $HP(Si(CH_3)_3)_2$ was prepared as previously described *vide supra*. The Teflon seal of the Schlenk flask was closed off, and the Schlenk flask was inverted to draw 2.5 mL (2 grams) of the $HP(Si(CH_3)_3)_2$ solution into a 6 mL disposable syringe outfitted with a 21G needle. This solution was then immediately injected into the solution of indium myristate as the temperature fell through 315 °C in a manner analogous to the synthesis performed with $P(Si(CH_3)_3)_3$.

In experiments run using tetrabutylammonium myristate, a solution of tetrabutylammonium myristate in octadecene was injected after the overnight degassing step, and the total amount of octadecene was kept the same as described above. Nanoparticles observed by TEM were of a similar size and shape as those synthesized using $P(Si(CH_3)_3)_3$ (Figure 2.11).

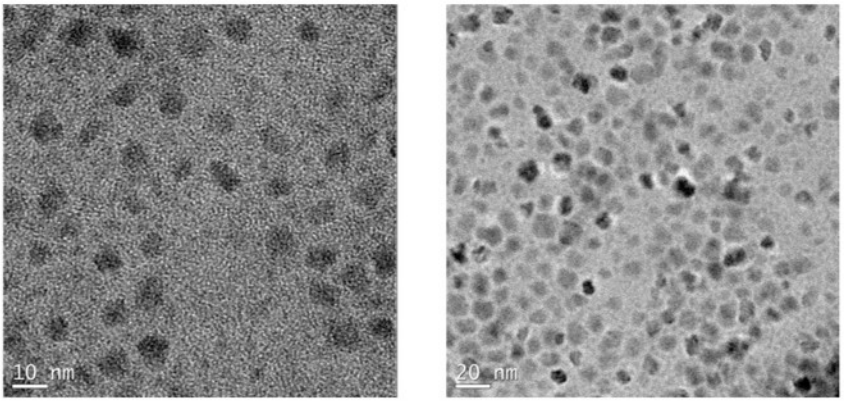

Figure 2.11 TEM microscopy images comparing InP nanoparticles synthesized via $P(Si(CH_3)_3)_3$ (left) and those synthesized using $HP(Si(CH_3)_3)_2$ (right)

2.4.7 UV-Vis Monitoring Procedure

Prior to each injection of $P(Si(CH_3)_3)_3$, a test tube rack was prepared with 13 test tubes. Each test tube was filled with 6 mL of n-hexane using a 6 mL disposable syringe outfitted with a 18G needle. Two beakers were placed beside the test tube rack for hexane and waste washes. Glass pipettes were placed nearby along with pipet bulbs. The baseline and zero absorbance of the UV-Vis spectrophotometer were set using fluorescence cuvettes filled with n-hexane in both sample beams. A timer was used to measure the time from injection of the $P(Si(CH_3)_3)_3$ solution. 50 μL aliquots of the reaction mixture were taken at specific times from injection using a 100 μL syringe and injected the test tubes with n-hexane. The fluorescence cuvette from the UV-Vis spectrophotometer used to baseline the instrument from the front beam was washed once with n-hexane and once with approximately one-third of the test tube solution before being filled with the test tube solution with the reaction aliquot and returned to the spectrophotometer for analysis.

2.4.8 Procedure for Gaussian Fitting

Gaussian curves were fit to the UV-Vis data in Excel using the equation:

$$f(x,\sigma) = B + Ae^{(-1*\frac{(x_0-x)^2}{2\sigma^2})}$$

Where B is equal to the energy of absorbance at 1.55 eV (assumed to have no contribution from the nanoparticles), A is equal to the absorbance of the lowest energy electronic transition, 2σ is the full width at half max of the distribution, and x_0 is the energy of the lowest energy electronic transition. The quality of each fit for each distribution was judged on the criteria that:

1. The absorbance at 1.55 eV be set as the baseline of the distribution (B = absorbance at 1.55 eV)
2. The difference between the distribution and the experimental data be minimal from the point of inflection of the UV-Vis data and the peak of the distribution.
3. The amplitude of the distribution be as close to the absorbance at the least energetic energy transition as possible without introducing a large difference in the distribution and the experimental data's point of inflection (criteria 2).

2.4.9 NMR Control Experiments with $P(Si(CH_3)_3)_3$ and Various Acids

For the control experiment with myristic acid, 0.007 grams of myristic acid was weighed out into a J. Young NMR tube. A Kim wipe was secured over the top of the NMR tube with a rubber band, and the NMR tube was transferred to the glovebox along with the J. Young NMR tube cap. Approximately 0.4 mL of octadecene and 0.3 mL of toluene were added to the NMR tube to dissolve the myristic acid. Nine microliters of $P(Si(CH_3)_3)_3$ were then injected into the NMR tube, and the NMR tube was sealed with the J. Young NMR tube cap, shaken to mix thoroughly, and removed from the glovebox for analysis. The octylammonium myristate control was run analogously with 1

equivalent of octylamine first premixed with the myristic acid along with solvent prior to injection of $P(Si(CH_3)_3)_3$. The ^1H NMR spectrum of the octylammonium myristate shown in Figure 2.4 shows complete conversion to octylammonium myristate.

For all other acids, (including trifluoroacetic acid, HCl, sparged methanol, and 18 MΩ Millipore water) Schlenk flasks were prepared in the glovebox with approximately 3.2 grams of octadecene for the studying water, and 1.6 grams of 1-octadecene for the study of each other acid and were labeled according to which acid was to be studied. A 46 μL portion of $P(Si(CH_3)_3)_3$ was injected into each of the Schlenk flasks with 1.6 grams of 1-octadecene and 92 μL of $P(Si(CH_3)_3)_3$ was injected into the Schlenk flask with 3.2 grams of 1-octadecene. A small egg-shaped magnetic stir bar was added to each Schlenk flask.

Each Teflon valve was closed and each Schlenk flask was sealed with a 24/40 Suba seal septum and brought out of the glovebox. Each Schlenk flask was suspended from a claw clamp over a stir plate set to stir. After cycling the Schlenk line three times with nitrogen, the flask was placed under a flow of nitrogen. Methanol was sparged for 10 min, and 6.3 μL of the sparged methanol was injected into the Schlenk flask labeled methanol using a 25 μL syringe. An air-free container of trifluoroacetic acid was suspended from a claw clamp over a stir plate and connected to the Schlenk line. After cycling the line three times with nitrogen, the flask was placed under a flow of nitrogen. The Teflon valve of the air-free flask was exchanged for a rubber septum under a counter-flow of nitrogen, and electrical tape was wrapped around the septum to ensure an airtight seal. Twelve microliters of trifluoroacetic acid was drawn from the air-free container using a 25 μL syringe and injected into the Schlenk flask labeled trifluoroacetic acid. Three microliters of 18 MΩ Millipore water were injected into the Schlenk flask labeled water. Three NMR tubes sealed with septa and electrical tape as described above were prepared in the glovebox and taken out of the glovebox. A 0.4 mL portion of each Schlenk flask

solution was injected into an NMR using a 1 mL disposable syringe and long needle, and each NMR tube was appropriately labeled for analysis.

2.4.10 Procedures for *in situ* Aliquoting for ^{31}P $\{^{1}H\}$ NMR

Room Temperature Control

An indium myristate solution with excess myristic acid was prepared from indium acetate (0.117 grams 0.400 mmoles) and myristic acid (0.331 grams, 1.45 mmoles) in 1-octadecene. This solution was placed under a flow of nitrogen, and allowed to come to room temperature. A syringe of $P(Si(CH_3)_3)_3$ (58 μL, 0.20 mmol) in 1-octadecene was prepared in a nitrogen filled glovebox and sealed by inserting the needle of the syringe into a 14/20 Suba seal septum. An NMR tube was sealed with a septum and the seal was secured with electrical tape in the glovebox. The syringe and the NMR tube were removed from the glovebox. A 1 mL glass syringe was outfitted with a 19G needle and inserted into the indium myristate solution. The $P(Si(CH_3)_3)_3$ solution was injected into the indium myristate solution, and approximately 0.4 mL of the reaction solution was immediately drawn into the glass syringe and injected into the NMR tube for analysis.

Competitive Phosphine Control Experiment

An indium myristate solution was prepared from indium acetate (0.117 grams, 0.40 mmoles) and myristic acid (0.27 grams, 1.2 mmol) in 1-octadecene. A 0.10 mmol solution of $HP(Si(CH_3)_3)_2$ in 2.5 grams of 1-octadecene was prepared in the same manner as previously employed above. A syringe with 290 μL of $P(Si(CH_3)_3)_3$ in 2.5 grams of 1-octadecene was prepared along with two NMR tubes sealed with septa and wrapped with electrical tape in manner previously employed above. Approximately ten hours after injecting the sparged methanol into the Schlenk flask, the syringe of

$P(Si(CH_3)_3)_3$ and the sealed NMR tubes were removed from the glovebox. The $P(Si(CH_3)_3)_3$ solution was injected into the $HP(Si(CH_3)_3)_2$ solution with vigorous stirring, and 0.4 mL of the resulting solution was drawn and injected into one of the sealed NMR tubes to confirm approximately equal proportions of both targeted phosphines. A dry ice/acetone bath was prepared in a wide mouth dewer flask. The NMR tube was removed from the glovebox and suspended in the dry ice/acetone bath. The indium myristate solution was then heated to 316 °C. The temperature controller was then set to keep a temperature of 285 °C. The syringe and the NMR tube were removed from the glovebox. A 1 mL glass syringe was outfitted with a 19G needle and inserted into the indium myristate solution. The temperature controller was set to keep a temperature of 285 °C. The $P(Si(CH_3)_3)_3$ solution was injected into the indium myristate solution just as the solution fell to the temperature reading of 315 °C and approximately 0.4 mL of the reaction solution was immediately drawn into the glass syringe and injected into the NMR tube for analysis.

2.5 References

(1) Battaglia, D.; Peng, X. *Nano Letters* **2002**, *2* (9), 1027–1030.

(2) Allen, P. M.; Walker, B. J.; Bawendi, M. G. *Angewandte Chemie International Edition* **2010**, *49* (4), 760–762.

(3) Green, M. *Current Opinion in Solid State and Materials Science* **2002**, *6* (4), 355–363.

(4) Wells, R. L.; Gladfelter, W. L. *Journal of Cluster Science* **1997**, *8* (2), 217–238.

(5) Baek, J.; Allen, P. M.; Bawendi, M. G.; Jensen, K. F. *Angewandte Chemie International Edition* **2011**, *50* (3), 627–630.

(6) Li, L.; Protière, M.; Reiss, P. *Chemistry of Materials* **2008**, *20* (8), 2621–2623.

(7) Lim, T. H.; Ravi, S.; Bumby, C. W.; Etchegoin, P. G.; Tilley, R. D. *Journal of Materials Chemistry* **2009**, *19* (27), 4852.

(8) Xu, S.; Kumar, S.; Nann, T. *Journal of the American Chemical Society* **2006**, *128* (4), 1054–1055.

(9) Carenco, S.; Demange, M.; Shi, J.; Boissière, C.; Sanchez, C.; Le Floch, P.; Mézailles, N. *Chemical Communications* **2010**, *46* (30), 5578.

(10) Carenco, S.; Hu, Y.; Florea, I.; Ersen, O.; Boissière, C.; Mézailles, N.; Sanchez, C. *Chemistry of Materials* **2012**, *24* (21), 4134–4145.

(11) Harris, D. K.; Bawendi, M. G. *Journal of the American Chemical Society* **2012**, *134* (50), 20211–20213.

(12) Adachi, S. *Properties of Group-IV, III-V and II-VI Semiconductors: Adachi/Properties of Group-IV, III-V and II-VI Semiconductors*; John Wiley & Sons, Ltd: Chichester, UK, 2005.

(13) Douglas, T.; Theopold, K. H. *Inorganic Chemistry* **1991**, *30* (4), 594–596.

(14) Becker, G.; Schmidt, H.; Uhl, G.; Uhl, W.; Regitz, M.; Rsch, W.; Vogelbacher, U.-J. In *Inorganic Syntheses*; Ginsberg, A. P., Ed.; John Wiley & Sons, Inc.: Hoboken, NJ, USA, 1990; Vol. 27, pp 243–249.

(15) Goel, S. C.; Chiang, M. Y.; Rauscher, D. J.; Buhro, W. E. *Journal of the American Chemical Society* **1993**, *115* (1), 160–169.

(16) Xie, R.; Battaglia, D.; Peng, X. *Journal of the American Chemical Society* **2007**, *129* (50), 15432–15433.

(17) Mutlugun, E.; Hernandez-Martinez, P. L.; Eroglu, C.; Coskun, Y.; Erdem, T.; Sharma, V. K.; Unal, E.; Panda, S. K.; Hickey, S. G.; Gaponik, N.; Eychmüller, A.; Demir, H. V. *Nano Letters* **2012**, *12* (8), 3986–3993.

(18) Li, L.; Reiss, P. *Journal of the American Chemical Society* **2008**, *130* (35), 11588–11589.

(19) Thuy, U. T. D.; Huyen, T. T. T.; Liem, N. Q.; Reiss, P. *Materials Chemistry and Physics* **2008**, *112* (3), 1120–1123.

(20) Cros-Gagneux, A.; Delpech, F.; Nayral, C.; Cornejo, A.; Coppel, Y.; Chaudret, B. *Journal of the American Chemical Society* **2010**, *132* (51), 18147–18157.

(21) Mićić, O. I.; Cheong, H. M.; Fu, H.; Zunger, A.; Sprague, J. R.; Mascarenhas, A.; Nozik, A. J. *The Journal of Physical Chemistry B* **1997**, *101* (25), 4904–4912.

(22) Atkins, P. *Shriver and Atkins' Inorganic Chemistry*; OUP Oxford, 2010.

(23) McLean, D. S.; Vercoe, D.; Stack, K. R.; Richardson, D. E. *Appita Journal* **2005**, *58* (5), 362–366.

(24) Xie, L.; Zhao, Q.; Jensen, K. F.; Kulik, H. J. *The Journal of Physical Chemistry C* **2016**, *120* (4), 2472–2483.

(25) Cottrell, T. L. *The Strengths of Chemical Bonds*, 2nd edition.; Academic Press/Butterworths, 1958.

(26) Owen, J. S.; Park, J.; Trudeau, P.-E.; Alivisatos, A. P. *Journal of the American Chemical Society* **2008**, *130* (37), 12279–12281.

(27) Anderson, N. C.; Owen, J. S. *Chemistry of Materials* **2013**, *25* (1), 69–76.

(28) Frederick, M. T.; Achtyl, J. L.; Knowles, K. E.; Weiss, E. A.; Geiger, F. M. *Journal of the American Chemical Society* **2011**, *133* (19), 7476–7481.

(29) Fritzinger, B.; Capek, R. K.; Lambert, K.; Martins, J. C.; Hens, Z. *Journal of the American Chemical Society* **2010**, *132* (29), 10195–10201.

(30) Yu, W. W.; Peng, X. *Angewandte Chemie International Edition* **2002**, *41* (13), 2368–2371.

(31) Bullen, C. R.; Mulvaney, P. *Nano Letters* **2004**, *4* (12), 2303–2307.

(32) Alivisatos, A. P.; Peng, X.; Manna, L.; Yang, W.; Wickham, J.; Scher, E.; Kadavanich, A. *Nature* **2000**, *404* (6773), 59–61.

(33) Peng, X.; Wickham, J.; Alivisatos, A. P. *Journal of the American Chemical Society* **1998**, *120* (21), 5343–5344.

(34) Franke, D.; Harris, D. K.; Xie, L.; Jensen, K. F.; Bawendi, M. G. *Angewandte Chemie International Edition* **2015**, *54* (48), 14299–14303.

(35) Wang, F.; Tang, R.; Buhro, W. E. *Nano Letters* **2008**, *8* (10), 3521–3524.

(36) Wang, F.; Tang, R.; Kao, J. L.-F.; Dingman, S. D.; Buhro, W. E. *Journal of the American Chemical Society* **2009**, *131* (13), 4983–4994.

(37) García-Rodríguez, R.; Hendricks, M. P.; Cossairt, B. M.; Liu, H.; Owen, J. S. *Chemistry of Materials* **2013**, *25* (8), 1233–1249.

(38) Evans, C. M.; Evans, M. E.; Krauss, T. D. *Journal of the American Chemical Society* **2010**, *132* (32), 10973–10975.

(39) Hendricks, M. P.; Cossairt, B. M.; Owen, J. S. *ACS Nano* **2012**, *6* (11), 10054–10062.

(40) Cossairt, B. M.; Owen, J. S. *Chemistry of Materials* **2011**, *23* (12), 3114–3119.

Chapter 3: Investigation of the Effect of Precursor Conversion Kinetics on the Nucleation and Growth of InP Nanocrystals via Arylsilylphosphines and Alkylsilylphosphines

3.1 Introduction

The most successful and widely studied syntheses of colloidal InP rely on the hot injection method, where $P(Si(CH_3)_3)_3$ is introduced into an indium carboxylate salt in a high-boiling point solvent near 300 °C.[1–5] $P(Si(CH_3)_3)_3$ is commonly employed because it has the correct electronic disposition to deliver P^{3-} to the In^{3+} without the need for distinct oxidation or reduction steps. However, this highly reactive silylphosphine is completely consumed within seconds of injection, precluding the necessary existence of monomer reserves for an extended growth period.[2–4] Moreover, the reactivity of $P(Si(CH_3)_3)_3$ creates a situation in which precursor conversion, nucleation, and growth (the three stages of colloid formation according to the LaMer model of crystallization shown in Scheme 3.1[5]) all occur simultaneously. Thus, this reagent is unable to temporally separate nucleation and growth events and does not maintain adequate monomer reserves for prolonged periods of growth, therefore limiting access to InP semiconductor nanocrystals (quantum dots, QDs) over a wide range of sizes.[6–8] Therefore, new syntheses of InP aimed at controlling monomer delivery rates using alternative precursors are needed, few of which have been documented.[9]

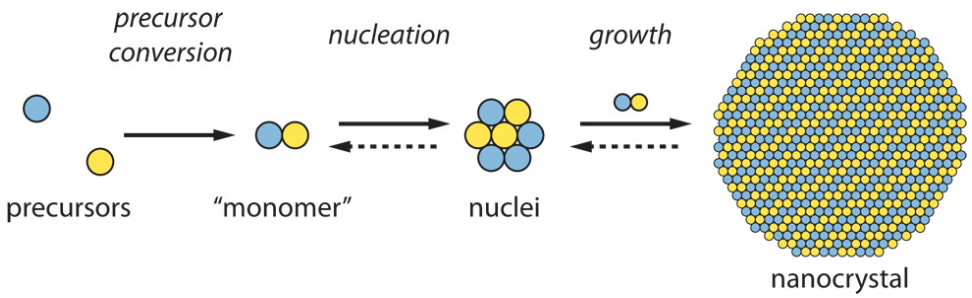

Scheme 3.1 Cartoon depiction of the three stages of colloidal crystallization: precursor conversion, nucleation, and growth.

In Chapter 2, we discovered that even when employing non-protic myristate sources to avoid the protonolysis of $P(Si(CH_3)_3)_3$, precursor conversion rates were still rapid enough to completely deplete monomer reserves during the nucleation event (see Chapter 2 Figure 2.10).[4] In order to enable kinetic size control of InP nanocrystals a slow, steady production of monomers from precursor conversion must be achieved so that the growth is reaction limited rather than diffusion limted.[10–12,8,13,14] Previous efforts have focused on synthesizing less reactive analogues of $P(Si(CH_3)_3)_3$ with the aim of decreasing P–X bond strength[9] (substituting Ge for Si, for example) or increasing steric bulk about the P atom[15] with the aim of decreasing precursor conversion rates. Inspired by these approaches, we set out to combine these strategies by synthesizing a new class of sterically encumbered triarylsilylphosphines ($P(Si(C_6H_4X)_3)_3$) (where X = H, CH_3, CF_3, or Cl) in hopes of fine-tuning precursor conversion rates by choice of electron withdrawing or donating groups to modulate P–Si bond strength. DFT calculations were performed to obtain an optimized geometry for $P(Si(C_6H_5)_3)_3$. These calculations predicted $P(Si(C_6H_5)_3)_3$ should exhibit a significant distortion from the tetrahedral geometry about the phosphorus atom seen for $P(Si(CH_3)_3)_3$ to a nearly trigonal planar geometry due to the steric bulk of the triarylsilyl groups. Despite the steric bulk about the phosphorus atom, $P(Si(C_6H_5)_3)_3$ is a known compound[16] (X = H) which provided strong evidence that the synthesis of this new class of arylsilylphosphines would be feasible.

3.2 Results and Discussion

3.2.1 Employing $P(Si(C_6H_4X)_3)_3$ as a P^{3-} Precursor for InP QDs (where X = H, Cl, CF_3, and CH_3)

A series of sterically demanding para-substituted triarylsilylphosphines were prepared from red phosphorus, $HSiCl_3$, and the appropriate aryl Grignard reagent to explore their effect on monomer delivery rate in the synthesis of InP nanocrystals. Our original hypothesis was that electron-donating groups (EDGs) or electron-withdrawing groups (EWGs) at the para position in each aromatic ring would provide a means of controlling the rate of delivery of the InP monomer to the system by fine-tuning the P–Si bond polarity as well as the basicity at phosphorus. InP QDs were grown by injecting a room-temperature solution of silylphosphine (1 equivalent) in a eutectic mixture of diphenyl ether and biphenyl[9] into a solution of indium myristate (2 equivalents) and myristic acid (0.6 equivalents) in 1-octadecene at 315 °C. Growth was then maintained at 270 °C for 90 minutes (Scheme 3.2). The QD growth was monitored by UV-Vis absorption spectroscopy using aliquots taken over the course of the reaction. All InP QDs explored in this study using either the newly prepared triarylsilylphosphines or tris(trimethylsilyl)phosphine exhibit photoluminescence quantum yields of <1%, consistent with previous reports of bare InP cores.[17,18]

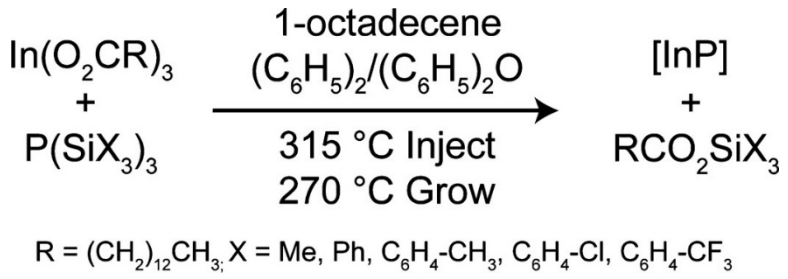

Scheme 3.2 Reaction scheme for the synthesis of InP nanocrystals from silylphosphines and indium carboxylates.

The absorbance at 310 nm, a region in which the InP extinction coefficient is relatively size-independent[9,19] and thus indicative of InP concentration in all forms, revealed two distinct InP production rates for $P(Si(CH_3)_3)_3$, $P(Si(C_6H_5)_3)_3$, $P(Si(C_6H_4CH_3)_3)_3$, $P(Si(C_6H_4Cl)_3)_3$, and $P(Si(C_6H_4CF_3)_3)_3$ rather than a continuum of InP formation rates as originally hypothesized (Figure 3.1A). The normalized absorbance at 310 nm shows that $P(Si(C_6H_4CF_3)_3)_3$ and $P(Si(C_6H_4Cl)_3)_3$ (panels D and F of Figure 3.1, respectively) resulted in rapid formation of InP with approximately 90% conversion to InP within 30 minutes, as indicated by the absorption at 310 nm in the UV-Vis spectrum. This rapid formation of InP is also observed for syntheses solely employing $P(Si(CH_3)_3)_3$ (Figure 3.1B). In contrast, both $P(Si(C_6H_5)_3)_3$ and $P(Si(C_6H_4CH_3)_3)_3$ require approximately 60 minutes to exhibit a similar degree of precursor conversion (panels C and E of Figure 3.1, respectively). Similarly, the wavelength of maximal absorbance (λ_{max}) for the lowest energy electronic transition (LEET) from the UV-Vis spectra of the 90 minutes timed aliquots of analogous syntheses reveals two distinct final particle sizes with a λ_{max} of approximately 530 nm for the rapidly reacting precursors $P(Si(CH_3)_3)_3$, $P(Si(C_6H_4Cl)_3)_3$ and $P(Si(C_6H_4CF_3)_3)_3$ and a λ_{max} of approximately 585 nm for $P(Si(C_6H_5)_3)_3$ and $P(Si(C_6H_4CH_3)_3)_3$ indicative of average particle diameters of approximately 3 and 4 nm, respectively.[20]

That we see two distinct rates rather than a continuum of rates for the para-substituted triarylsilylphosphines is suggestive of two distinct mechanistic pathways in this class of compounds (or one mechanism with two different rate-determining steps). Steric bulk was expected to play a major role in altering the reactivity of the phosphine precursors; however, all the para-substituted triarylsilylphosphines have similar cone angles (Σ Si–P–Si angles of 335 ± 1° for all triarylsilylphosphines from DFT calculations), yet we see that silylphosphines with EDGs react slowly and silylphosphines with EWGs rapidly. Two potential mechanisms are presented in Scheme 3.3, one involving preformation of an In–phosphine complex and subsequent S_N2-like reactivity (Scheme 3.3

mechanism A) and the other involving P–Si bond ionization prior to reaction with indium carboxylate (Scheme 3.3 mechanism B). We would suspect that mechanism A would be facilitated by EWGs in the para positions placing a partial positive charge on the silicon and facilitating attack by the oxygen nucleophile. In the case of EDGs, such a pathway might be prohibitively slow, raising the possibility of mechanism B. This makes sense from an electronic structure perspective and is provocative with respect to designing new phosphine precursors with covalent or ionic character for phosphide material synthesis.

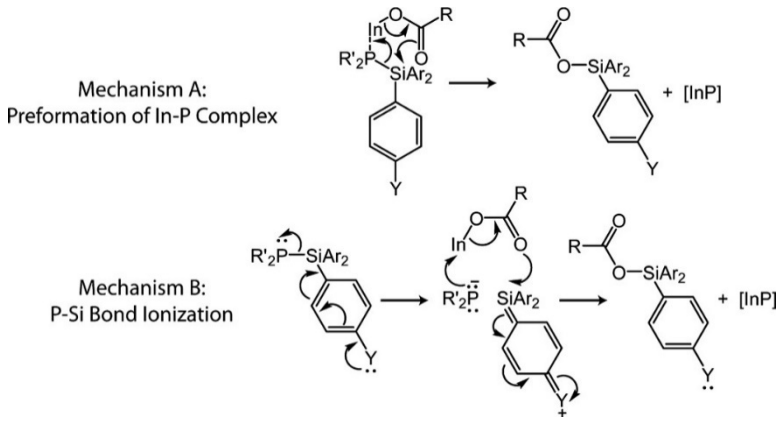

Scheme 3.3 Two proposed mechanisms for InP formation from $P(Si(C_6H_5Y)_3)_3$ and $In(O_2CR)_3$.

Observation of a chemical transformation of the P^{3-} precursor prior to incorporation into InP would undermine the efforts of designing these novel reaction-limiting precursors. In the case of the sluggishly reacting $P(Si(C_6H_5)_3)_3$ precursor, nuclear magnetic resonance (NMR) spectroscopy should allow an opportunity to track its conversion prior to incorporation into nanocrystals. Using this technique, previous investigations in our lab have uncovered the detrimental speciation of $P(Si(CH_3)_3)_3$ to $H_nP(Si(CH_3)_3)_{3-n}$ prior to InP formation in the presence of various proton sources, such as carboxylic acids, which are commonly used as ligands in QD syntheses.[4] Control experiments that yield InP QDs performed with 2 equivalents of $In(O_2C(CH_2)_{12}CH_3)_3$, 1 equivalent of $P(Si(C_6H_5)_3)_3$, and 0.6 equivalents of $HO_2C(CH_2)_{12}CH_3$ in a sealed J. Young NMR tube heated to 285 °C demonstrate

the slow, monotonic disappearance of $P(Si(C_6H_5)_3)_3$ over the same time period as InP growth is observed by UV-Vis spectroscopy (Figure 3.2). The fact that no speciation byproducts or molecular intermediates are observed during this slow reaction suggests strongly that precursor conversion is the rate-limiting step in the synthesis of InP QDs from $P(Si(C_6H_5)_3)_3$. These results, in conjunction with the absorbance at 310 nm from the UV-Vis spectra of time aliquots of reactions solely utilizing $P(Si(C_6H_5)_3)_3$, suggest that precursor conversion remains rate-limiting throughout the growth of the nanoparticles with the exclusion of any appreciable buildup of molecular intermediates, such as $(RCO_2)_2In–P(Si(C_6H_5)_3)_2$, which is one possible monomer candidate.

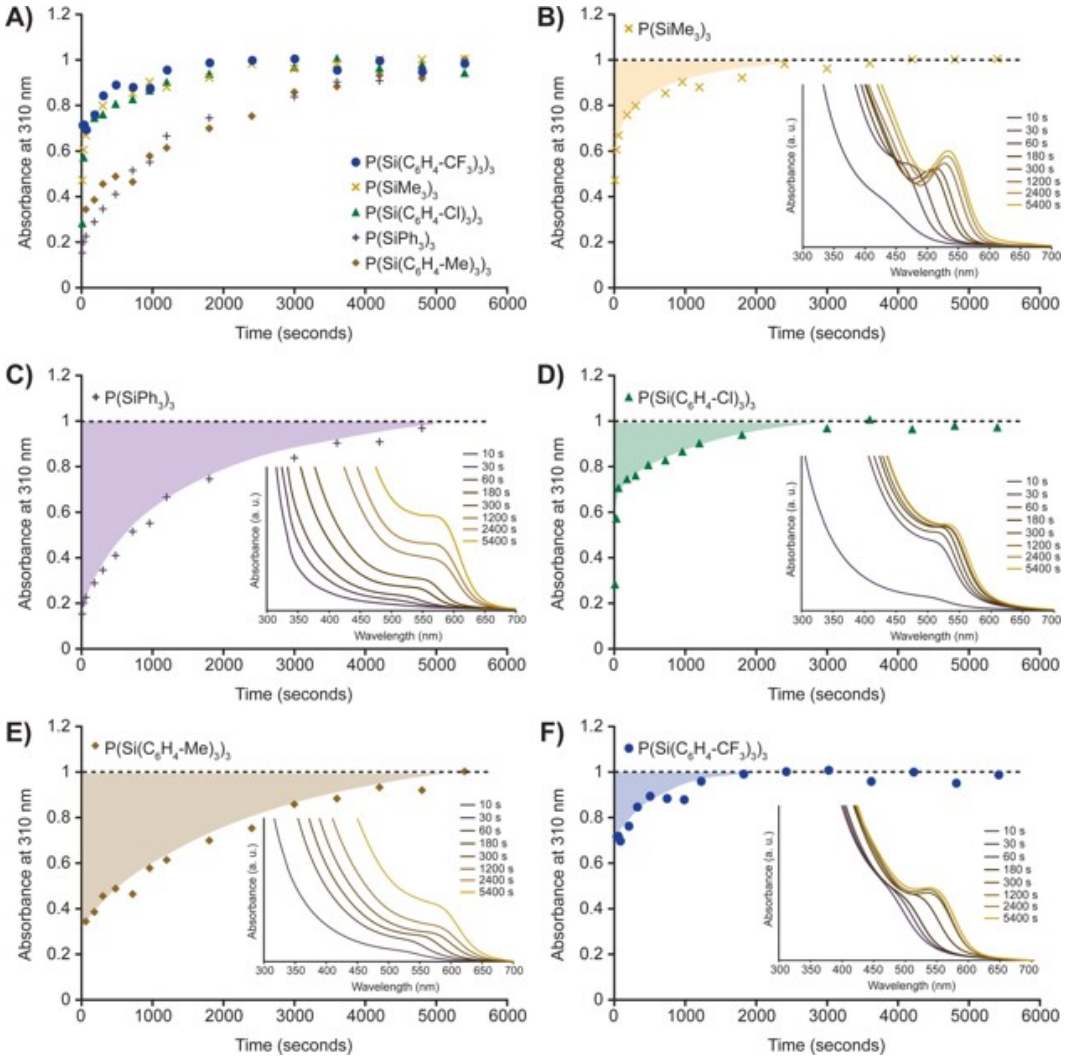

Figure 3.1 (A) Normalized absorbance at 310 nm for all phosphines plotted on a single scale to visualize the two distinct precursor reactivity regimes. All curves are an average of three separate InP syntheses. (B–F) Normalized absorbance at 310 nm and UV-Vis time aliquots for InP growth from (B) $P(Si(CH_3)_3)_3$, (C) $P(Si(C_6H_5)_3)_3$, (D) $P(Si(C_6H_4Cl)_3)_3$, (E) $P(Si(C_6H_4CH_3)_3)_3$, and (F) $P(Si(C_6H_4CF_3)_3)_3$.

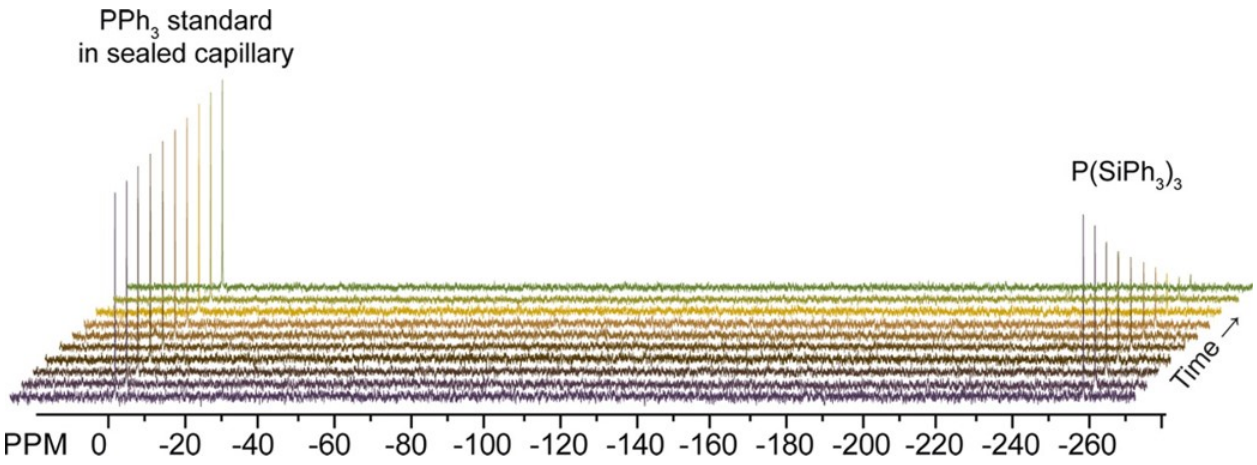

Figure 3.2 $^{31}P\{^{1}H\}$ NMR spectra monitoring the disappearance of $P(Si(C_6H_5)_3)_3$ in the presence of $In(O_2C(CH_2)_{12}CH_3)_3$ and myristic acid at 285 °C over the course of 120 minutes. Each spectrum was separately acquired after the sample had been cooled to 25 °C.

3.2.2 Analysis of InP Consumption from Nucleation and Growth from $P(Si(C_6H_4X)_3)_3$ Precursors

Given the varied reactivity of our $P(Si(C_6H_4X)_3)_3$ precursors, we were curious about their relative abilities to separate nucleation and growth during the synthesis of InP. The ability to temporally separate nucleation and growth allows for minimizing the disparity in particle growth history and is therefore one effective strategy for targeting monodisperse particles.[6–8] The low reactivity of $P(Si(C_6H_5)_3)_3$ and $P(Si(C_6H_4CH_3)_3)_3$ relative to $P(Si(CH_3)_3)_3$ as observed by $^{31}P\{^{1}H\}$ NMR spectroscopy and normalized absorbance at 310 nm casts doubt on the idea that nucleation and growth are distinct processes in syntheses that employ these precursors. Calculations were performed to determine if the total fraction of InP required for nanocrystal growth based on a spherical, stoichiometric model from the first observed size distribution (30 seconds time aliquot) agreed with the total amount of InP available to the system at that point (assuming complete consumption of

phosphorus at 100% conversion). These calculations suggest that approximately 70% of the InP produced during the growth process as observed by the increase in absorbance at 310 nm in syntheses using $P(Si(C_6H_5)_3)_3$ cannot be ascribed to the growth of the initially produced (30 second aliquot) particles alone. This discrepancy requires that additional nuclei are being formed during the growth process in the case of $P(Si(C_6H_5)_3)_3$ and $P(Si(C_6H_4CH_3)_3)_3$. The exact opposite trend is obtained from calculations performed for $P(Si(CH_3)_3)_3$. This precursor not only consumes a very large fraction of the available phosphorus in the form of InP within 30 seconds but also exhibits a rather wide growth range. An additional 40% of the total phosphorus relative to the amount initially supplied to the system would be required for growth to arise exclusively from molecular precursors in the $P(Si(CH_3)_3)_3$ system as modeled. We interpret this discrepancy to indicate that the majority of the growth indicated by the bathochromic shift in the spectra of timed aliquots arises from a ripening growth mechanism. This result reinforces the hypothesis that $P(Si(CH_3)_3)_3$ does not have the ideal reactivity properties to give itself temporally resolved nucleation and growth windows and that improved precursors should be sought. While these calculations are very rough approximations of each system, the results are qualitatively significant for comparison among all precursors.

None of the QD syntheses with substituted triarylsilylphosphines exhibited final size distributions that were improved or even comparable to that of $P(Si(CH_3)_3)_3$ (Figure 3.1). This is not surprising for precursors with EDGs, where nucleation and growth occur simultaneously and monomer concentrations are low throughout the growth process because of slow precursor conversion. Another explanation is needed, however, to understand why $P(Si(C_6H_4Cl)_3)_3$ and $P(Si(C_6H_4CF_3)_3)_3$ do not exhibit size distributions as narrow as those observed for $P(Si(CH_3)_3)_3$ when all three precursors exhibit nearly identical rates of InP formation and final particle sizes. A clue may be provided in the comparison of the change in λ_{max} at the LEET throughout the growth process for the substituted triarylsilylphosphines versus $P(Si(CH_3)_3)_3$. For $P(Si(C_6H_4Cl)_3)_3$, the first spectral feature

indicative of a distinct band gap transition is observed for the 10 second aliquot with a λ_{max} of approximately 515 nm. From there, the timed aliquots reveal rapid growth, to the final position of 535 nm after ~12 minutes (Figure 3.1D). While the growth is also relatively fast for $P(Si(CH_3)_3)_3$, the first spectral feature indicative of a distinct band gap is observed for the 30 second aliquot with a λ_{max} of 455 nm and grows to the same final position of 535 nm after ~30 minutes (Figure 3.1B). One explanation for these results is that while both of these precursors form similar numbers of stable nuclei and consume similar amounts of InP during their growth phases, the active monomer species responsible for growth generated from $P(Si(C_6H_4Cl)_3)_3$ is considerably more reactive than the species generated by $P(Si(CH_3)_3)_3$ and therefore leads to a more rapid consumption of the active monomer. A trend similar to that of $P(Si(C_6H_4Cl)_3)_3$ is observed for $P(Si(C_6H_4CF_3)_3)_3$ (see Figure 3.1F). This may be related to the greater covalency of the P–Si bond for the Cl and CF_3 substituted triarylsilylphosphines and potentially different mechanisms of monomer formation and/or consumption as compared with $P(Si(CH_3)_3)_3$, $P(Si(C_6H_5)_3)_3$, and $P(Si(C_6H_4CH_3)_3)_3$ reagents, as mentioned previously (Scheme 3.3).

To further illustrate this point, using the same spherical, stoichiometric model assumed previously, the number of InP units required to grow the nanocrystals from the 30 second time aliquot to the 90-minute time aliquot was calculated. For each nanocrystal, 200 InP units were required in the case of $P(Si(CH_3)_3)_3$ on average, while only 70 InP units were required in the case of $P(Si(C_6H_4Cl)_3)_3$. The large growth window of $P(Si(CH_3)_3)_3$ demonstrates that even though precursor conversion is as rapid as that observed for $P(Si(C_6H_4Cl)_3)_3$ and $P(Si(C_6H_4CF_3)_3)_3$, growth from InP monomers is still slower than what is observed for the triarylsilylphosphines with EWGs. Additionally, size distributions from the syntheses that employ $P(Si(CH_3)_3)_3$ as the sole P^{3-} source are more narrow than either those that incorporate $P(Si(C_6H_4CF_3)_3)_3$ or $P(Si(C_6H_4CF_3)_3)_3$. If this interpretation is valid, it serves to highlight another important criterion for the synthesis of monodisperse InP beyond the separation of the nucleation and growth events: the active monomer species must not be so reactive as to lead to

rapid depletion of monomer feedstock with indiscriminate growth. This is particularly a concern in InP and similarly covalent materials because of the potential lack of reversibility in the nucleation and growth reactions.

3.2.3 Employing a Two-Phosphine Strategy in Order to Separate Nucleation and Growth

Colloidal, binary semiconductor nanoparticle syntheses typically incorporate either a single source precursor or, at most, a single chemical species as the sole precursor for each element of the semiconductor.[1–3,21–24] Though the method is unconventional, the substantial differences in both the fraction of total InP consumed during nucleation and the disparate precursor conversion rates imply that utilizing both $P(Si(CH_3)_3)_3$ and $P(Si(C_6H_5)_3)_3$ simultaneously could have a synergistic effect. In such a scheme, $P(Si(CH_3)_3)_3$ would serve as a source of InP nuclei, while $P(Si(C_6H_5)_3)_3$ would act as an *in situ* reservoir of InP monomers to grow on the nuclei generated by $P(Si(CH_3)_3)_3$. In this way, it may be possible to artificially replicate a LaMer-like growth profile by independently toggling nucleation and growth, an approach that is not feasible for a single P^{3-} source. We sought to test this hypothesis by synthesizing InP QDs from mixtures of P^{3-} precursors.

The final particle size obtained from these syntheses decreases with an increase in the $P(Si(CH_3)_3)_3$: $P(Si(C_6H_5)_3)_3$ ratio, suggesting that the total number of nuclei formed increases with an increase in the $P(Si(CH_3)_3)_3$: $P(Si(C_6H_5)_3)_3$ ratio, as would be expected from classical nucleation theory and studies of related colloidal systems (Figure 3.3).[7,25–30] Further, the range of average particle band gaps observed in a single reaction is large (2.25–2.61 eV), suggesting independent nucleation and growth regimes (Figure 3.4). The FWHM of the 90 minute time aliquot decreases with an increase in the $P(Si(CH_3)_3)_3$: $P(Si(C_6H_5)_3)_3$ ratio from 80 nm for the 0.1:1 case to 65 nm for the 3:1 case.(21) This indicates that even though nucleation and growth are better separated in reactions run with dual P^{3-}

sources than with $P(Si(C_6H_5)_3)_3$ alone, the precursor conversion rate of $P(Si(C_6H_5)_3)_3$ is too slow (monomer concentrations remain too low) for $P(Si(C_6H_5)_3)_3$ to act as an ideal reservoir of InP monomers and supplement the nuclei generated by $P(Si(CH_3)_3)_3$. If the delivery of InP monomer from conversion of $P(Si(C_6H_5)_3)_3$ and $In(O_2C(CH_2)_{12}CH_3)_3$ could be accelerated, the dual P^{3-} sources might be able to better complement each other. With this in mind, experiments were conducted to determine if the precursor conversion rate of $P(Si(C_6H_5)_3)_3$ and $In(O_2C(CH_2)_{12}CH_3)_3$ could be increased by modifying the reaction conditions. Reactions were conducted at 2 and 4 times the total concentration (0.17 M In with 0.086 M P and 0.34 M In with 0.17 M P, respectively) of all reagents using $P(Si(C_6H_5)_3)_3$ as the sole source of P^{3-} to assess the dependency of the InP monomer production rate on total concentration. The 2 times total concentration experiment showed a dramatic increase in the production rate of InP as seen in the normalized absorbance at 310 nm (Figure 3.5). The 4 times concentration experiment showed almost no difference from the 2 times total concentration experiment in the rate of InP formation (Figure 3.5).

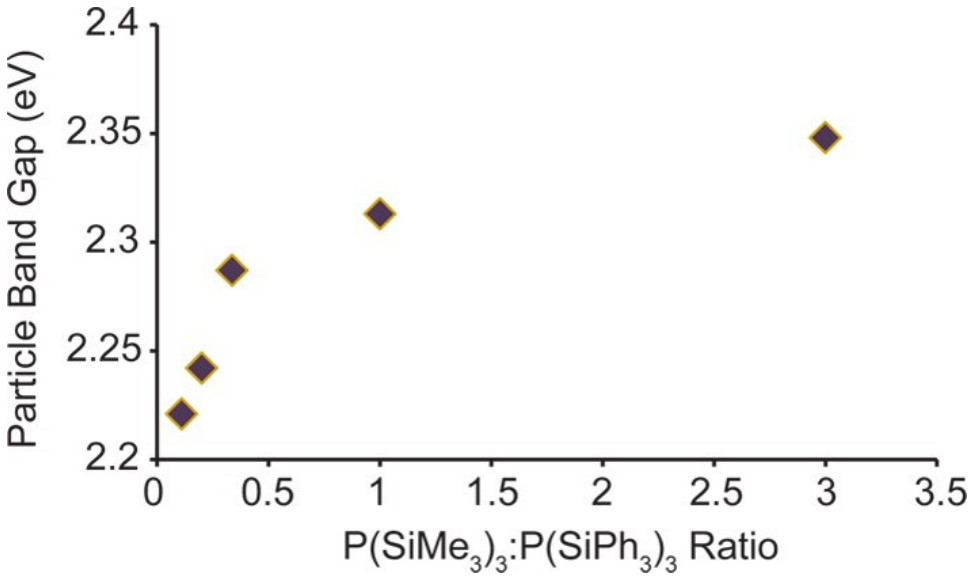

Figure 3.3 Plot of band gap energy vs $P(Si(CH_3)_3)_3$: $P(Si(C_6H_5)_3)_3$ ratio for 90-minute time aliquots. As the $P(Si(CH_3)_3)_3$: $P(Si(C_6H_5)_3)_3$, ratio increase, particle size decreases which is consistent with a reaction scheme where nucleation proceeds via conversion of $P(Si(CH_3)_3)_3$ to InP and subsequent growth occurs via precursor conversion of $P(Si(C_6H_5)_3)_3$ to InP.

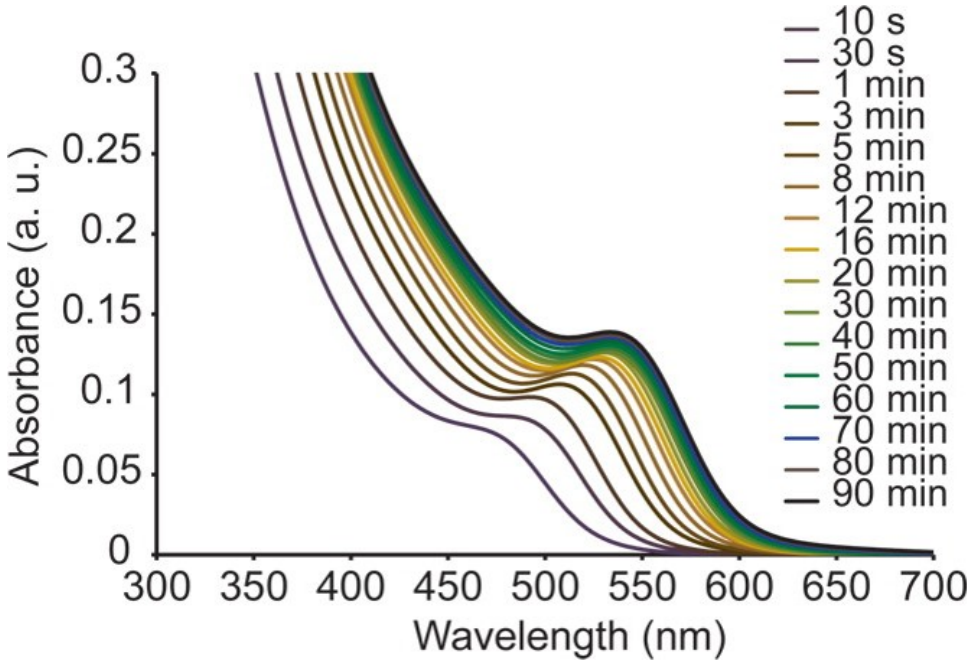

Figure 3.4 Representative growth profile for InP QDs prepared using a 0.33:1 $P(Si(CH_3)_3)_3$: $P(Si(C_6H_5)_3)_3$ mixture. Growth of InP (as observed by the red-shift of the LEET) is accompanied by an increase in total absorbance in the UV suggestive that nanoparticle growth occurs via new monomer production rather than ripening processes

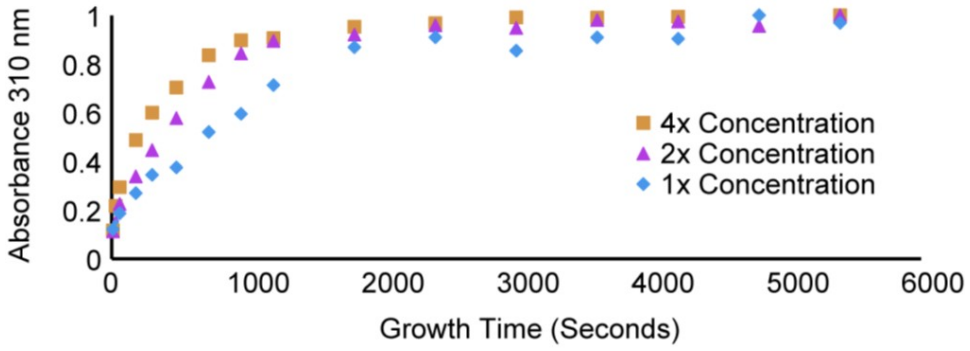

Figure 3.5 Normalized absorbance at 310 nm for InP QDs grown from $P(Si(C_6H_5)_3)_3$ at 1 times (0.086 M In with 0.043 M P), 2 times (0.17 M In with 0.086 M P) and 4 times (0.34 M In with 0.17 M P) total concentration. The rate of InP formation increased considerably from the first increase in concentration, but only shows a modest increase from the second increase in concentration.

These results suggest that the rate of InP formation can be significantly altered by concentration, as would be expected for a reaction that is limited by the rate of the precursor conversion process, but the system is saturated beyond a certain point, where precursor conversion is no longer influenced by an increase in the total concentration. While the final particle size and total fraction of InP produced are independent of total concentration, the 2 times total concentration experiment shows a definitive narrowing of the final size distribution relative to the 1 and 4 times concentration experiments. This suggests that there is an optimal total concentration for selective growth that exists between the 4 and 1 times syntheses (Figure 3.6).

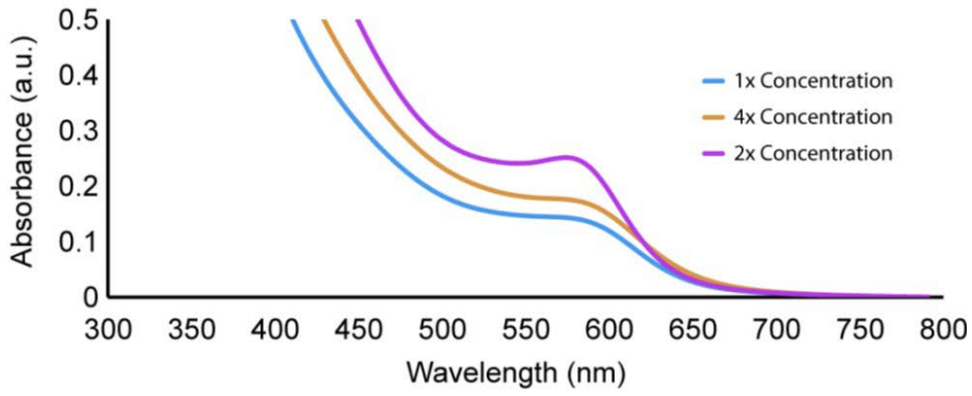

Figure 3.6 UV-Vis spectra of 90 minute (final) time aliquots for InP QDs synthesized with $P(Si(C_6H_5)_3)_3$ at various total concentrations. The two times total concentration ((0.17 M In with 0.086 M P) was found to be optimal for syntheses employing $P(Si(C_6H_5)_3)_3$ as the sole P^{3-} source.

In a final set of experiments, InP QDs were grown using a mixture of $P(Si(CH_3)_3)_3$ and $P(Si(C_6H_5)_3)_3$ with $P(Si(C_6H_5)_3)_3$ at double concentration [Figure 3.7A, 0.086 M In, 0.086 M $P(Si(C_6H_5)_3)_3$, and 0.043 M $P(Si(CH_3)_3)_3$]. These conditions showed a broader range of isolable sizes and compared to the previous data shown in Figure 3.4. TEM analysis of InP QDs grown under these conditions shows faceted particles exhibiting average sizes in agreement with those computed from the position of the LEET (~3.5 nm) and show somewhat elevated polydispersity as evidenced by TEM (Figure 3.7) and the FWHM of the LEET (0.28 eV, 70 nm) when compared with QDs prepared from $P(Si(CH_3)_3)_3$ alone (0.27 eV, 62 nm).

This result serves to highlight the conditions for optimal synergy between these two P^{3-} sources (shown schematically in Figure 3.7B). While nucleation and growth are distinct processes for $P(Si(CH_3)_3)_3$ even at low concentrations because of its extreme reactivity, $P(Si(C_6H_5)_3)_3$ requires greater solution concentrations of P relative to In (1.5:1 P:In ratio depicted in Figure 3.7) to preserve a narrow size distribution. Further, the optimal ratio of $P(Si(CH_3)_3)_3$ to $P(Si(C_6H_5)_3)_3$ was 1:2 (depicted in Figure

3.7). Under these conditions, nucleation and growth are temporally distinct processes. For comparison, note that increasing the concentration of $P(Si(CH_3)_3)_3$ relative to that of $P(Si(C_6H_5)_3)_3$ without modifying any other reagent concentration did not significantly narrow size distributions but rather narrowed the spectral window of isolable sizes due to a smaller total fraction of InP produced from the growth event. On the basis of our results, it is reasonable to assume that the majority of the InP produced during the nucleation event was due to the consumption of $P(Si(CH_3)_3)_3$ and the growth on the nuclei to produce InP QDs is mainly from consumption of $P(Si(C_6H_5)_3)_3$. This is evident from the longer time profile for the bathochromic shift in the spectra, indicative of $P(Si(C_6H_5)_3)_3$-like growth. This interpretation is further reinforced with calculations based on a spherical model, which suggest nearly all of the InP generated after the 30 seconds time aliquot serves solely to grow the particles to their final size with a minimal contribution from nonmolecular ripening.

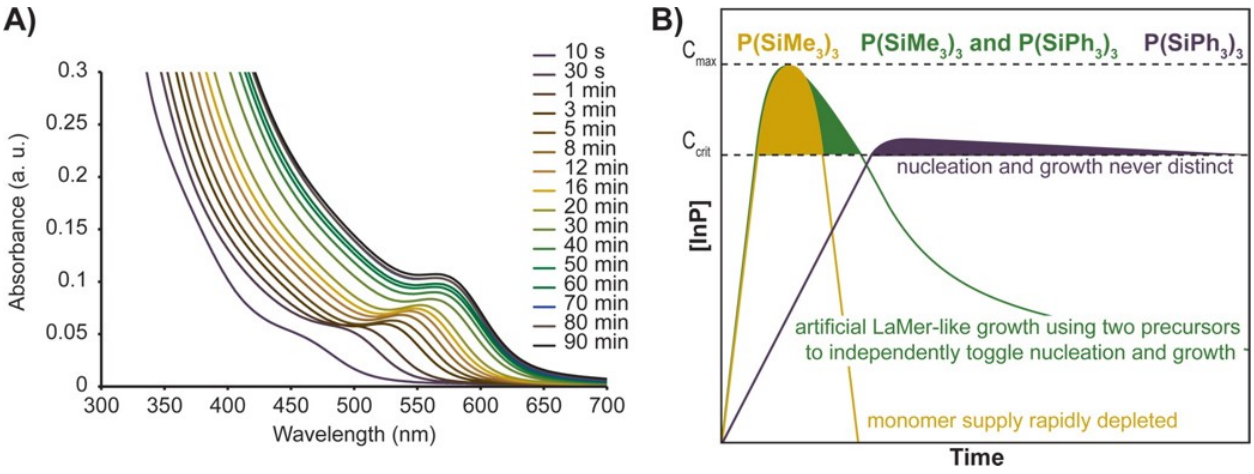

Figure 3.7 (A) Representative growth profile for InP QDs prepared using a mixture of $P(Si(CH_3)_3)_3$ and $P(Si(C_6H_5)_3)_3$ with 2 equivalents of $P(Si(C_6H_5)_3)_3$ (0.086 M) and 1 equivalent of $P(Si(CH_3)_3)_3$ (0.043 M). (B) Schematic representation of the InP concentration vs time for $P(Si(CH_3)_3)_3$ (gold), $P(Si(C_6H_5)_3)_3$ (purple), and the mixture of the two reagents (green) depicting how taking two reagents with disparate reactivity allows for the separation of nucleation and growth while maintaining a monomer reservoir.

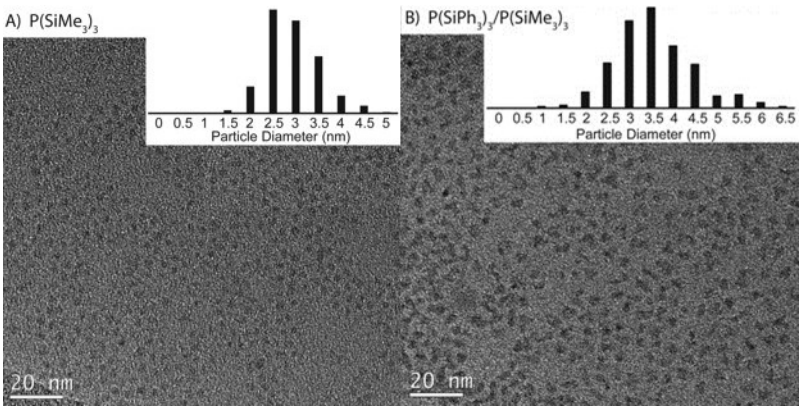

Figure 3.8 Representative TEM images for InP QDs prepared using (A) $P(Si(CH_3)_3)_3$ (2.6 ± 0.6 nm) and (B) a 1:2 $P(Si(CH_3)_3)_3$: $P(Si(C_6H_5)_3)_3$ mixture (3.4 ± 1.0 nm). Histograms of average sizes represent data from at least 300 individual QDs.

Corroboration of our interpretation of growth solely from $P(Si(C_6H_5)_3)_3$ is provided by delayed injection of the $P(Si(C_6H_5)_3)_3$ into InP particles already prepared with $P(Si(CH_3)_3)_3$. Experiments performed with injection of $P(Si(C_6H_5)_3)_3$ after 1, 5, or 30 minutes show no difference in terms of the final particle size (580–585 nm LEET) compared with the results of experiments in which $P(Si(CH_3)_3)_3$ and $P(Si(C_6H_5)_3)_3$ were combined in a single injection as described for the data presented in Figure 3.7 (575 nm LEET). Indeed, injection after 1 minute gives both a final size and a final size distribution comparable with what is observed in experiments in which both reagents are combined in a single syringe. It appears, however, that monodispersity suffers (as evidenced by the FWHM of the LEET) if injection after 5 or 30 minutes is not also accompanied by the addition of indium myristate, which is common for more traditional seeded growth approaches.[1]

Several notable literature examples of InP nanocrystal formation over a range of sizes provide a basis for comparing our results. In 2002, Peng and co-workers detailed the synthesis of high-quality InP QDs over a range of sizes using multiple injections of $P(Si(CH_3)_3)_3$.[1] This procedure relied on

maintaining an indium-rich environment and therefore necessitated alternating injections of indium(III) and $P(Si(CH_3)_3)_3$. Over a total of 10 injections, the researchers were able to grow the particles from an initial size of 3.3 nm (550 nm LEET) to a final size of 3.9 nm (590 nm LEET). Modeling this as growth solely from addition of new InP monomers and assuming a spherical and stoichiometric model suggest the addition of 252 InP units per QD. Numerous related studies, including those targeting highly emissive core–shell structures, have produced similar results.[21,31,32] Analyzing our best results from the combination of $P(Si(CH_3)_3)_3$ and $P(Si(C_6H_5)_3)_3$, we see growth from an initial size of 2.3 nm (465 nm LEET) to a final size of 3.7 nm (574 nm LEET), with 378 InP monomers added to each QD during growth from $P(Si(C_6H_5)_3)_3$. This demonstrates a notable improvement in size range over the multiple-$P(Si(CH_3)_3)_3$ injection approach. Another system in which a broad range of InP QD sizes was targeted was the supercritical octane microflow system devised by Bawendi and co-workers in 2011.[33] This system allows different sized InP QDs to be targeted on the basis of the reactor flow rate and the In:P ratio used in a given experiment, allowing particles from about 2 to 3.2 nm to be accessed.[20] This synthetic scheme, however, necessitates the use of a microfluidic system and solvents that permit high pressures to be obtained, making the system of limited utility in terms of scalability and adaptability to different ligand sets. Notably, our two-precursor approach is complementary to and could be used in conjunction with all these previously developed techniques to further extend the available size range of InP QDs.

3.3 Conclusions

We have successfully perturbed the rate of InP delivery during the synthesis of InP QDs by modifying precursor reactivity. Notably, two distinct reactivity regimes were observed for a series of newly synthesized, sterically encumbered triarylsilylphosphine precursors, suggesting a possible

change in the precursor conversion mechanism within this class of precursors. This mechanistic detail will be illuminated in a future study by density functional theory calculations and further chemical reactivity investigations. For $P(Si(C_6H_5)_3)_3$, precursor conversion was observed to unambiguously be the rate-determining step in the reaction according to data acquired via UV-Vis absorption and $^{31}P\{^1H\}$ NMR spectroscopy. In this case, however, nucleation and growth were not temporally distinct, leading to poor particle size dispersity. Given the sluggish reactivity of $P(Si(C_6H_5)_3)_3$, we combined it with $P(Si(CH_3)_3)_3$, a very rapidly reacting precursor, to act as a monomer reservoir to grow on nuclei generated from $P(Si(CH_3)_3)_3$. From the understanding we gained of the dependence of precursor conversion rates and separation of nucleation and growth on concentration for each precursor, we have succeeded in adjusting the system appropriately to enforce LaMer-like growth. We have demonstrated, however, that separation of nucleation and growth is not sufficient to obtain monodisperse colloids for the covalent InP system, an observation that runs contrary to previous thoughts on this material.[2] This novel two-phosphine approach allows for independently controlling nucleation and growth while maintaining a monomer reservoir and may be a viable approach for many other classes of materials.

3.4 Experimental Section

3.4.1 General Considerations

Sodium (dry stick, ACS reagent), potassium (in mineral oil, 98%), red phosphorus (99.999%), trichlorosilane (99%), palladium dichloride (99%), hexachloroethane (99%), magnesium sulfate (anhydrous, ≥99.5%), 4-bromotoluene (98%), 1-bromo-4-chlorobenzene (99%), 4-bromobenzotrifluoride (99%), iodine (chips, ≥99%), chlorotriphenylsilane (96%), chlorotrimethylsilane (≥99%), indium acetate (99.99%), myristic acid (≥99%), biphenyl (99.5%), diphenyl ether (≥99%), magnesium turnings (98%), and Celite 545 were purchased from Sigma-

Aldrich Chemical Co. and used without further purification. All solvents, including 1-octadecene (≥95%), 1,2-dimethoxyethane (99%), toluene, hexanes, diethyl ether, and tetrahydrofuran, were purchased from Sigma-Aldrich Chemical Co., dried by being stirred overnight with CaH_2, distilled, and stored over 4 Å molecular sieves. C_6D_6 and $CDCl_3$ were purchased from Cambridge Isotope Laboratories and were dried similarly. Concentrated hydrochloric acid was purchased from Fisher Scientific. Magnesium turnings were activated following literature procedures prior to use.[34] ^{1}H, ^{31}P, ^{13}C, and ^{19}F NMR spectra were recorded on 300 and 500 MHz Bruker Avance spectrometers. UV-Vis spectra were recorded on a Cary 5000 spectrophotometer from Agilent. Fluorescence spectra were acquired on a Horiba FL3-21tau fluorescence spectrometer. Powder XRD spectra were collected on a Bruker D8 Discover spectrometer with a GADDS 2-D XRD system. TEM images were collected on an FEI Tecnai G2 F20 microscope. TEM analysis was performed using manual analysis with the help of ImageJ.[35] Geometry optimizations were performed in Gaussian 09 and GaussView 5 using DFT B3LYP with a 6-31G basis set.[36,37] Frequencies were also calculated to ensure the optimized structures corresponded to the ground state geometry.

3.4.2 Synthesis of $(p\text{-}H_3CC_6H_4)_3SiH$

This synthesis was adapted from a literature procedure.[38] In a 250 mL three-neck flask, 100 mL of diethyl ether, activated magnesium (2.67 g, 110 mmol), and one iodine chip were added under N_2. Then 16.83 grams (98.4 mmol) of p-bromotoluene were added. The reaction mixture was refluxed and briefly heated with a heat gun. After ~6 minutes, the solution became cloudy and darkened to an orange color. After 4.5 hours, the solution was transferred via cannula to a 250 mL three-neck flask set up with a pressure-equalizing dropping funnel, a septum, and a Schlenk flow adapter that had been purged with N_2. Ten milliliters of diethyl ether was added to the dropping funnel; 3.4 mL (33.7 mmol)

of trichlorosilane was added via syringe under N_2. The diethyl ether/silane solution was added dropwise at a rate of ~1 drop/second. Once added, the solution was left to stir for 30 minutes. The reaction was then quenched with a 0.5–1 M HCl solution. The aqueous layer was washed three times with 20 mL of diethyl ether. The organic layers were combined and dried with magnesium sulfate. The solution was filtered through a paper filter. The diethyl ether was removed under reduced pressure, resulting in a yellow oil. The oil was dissolved in hexanes and put in a –30 °C freezer. The resulting solids were collected. These solids were further purified by being stirred in hot methanol (60 °C) for 2 hours and collected on a frit. The yield for this reaction was 1.7 g. The average percent yield was 30% (seven runs). ^{1}H NMR (301 MHz): $CDCl_3$, (d, 7.47, 6H), (d, 7.19, 6H), (s, 5.42, 1H), (s, 2.37, 9H)

3.4.3 Synthesis of $(p\text{-}ClC_6H_4)_3SiH$

This synthesis was adapted from a literature procedure.[39] Activated magnesium (4.5 g, 185 mmol) was added to 30 mL of diethyl ether and a chip of iodine in a 250 mL three-neck flask under N_2. A saturated diethyl ether solution containing 31.61 grams (165 mmol) of 1-bromo-4-chlorobenzene was added to the flask. The solution started refluxing on its own after 15 minutes and turned brown. Warning: The next step is very exothermic and should be conducted in an ice bath. After 40 minutes, 5.45 mL (54 mmol) of trichlorosilane was added via syringe under N_2. The reaction mixture was refluxed in an oil bath for 4 hours. The reaction was quenched by pouring the solution into a 600 mL beaker with an ice/5% HCl mixture. The aqueous layer was washed with three 20 mL portions of diethyl ether. The diethyl ether layers were combined and dried with magnesium sulfate. The solution was filtered through a paper filter. The diethyl ether was removed under reduced pressure, yielding an oil. Upon the addition of pentane, a white precipitate formed. The solution was

put in a –30 °C freezer to encourage further precipitation. The white solids were collected and recrystallized in ethanol. The yield was 6.9 g. The average percent yield was 46% (two runs). ^{1}H NMR (300 MHz): $CDCl_3$, (d, 7.46, 6H), (d, 7.36, 6H), (s, 5.42, 1H)

3.4.4 Synthesis of $(p\text{-}F_3CC_6H_4)_3SiH$

This synthesis was adapted from a literature procedure.[39] In a typical synthesis targeting 10 grams of the desired product, 3 grams (123 mmol) of activated magnesium was added to 100 mL of diethyl ether in a three-neck 250 mL flask under N_2. Next, 9 mL (64 mmol) of 4-bromobenzotrifluoride and one chip of iodine were added to the flask. The reaction mixture was refluxed for 2 hours and then cooled to room temperature. Another three-neck 250 mL flask was set up with a pressure-equalizing dropping funnel and a septum under N_2. The reaction mixture was transferred via cannula into the second three-neck flask. To the dropping funnel were added 50 mL of diethyl ether and 2.2 mL (21.8 mmol) of trichlorosilane under N_2. This solution was added dropwise, and the reaction mixture was cooled over ice during the addition. The solution was brought to reflux in an oil bath and left overnight. The solution was then cooled to room temperature and the reaction quenched over an ice/5% HCl solution in a 600 mL beaker. The aqueous layer was washed with three 20 mL portions of ether. The ether layers were collected and dried with magnesium sulfate. This solution was filtered through a paper filter, and the solvent was removed by vacuum. The resulting yellow solid was recrystallized twice from pentane. The yield was 3.7 g. The average percent yield was 48% (three runs). ^{1}H NMR (300 MHz): $CDCl_3$, (m, 7.69, 12H), (s, 5.60, 1H). ^{19}F (282 MHz): −64.06 ppm

3.4.5 Synthesis of $(p\text{-}H_3CC_6H_4)_3SiCl$

The synthesis was modified from literature procedures[40,41] and was performed in an inert atmosphere glovebox. In a typical synthesis, 0.0198 grams (0.1 mmol) of palladium dichloride and 0.594 grams (2.5 mmol) of hexachloroethane were measured into a 100 mL round-bottom flask. Then 2.93 grams (9.7 mmol) of $(p\text{-}H_3CC_6H_4)_3SiH$ was added. Next, 2.22 grams of tetrahydrofuran was added. Upon addition of the solvent, the solution turned black and started giving off gas. The reaction flask was loosely stoppered, and the reaction mixture was stirred at room temperature overnight. The reaction mixture was analyzed by ^1H NMR spectroscopy prior to being worked up to ensure the reaction went to completion. The THF was removed under reduced pressure and the precipitate was redissolved in copious amounts of pentane. The solution was filtered through Celite. The pentane was removed under reduced pressure, yielding a white solid that did not require further purification. The yield was 1.23 g. The average percent yield was 63% (five runs). ^1H NMR (300 MHz): CDCl3, (d, 7.53, 6H), (d, 7.22, 6H), (s, 2.38, 9H)

3.4.6 Synthesis of $(p\text{-}F_3CC_6H_4)_3SiCl$

A 100 mL Schlenk flask was placed in an inert atmosphere glovebox. The following reagents were then added: 0.2043 grams (1.2 mmol) of palladium dichloride, 1.2292 grams (5.2 mmol) of hexachloroethane, and 9.6462 grams (20.8 mmol) of $(p\text{-}ClC_6H_4)_3SiH$. THF (4.6302 g) was then added. The Schlenk flask was stoppered, removed from the glovebox, and put under nitrogen on a Schlenk line. The reaction mixture was left to stir, and the progress was monitored by ^1H NMR. After 5 days,

the reaction had gone to completion. The reaction vessel was brought into the box, and the THF was removed under reduced pressure. The solid was then dissolved in pentane and filtered through Celite. The pentane was removed under reduced pressure, yielding a pale yellow solid that did not require further purification. The yield was 9.44 grams (91%). ^{1}H NMR (300 MHz): $CDCl_3$, (m, 7.73, 12H). ^{19}F (282 MHz): $CDCl_3$, −64.17 ppm

3.4.7 Synthesis of $(p\text{-}ClC_6H_4)_3SiCl$

This synthesis was performed in an inert atmosphere glovebox. In a typical synthesis, 0.130 grams (0.7 mmol) of palladium dichloride and 0.866 grams (3.7 mmol) of hexachloroethane were weighed out into a 100 mL round-bottom flask. $(p\text{-}ClC_6H_4)_3SiH$ (5.253 g, 14.4 mmol) was added. THF (3.17 g) was then added. A septum was used to loosely stopper the reaction flask, and the reaction mixture was stirred at room temperature overnight. Again, the extent of the reaction was monitored by 1H NMR spectroscopy and was determined to be complete prior to workup. The THF was removed under reduced pressure, and the solid was redissolved in pentane. This mixture was filtered through Celite. The pentane was removed by vacuum, leaving a sticky oil. The oil was redissolved in pentane and put in a freezer. The next day a white solid had precipitated and was collected by filtration. The yield was 4.46 g. The average percent yield was 54% (four runs). ^{1}H NMR (300 MHz): $CDCl_3$, (d, 7.52, 6H), (d, 7.41, 6H)

3.4.8 Synthesis of $P(Si(C_6H_5)_3)_3$

This synthesis was adapted from literature procedures.[16,42] **Warning**: This reaction uses Na/K alloy, which is highly pyrophoric and should be handled with absolute exclusion of both oxygen and

water. Certain byproducts and unreacted starting materials remaining at the end of this reaction may be pyrophoric and should be quenched as described below. In a typical synthesis, Na/K alloy was prepared by measuring out 0.479 grams (20.8 mmol) of sodium and 0.629 grams (16.1 mmol) of potassium with fresh surfaces exposed in an inert atmosphere glovebox. These were mixed in a three-neck 250 mL flask until the eutectic liquid was obtained. Next, 100 mL of 1,2-dimethoxyethane (DME) was added to the flask. The flask was closed with two Teflon stoppers and a Schlenk gas flow adapter. Warning: The following operation requires extreme care. The apparatus was removed from the box and transferred onto a nitrogen gas line by first performing three nitrogen/vacuum backfill cycles. The Na/K solution was refluxed for 2 hours. The solution was cooled to room temperature. While the solution was being cooled, 0.392 grams (12.6 mmol) of red phosphorus was weighed out in an inert atmosphere glovebox and placed in a solid addition funnel that was capped in a 100 mL round-bottom flask. This apparatus was brought out of the glovebox, and once the Na/K solution had cooled, the solid addition funnel was transferred under a counterflow of N_2 into the side neck and the red phosphorus added. This solution was then brought back to reflux for 24 hours. During that time, the solution turned pitch black, indicating formation of $(Na/K)_3P$. After 24 hours, the solution was cooled to room temperature. A pressure-equalizing dropping funnel was exchanged for the reflux condenser under a counterflow of N_2. Chlorotriphenylsilane (10.919 g, 37 mmol) was dissolved in 50 mL of DME in an inert atmosphere glovebox and added to a Schlenk flask. This solution was transferred via cannula to the addition funnel under nitrogen. This solution was then added dropwise to the phosphide suspension. The solution was brought back to reflux for 24 hours following the addition. The reaction mixture was then placed in an inert atmosphere glovebox and stirred with 100 mL of toluene overnight. This solution was filtered through Celite, and the solvent was removed under reduced pressure. The resulting white solid was recrystallized from DME. The yield was 2.9 g. The average percent yield was 25% (five runs). To quench the byproducts and unreacted metal remaining

at the end of the reaction, all of the solid waste generated upon filtration was placed in a three-neck flask in the glovebox and transferred to a Schlenk line under nitrogen. DME, followed by 2-propanol and finally water, was injected through a septum to safely quench these materials. 1H NMR (500 MHz): C_6D_6, (d, 7.47, 18H), (t, 7.03, 9H), (t, 6.92, 18H). $^{31}P\{^1H\}$ NMR (121.5 MHz): C_6D_6, (s, −262.3). ^{13}C NMR (125.7 MHz): C_6D_6, (d, 137.06), (d, 135.74), (s, 129.33), (s, 127.73)

3.4.9 Synthesis of $P(Si(C_6H_4CH_3)_3)_3$

This reaction was conducted and the product isolated by adaptation of the synthesis for $P(Si(C_6H_5)_3)_3$ described above using 7.65 grams of $ClSi(p\text{-}(H_3C)C_6H_4)_3$. The yield was 1.83 grams (26%). ^1H NMR (300 MHz): C_6D_6, (d, 7.63, 18H), (d, 6.82, 18H), (s, 2.06, 27H). $^{31}P\{^1H\}$ NMR (121.5 MHz): C_6D_6, −259.47. ^{13}C NMR (125.7 MHz): C_6D_6, (s, 138.67), (d, 127.29), (d, 132.99), (s, 128.37), (s, 21.45)

3.4.10 Synthesis of $P(Si(C_6H_4Cl)_3)_3$

This reaction was conducted and the product isolated by adaptation of the synthesis for $P(Si(C_6H_5)_3)_3$ described above using 10.9380 grams of $ClSi(p\text{-}ClC_6H_4)_3$. The yield was 1.89 grams (20%). ^1H NMR (300 MHz): C_6D_6, (d, 7.09, 18H), (d, 6.91, 18H). $^{31}P\{^1H\}$ NMR (121.5 MHz): C_6D_6, −257. ^{13}C NMR (125.7 MHz): C_6D_6, (d, 137.70), (s, 137.28), (d, 131.93), (s, 128.36)

3.4.11 Synthesis of $P(Si(C_6H_4CF_3)_3)_3$

This reaction was conducted and the product isolated by adaptation of the synthesis for $P(Si(C_6H_5)_3)_3$ described above using 9.43 grams of $ClSi(p\text{-}(F_3C)C_6H_4)_3$. The yield was 0.85 grams (10%). 1H NMR (500 MHz): $CDCl_3$, (m, 7.33, 36H). $^{31}P\{^1H\}$ NMR (202.4 MHz): $CDCl_3$, −261.32. ^{13}C NMR (125.7 MHz): $CDCl_3$, 123.4 (complex q, 1JCF = 274 Hz), 124.6 (m), 132.6 (complex q, $2J_{CF}$ = 33 Hz), 135.7 (m), 136.8 (m)

3.4.12 Synthesis of $In(O_2C(CH_2)_{12}CH_3)_3$

In a typical synthesis, 0.058 grams (0.20 mmol) of indium acetate and 0.166 grams (0.73 mmol) of myristic acid were weighed out into a 15 mL, 14/20, three-neck round-bottom flask with a small egg-shaped magnetic stir bar. A 14/20 thermocouple probe adapter and a 14/20 reflux condenser were greased with H grease and the middle and side necks of the three-neck flask, respectively. The remaining neck was stoppered with a 14/20 Suba-Seal septum. A 14/20 hose adapter was greased with silicone grease and inserted into the reflux condenser. A 2.5 mL portion of dry 1-octadecene was drawn up into a syringe in a nitrogen-filled glovebox. The syringe was removed from the glovebox, and the 1-octadecene was delivered to the three-neck flask by being injected through the Suba-Seal septum. The hose adapter was connected to the Schlenk line, and the apparatus was evacuated with vigorous stirring. The Schlenk flask was then lowered into a heating mantle and wrapped with glass wool for insulation. A temperature probe was inserted into the thermocouple probe adapter, and both the heating mantle and the temperature probe were plugged into a temperature controller. The temperature controller was set to 100 °C. The solution was allowed to off-gas acetic acid under reduced pressure for approximately 12 hours at 100 °C to generate the $In(O_2C(CH_2)_{12}CH_3)_3$ solution.

The $In(O_2C(CH_2)_{12}CH_3)_3$ solution was not further isolated or purified prior to use for InP nanocrystal syntheses.

3.4.13 Synthesis of InP QDs from $P(Si(C_6H_5)_3)_3$ and $In(O_2C(CH_2)_{12}CH_3)_3$

A 2.00-gram portion of diphenyl ether, a 0.60-gram portion of biphenyl, and 0.081 grams of $P(Si(C_6H_5)_3)_3$ (0.10 mmol) were weighed out into separate scintillation vials in the glovebox. The biphenyl was added to the diphenyl ether scintillation vial with the aid of a plastic funnel, and the scintillation vial was capped. This scintillation vial was shaken vigorously until a homogeneous eutectic mixture was obtained. The eutectic mixture was then added to the $P(Si(C_6H_5)_3)_3$ with a glass pipet. A small stir bar was added to the solution, the scintillation vial was capped, and the solution was allowed to stir for approximately 30 minutes until a colloidal solution had been obtained. This solution was drawn into a 6 mL disposable syringe outfitted with a needle, and then the needle was inserted into the end of a 24/40 septum to seal off the $P(Si(C_6H_5)_3)_3$ solution. The $In(O_2C(CH_2)_{12}CH_3)_3$ flask was brought to 316 °C using the temperature controller. The syringe was brought out of the glovebox and injected into the $In(O_2C(CH_2)_{12}CH_3)_3$ solution when the temperature controller read 315 °C as the temperature of the solution was falling, after the temperature had been adjusted to 270 °C, the QD growth temperature. For variable concentration experiments, all reagent quantities were doubled (2 times the concentration) or quadrupled (4 times the concentration) while the total volume was kept constant. Figure 3.8 is XRD of powder samples of InP QDs synthesized via $P(Si(C_6H_5)_3)_3$ taken to confirm that syntheses that employ $P(Si(C_6H_5)_3)_3$ yield crystalline InP.

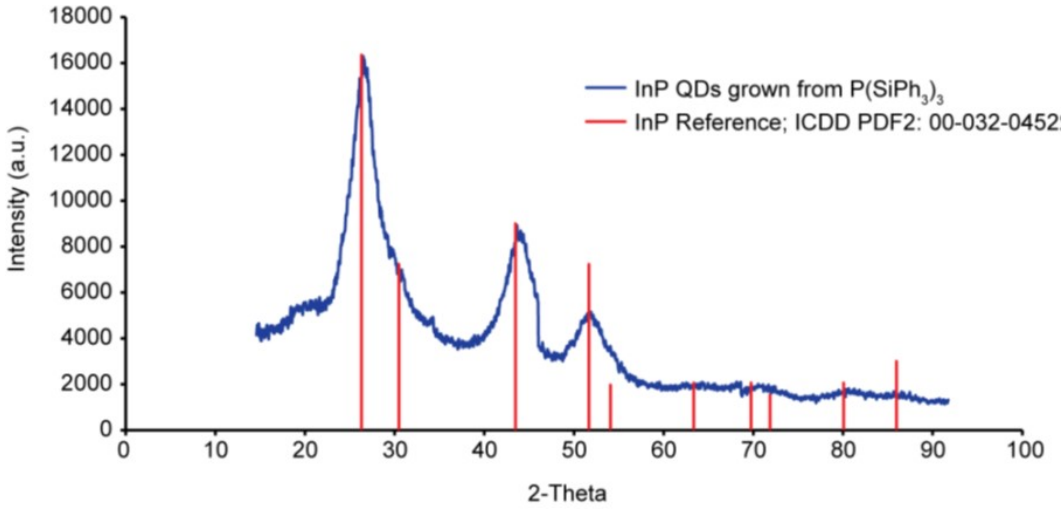

Figure 3.9 Powder XRD analysis of InP grown using $P(Si(C_6H_5)_3)_3$.

3.4.14 Synthesis of InP QDs from $P(Si(C_6H_4Cl)_3)_3$ and $In(O_2C(CH_2)_{12}CH_3)_3$

The procedure was the same as that described above for $P(Si(C_6H_5)_3)_3$ using 0.12 grams of $P(Si(C_6H_4Cl)_3)_3$ (0.10 mmol).

3.4.15 Synthesis of InP QDs from $P(Si(C_6H_4CH_3)_3)_3$ and $In(O_2C(CH_2)_{12}CH_3)_3$

The procedure was the same as that described above for $P(Si(C_6H_5)_3)_3$ using 0.094 grams of $P(Si(C_6H_4CH_3)_3)_3$ (0.10 mmol).

3.4.16 Synthesis of InP QDs from $P(Si(C_6H_4CF_3)_3)_3$ and $In(O_2C(CH_2)_{12}CH_3)_3$

The procedure was the same as that described above for $P(Si(C_6H_5)_3)_3$ using 0.14 grams of $P(Si(C_6H_4CF_3)_3)_3$ (0.10 mmol).

3.4.17 Synthesis of InP QDs from $P(Si(CH_3)_3)_3$ and $In(O_2C(CH_2)_{12}CH_3)_3$

The procedure was the same as that described above for $P(Si(C_6H_5)_3)_3$ using 29 μL (25 mg) of $P(Si(CH_3)_3)_3$ (0.10 mmol).

3.4.18 Synthesis of InP QDs from $P(Si(C_6H_5)_3)_3$, $P(Si(CH_3)_3)_3$, and $In(O_2C(CH_2)_{12}CH_3)_3$

The procedure was the same as that described above for $P(Si(C_6H_5)_3)_3$ but substituting the appropriate ratio of $P(Si(C_6H_5)_3)_3$ and $P(Si(CH_3)_3)_3$ with the total quantity of phosphorus precursor equal to 0.10 mmol.

3.4.19 Synthesis of InP QDs from $P(Si(CH_3)_3)_3$ with Delayed Injection of $P(Si(C_6H_5)_3)_3$

A typical $In(O_2C(CH_2)_{12}CH_3)_3$ solution was prepared as previously described *vide supra*. A solution of 29 μL (0.1 mmol) of $P(Si(CH_3)_3)_3$ in 2.5 mL of 1-octadecene was prepared in a nitrogen-filled glovebox and drawn up into a 6 mL disposable syringe. A separate solution of $P(Si(C_6H_5)_3)_3$ (0.16 grams, 0.2 mmol) in a eutectic mixture of biphenyl and diphenyl ether was prepared as described in Section 3.4.13 and was also drawn into a 6 mL disposable syringe outfitted with a needle. In cases where additional In^{3+} was also used, 0.2 mmol of $In(O_2C(CH_2)_{12}CH_3)_3$ was also added to this syringe. The 1-octadecene was substituted for the eutectic mixture for the $P(Si(CH_3)_3)_3$ injection solution as it was found that the solubility of the QDs decreased after injection of the $P(Si(C_6H_5)_3)_3$ in experiments in which both phosphines were dissolved in the eutectic mixture as indicated by an increased level of scattering in the UV-Vis spectra. Both syringes were sealed by stoppering the needle in a rubber septum. The syringe with the solution of $P(Si(CH_3)_3)_3$ in 1-octadecene was brought out of the glovebox

along with the syringe with the solution of $P(Si(C_6H_5)_3)_3$ in the eutectic mixture. The solution of $P(Si(CH_3)_3)_3$ in 1-octadecene was rapidly injected into the $In(O_2C(CH_2)_{12}CH_3)_3$ solution at 315 °C as described in Section 3.4.13. At the specified time after the injection (1 or 5 minutes), the solution of $P(Si(C_6H_5)_3)_3$ in the eutectic mixture was then rapidly injected into the solution. The temperature decreased considerably from the growth temperature (270 °C) to ~240 °C but recovered after ~5 minutes.

3.4.20 UV-Vis Monitoring Procedure

Prior to each injection of $P(Si(C_6H_5)_3)_3$, $P(Si(C_6H_4Cl)_3)_3$, $P(Si(C_6H_4CH_3)_3)_3$, $P(Si(C_6H_4CF_3)_3)_3$, $P(Si(CH_3)_3)_3$, or a mixture of $P(Si(C_6H_5)_3)_3$ and $P(Si(CH_3)_3)_3$, a test tube rack was prepared with 16 test tubes. Each test tube was filled with 6 mL of hexanes. All reactions were monitored for a total of 90 minutes; 50 µL aliquots of the reaction mixture were taken at specific times from injection using a 100 µL syringe.

3.4.21 Modeling Nucleation and Growth

Calculations to were performed to determine the total amount of InP required to grow from the population implied by the 30 second timed aliquot to the population implied by the 90-minute time aliquot. The diameter for the initial and final sizes was determined from λ_{max} of the LEET from the 30 second timed aliquot and the 90 minute timed aliquot according to the equation derived by Cho and coworkers.[20]

Diameter in nanometers: $d_{QD}(t) = \left(\frac{3.349}{\left(\frac{1239.884817}{\lambda_{max}(t)}\right)-1.401}\right)^{\frac{1}{1.172}}$

Where $\lambda_{max}(t)$ is equal to the wavelength (nm) at the LEET at time t.

From here, the particles were modeled as perfect spheres, and hence their volume would be:

Volume in cubic nanometers: $V_{QD}(t) = \frac{4\pi}{3} * (\frac{d_{QD}(t)}{2})^3$

The initial and final masses of the InP nanoparticles can now be calculated by using the density of bulk InP and the volume of the particle.

Mass of InP QD in grams: $m_{QD}(t) = volume\ of\ nanoparticle * bulk\ density\ of\ InP = V_{QD}(t) * \left(\frac{4.81\ g}{cm^3}\right) * (\frac{cm}{10{,}000{,}000\ nm})^3$

The number of InP units composing a nanocrystal so far modeled would simply be:

Number of InP units/nanocrystal: $InP_{QD}(t) = \left(\frac{m_{QD}(t)}{(114.82+30.974)\frac{g\ InP}{mol\ InP}}\right) * (\frac{6.02214129*10^{23} InP\ units}{mol\ InP})$

The number of indium phosphide nanoparticles present 30 seconds after injection can be calculated from the initial mass of such a particle and the normalized absorbance at 310 nm

(where $A_{310}(final) = 1$) for the 30 second aliquots as follows:

Number of InP nanoparticles generated after injection: $n_{InP}(t) = (\frac{m_{tot} * A_{310} * \left(\frac{6.02214129*10^{23} InP\ units}{mole\ InP}\right)}{InP_{QD}(t)})$

Where $A_{310}(t)$ is the absorbance at 310 nm from the UV-Vis spectra at time t, and m_{tot} is the mmol of possible InP generated as dictated by the amount of limiting reagent added.

The total amount of InP required to grow from the initial particle size to the final particle size is then calculated from the $n_{InP}(30\ seconds)$, $InP_{QD}(30\ seconds)$, and $InP_{QD}(90\ minutes)$ (a.k.a. initial number of particles, initial size, and final size) as follows:

Total amount of InP required for growth in moles:

$$InP_{req} = \frac{(InP_{QD}(30\ seconds) - InP_{QD}(90\ minutes)) * nInP(30\ seconds)}{(\frac{6.02214129*10^{23} InP\ units}{mole\ InP})}$$

The total amount of InP available to the system for growth is taken as follows (where P^{3-} is limiting):

Total amount of InP available for growth: $InP_{Avail}(t) = \left(1 - A_{310}(30\ seconds)\right) * m_{tot}$

The following data are necessary from the UV-Vis spectra to carry out these calculations

1.) λ_{max} of LEET of 30 second and 90 minute timed aliquots

2.) Normalized absorbance at 310 nm of the 30 second aliquot ($A_{310}(30\ seconds)$). This is normalized relative to the 90-minute time aliquot, which is set to 1.

The following values were used to perform these calculations in the paper for $P(Si(CH_3)_3)_3$, $P(Si(C_6H_5)_3)_3$, and the 1:2 optimal ratio for $P(Si(CH_3)_3)_3$: $P(Si(C_6H_5)_3)_3$ systems

For $P(Si(CH_3)_3)_3$:

$\lambda_{max}(30\ seconds)$ = 460 nm

$\lambda_{max}(90\ minutes)$ = 535 nm

$A_{310}(30\ seconds)$ = 0.5758

For $P(Si(C_6H_5)_3)_3$:

$\lambda_{max}(30\ seconds)$ = 535 nm

$\lambda_{max}(90\ minutes)$ = 580 nm

$A_{310}(30\ seconds)$ = 0.1491

For 1:2 ratio of $P(Si(CH_3)_3)_3$: $P(Si(C_6H_5)_3)_3$

$\lambda_{max}(30\ seconds)$ = 498 nm

$\lambda_{max}(90\ minutes)$ = 574 nm

$A_{310}(30\ seconds)$ = 0.3406

The results of these calculations are summarized in Table 3.1

	$P(Si(C_6H_5)_3)_3$	$P(Si(C_6H_5)_3)_3$ and $P(Si(CH_3)_3)_3$	$P(Si(CH_3)_3)_3$
mmol InP required for growth (InP_{req})	0.0111	0.1216	0.0817
mmol of InP available to the system for growth (InP_{avail})	0.0850	0.1197	0.0424
mmol of InP unaccounted for from separate nucleation and growth	0.0739	-0.0019	-0.0393
%InP unaccounted for from separate nucleation and growth	73.92	-0.95	-39.3233

Table 3.1 Comparison of the total amount of InP needed for growth from the initial particle size to the final particle size (InP_{req} (t), mmol) and the total amount of InP that should be available for growth based upon the assumption that silylphosphines are the limiting reagent (InP_{avail} (t), mmol) as well as the total amount of InP that cannot be accounted for during the growth process. Negative numbers for unaccounted InP imply that the final particle size is larger than can be accounted for from growth (probably because growth proceeded mainly via ripening processes) while positive numbers imply that the final particle size should be larger than what is observed based upon the amount of InP available to the system (probably because nucleation and growth were not temporally separate).

The following assumptions are made in this model:

1.) All of the limiting reagent (typically the phosphine) is consumed in the reaction to make InP. This assumption has been verified by $^{31}P\{^1H\}$ NMR spectroscopy in the case of limiting $P(Si(CH_3)_3)_3$ and limiting $P(Si(C_6H_5)_3)_3$.

2.) The UV-Vis absorbance at 310 nm of timed aliquots is indicative of the total fraction of InP that has formed in the reaction after being normalized to the maximum value obtained 90 minutes after injection.

3.) The equation for band gap as a function of diameter determined in reference 1 is valid for the sizes we are modeling.

4.) The density of a QD lattice is equivalent to that in the bulk state.

5.) The InP nanoparticles formed can be modeled as perfect, stoichiometric InP spheres of equivalent size for a given timed aliquot with disregard of surface charge equalization.

6.) The only two factors that can cause deviation from the fraction of InP required for growth from the calculation and the actual fraction consumed from the normalized absorbance at 310 nm is non-molecular ripening and the convolution of nucleation and growth.

The model was used to interpret the whether or not nucleation and growth were temporally distinct for a synthesis in the following manner:

1.) If the total amount of InP required for growth from calculation is greater than the amount known to be available to the system, then it is implied that growth is proceeding through nonmolecular mechanisms (ripening or aggregation) rather than remaining precursor reserves alone.

2.) If the total amount of InP required for growth from calculation is less than the amount known to be available to the system, then it is implied that new nuclei are forming during growth in such a system, and hence the average particle diameter is less than the model forecast.

3.) If the total amount of InP required for growth from calculation agrees well with that known to be available to the system, there are two interpretations by this method. Note that a wide window for growth and a narrow FWHM are spectral features that strongly suggest interpretation one is a more accurate depiction of the system.

These interpretations are:

3A.) Interpretation 1: nucleation and growth are temporally separate with the absence of nonmolecular ripening and the model is an accurate depiction of the system in accounting for the role of InP throughout the reaction.

3B.) Interpretation 2: the two factors that can cause deviation from the model and the spectra have canceled each other out.

3.4.22 InP QD Workup Procedure

To halt the QD reaction for further workup and characterization, the three-neck reaction flask was removed from the heating mantle and dipped into a room-temperature silicone oil bath. The solution was transferred via cannula to a 50 mL Schlenk flask. The solvents were distilled off under vacuum at 150 °C. The Schlenk flask was brought into a nitrogen-filled inert atmosphere glovebox, and all actions from this point were performed under an inert atmosphere. The crude QD were suspended in pentane. The pentane solution was centrifuged to remove insoluble materials. The now transparent supernatant was transferred to a second centrifuge tube. Ten milliliters of ethyl acetate were added followed by 5 mL of acetonitrile to precipitate the nanocrystals. The suspension was centrifuged. The supernatant was decanted, and the nanocrystals were redissolved in a minimal amount of pentane. Again a mixture of 10 mL of ethyl acetate and 5 mL of acetonitrile was added, and the suspension was centrifuged. This was repeated for a total of five cycles of precipitation. The nanocrystals were finally dissolved in 5 mL of pentane and centrifuged once more to remove any last bit of insoluble material. The resulting particles did not display any differences in the UV-Vis spectrum when compared with those of the final time aliquots (no red shift or broadening was observed). These particles are virtually nonfluorescent as isolated (PLQY < 1%)

3.4.23 J. Young NMR Tube Experiments

Approximately 0.3 grams of biphenyl was added to approximately 0.7 grams of diphenyl ether in a scintillation vial and shaken vigorously to obtain the eutectic mixture. This solution was added to approximately 0.1 grams of triphenylphosphine (Fischer Scientific, Acros Organics, 99% reagent grade) in a separate scintillation vial and thoroughly shaken to fully dissolve the triphenylphosphine. The narrow end of a glass pipet was flame-sealed to give a round appearance near the bottom and broken off (~3 inches from the bottom). from the sealed end. A 25 μL glass syringe was used to deliver 10 μL of the triphenylphosphine solution into the capillary tube while being sure to leave at least 1 inch of open head space. The top part of the capillary tube was then flame-sealed ~1 inch from the open end of the tube by being held in a flame and pulled from both ends. Prior to each experiment, an $In(O_2C(CH_2)_{12}CH_3)_3$ solution was prepared as described above. A sand bath was also set up prior to sample preparation using a heating mantle and temperature probe both connected to a temperature controller set to 325 °C, 200 μL of an $In(O_2C(CH_2)_{12}CH_3)_3$ solution was drawn from the flask and injected into a J. Young NMR tube that had been dried in an oven at 160 °C for 1 hour, and the sealed capillary tube was added to the J. Young tube and the tube degassed and transferred to the glovebox. In the glovebox, 0.095 grams of biphenyl was added to 0.33 grams of diphenyl ether in a scintillation vial and vigorously shaken to obtain a eutectic mixture. The solution was then added to 6.3 milligrams of $P(Si(C_6H_5)_3)_3$, and the solution was stirred on a stir plate for ~30 minutes to obtain a colloidal mixture. The mixture was added to the NMR tube using a disposable syringe outfitted with a needle. The J. Young tube was sealed with the J. Young tube cap and brought out of the glovebox. The J. Young tube was connected to a Schlenk line and evacuated briefly to 500 mTorr. The J. Young tube was sealed again, taken off the line, and submerged into the sand bath for 1 minute at 325 °C. The J. Young tube was removed from the sand bath; the temperature controller was set to 285 °C, and a

$^{31}P\{^{1}H\}$ NMR spectrum of the sample was recorded. Subsequent heating was performed at 285 °C with longer incubation times before spectra were acquired.

3.5 References

(1) Battaglia, D.; Peng, X. *Nano Letters* **2002**, *2* (9), 1027–1030.

(2) Allen, P. M.; Walker, B. J.; Bawendi, M. G. *Angewandte Chemie International Edition* **2010**, *49* (4), 760–762.

(3) Micic, O. I.; Sprague, J. R.; Curtis, C. J.; Jones, K. M.; Machol, J. L.; Nozik, A. J.; Giessen, H.; Fluegel, B.; Mohs, G.; Peyghambarian, N. *The Journal of Physical Chemistry* **1995**, *99* (19), 7754–7759.

(4) Gary, D. C.; Cossairt, B. M. *Chemistry of Materials* **2013**, *25* (12), 2463–2469.

(5) LaMer, V. K.; Dinegar, R. H. *Journal of the American Chemical Society* **1950**, *72* (11), 4847–4854.

(6) Sugimoto, T. In *Monodispersed Particles*; Elsevier, 2001; pp 368–452.

(7) Sugimoto, T. *Journal of Colloid and Interface Science* **2007**, *309* (1), 106–118.

(8) Sugimoto, T. *Advances in Colloid and Interface Science* **1987**, *28*, 65–108.

(9) Harris, D. K.; Bawendi, M. G. *Journal of the American Chemical Society* **2012**, *134* (50), 20211–20213.

(10) Wilhelm Ostwald. *Z. Phys. Chem.* **1901**, *37*, 385.

(11) Lifshitz, I. M.; Slyozov, V. V. *Journal of Physics and Chemistry of Solids* **1961**, *19* (1–2), 35–50.

(12) Carl Wagner. *Z. Elektrochem.* **1961**, *65*, 581–591.

(13) Yin, Y.; Alivisatos, A. P. *Nature* **2005**, *437* (7059), 664–670.

(14) Talapin, D. V.; Rogach, A. L.; Haase, M.; Weller, H. *The Journal of Physical Chemistry B* **2001**, *105* (49), 12278–12285.

(15) Joung, S.; Yoon, S.; Han, C.-S.; Kim, Y.; Jeong, S. *Nanoscale Research Letters* **2012**, *7* (1), 93.

(16) Becker, G.; Schmidt, H.; Uhl, G.; Uhl, W.; Regitz, M.; Rsch, W.; Vogelbacher, U.-J. In *Inorganic Syntheses*; Ginsberg, A. P., Ed.; John Wiley & Sons, Inc.: Hoboken, NJ, USA, 1990; Vol. 27, pp 243–249.

(17) Fu, H.; Zunger, A. *Physical Review B* **7**, *56* (3), 1496–1508.

(18) Mićić, O. I.; Sprague, J.; Lu, Z.; Nozik, A. J. *Applied Physics Letters* **1996**, *68* (22), 3150.

(19) Talapin, D. V.; Gaponik, N.; Borchert, H.; Rogach, A. L.; Haase, M.; Weller, H. *The Journal of Physical Chemistry B* **2002**, *106* (49), 12659–12663.

(20) Cho, E.; Jang, H.; Lee, J.; Jang, E. *Nanotechnology* **2013**, *24* (21), 215201.

(21) Xie, R.; Battaglia, D.; Peng, X. *Journal of the American Chemical Society* **2007**, *129* (50), 15432–15433.

(22) Gao, S.; Zhang, C.; Liu, Y.; Su, H.; Wei, L.; Huang, T.; Dellas, N.; Shang, S.; Mohney, S. E.; Wang, J.; Xu, J. *Opt. Express* **2011**, *19* (6), 5528–5535.

(23) Green, M. *Current Opinion in Solid State and Materials Science* **2002**, *6* (4), 355–363.

(24) Guzelian, A. A.; Katari, J. E. B.; Kadavanich, A. V.; Banin, U.; Hamad, K.; Juban, E.; Alivisatos, A. P.; Wolters, R. H.; Arnold, C. C.; Heath, J. R. *The Journal of Physical Chemistry* **1996**, *100* (17), 7212–7219.

(25) Abe, S.; Čapek, R. K.; De Geyter, B.; Hens, Z. *ACS Nano* **2012**, *6* (1), 42–53.

(26) Bullen, C. R.; Mulvaney, P. *Nano Letters* **2004**, *4* (12), 2303–2307.

(27) Finney, E. E.; Finke, R. G. *Journal of Colloid and Interface Science* **2008**, *317* (2), 351–374.

(28) Owen, J. S.; Chan, E. M.; Liu, H.; Alivisatos, A. P. *Journal of the American Chemical Society* **2010**, *132* (51), 18206–18213.

(29) Qu, L.; Yu, W. W.; Peng, X. *Nano Letters* **2004**, *4* (3), 465–469.

(30) Rempel, J. Y.; Bawendi, M. G.; Jensen, K. F. *Journal of the American Chemical Society* **2009**, *131* (12), 4479–4489.

(31) Narayanaswamy, A.; Feiner, L. F.; Meijerink, A.; van der Zaag, P. J. *ACS Nano* **2009**, *3* (9), 2539–2546.

(32) Xu, S.; Kumar, S.; Nann, T. *Journal of the American Chemical Society* **2006**, *128* (4), 1054–1055.

(33) Baek, J.; Allen, P. M.; Bawendi, M. G.; Jensen, K. F. *Angewandte Chemie International Edition* **2011**, *50* (3), 627–630.

(34) Brown, A. C.; Carpino, L. A. *The Journal of Organic Chemistry* **1985**, *50* (10), 1749–1750.

(35) Michael D Abràmoff. *Biophotonics International* **2004**, *11* (7), 36–42.

(36) Frisch, M. J.; Trucks, G. W.; Schlegel, H. B.; Scuseria, G. E.; Robb, M. A.; Cheeseman, J. R.; Scalmani, G.; Barone, V.; Mennucci, B.; Petersson, G. A.; Nakatsuji, H.; Caricato, M.; Li, X.; Hratchian, H. P.; Izmaylov, A. F.; Bloino, J.; Zheng, G.; Sonnenberg, J. L.; Hada, M.; Ehara, M.; Toyota, K.; Fukuda, R.; Hasegawa, J.; Ishida, M.; Nakajima, T.; Honda, Y.; Kitao, O.; Nakai, H.; Vreven, T.; Montgomery, J. A., Jr.; Peralta, J. E.; Ogliaro, F.; Bearpark, M.; Heyd, J. J.; Brothers, E.; Kudin, K. N.; Staroverov, V. N.; Kobayashi, R.; Normand, J.; Raghavachari, K.; Rendell, A.; Burant, J. C.; Iyengar, S. S.; Tomasi, J.; Cossi, M.; Rega, N.; Millam, N. J.; Klene, M.; Knox, J. E.; Cross, J. B.; Bakken, V.; Adamo, C.; Jaramillo, J.; Gomperts, R.; Stratmann, R. E.; Yazyev, O.; Austin, A. J.; Cammi, R.; Pomelli, C.; Ochterski, J. W.; Martin, R. L.; Morokuma, K.; Zakrzewski, V. G.; Voth, G. A.; Salvador, P.; Dannenberg, J. J.; Dapprich, S.; Daniels, A. D.; Farkas, O.; Foresman, J. B.; Ortiz, J. V.; Cioslowski, J.; Fox, D. J. *Gaussian 09*; Gaussian, Inc.: Wallingford, CT, 2009.

(37) Dennington, R.; Keith, T.; Millam, J. *GaussView, version 5*; Semichem, Inc.: Shawnee Mission, KS, 2009.

(38) Prince, P. D.; Bearpark, M. J.; McGrady, G. S.; Steed, J. W. *Dalton Trans.* **2008**, No. 2, 271–282.

(39) Benkeser, R. A.; Riel, F. J. *Journal of the American Chemical Society* **1951**, *73* (7), 3472–3474.

(40) Pongkittiphan, V.; Theodorakis, E. A.; Chavasiri, W. *Tetrahedron Letters* **2009**, *50* (36), 5080–5082.

(41) Savela, R.; Zawartka, W.; Leino, R. *Organometallics* **2012**, *31* (8), 3199–3206.

(42) Hassler, K. *Monatshefte für Chemie Chemical Monthly* **1982**, *113* (4), 421–425.

Chapter 4: Magic-Size Cluster Intermediates Decouple Precursor Conversion Kinetics from the Subsequent Nucleation and Growth of InP Nanocrystals

4.1 Introduction

Previous attempts to improve the quality of InP nanocrystals (quantum dots QDs) through colloidal synthesis have focused primarily on the precursor conversion event.[1–3] The most common phosphorus precursor reported for the colloidal synthesis of InP QDs is tris(trimethylsilyl)phosphine ($P(Si(CH_3)_3)_3$).[4–11] The extreme reactivity of this silylphosphine leads to a situation where molecular precursors are completely consumed within seconds of a hot-injection. In this scenario, all InP monomers produced from molecular precursors are depleted during the nucleation event. This rapid nucleation precludes size-selective growth, which requires InP monomer reserves.[12,13] Additionally, $P(Si(CH_3)_3)_3$ has been shown to promote detrimental side reactions with carboxylic acids, which are typically employed as ligands in such syntheses.[5,7] We discovered in Chapter 3 that tris(triphenylsilyl)phosphine ($P(Si(C_6H_5)_3)_3$) can be employed as a phosphorus precursor for InP QDs.[3] By employing $P(Si(C_6H_5)_3)_3$ to provide monomer reserves in tandem with $P(Si(CH_3)_3)_3$ to induce rapid nucleation in a single injection, a synergistic effect was achieved where nucleation and growth can be independently tuned through control of stoichiometry. Although this approach afforded a wide window of growth from a single injection, it did not improve the final size distribution relative to syntheses that employed $P(Si(CH_3)_3)_3$ as the sole phosphorus precursor. These results are contrary to classical nucleation theory and suggest that control of precursor conversion rate alone is not sufficient to obtain a monodisperse sample of InP.[12,13]

The origin for this departure from classical nucleation theory as discussed herein was illuminated by lowering the temperature at which the crystallites grew. When the growth temperature

of the reaction was lowered to 120 °C, a peak was observed in the UV-Vis spectrum with a lowest energy electronic transition (LEET) at 386 nm. This feature is precisely reproducible from batch to batch for growth temperatures up to 120 °C, which is indicative of a magic-size cluster (MSC). MSCs differ from other ultrasmall nanoparticles in that MSCs exhibit remarkable thermodynamic stability relative to similar sizes.[14] This stability leads to a quantized growth from one family of MSCs to another (heterogeneous growth) rather than continuous growth without any preference for a specific size (homogeneous growth), which is observed for larger nanoparticle sizes.[15] At temperatures of 150 °C and higher, UV-Vis spectra of timed aliquots revealed heterogeneous growth from MSCs directly to InP QDs with an initial diameter of approximately 3 nm. This change in LEET corresponds to a difference in particle diameter of about 1–2 nm. Such a drastic change in particle size without observation of intermediate sizes suggests that this cluster plays an integral role in the nucleation and growth of colloidal InP QDs from molecular precursors.

Two possible explanations for this large heterogeneous growth are that nucleation of InP QDs either proceeds via dissolution of MSCs back to monomers followed by a second nucleation event or MSCs aggregate to yield QDs. Either scenario would undermine previous research efforts to synthesize less reactive phosphorus precursors in order to maintain an InP monomer reservoir. In the case of a second nucleation event, precision control of monomer production rates would be difficult or impossible to achieve through fine-tuning of molecular precursor reactivity when there are multiple reaction pathways for monomer production. Nucleation through aggregation would impede efforts to separate nucleation and growth as monomers from precursor conversion could either grow on existing QDs or form MSCs to nucleate new QDs. It is evident that these MSCs play a critical role in the nucleation and growth of InP and warrant further investigation.

A variety of binary semiconductor MSCs have been investigated including lead selenide (PbSe),[16] zinc selenide (ZnSe),[17] zinc telluride (ZnTe),[18,19] cadmium sulfide (CdS),[20] cadmium selenide

(CdSe),[15,21–25] cadmium telluride (CdTe),[23] and cadmium phosphide (Cd_3P_2).[26] This class of nanocluster has shown utility for applications ranging from white LEDs,[15] blue LEDs,[22] room-temperature nucleants for nanoplatelets,[27] to *in vivo* biological imaging.[16] CdSe clusters in particular have proven to be a versatile starting material for a variety of nanostructures such as rods, rice, tadpoles,[28] ribbons,[29] nanosheets,[30] and quantum belts.[31]

Although there have been numerous studies of II-VI MSCs, there has been, to date, only two reports of III-V MSCs to the best of our knowledge.[32,33] In the first study by Xie et al., two MSCs of InAs were observed to precede the formation of InAs QDs. In the second study, Xie et al. employed InP MSCs as a convenient probe to study the kinetics of InP synthesis from molecular precursors. These clusters were chosen as the ideal end product due to their stability across a wide range of growth temperatures and precursor concentrations as well as having a distinct optical absorption spectrum in the visible region. The UV-Vis spectrum of the InP MSCs that we observe is identical to that reported by Xie et al. It is peculiar, given the unique properties exhibited by MSCs for other materials as well as their utility as precursors for a range of nanostructures, that this III-V cluster has not been investigated beyond the kinetics of its formation. One report by Yang et al. may have already demonstrated such utility.[34] In this study, $P(Si(CH_3)_3)_3$ was injected into $In(O_2C(CH_2)_{12}CH_3)$ at room temperature under inert atmosphere to preform yellow InP nuclei that were not further characterized. These nuclei were superior to molecular precursors for synthesizing high-quality InP/ZnS QDs.

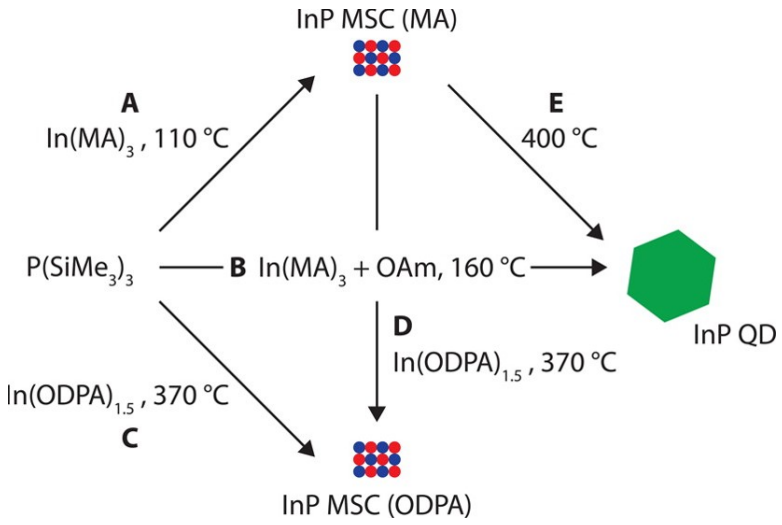

Scheme 4.1 Reaction pathways from molecular precursors to InP MSCs and QDs that will be further outlined in this chapter.

In this study, we report that the carboxylate-capped InP MSCs first reported by Xie et al. are important intermediates in the growth of InP QDs from molecular precursors (Scheme 4.1A). The stability of the MSCs were found to be highly dependent on the presence of additives such as amines (Scheme 4.1B), which have typically been employed in such syntheses to lower the temperature necessary for QD growth.[6,10] The thermodynamic stability, absorption spectrum, and core structure of the MSC was found to be dependent on the choice of ligand set (Scheme 4.1C,D). The utility of the MSC as a single-source precursor (SSP) was evaluated by hot-injection of isolated clusters into a noncoordinating solvent (Scheme 4.1E). The simplicity of using MSCs, which are isolable on the gram scale, as SSPs has enabled us to better understand the nucleation and growth of InP QDs.

4.2 Results and Discussion

4.2.1 Evidence for Kinetically Persistent Clusters from the Reaction of $P(SiR_3)_3$ and $In(O_2CR)_3$ Prior to Heterogeneous Growth to Nanocrystals

We have observed the formation of InP clusters with a LEET at 386 nm from the reaction of $In(O_2C(CH_2)_{12}CH_3)$ as an In^{3+} precursor with either $P(Si(CH_3)_3)_3$, $HP(Si(CH_3)_3)_2$, $H_2P(Si(CH_3)_3)$, or $P(Si(C_6H_5)_3)_3$ as a P^{3-} precursor (Figures 4.1 and Figure 4.2).[3,7] The final spectrum is indicative of at least two distinct cluster sizes as there is shoulder present at 420 nm just before the LEET. This collection of clusters appears to be kinetically persistent below 120 °C for at least 24 hours in hydrocarbon solvent and have thus been hypothesized to be MSCs (Scheme 4.1A and Figures 4.1A and 4.1B). Once isolated from solution, the MSCs can be stored as a solid at room temperature under nitrogen indefinitely. At temperatures of 150 °C and higher, the MSCs were observed to undergo heterogeneous growth directly to InP QDs without the observation of intermediate-sized particles. The first peak indicating formation of InP QDs exhibits a LEET that corresponds to an initial diameter of about 3 nm. There are no intermediate sizes observed in this reaction from timed aliquots by UV-Vis spectroscopy (Figure 4.3B). The spectra of the QDs synthesized *in situ* via MSCs at modest temperatures (150 °C) red-shifted and broadened over time as the peak from the nanoclusters grew out until only QDs remained over the course of approximately 20 hours (Figure 3.1B). The insensitivity of the size and size distribution of the MSCs to the reactivity of the P^{3-} source as well as the observation of heterogeneous growth from clusters directly to QDs further support the assignment of these clusters as MSCs.

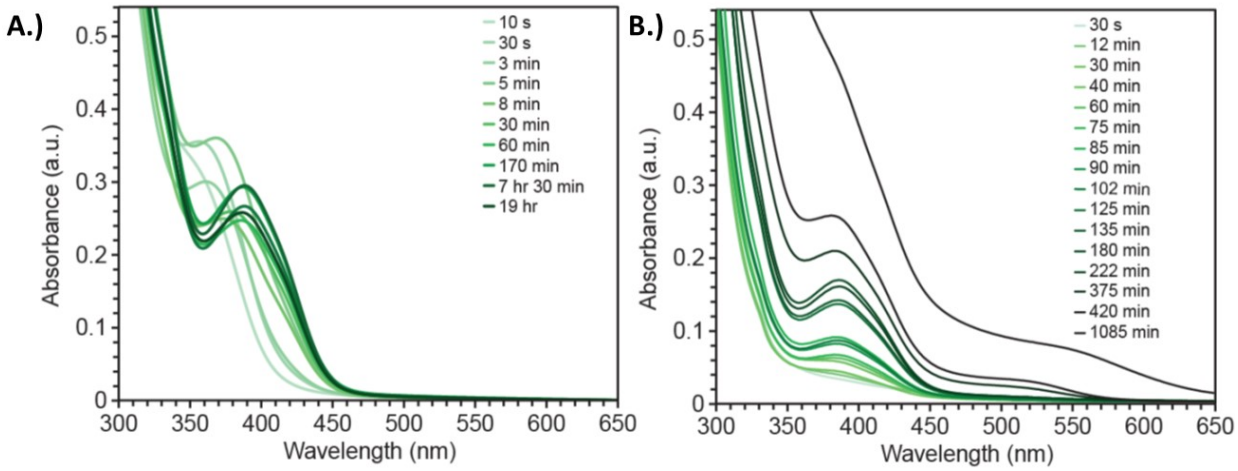

Figure 4.1 UV-Vis spectra of time aliquots from the reaction mixture of 0.2 mmol of (A) $P(Si(CH_3)_3)_3$ or (B) $P(Si(C_6H_5)_3)_3$ and 0.2 mmol and $In(O_2C(CH_2)_{12}CH_3)$. In (A), the injection was carried out at 130 °C and growth at 120 °C, and in (B) the injection was carried out at 315 °C and growth at 150 °C. Once formed, InP MSCs heterogeneously grew to InP QDs for the experiment where the temperature was held at 150 °C (B) but not at the synthesis where the temperature was held at 130 °C, suggesting the minimal temperature for thermolysis of MSC is somewhere between 130 °C and 150 °C.

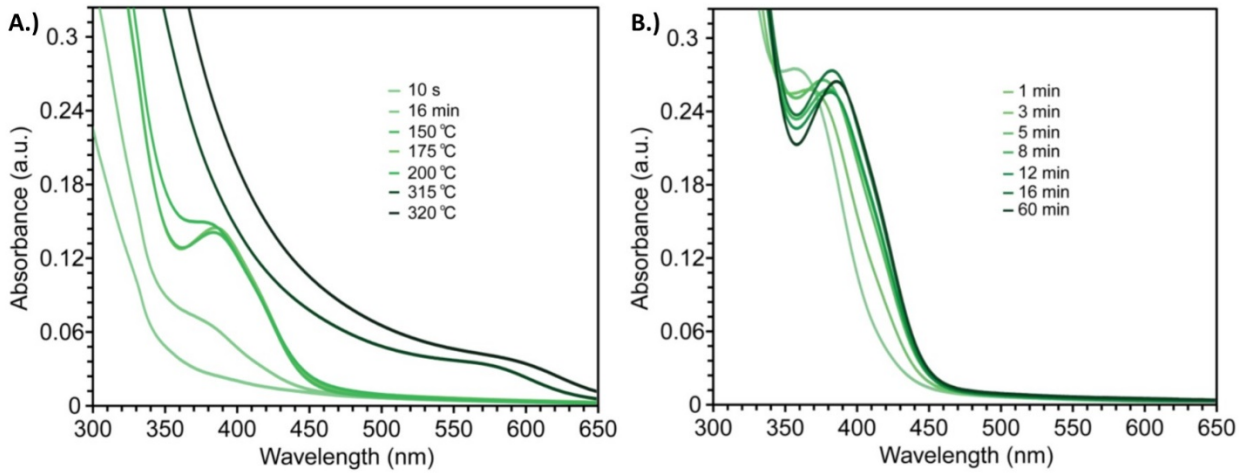

Figure 4.2 UV-Vis spectra of time aliquots from the reactions with 0.200 mmol of (A) $H_2P(Si(CH_3)_3)$ or (B) $HP(Si(CH_3)_3)_2$ and (0.2 mmol) $In(O_2C(CH_2)_{12}CH_3)$ in in 1-octadecene. In (A), the injection was carried out at 130 °C in 1-octadecene followed with subsequent, rapid heat up to 320 °C after 16 minutes at 120 °C. Conversion of precursors to InP MSCs with a LEET of 386 nm is nearly complete after ~ 16 minutes of growth at 120 °C and subsequent heat up yields InP QDs. For (B) the injection was carried out at 130 °C and growth at 120 °C. Conversion of precursors to InP MSCs with a LEET of 386 nm was nearly complete after ~16 minutes of growth, and proceeded to completion over 60 min. Heterogeneous growth to QDs was not observed at 120 °C these observations are consistent with the spectra from Figure 4.1 which determined that the minimal temperature necessary for thermolysis of InP MSCs is somewhere between 130 °C and 150 °C.

4.2.2 Thermal Stability of InP Magic-Size Clusters in the Presence of Primary Amines

InP QD syntheses that employ fatty acid ligands and their indium salts typically require elevated growth temperatures (200 °C or higher) in order to obtain high-quality, crystalline particles

with narrow size distributions.[4,6] Xie et al. discovered that incorporating primary amines into these syntheses enabled the formation of high quality samples of InP with LEETs ranging from 390 to 720 nm at temperatures below 190 °C.[6] Since this discovery, primary alkyl amines have been utilized as "precursor activating agents" for the preparation of InP QDs at lower temperatures.[10,35,36]

Primary alkyl amines have been assigned multiple roles in the synthesis of InP QDs ranging from ligands,[37] to a base that modulates the protonolysis of $P(Si(CH_3)_3)_3$ by myristic acid.[7] Allen et al. were able to demonstrate that primary amines inhibit precursor conversion conflicting with previous claims that amines are precursor activating agents.[6,38] The direct condensation reaction between carboxylic acids and amines at elevated temperatures (up to 160 °C) has been reported to proceed with high yields even in the absence of a catalyst.[39] The *in situ* water generated from this reaction has been proposed to hydrolyze the surface bound indium to form an In_2O_3 shell, inhibiting further growth, further compounding the precise role of primary amines in particle growth.[36]

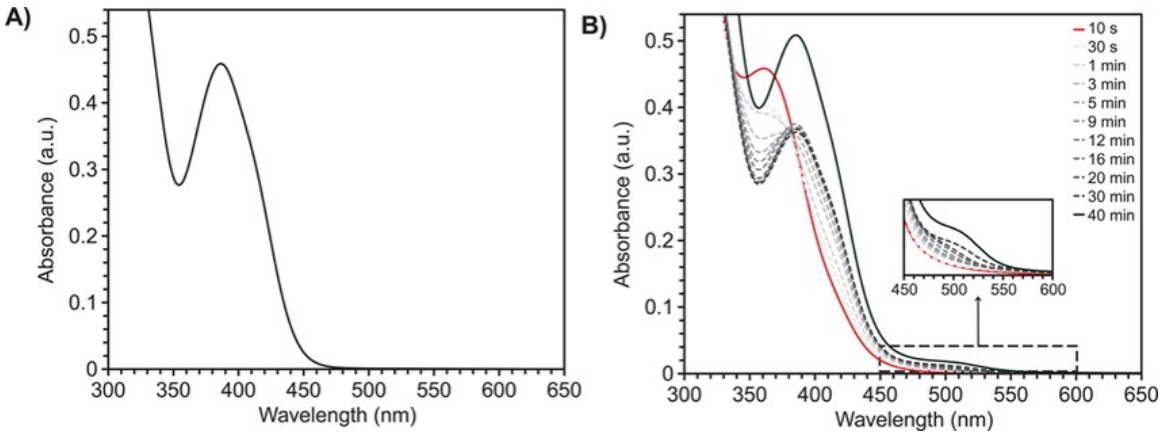

Figure 4.3 (A) UV-Vis spectrum of InP MSCs grown in toluene at 110 °C from $P(Si(CH_3)_3)_3$ and $In(O_2C(CH_2)_{12}CH_3)$. (B) UV-Vis spectra of timed aliquots depicting the formation of InP MSCs in 1-octadecene followed by heterogeneous growth directly to InP QDs at 160 °C. The inset shows a close-up of the region depicting InP QD growth.

The experimental conditions where we have observed heterogeneous growth of QDs directly from MSCs are analogous to previously reported syntheses of InP QDs at temperatures below 200 °C with the exception of the primary alkyl amine. We have performed experiments in order to assess the effect of octylamine ($H_2N(CH_2)_7CH_3$, OAm) on the formation of MSCs and their subsequent conversion to QDs. In contrast to experiments where amine is excluded (Figure 4.1B), we observe homogeneous growth of ultrasmall nanoparticles at 160 °C with LEETs ranging from 415 to 455 nm when OAm is included in the injection syringe without the appearance of the MSCs at 386 nm (Scheme 4.1B). A separate QD population was not observed when the primary amine was present even after 48 hours of growth at 160 °C (Figure 3.2A). A subsequent heating of this reaction to 300 °C revealed further homogeneous growth until a LEET at 500 nm was obtained. Finally, OAm was added to the flask where amine was originally excluded from the injection. The remaining MSCs rapidly switched from a heterogeneous growth pathway to a homogeneous growth pathway in a manner analogous to incorporating amine in the initial injection syringe (Figure 3.2B). It was detrimental to the final size distribution of QDs to allow the MSCs to fully form as is evident from the comparison of the full width at half-maximum of the spectra from Figure 4A and Figure 4B.

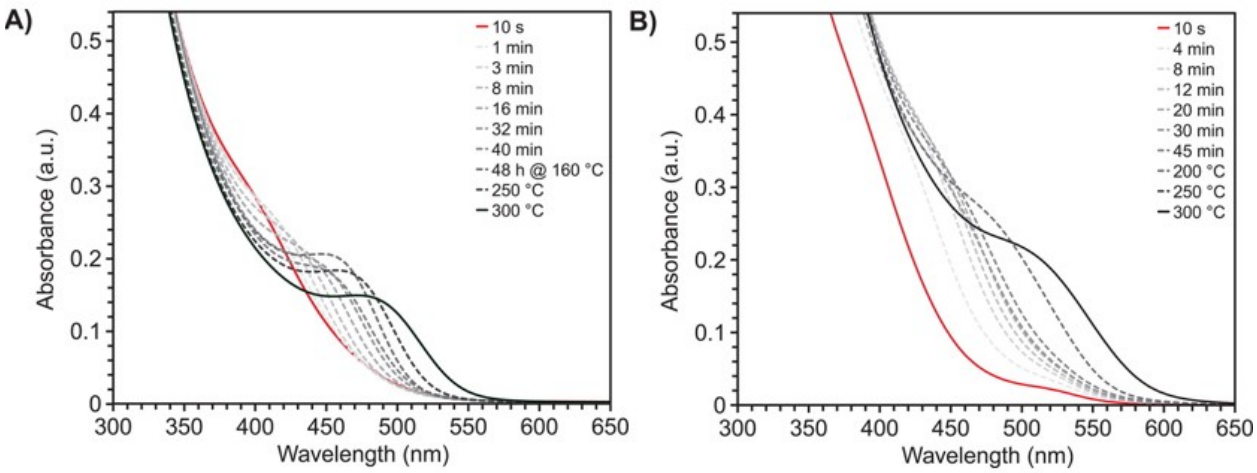

Figure 4.4 (A) UV-Vis spectra of timed aliquots from a hot-injection reaction of $P(Si(CH_3)_3)_3$, OAm, and $In(O_2C(CH_2)_{12}CH_3)$ in 1-octadecene, where OAm was included in the injection syringe with $P(Si(CH_3)_3)_3$. After 48 hours of growth at 160 °C, the reaction was heated up to 300 °C with aliquots monitored every 50 °C. (B) UV-Vis spectra of timed aliquots from the addition of OAm to InP MSCs at 160 °C. 48 hours after OAm injection, the reaction was heated up to 300 °C.

These results suggest that the main effect of primary amines is to destabilize the MSCs and thereby switch the growth profile of InP QDs from heterogeneous from MSCs, to homogeneous from molecular precursors. In this way, amine can still facilitate formation of InP QDs with narrow size distributions at low temperatures despite the inhibition of the precursor conversion event.(46) This behavior is similar to that recently reported for ZnTe MSCs.[19] In this report, Zhang et al. discovered that ZnTe MSCs would undergo stepwise growth to nanowires in the absence of oleic acid and continuous growth in the presence of oleic acid. The absorption spectra of purified samples of InP MSCs with myristate (MA) ligands were also found to broaden and red shift when exposed to OAm at room temperature in a nitrogen filled glovebox, suggesting that this effect is due to a direct interaction of the amine with the MSCs rather than a side reaction (Figure 4.5).

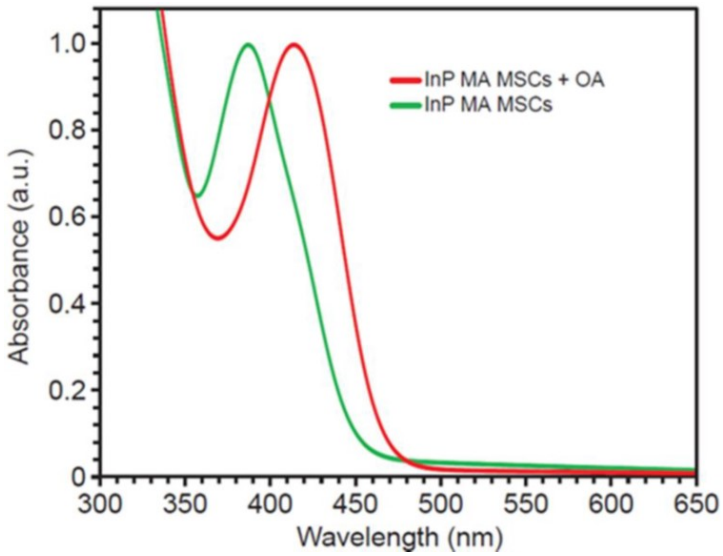

Figure 4.5 Air-free UV-Vis spectra of a solution of InP MA MSCs in toluene before (green trace) and after the addition of oleylamine. Addition of oleylamine was carried out in an N_2 filled glovebox at room temperature.

4.2.3 Increasing Thermal Stability of InP Magic-Size Clusters by Exchanging Carboxylate Ligands for Phosphonate Ligands

The effect of amines on the MSCs suggests that surface chemistry plays a critical role on the thermal stability of the InP MSCs. This reaction will be discussed in further detail in chapter 6. In line with this hypothesis, we set out to replace the carboxylate ligand set of InP MSCs and assess the stability of the resultant MSCs. Phosphonic acids have been identified as more strongly coordinating capping ligands than carboxylic acids for CdSe QDs due to their superior binding strength.[40,41] We synthesized InP MSCs with a phosphonate ligand set via $P(Si(CH_3)_3)_3$, indium octadecylphosphonate ($In(O_3P(CH)_{17}CH_3)_{1.5}$) , and octadecylphosphonic acid ($H_2O_3P(CH)_{17}CH_3$) (Scheme 4.1C, Figure 4.3A). Comparing the UV-Vis absorption spectra of timed aliquots from both the InP MA MSCs and the octadecylphosphonate (ODPA) terminated InP MSCs reveals sharper features (FWHM 18 nm

versus 72 nm) for the InP ODPA MSC including three additional high energy electronic transitions beyond the LEET (397 nm) at 355 nm, 285 nm, and 238 nm.

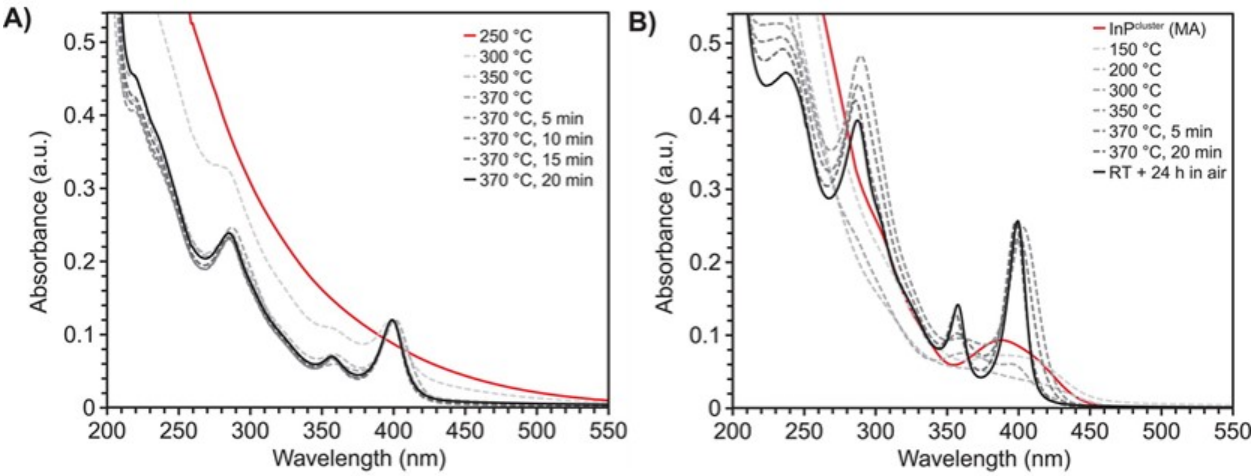

Figure 4.6 (A) InP ODPA MSCs synthesized by injection of $P(Si(CH_3)_3)_3$ into $In(O_3P(CH)_{17}CH_3)_{1.5}$ at 250 °C followed by rapid heat up to 370 °C (B) Synthesis of InP ODPA MSCs via injection of InP MA MSCs (red color trace) into a solution of $In(O_3P(CH)_{17}CH_3)_{1.5}$ at 150 °C followed by rapid heat up to 370 °C. The black trace is of the final product after cooling to room temperature and exposure to air for 24 hours.

At first glance, these spectra resemble those reported for CdSe nanoplatelets.[42,43] Simple mathematical calculations were performed to assess if the final spectrum of InP ODPA MSCs could be interpreted through the model of an infinite one-dimensional potential quantum well as has been previously reported for CdSe platelets (Experimental Section 4.4.8).[42] According to these calculations, such a structure with a LEET of 397 nm would have higher energy transitions at 327 nm and 253 nm for heavy hole transitions and at 320 nm, 182 nm, and 106 nm for light hole transitions, instead of those observed at 355 nm 285 nm and 238nm. Furthermore, it is unlikely that the final spectrum is indicative of four separate MSCs since we observe all four absorption peaks growing in over the same

time period for several syntheses. One would expect smaller MSCs to precede larger MSCs, especially in a synthesis from molecular precursors. Also, the final spectrum of InP ODPA MSCs persists for at least 3 days at 370 °C (Figure 3.7) with all transitions still present at the same relative intensities after this time. These observations support the assignment of the final spectra in Figure 4.3 as a single phosphonate terminated InP MSC with at least 4 distinct transitions rather than four separate absorbers.

The UV-Vis spectra of the phosphonate clusters are completely unaltered after exposure to air for 24 hours (Figure 4.8) suggesting that the InP ODPA MSC is air stable. In contrast, the peak in the UV-Vis spectrum of purified carboxylate clusters was found to broaden significantly after 20 hours in air. As envisioned, the phosphonate ligand set did enhance the thermal stability of the resultant InP MSC. The MSC with a phosphonate ligand set are stable in solution at 370 °C for at least three days (Figure 4.7). In contrast to the InP MA MSCs, the UV-Vis spectrum of the InP ODPA MSC persists even upon exposure to primary, secondary, or tertiary fatty amines at elevated temperatures (Figure 4.7).

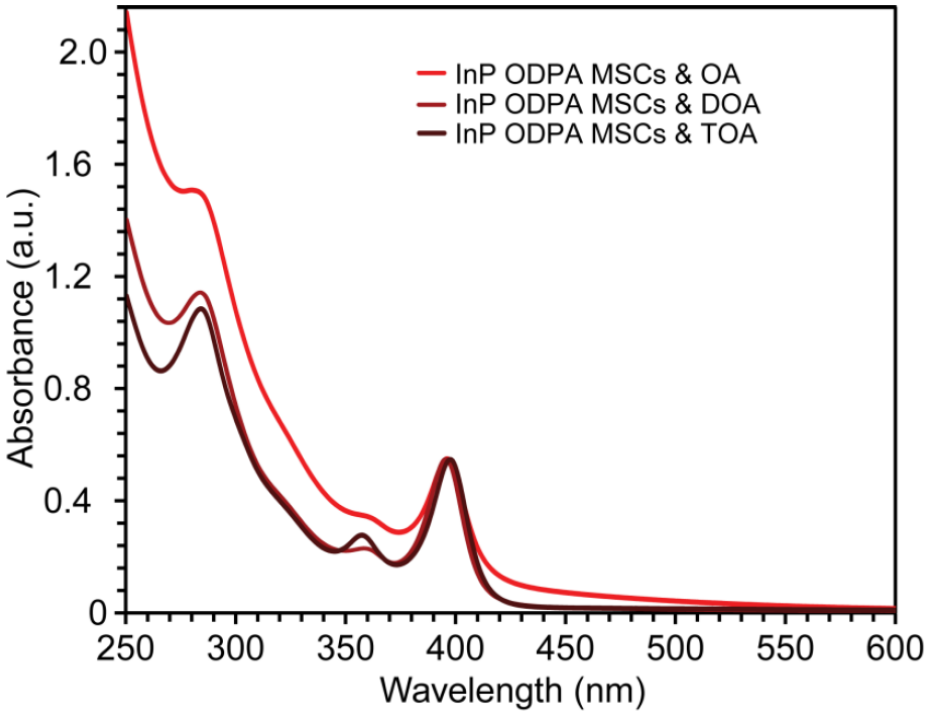

Figure 4.7 UV-Vis of InP ODPA MSCs synthesized with $P(Si(CH_3)_3)_3$ (1 equivalent), $In(O_3P(CH)_{17}CH_3)_{1.5}$ (2 equivalents), and octylamine, dioctylamine, or trioctylamine (3.6 equivalents). Injections were performed at 250 °C and grown at 370 °C. InP ODPA MSCs persist even in the presence of primary amines at elevated temperatures (compare to Figure 4.3 for the reactivity of InP MA MSCs in the presence of octylamine).

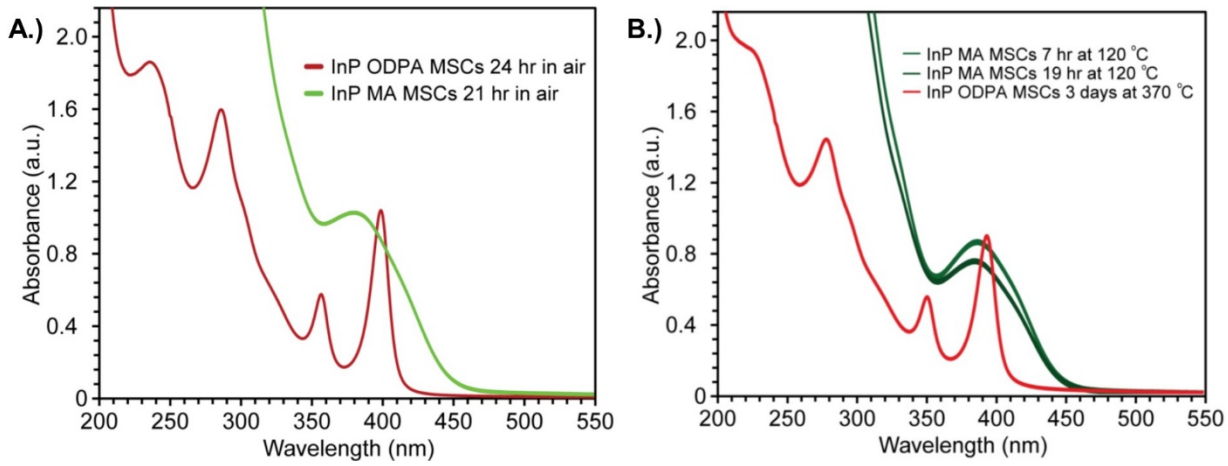

Figure 4.8 UV-Vis of InP MSCs with ODPA and MA ligands after prolonged exposure to air. Clusters with a MA ligand set are air sensitive, but clusters with an ODPA ligand set are not. UV-Vis spectra of timed aliquots for InP ODPA MSCs at 370 °C and InP MA MSCs at 120 °C. The red trace shows InP ODPA MSCs after 3 days at 370 °C in squalane. To the best of our knowledge, these clusters are stable indefinitely at these temperatures in the reaction solution.

This observation of the strong dependence of MSC thermal stability on the nature of the ligand set is mirrored by reports in the CdSe literature. Thermal stability of CdSe MSCs ranges from room-temperature nucleants for nanoplatelets (amine terminated),[27] to quantized growth through families of MSCs at temperatures up to 115 °C (mixture of carboxylate and amine ligands),[21,25] and finally to MSCs that are present at temperatures as high as 300 °C for ~30 minutes (phosphonate ligand set).[44]

The most convincing piece of evidence we observed for the greater stability of the phosphonate MSC relative to the carboxylate MSCs is that the carboxylate MSCs can be used as precursors for the phosphonate MSC. If isolated carboxylate MSCs are injected into $In(O_3P(CH)_{17}CH_3)_{1.5}$ and heated up to 370 °C we observe similar, yet sharper

(LEET FWHM = 12 nm) features in the UV-Vis to the synthesis that employed $P(Si(CH_3)_3)_3$ (Scheme 4.1D, Figure 4.3B). We have synthesized the InP ODPA MSC via oleic acid terminated MSCs in order to assess whether carboxylate ligands are retained in this reaction. ^{1}H NMR of purified InP MSCs reveal a phosphonate to carboxylate ratio of about 44:1 demonstrating nearly full conversion to a phosphonate ligand set. (Figure 4.9) It is interesting to note that the LEET we observe for the phosphonate cluster is within 0.032 eV of the HOMO–LUMO gap from DFT calculations of a an InP cluster ($[InP]_{65}$, diameter = 1.86 nm) predicted to be a magic-size for InP.[8] This is the only prediction of a magic-size for InP to the best of our knowledge.

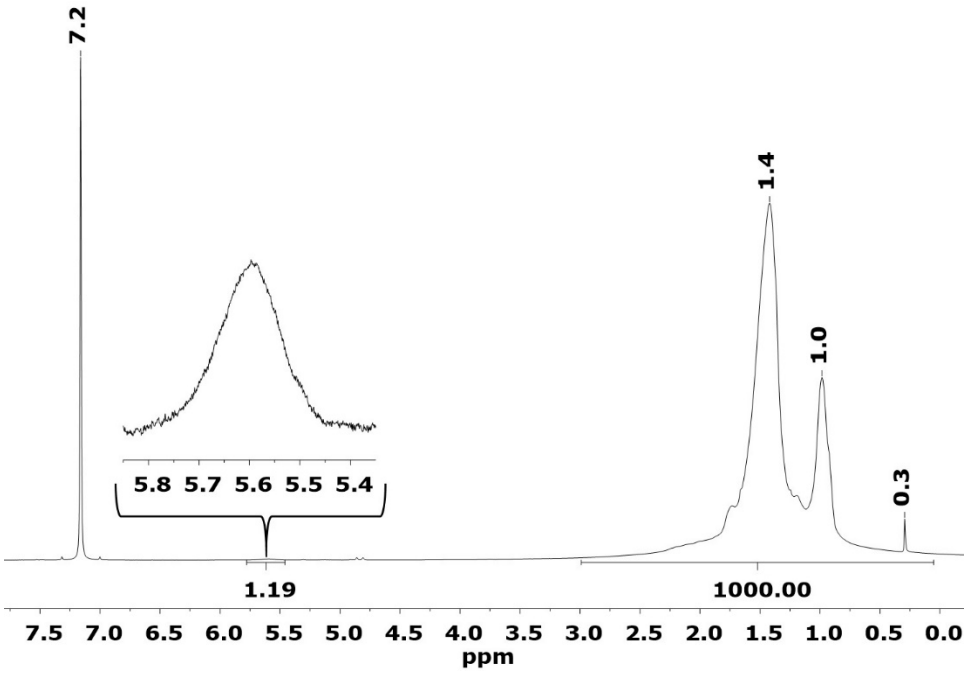

Figure 4.9 ^{1}H NMR (500 MHz C_6D_6) of InP H2ODPA MSCs synthesized from $HO_2C(CH_2)_7CH{=}CH(CH_2)_7CH_3$ (oleic acid) ligated InP MSCs. This experiment was performed in order to determine if any carboxylate ligands are retained when using carboxylate terminated clusters as a P^{3-} source for InP ODPA MSCs. The ratio of the alkene peak for bound carboxylates to bound phosphonates gives a ligand set that is approximately 2.2% carboxylate and 97.8% phosphonate, suggesting that carboxylate ligands are largely not retained in this process.

InP QDs synthesized with MA ligands do not yield InP ODPA MSCs even when exposed to $In(O_3P(CH)_{17}CH_3)_{1.5}$ at elevated temperatures (370 °C) for four days (Figure 4.10). These results suggest that the relative stability is as follows: carboxylate-terminated InP MSCs < phosphonate terminated InP MSC < InP QDs (Scheme 2.1).

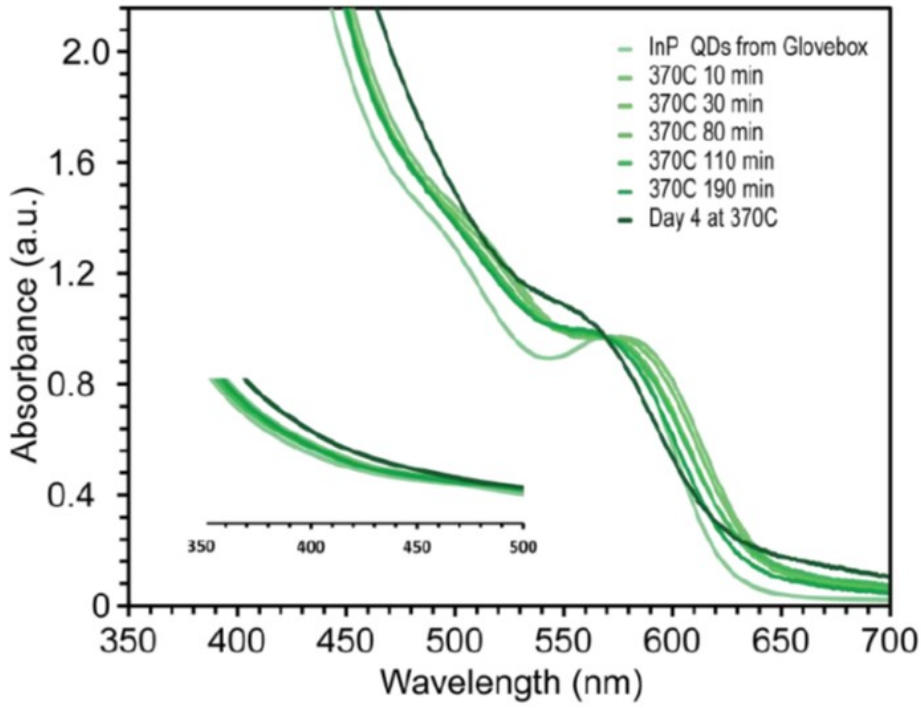

Figure 4.10 Attempt to make InP ODPA MSCs from InP MA QDs (0.2 g) by heating up in the presence of $In(O_3P(CH)_{17}CH_3)_{1.5}$ (0.4 mmol). The inset shows the region where InP ODPA MSCs were observed in previous syntheses.

4.2.4 Characterizing and Contrasting InP Magic-Size Clusters with Carboxylate and Phosphonate Ligand Sets

$^{31}P\{^1H\}$ NMR spectroscopy was used to further characterize InP MSCs with both kinds of ligand sets (Figure 4.4). In the spectrum of the MSC with the phosphonate ligand set we observe three distinct peaks at 34, 30, and 26 ppm which we assign to ^{31}P environments in the phosphonate ligand set because their chemical shifts are similar to those seen for bound phosphonate ligands on CdSe QDs.[41] We also observe a broader peak at −224 ppm that we assign to ^{31}P−In environments in the MSC based upon $^{31}P\{^1H\}$ MAS NMR spectra of powder samples of InP QDs.[5] In contrast, the $^{31}P\{^1H\}$ NMR spectrum of the InP MSCs with the carboxylate ligand set exhibit at least 9 distinct

peaks ranging from −181 ppm to −243 ppm. Although this result was unexpected, this spectrum is reproducible from batch to batch. Variable temperature (VT) $^{31}P\{^{1}H\}$ NMR spectra for the myristate-terminated cluster reveal that the ^{31}P environments in this material are temperature dependent and the presumed structural changes are fully reversible between 25 and 70 °C (Figure 4.11).

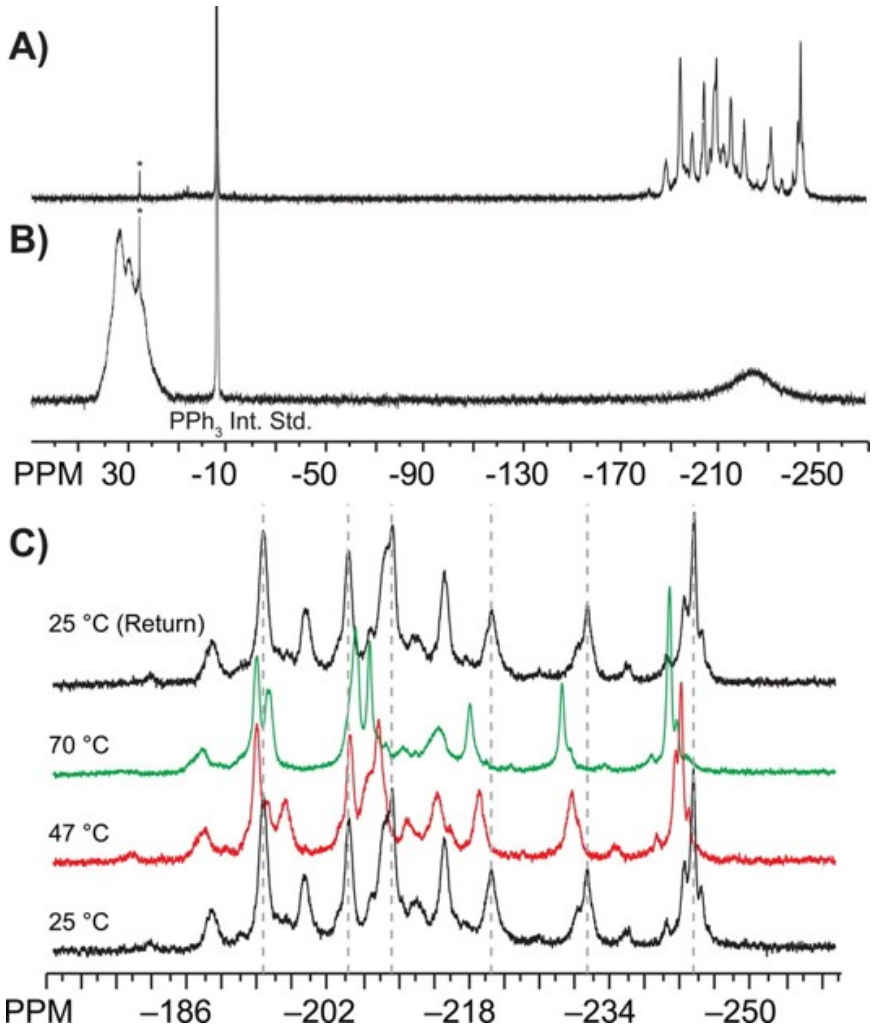

Figure 4.11 (A) $^{31}P\{^{1}H\}$ NMR spectrum of InP MA MSCs acquired at 202.4 MHz in C_6D_6. (B) $^{31}P\{^{1}H\}$ NMR spectrum of the InP ODPA MSC acquired at 202.4 MHz in C_6D_6. (C) Variable-temperature $^{31}P\{^{1}H\}$ NMR spectra of the InP MA MSCs acquired at 202.4 MHz in C_6D_6 collected at 25 °C, 47 °C, 70 °C, and at 25 °C after the sample was heated to 70 °C. Dotted lines serve as a guide to the eye for five peaks that shift downfield when heated and return upon cooling to 25 °C.

Further evidence for the structural differences between the carboxylate and phosphonate-capped MSCs is seen in the powder X-ray diffraction (XRD) (Figure 4.12) pattern and the atomic pair

distribution function (PDF) analysis (Figure 4.13). The XRD pattern for MSCs of both ligand sets are similar to those reported for powder samples of InP QDs, but with considerable peak broadening as would be expected from a small particle size. The carboxylate terminated clusters exhibit a broad peak at 20° 2θ that is not present for the phosphonate cluster or for either QD sample, possibly suggestive of amorphous material. The position of the (220) plane for the carboxylate terminated cluster is also significantly shifted from the values for bulk InP while the phosphonate terminated cluster shows no appreciable shift. The PDF analysis of clusters with each ligand set demonstrate that while both clusters are of a similar size (1–2 nm), intramolecular atomic distances reveal very different internal structures.

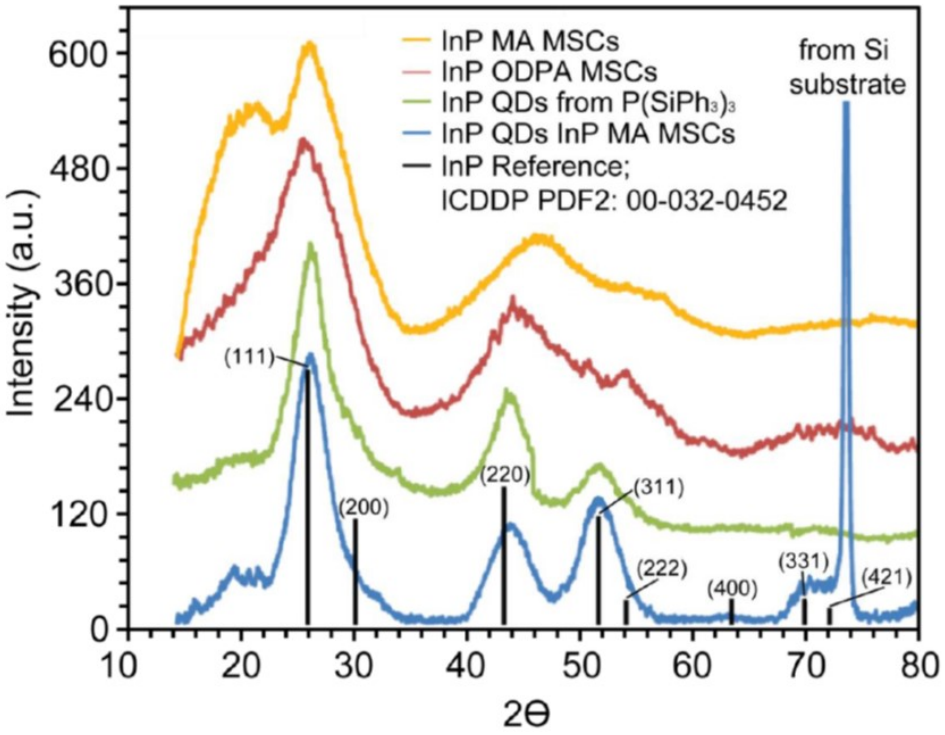

Figure 4.12 XRD spectra of InP MA MSCs, InP ODPA MSCs, InP QDs powder from $P(Si(C_6H_5)_3)_3$, InP QDs from MA MSCs as single source precursors (SSPs), and InP powder reference. InP MA MSCs exhibit a peak at ~20° 2θ that is not observed in any other InP pattern, suggesting the presence of amorphous material. While both QD samples have a well-defined peak for the (311) plane, no definitive peak is seen for this plane in either of the cluster samples.

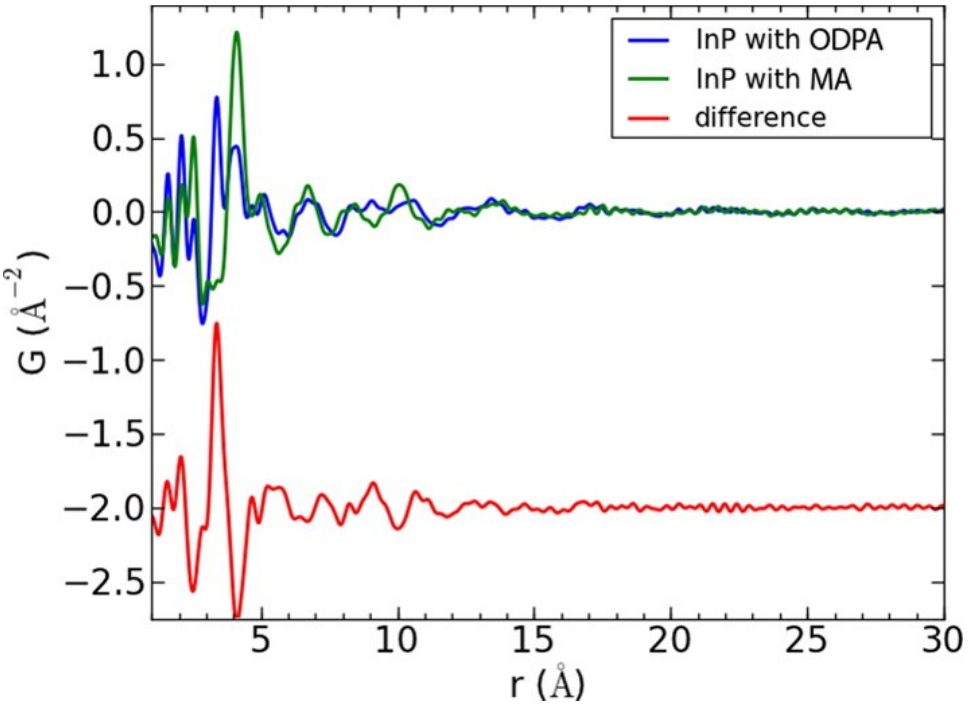

Figure 4.13 PDF analysis of InP MSCs with ODPA (blue) or MA ligands (green), and their difference (red). Sharp correlations indicate intracluster distances up to ~12 Å. There is some suggestion that intramolecular correlations survive to 15–17 Å in the MA capped particles, most clearly evident in the difference curve. Broad particle-to-particle correlations can be observed in the high-r region indicative of particle diameters of approximately 1–2 nm. The difference between the two radial distribution functions obtained suggests that although particle size is similar, the core structure of the MSC is dependent on the ligand set.

4.2.5 A Proposed Two-Step Nucleation Model for InP Nanocrystals from $P(SiR_3)$ and $In(O_2CR)_3$

Taking into consideration the significant change in particle size during heterogeneous growth of InP MSCs to QDs, as well as the thermal stability of InP MSCs, we propose a two-step nucleation model for the formation of InP QDs from silylphosphines and indium carboxylate precursors (Figure 4.6). This model was inspired by similar multistep nucleation schemes proposed for CaCO3 and

Ca3P2 wherein crystallization proceeds through aggregation of stable prenucleation clusters.[45–51] In this model, the MSC is a stable intermediate species that either dissolves back into solution to restore InP monomers that accumulate until a second nucleation event yields InP QDs or MSCs directly aggregate to give InP QDs. Envisioning nucleation of InP via a two-step nucleation scheme has an advantage over classical nucleation theory in that it emphasizes the importance of thermal stability of MSCs on the nucleation and growth of QDs instead of focusing on the precursor conversion event to explain nucleation and growth trends. According to a two-step model, a synthesis targeting a narrow size distribution of QDs from a single hot injection with molecular precursors should aim to minimize the lifetime of the MSCs in order to reduce disparity in particle growth history. This is in agreement with the observation that syntheses for high-quality InP QDs employ either elevated temperatures or primary amines.

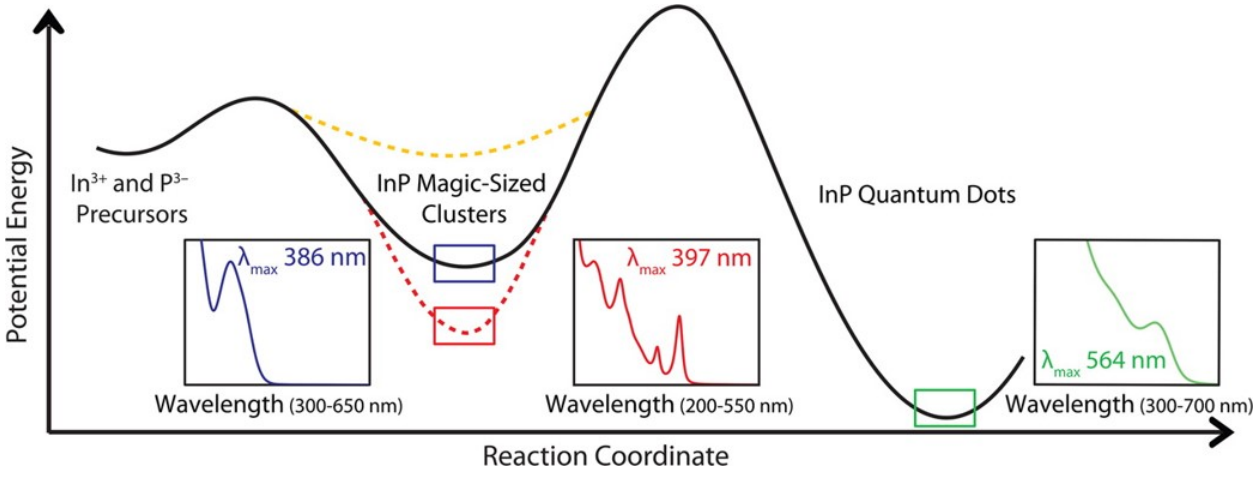

Scheme 4.2 Illustration of the two-step nucleation mechanism for the growth of InP QDs from In^{3+} and P^{3-} precursors depicting the MSC as an isolable intermediate species that acts as a bottleneck for InP monomers. Amines destabilize the MSC (increase potential energy), whereas a phosphonate ligand set increases the stability of the MSC relative to a carboxylate ligand set.

4.2.6 Employing InP Magic-Size Clusters as Single Source Precursors to InP Nanocrystals

Previous studies have demonstrated that inorganic clusters of CdSe can be employed as SSPs for crystalline CdSe QDs with narrow size distributions.[52] CdSe and copper organometallic clusters have been used in tandem as a means to synthesize precision doped CdSe:Cu QDs.[48] Inspired by these syntheses, we explored the utility of InP MSCs as SSPs to InP QDs. InP MSCs with a carboxylate ligand set were chosen to carry out these studies instead of the MSC with a phosphonate ligand set because the extreme thermal stability of phosphonate-capped clusters precludes a second nucleation unless indium myristate is added to the reaction to destabilize the cluster. Additionally, thermal decomposition of indium myristate sets an upper limit on the injection temperature for the synthesis of InP QDs from the InP ODPA MSC to ~320 °C (Figure 4.14).

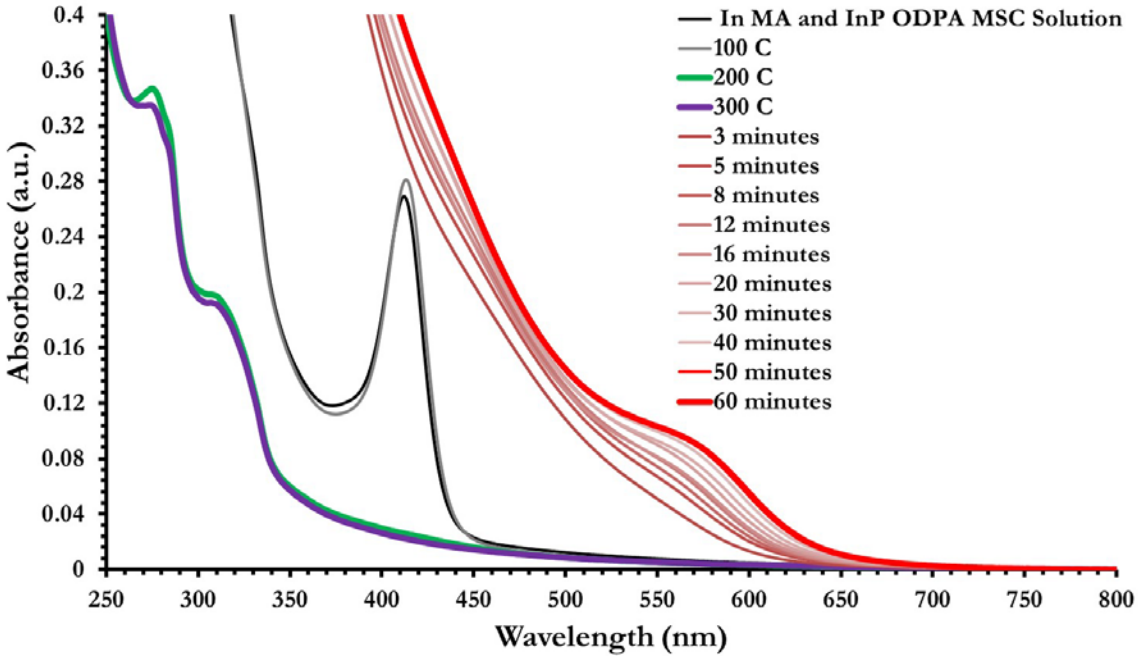

Figure 4.14 UV-Vis spectra of aliquots taken from the reaction of purified InP ODPA MSCs (100 mg), injected into $In(O_2C(CH_2)_{12}CH_3)$, (0.4 mmol), and $HO_2C(CH_2)_{12}CH_3$, (0.25 mmol) with subsequent heat up to 370 °C. At lower temperatures (100 °C, gray trace) the InP ODPA MSCs begin to show narrower size distributions. At higher temperatures, the ODPA MSCs dissolve back into solution to give some unidentified molecular species (200 °C, green trace and 300 °C, purple trace). Upon reaching the desired growth temperature of 370 °C the molecular species are lost and the growth of quantum dots is observed over the course of an hour (red traces). This reluctance to thermal decomposition suggests that ligand exchange from ODPA to MA proceeds thermolysis and requires elevated temperatures.

Our approach of using InP MA MSCs as SSPs differs from the previous syntheses that employ inorganic molecular complexes as SSPs,[52,53] in that the MSCs were not designed specifically to serve as an SSP. Rather, they are intermediates to QDs when employing silylphosphines and indium carboxylates as the molecular precursors. Utilizing the MSCs as SSPs effectively decouples the

formation of the MSCs from the subsequent secondary nucleation and growth of QDs. The monomers produced solely from InP MA MSCs should be inherently different than the monomers used in the first nucleation event to produce the MSCs because we observe $Si(CH_3)_3$ groups are not retained for purified InP MA MSCs by ^1H NMR (Figure 4.15).

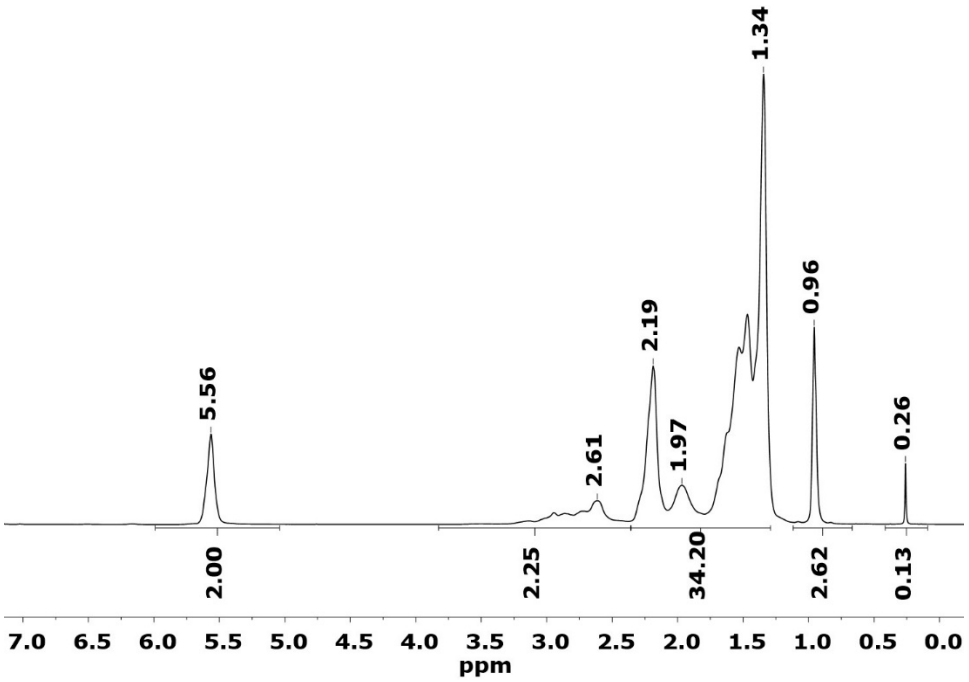

Figure 4.15 ^1H NMR spectra of purified InP MSCs with myristic acid ligands taken on a 500 MHz spectrometer in C_6D_6. All 28 ^1H are accounted for with broad peaks which are typically for ligands on the surface of nanocrystals due to slow tumbling on the NMR timescale.[54] Any $Si(CH_3)$ groups bound to the surface of the nanocrystal would be expected to come in around 0 ppm.

Purified MSCs were directly substituted for molecular precursors in a hot-injection synthesis. This technique did indeed yield high quality InP QDs within 1 minute of injection of MSCs into squalane at 400 °C (Figure 4.16). Additionally, XRD of QDs synthesized from MA MSCs as SSPs

confirm that the particles produced are highly crystalline despite a growth time of only one minute (Figure 4.12). Employing purified MSCs as SSPs effectively decouples the precursor conversion event from the second nucleation event. This eliminates the role of precursor conversion in the rate of InP monomer generation for the second nucleation event, thereby simplifying the overall reaction scheme and improving the reproducibility of the synthesis. Additional free ligands should not be necessary in this synthesis as the total amount of indium and phosphorus will remain constant throughout the synthesis, whereas the total surface area to volume ratio will decrease from the conversion of MSCs to QDs.

To assess the effect of concentration on these syntheses, the total amount of MSCs injected was varied while holding all other parameters constant (Figure 4.16B). UV-Vis spectra of 1 minute timed aliquots from each of these syntheses followed the expectations of classical nucleation theory across a large range of concentrations. First, at higher concentrations (12–400 mg of MSCs in 3.5 mL of squalane), we observed that an increase in concentration of MSCs corresponded to an increase in the final QD size. Second, for low concentrations of MSCs (3–6 mg of MSCs in 3.5 mL of squalane), we observe a reversal of the trend seen at higher concentrations. UV-Vis spectra of 1 minute timed aliquots exhibit a red shift and broadening of the LEET as concentration decreases in a low-concentration regime. This threshold concentration for distinct nucleation and growth is readily explained from inferring a LaMer mechanism.[55] In a high concentration regime, a larger portion of InP monomers remain after the nucleation event for further growth while at lower concentrations nucleation and growth are not temporally distinct due to relatively low InP monomer concentrations. Beyond a given threshold, lower InP monomer concentrations result in a greater portion of the monomers produced being consumed for growth rather than for nucleation. This results in a larger final particle size.

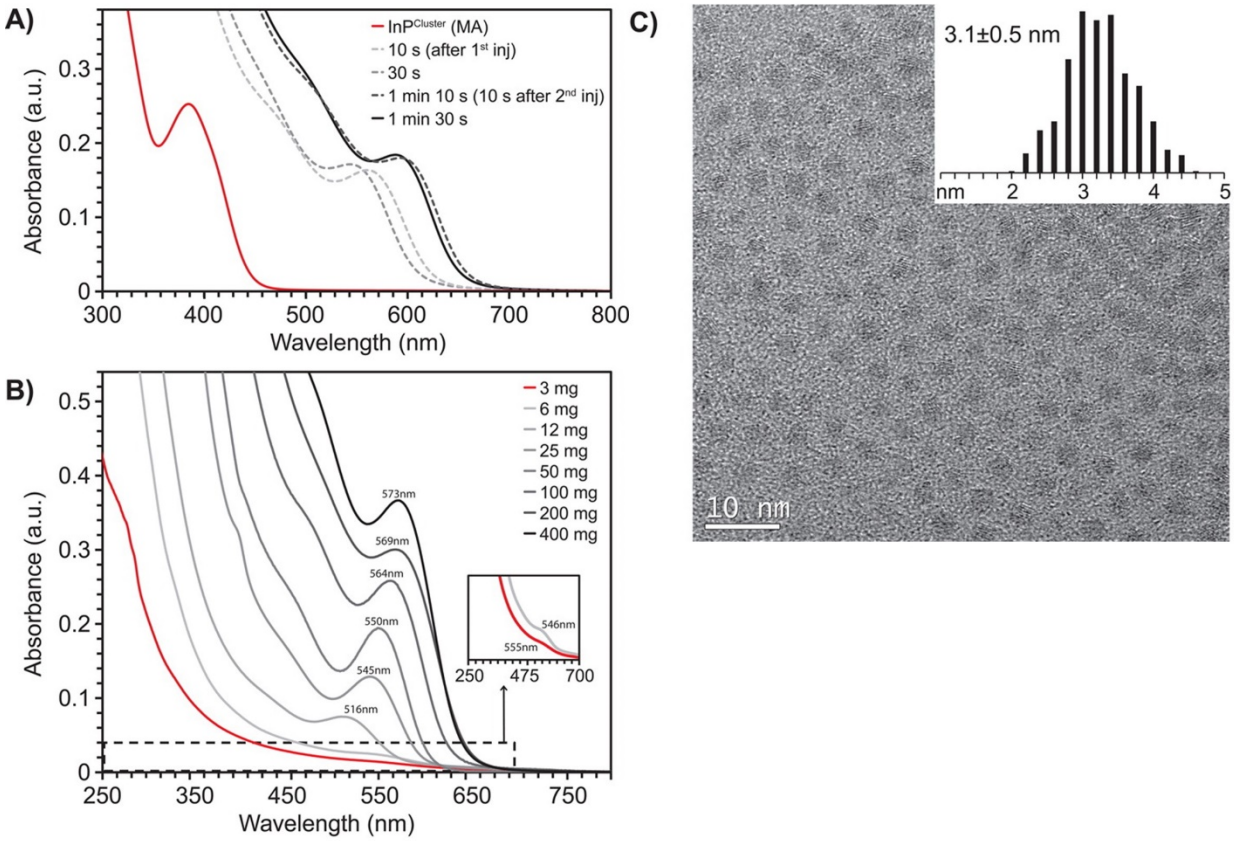

Figure 4.16 (A) UV-Vis spectra of timed aliquots from the hot-injection of MSCs into squalane. (B) UV-Vis of 1 minute timed aliquots of InP QDs grown using MSCs as SSPs with varying concentration of MSCs employed (squalane volume held at 3.5 mL). The synthesis that yielded the narrowest size distribution, as depicted in (C), employed 50 mg of MSCs (3.1 ± 0.5 nm). (C) TEM image of InP QDs synthesized from MSCs as SSPs using 50 mg of MSCs and 3.5 mL of squalane.

These trends suggest that the conversion of InP MSCs to QDs proceeds via a supersaturated solution rather than direct aggregation of MSCs in line with a two-step nucleation model. Additionally, transmission electron microscopy (TEM) images of InP QDs synthesized by this method show a uniform, spherical shape (Figure 4.16C). If growth proceeded through a purely aggregative mechanism, particle shape should show a significant deviation from spherical, and particle size distributions should not drastically broaden below a given concentration.

4.3 Conclusions

We have observed that the growth of InP QDs synthesized from indium carboxylates and silylphosphines proceeds via formation of MSCs followed by subsequent heterogeneous growth from the MSCs directly to QDs. We have proposed a two-step nucleation model to account for these observations where the MSCs are kinetically persistent, isolable intermediates. The two nucleation events can be decoupled by means of utilizing isolated MSCs as SSPs. This simple approach has afforded high-quality InP QDs without any free ligand, additives, or additional In^{3+} or P^{3-} sources. By varying the concentration of MSCs employed as SSPs, two trends in final particle size were observed. These two trends can readily be explained from the perspective of a LaMer mechanism of nucleation and growth. This suggests that the second nucleation event proceeds via precipitation from a supersaturated solution of monomers created from dissolution of MSCs rather than an aggregative mechanism directly from MSCs.

Addition of primary amine modulates the growth from a heterogeneous pathway to a homogeneous pathway. Primary amines can interact directly with the MSCs, as can be seen from UV-Vis spectra of purified samples prepared under nitrogen. In contrast, the stability of the MSCs is drastically increased by substitution of the carboxylate ligand set for a phosphonate ligand set. The optical properties as well as the structure of the MSC is significantly altered after this conversion as seen from UV-Vis and $^{31}P\{^{1}H\}$ NMR spectroscopy, as well as XRD and PDF analysis.

These results demonstrate that although MSCs are not predicted by classical nucleation theory they are an important intermediate species in the growth of InP QDs. The two-step nucleation model proposed in this study may help to explain observations for other materials which also have shown heterogeneous growth from MSCs directly to QDs such as Cd3P2.[26] The choice of ligand set and additives has a dramatic effect on the stability, structure, and optical properties of such MSCs. Future studies will focus on characterization of InP MSCs with an emphasis on solution $^{31}P\{^{1}H\}$ NMR and

single-crystal X-ray diffraction. The utility of MSCs as precursors to other kinds of nanomaterials as well as their potential use as luminophores will also be explored.

4.4 Experimental Section

4.4.1 General Considerations

Indium acetate (99.99%), myristic acid (≥99%), oleic acid (≥99%), toluene (99.5%), hexanes (98.5%), and Celite 545 were purchased from Sigma-Aldrich Chemical Co. and used without further purification. Squalane and 1-octadecene (≥95%) were purchased from Sigma-Aldrich Chemical Co., dried by stirring overnight with CaH_2, distilled, and stored over 4 Å molecular sieves prior to use. Triphenylphosphine (99%) was purchased from Acros Organics and used without further purification. C_6D_6 and $CDCl_3$ were purchased from Cambridge Isotope Laboratories and were dried similarly. ^1H and ^{31}P NMR spectra were recorded on 300 and 500 MHz Bruker Avance spectrometers. UV-Vis spectra were recorded on a Cary 5000 spectrophotometer from Agilent. Powder XRD spectra were collected on a Bruker D8 Discover spectrometer with a GADDS 2-D XRD system. TEM images were collected on an FEI Tecnai G2 F20 microscope. TEM analysis was performed using manual analysis with the help of ImageJ. Histogram, average size, and standard deviation of size for InP QDs from InP MA MSC SSPs were obtained by manual analysis of over 550 particles. Fluorescence spectra were acquired on a Horiba FL3–21tau fluorescence spectrometer. $P(Si(CH_3)_3)_3$ and ODPA were prepared according to literature procedures.[7,56–59]

4.4.2 Preparation of $In(O_2C(CH_2)_{12}CH_3)$ Solution

In a typical synthesis, 0.93 grams (3.20 mmol) of indium acetate and 2.65 grams (11.6 mmol) of myristic acid were weighed out into a 100 mL, 14/20, three-neck round-bottom flask equipped with a thermocouple probe adapter, reflux condenser, and septum. The apparatus was evacuated with stirring and raised in temperature to 100 °C. The solution was allowed to off-gas acetic acid under reduced pressure for approximately 12 hours at 100 °C to generate the $In(O_2C(CH_2)_{12}CH_3)$ solution. Afterward, the flask was filled with nitrogen, and a 20 mL portion of dry toluene was added.

4.4.3 Synthesis of InP MA MSCs from $In(O_2C(CH_2)_{12}CH_3)$ Solution and $P(Si(CH_3)_3)_3$

In a nitrogen filled glovebox, 465 μL of $P(Si(CH_3)_3)_3$ was added to 10 mL of toluene, drawn into a syringe and sealed with a rubber stopper. The $In(O_2C(CH_2)_{12}CH_3)$ flask was brought up to 110 °C and the $P(Si(CH_3)_3)_3$ solution was injected. The formation of MSCs was monitored via UV-Vis of timed aliquots taken from the reaction solution until the MSCs had fully formed as indicated by no further changes in the UV-Vis spectra. This procedure can be easily adapted for a wide variety of fatty carboxylic acids in place of myristic acid.

4.4.4 Synthesis of InP ODPA MSCs from $In(O_3P(CH)_{17}CH_3)_{1.5}$ Solution and $P(Si(CH_3)_3)_3$

In a typical synthesis, 0.117 grams (0.40 mmol) of indium acetate and 0.242 grams (0.725 mmol), of octadecylphosphonic acid were weighed out into a 25 mL 14/20 3-neck round-bottom flask equipped with a stir bar, thermocouple probe adapter, reflux condenser, and septum. Dry squalane (5 mL) was quickly injected into the 3-neck flask.

The apparatus was evacuated and raised in temperature to 120 °C. The solution was allowed to off-gas acetic acid under reduced pressure to generate the $In(O_3P(CH)_{17}CH_3)_{1.5}$ solution for approximately 12 hours at 120 °C.

In the glovebox, a solution of 58 μL (0.20 mmol) of $P(Si(CH_3)_3)_3$ in 2.5 mL of squalane was prepared and drawn up into a plastic syringe and stoppered. The 3-neck flask was then filled with nitrogen and rapidly heated by setting the temperature controller to the maximum setting (450 °C). The $P(Si(CH_3)_3)_3$ solution was injected into the indium octadecylphosphonate solution when the temperature controller read 250 °C as the temperature of the solution was rising. Aliquots were taken during the reaction taking note of the time after injection and the temperature of the flask. Once the reaction solution reached a temperature of 350 °C, the temperature controller was set to 370 °C for further growth. If the $P(Si(CH_3)_3)_3$ solution is injected at a temperature too far below or above 250 °C, then the MSC will not form. The temperature does not need to be this high or well controlled during injection if employing InP MA MSCs instead of $P(Si(CH_3)_3)_3$ as described below.

4.4.5 Synthesis of InP ODPA MSCs from $In(O_3P(CH)_{17}CH_3)_{1.5}$ Solution and InP MA MSCs

The synthesis of the InP ODPA MSC from an $In(O_3P(CH)_{17}CH_3)_{1.5}$ solution and InP MA MSCs follows the same procedure as that for using $P(Si(CH_3)_3)_3$ with a few exceptions:

(1) Substitute 0.200 grams of purified InP MA MSCs for the 58 μL of $P(Si(CH_3)_3)_3$ for the injection solution.

(2) After the 12 hours degassing step for the $In(O_3P(CH)_{17}CH_3)_{1.5}$ solution, fill the flask with nitrogen, bring the temperature to 300 °C for a couple of minutes to form a clear, homogeneous solution, and finally bring the solution back to 120 °C and evacuate for another 2 hours degassing step.

(3) Inject the InP MA MSC solution at 100 °C instead of at 250 °C to ensure the InP MA MSCs are fully dissolved before reaction with the $In(O_3P(CH)_{17}CH_3)_{1.5}$ solution to form the InP ODPA MSCs.

4.4.6 InP Myristate Magic-Size Clusters Workup Procedure

After UV-Vis confirmed formation of MSCs, the flask was cooled and then carefully evacuated until all of the toluene was removed. The flask was transferred into a nitrogen filled glovebox. The crude MSCs were resuspended in toluene. The toluene solution was centrifuged to remove insoluble materials. The now transparent supernatant was transferred to a second centrifuge tube. Acetonitrile was added to the solution to precipitate the clusters. The suspension was centrifuged. The supernatant was decanted and discarded and the MSCs were redissolved in a minimal amount of toluene. Again acetonitrile was added, and the suspension was centrifuged. This was repeated for a total of four cycles of precipitation. The MSCs were finally dissolved in 5 mL of pentane and transferred to a scintillation vial. The scintillation vial was carefully evacuated in the glovebox until a yellow solid was obtained. ^{1}H NMR of this sample shows only bound myristate as evidenced by the broadened and shifted resonances (Figure 4.15). The purified MSCs did not display any differences in the UV-Vis spectrum (no broadening or red shift) when compared with those of the final timed aliquots. These particles are virtually nonfluorescent as isolated (PLQY < 1%).

4.4.7 InP Octadecylphosphonate Magic-Size Workup Procedure

The workup procedure for InP ODPA MSCs is the same for MSCs synthesized from $P(Si(CH_3)_3)_3$ and for those synthesized with InP MA MSCs. A Schlenk flask was filled with 25 mL of

hexanes, briefly evacuated, and backfilled with nitrogen three times prior to the synthesis of the particles. After UV-Vis confirmed complete conversion to the MSCs, the hot reaction mixture was drawn up into a 10 mL glass syringe. (Caution! The reaction solution will be incredibly hot (370 °C) and must be handled with extreme care.) The solution was rapidly injected into hexanes under nitrogen. Rapid cooling with dilution using this strategy was found to be optimal for maintaining the cluster's narrow spectroscopic features. Skipping this step and allowing the reaction flask to come to room temperature results in spectral red-shift and broadening, suggesting aggregation. The flask can be reheated to 370 °C and rapidly cooled by injecting into room temperature hexanes under nitrogen as previously described to restore the FWHM originally observed from timed aliquots. Following this rapid cooling and dilution, the hexanes were removed under reduced pressure and then the squalane was distilled off under vacuum at a temperature of 200 °C.

After the distillation, the crude MSCs were suspended in toluene and heated to 100 °C under nitrogen. After the particles had redissolved, the solution was centrifuged to remove any insoluble materials. The now transparent supernatant was transferred to a second centrifuge tube. Acetonitrile was added to the solution to precipitate the clusters. The suspension was centrifuged. The supernatant was decanted and discarded and the MSCs were redissolved in a minimal amount of toluene. The toluene solution as centrifuged again to remove insoluble materials and the supernatant was transferred to a new centrifuge tube. Three more iterations of alternating precipitations of insoluble material from toluene and MSCs from acetonitrile were conducted to ensure purity. The final particles show no molecular species by ^{1}H NMR (Figure 4.15). The MSCs were finally dissolved in 5 mL of pentane and transferred to a scintillation vial. The scintillation vial was evacuated until a yellow solid was obtained. The resulting MSCs did not display any differences in the UV-Vis spectrum when compared with those of the final time aliquots. These particles are virtually nonfluorescent as isolated (PLQY < 1%).

4.4.8 Calculations for Modeling UV-Vis Spectrum from the Reaction of $In(O_3P(CH)_{17}CH_3)_{1.5}$, and InP Myristate Magic-Size Clusters as Nanoplatelets Assuming an Infinite One-Dimensional Potential Quantum Well

Equations Used[42]

For heavy hole transitions: $\hbar\omega_n = E_g + E_{\mathrm{hhn}} + E_{en} = E_g + \frac{\hbar^2 n^2 \pi^2 2}{m_{hh} * d^2} + \frac{\hbar^2 n^2 \pi^2 2}{m_e * d^2}$

For light hole transitions: $\hbar\omega_n = E_g + E_{\mathrm{hhn}} + E_{en} = E_g + \frac{\hbar^2 n^2 \pi^2 2}{m_{lh} * d^2} + \frac{\hbar^2 n^2 \pi^2 2}{m_e * d^2}$

$\hbar\omega_n$ = energy of the n^{th} transition

E_g = bulk semiconductor band gap

$E_{\mathrm{hh}n}$ = energy contribution of the heavy hole to the n^{th} transition

$E_{\mathrm{lh}n}$ = energy contribution of the light hole to the n^{th} transition

E_{en} = energy contribution of the electron to the n^{th} transition

n = the number of the interband transition

$m_{\mathrm{hh}}*$ = the effective mass of the heavy hole

$m_{\mathrm{e}}*$ = the effective mass of the electron

d = the thickness of the quantum well

The following values were used in the calculations:

E_g = 1.34 eV

$m_{\mathrm{hh}*}$ = 0.531 m_0 (from Osiniki et al.[60])

$m_{\mathrm{lh}*}$ = 0.121 m_0 (from Osiniki et al.[60])

$m_{\mathrm{e}*}$ = 0.08 m_0 (from Vurgaftman et al.[61])

d = 1.783 * 10^{-9} m (This value was set to return an energy which corresponds to 397 nm absorbance for the LEET)

These calculations gave the following energies for the 1st, 2nd, 3rd, transitions for the heavy hole:

1st transition energy = 3.12 eV (397 nm absorbance (diameter was set to correspond to this value))

2nd transition energy = 3.79 eV (327 nm absorbance)

3rd transition energy = 4.90 eV (253 nm absorbance)

And the following energies for the 1st, 2nd, 3rd, transitions for the light hole:

1st transition energy = 3.88 eV (320 nm absorbance)

2nd transition energy = 6.81 eV (182 nm absorbance)

3rd transition energy = 11.7 eV (106 nm absorbance)

None of these correspond to the higher energy transitions observed in the UV-Vis spectrum at 355 nm, 285 nm, and 238 nm.

4.4.9 Synthesis of InP Nanocrystals from InP Magic-Size Clusters

The desired amount of purified InP MA MSCs were weighed out into a scintillation vial in a glovebox (masses ranged from 3 mg to 400 mg see Figure 4.16B) and dissolved into 1 mL of squalane, drawn into a syringe, and stoppered. In a 3-neck flask under nitrogen on a Schlenk line, 2.5 mL of squalane was preheated to 400 °C using a heating mantle with vigorous stirring. The InP MA MSC solution was rapidly injected into the squalane solution. After one minute of growth, the 3-neck flask was raised out of the heating mantle and lowered into a room temperature silicon oil bath for rapid cooling. (Caution! The reaction solution will be incredibly hot (400 °C) and must be handled with extreme care.) The resulting InP QDs were purified using the same procedure as outlined for InP ODPA MSCs.

4.4.10 UV-Vis Monitoring Procedure

Prior to each injection $P(Si(CH_3)_3)_3$ or a solution of InP MA MSCs, a test tube rack was prepared with 16 test tubes. Each test tube was filled with 6 mL of hexanes. 50 μL aliquots of the reaction mixture were taken at specific times from injection using a 100 μL syringe.

4.4.11 InP Magic-Size Clusters J. Young Tube Sample Preparation

0.3 grams of biphenyl was added to 0.7 grams of diphenyl ether in a scintillation vial and shaken vigorously to obtain a eutectic mixture. This solution was added to 0.1 grams of triphenylphosphine in a separate scintillation vial and thoroughly shaken to fully dissolve the triphenylphosphine. Ten μL of the triphenylphosphine solution was sealed into a capillary tube. A supersaturated solution of InP MA MSCs was prepared by dissolving purified MSCs in C_6D_6 (400 mg of MSCs in 0.4 mL of C6D6) and was sealed along with the capillary in a J. Young tube. The J. Young tube solution was sonicated and gently heated (40 °C) prior to collecting data at room temperature to obtain a solution that would remain homogeneous for at least 30 minutes. This action was not required for data collected at elevated temperatures.

4.4.12 Pair Distribution Function Analysis

X-ray total scattering experiments were conducted on beamline X17A at the National Synchrotron Light Source (NSLS) at Brookhaven National Laboratory. An X-ray beam of energy 67.419 keV (λ = 0.1839 Å) was focused on samples contained in Kapton capillaries at room temperature. Scattered intensity was collected using the rapid acquisition technique[62] on a Perkin-

Elmer 2D flat panel detector (2048 × 2048 pixels and 200 × 200 μm pixel size) mounted orthogonal to the beam path at a distance of 204.9599 mm from the sample. The experimental setup was calibrated with a Ni standard sample using Fit2D.[63] The measured 2D intensity was integrated azimuthally to 1D intensity versus the magnitude of the scattering vector Q using the integration software SrXplanar,[64] then converted to a real-space pair distribution function (PDF), G(r), by using PDFgetX3[65] in PDFgetXgui.[66] S(Q) is the total scattering structure function, and $Q_{minutes}$ and Q_{max} are the minimum and maximum values of the scattering momentum transfer considered.

4.5 References

(1) Harris, D. K.; Bawendi, M. G. *Journal of the American Chemical Society* **2012**, *134* (50), 20211–20213.

(2) Joung, S.; Yoon, S.; Han, C.-S.; Kim, Y.; Jeong, S. *Nanoscale Research Letters* **2012**, *7* (1), 93.

(3) Gary, D. C.; Glassy, (B (A; Cossairt, (B M. *Chemistry of Materials* **2014**, *26* (4), 1734–1744.

(4) Battaglia, D.; Peng, X. *Nano Letters* **2002**, *2* (9), 1027–1030.

(5) Cros-Gagneux, (A; Delpech, F.; Nayral, C.; Cornejo, (A; Coppel, Y.; Chaudret, (B *Journal of the American Chemical Society* **2010**, *132* (51), 18147–18157.

(6) Xie, R.; Battaglia, D.; Peng, X. *Journal of the American Chemical Society* **2007**, *129* (50), 15432–15433.

(7) Gary, D. C.; Cossairt, (B M. *Chemistry of Materials* **2013**, *25* (12), 2463–2469.

(8) Cho, E.; Jang, H.; Lee, J.; Jang, E. *Nanotechnology* **2013**, *24* (21), 215201.

(9) Rowland, C. E.; Liu, W.; Hannah, D. C.; Chan, M. K. Y.; Talapin, D. V.; Schaller, R. D. *ACS Nano* **2014**, *8* (1), 977–985.

(10) Thomas, (A; Nair, P. V.; George Thomas, K. *The Journal of Physical Chemistry C* **2014**, *118* (7), 3838–3845.

(11) Li, L.; Reiss, P. *Journal of the American Chemical Society* **2008**, *130* (35), 11588–11589.

(12) Yin, Y.; Alivisatos, (A P. *Nature* **2005**, *437* (7059), 664–670.

(13) Reiss, H. *The Journal of Chemical Physics* **1951**, *19* (4), 482–487.

(14) McBride, J. R.; Dukes Iii, (A D.; Schreuder, M. (A; Rosenthal, S. J. *Chemical Physics Letters* **9**, *498* (1–3), 1–9.

(15) Harrell, S. M.; McBride, J. R.; Rosenthal, S. J. *Chemistry of Materials* **2013**, *25* (8), 1199–1210.

(16) Evans, C. M.; Guo, L.; Peterson, J. J.; Maccagnano-Zacher, S.; Krauss, T. D. *Nano Letters* **2008**, *8* (9), 2896–2899.

(17) Zhang, L.-J.; Shen, X.-C.; Liang, H.; Yao, J.-T. *The Journal of Physical Chemistry C* **2010**, *114* (50), 21921–21927.

(18) Groeneveld, E.; van Berkum, S.; Meijerink, (A; de Mello Donegá, C. *Small* **2011**, *7* (9), 1247–1256.

(19) Zhang, J.; Rowland, C.; Liu, Y.; Xiong, H.; Kwon, S.; Shevchenko, E.; Schaller, R. D.; Prakapenka, V. (B; Tkachev, S.; Rajh, T. *Journal of the American Chemical Society* **2014**.

(20) Li, M.; Ouyang, J.; Ratcliffe, C. I.; Pietri, L.; Wu, X.; Leek, D. M.; Moudrakovski, I.; Lin, Q.; Yang, (B; Yu, K. *ACS Nano* **2009**, *3* (12), 3832–3838.

(21) Cossairt, (B M.; Owen, J. S. *Chemistry of Materials* **2011**, *23* (12), 3114–3119.

(22) Dolai, S.; Nimmala, P. R.; Mandal, M.; Muhoberac, (B (B; Dria, K.; Dass, (A; Sardar, R. *Chemistry of Materials* **2014**, *26* (2), 1278–1285.

(23) Dukes, (A D.; McBride, J. R.; Rosenthal, S. J. *Chemistry of Materials* **2010**, *22* (23), 6402–6408.

(24) Liu, X.; Jiang, Y.; Guo, W.; Lan, X.; Fu, F.; Huang, W.; Li, L. *Chemical Engineering Journal* **8**, *230* (0), 466–474.

(25) Kudera, S.; Zanella, M.; Giannini, C.; Rizzo, (A; Li, Y.; Gigli, G.; Cingolani, R.; Ciccarella, G.; Spahl, W.; Parak, W. J.; Manna, L. *Advanced Materials* **2007**, *19* (4), 548–552.

(26) Wang, R.; Ratcliffe, C. I.; Wu, X.; Voznyy, O.; Tao, Y.; Yu, K. *The Journal of Physical Chemistry C* **2009**, *113* (42), 17979–17982.

(27) Wang, Y.; Zhang, Y.; Wang, F.; Giblin, D. E.; Hoy, J.; Rohrs, H. W.; Loomis, R. (A; Buhro, W. E. *Chemistry of Materials* **2014**, *26* (7), 2233–2243.

(28) Peng, Z. (A; Peng, X. *Journal of the American Chemical Society* **2002**, *124* (13), 3343–3353.

(29) Joo, J.; Son, J. S.; Kwon, S. G.; Yu, J. H.; Hyeon, T. *Journal of the American Chemical Society* **2006**, *128* (17), 5632–5633.

(30) Son, J. S.; Wen, X.-D.; Joo, J.; Chae, J.; Baek, S.; Park, K.; Kim, J. H.; An, K.; Yu, J. H.; Kwon, S. G.; Choi, S.-H.; Wang, Z.; Kim, Y.-W.; Kuk, Y.; Hoffmann, R.; Hyeon, T. *Angewandte Chemie International Edition* **2009**, *48* (37), 6861–6864.

(31) Liu, Y.-H.; Wang, F.; Wang, Y.; Gibbons, P. C.; Buhro, W. E. *Journal of the American Chemical Society* **2011**, *133* (42), 17005–17013.

(32) Xie, R.; Peng, X. *Angewandte Chemie International Edition* **2008**, *47* (40), 7677–7680.

(33) Xie, R.; Li, Z.; Peng, X. *Journal of the American Chemical Society* **2009**, *131* (42), 15457–15466.

(34) Yang, X.; Zhao, D.; Leck, K. S.; Tan, S. T.; Tang, Y. X.; Zhao, J.; Demir, H. V.; Sun, X. W. *Advanced Materials* **2012**, *24* (30), 4180–4185.

(35) Gao, S.; Zhang, C.; Liu, Y.; Su, H.; Wei, L.; Huang, T.; Dellas, N.; Shang, S.; Mohney, S. E.; Wang, J.; Xu, J. *Opt. Express* **2011**, *19* (6), 5528–5535.

(36) Protiere, M.; Reiss, P. *Chemical Communications* **2007**, No. 23, 2417–2419.

(37) Xu, S.; Ziegler, J.; Nann, T. *Journal of Materials Chemistry* **2008**, *18* (23), 2653–2656.

(38) Allen, P. M.; Walker, (B J.; Bawendi, M. G. *Angewandte Chemie International Edition* **2010**, *49* (4), 760–762.

(39) Gooßen, L. J.; Ohlmann, D. M.; Lange, P. P. *Synthesis* **2008**, *2009* (1), 160–164.

(40) Gomes, R.; Hassinen, (A; Szczygiel, (A; Zhao, Q.; Vantomme, (A; Martins, J. C.; Hens, Z. *The Journal of Physical Chemistry Letters* **2011**, *2* (3), 145–152.

(41) Owen, J. S.; Park, J.; Trudeau, P.-E.; Alivisatos, (A P. *Journal of the American Chemical Society* **2008**, *130* (37), 12279–12281.

(42) Ithurria, S.; Dubertret, (B *Journal of the American Chemical Society* **2008**, *130* (49), 16504–16505.

(43) Ithurria, S.; Tessier, M. D.; Mahler, (B; Lobo, R. P. S. M.; Dubertret, (B; Efros, (A L. *Nat Mater* **2011**, *10* (12), 936–941.

(44) Jiang, Z.-J.; Kelley, D. F. *ACS Nano* **2010**, *4* (3), 1561–1572.

(45) Pouget, E. M.; Bomans, P. H. H.; Goos, J. (A C. M.; Frederik, P. M.; de With, G.; Sommerdijk, N. (A J. M. *Science* **2009**, *323* (5920), 1455–1458.

(46) Gebauer, D.; Völkel, (A; Cölfen, H. *Science* **2008**, *322* (5909), 1819–1822.

(47) Wallace, (A F.; Hedges, L. O.; Fernandez-Martinez, (A; Raiteri, P.; Gale, J. D.; Waychunas, G. (A; Whitelam, S.; Banfield, J. F.; De Yoreo, J. J. *Science* **2013**, *341* (6148), 885–889.

(48) Erdemir, D.; Lee, (A Y.; Myerson, (A S. *Accounts of Chemical Research* **2009**, *42* (5), 621–629.

(49) Gebauer, D.; Kellermeier, M.; Gale, J. D.; Bergstrom, L.; Colfen, H. *Chemical Society Reviews* **2014**, *43* (7), 2348–2371.

(50) Betts, F.; Blumenthal, N. C.; Posner, (A S.; Becker, G. L.; Lehninger, (A L. *Proceedings of the National Academy of Sciences* **1975**, *72* (6), 2088–2090.

(51) Betts, F.; Posner, (A S. *Materials Research Bulletin* **3**, *9* (3), 353–360.

(52) Cumberland, S. L.; Hanif, K. M.; Javier, (A; Khitrov, G. (A; Strouse, G. F.; Woessner, S. M.; Yun, C. S. *Chemistry of Materials* **2002**, *14* (4), 1576–1584.

(53) Jawaid, (A M.; Chattopadhyay, S.; Wink, D. J.; Page, L. E.; Snee, P. T. *ACS Nano* **2013**, *7* (4), 3190–3197.

(54) Piveteau, L.; Ong, T.-C.; Rossini, (A J.; Emsley, L.; Copéret, C.; Kovalenko, M. V. *Journal of the American Chemical Society* **2015**, *137* (43), 13964–13971.

(55) LaMer, V. K.; Dinegar, R. H. *Journal of the American Chemical Society* **1950**, *72* (11), 4847–4854.

(56) Becker, G.; Schmidt, H.; Uhl, G.; Uhl, W.; Regitz, M.; Rösch, W.; Vogelbacher, U.-J. In *Inorganic Syntheses*; John Wiley & Sons, Inc., 2007; pp 243–249.

(57) Kosolapoff, G. M. *Journal of the American Chemical Society* **1945**, *67* (7), 1180–1182.

(58) Zhang, N.; Casida, J. E. *The Journal of Organic Chemistry* **2001**, *66* (1), 327–329.

(59) Gaboyard, M.; Hervaud, Y.; Boutevin, (B *Phosphorus, Sulfur, and Silicon and the Related Elements* **2002**, *177* (4), 877–891.

(60) Osinski, M. IEEE, 1990; pp 330–333.

(61) Vurgaftman, I.; Meyer, J. R.; Ram-Mohan, L. R. *Journal of Applied Physics* **2001**, *89* (11), 5815–5875.

(62) Chupas, P. J.; Qiu, X.; Hanson, J. C.; Lee, P. L.; Grey, C. P.; Billinge, S. J. L. *Journal of Applied Crystallography* **2003**, *36* (6), 1342–1347.

(63) Hammersley, (A P.; Svensson, S. O.; Hanfland, M.; Fitch, (A N.; Hausermann, D. *High Pressure Research* **1996**, *14* (4–6), 235–248.

(64) Yang, X.; Juhas, P.; Billinge, S. J. L. *Journal of Applied Crystallography* **2014**, *47* (4), 1273–1283.

(65) Juhas, P.; Davis, T.; Farrow, C. L.; Billinge, S. J. L. *Journal of Applied Crystallography* **2013**, *46* (2), 560–566.

(66) Yang, X.; Juhas, P.; Farrow, C. L.; Billinge, S. J. L. *arXiv:1402.3163 [cond-mat]* **2014**.

Chapter 5: Sub-Angstrom Resolution Single Crystal X-Ray Crystal Structure of Carboxylate-Ligated Magic-Size InP as $In_{37}P_{20}(O_2CR)_{51}$ Revealed Unanticipated Molecular Geometry and Enabled Determination of Electronic Structure by TDDFT

5.1 Introduction

Quantum-confined semiconductor nanocrystals (quantum dots, QDs) exhibit strongly size-dependent optical and electronic properties. As a result, considerable effort has been aimed at their integration into light-harvesting and light-emitting devices both in the research laboratory and in the marketplace.[1,2] Predicting the properties of QDs requires detailed knowledge of their size, shape, and composition. A longstanding challenge in this field has been to prepare a homogeneous sample and to grow a single crystal in order to determine a high-resolution structure that allows for unambiguous assignment of these three properties. While there is a rich history of structural interrogation of transition metal and main group cluster molecules,[3–9] to date a complete, atomically precise structural picture of a binary semiconductor QD remains elusive.

Magic-size nanoclusters have emerged as an important class of intermediates at the interface of small molecules and QDs.[10–17] As a class of truly monodisperse nanomaterials, magic-size nanoclusters can offer unique insight into the structure of their larger QD counterparts. Several group II-VI magic-size clusters have been identified and structurally characterized;[3,4,8] however, these clusters do not appear to be directly involved in the high-temperature nucleation of group II-VI QDs since their thermal instability precludes their buildup in these traditional syntheses where kinetics are readily controlled by precursor conversion chemistry.[18–21] For group III-V QDs, on the other hand, precursor conversion chemistry does not appear to be the rate-determining step in the overall growth mechanism,[12,22,23] and magic-size clusters have been implicated as kinetically persistent intermediates whose thermal transformation may be an important step in QD nucleation (See Chapter 4).[12,24,25] Given

the potential significance of these cluster intermediates in elucidating the mechanism of III-V QD formation and in understanding the physical and electronic structure of carboxylate-terminated QDs, we sought to isolate and structurally characterize one such cluster.

5.2 Experimental

5.2.1 Obtaining Diffraction Quality Single Crystals of $In_{37}P_{20}(O_2CCH_2C_6H_5)_{51}$

Herein, we report the first single-crystal X-ray diffraction (XRD) structure of an indium phosphide (InP) magic-size nanocluster with 0.83 Å resolution, including all ligands. This nanocrystal ($In_{37}P_{20}(O_2CCH_2C_6H_5)_{51}$) exhibits a non-stoichiometric core, a geometry that does not correspond to that of bulk InP, and unanticipated ligand binding modes. The electronic structure of $In_{37}P_{20}(O_2CCH_2C_6H_5)_{51}$ is determined using a combination of spectroscopic and time-dependent density functional theory (TDDFT) methods, providing an unprecedented understanding of the way in which the surface of these nanoclusters impacts their optoelectronic properties.

Solution-based syntheses of semiconductor nanocrystals typically yield an ensemble of particles that range in terms of size, shape, and surface composition. However, $In_{37}P_{20}(O_2CR)_{51}$ is the sole nanocrystalline product that we obtain from reaction of tris(trimethylsilyl)phosphine, indium acetate, and carboxylic acid at 100 °C, as evident from elemental analysis and ^{31}P NMR spectroscopy (See Experimental). This cluster has previously been identified by its spectroscopic signatures as a magic size in the growth profile of InP QDs.[12,24] Crystals suitable for single-crystal X-ray analysis were grown from a supersaturated solution of particles ($R = CH_2C_6H_5$) in ethyl acetate and formed as yellow prisms.

5.2.2 Structure of $In_{37}P_{20}(O_2CCH_2C_6H_5)_{51}$: The Nonstoichiometric, Charged Core $[In_{21}P_{20}]^{3+}$

The structure of $In_{37}P_{20}(O_2CCH_2C_6H_5)_{51}$ (Figures 5.1, Figure 5.2, Figure 5.3, Figure 5.4, and Figure 5.5) exhibits several unanticipated features that deviate from the conventional model of a nanoparticle. Binary semiconductor nanocrystals are typically envisioned as possessing a crystalline, stoichiometric core structure that corresponds to a known bulk phase and is unaltered during ligand exchange reactions post-synthesis.[26,27] Additionally, this core would be surrounded by a shell of neutral, datively bound ligands or by a shell of excess metal cations charge-balanced by anionic ligands.[27,28] In the structure of $In_{37}P_{20}(O_2CCH_2C_6H_5)_{51}$ there is no subset of atoms that can accurately be described as a stoichiometric, charge-neutral core of InP. The nanocrystal core, which consists solely of fused 6-membered rings with all phosphorus atoms coordinated to four indium atoms in a pseudo-tetrahedral arrangement (Figure 5.1), has the formula $[In_{21}P_{20}]^{3+}$. This subset of atoms possesses a C_2 rotation axis that bisects two phosphorus atoms and a single indium atom located at the center of the particle, and measures approximately 1.3 nm × 1.0 nm × 1.0 nm. This arrangement of core atoms deviates from that of the known bulk phases of InP.[29] A dihedral angle of 160 ± 3° is consistent along the longest straight In–P chain and demonstrates a clear deviation from zincblende ($\phi = \pm 60°$ or $\pm 180°$) and wurtzite ($\phi = \pm 120°$) (Figure 5.2). The average In–P bond length in the $[In_{21}P_{20}]^{3+}$ core is 2.528 Å (minutes2.479 Å, max 2.624 Å), and the average P–In–P bond angle is 109.2° (minutes97.7°, max 119.9°), while those of the zincblende lattice are 2.541 Å and 109.5°, respectively. An additional 16 indium atoms are singly bound to this core through surface-exposed phosphorus atoms (Figure 5.3), with an average bond length of 2.482 Å (minutes2.450 Å, max 2.515 Å). Since the sum of the single-bond covalent radii for In and P is 2.53 Å, it is inferred that the bonding in the inorganic core of this cluster may be best viewed as covalent in nature, with differences in bond lengths between In–P in the core and In–P at the surface arising from internal strain.[30]

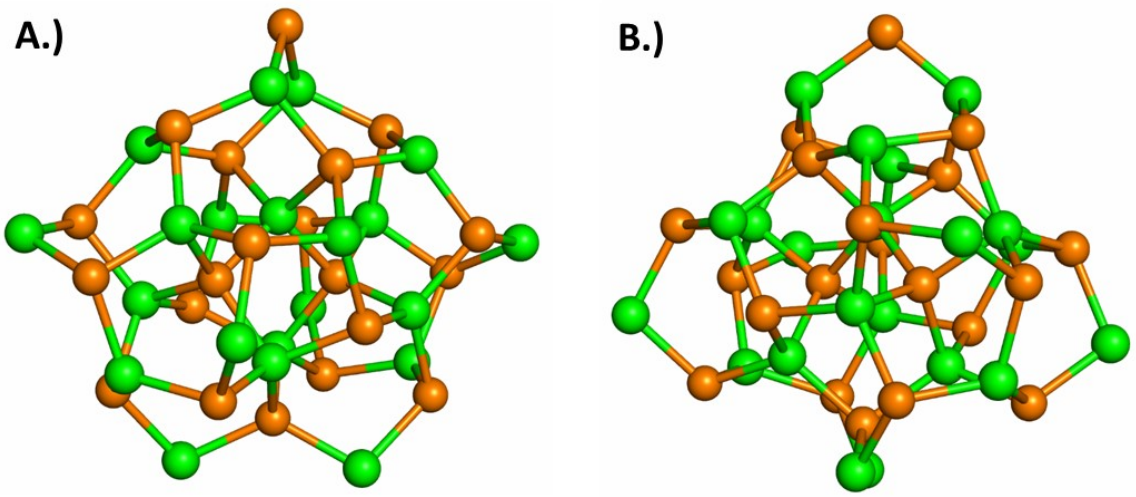

Figure 5.1 (A) Molecular geometry of the subset: $[In_{21}P_{20}]^{3+}$. Color legend: indium = green, phosphorus = orange. This subset of atoms exhibits a pseudo C_2 symmetry in which two P atoms and one In atom lies along the principle rotation axis. (B) Shows the arrangement of $[In_{21}P_{20}]^{3+}$ after rotation by 90° along the principle axis.

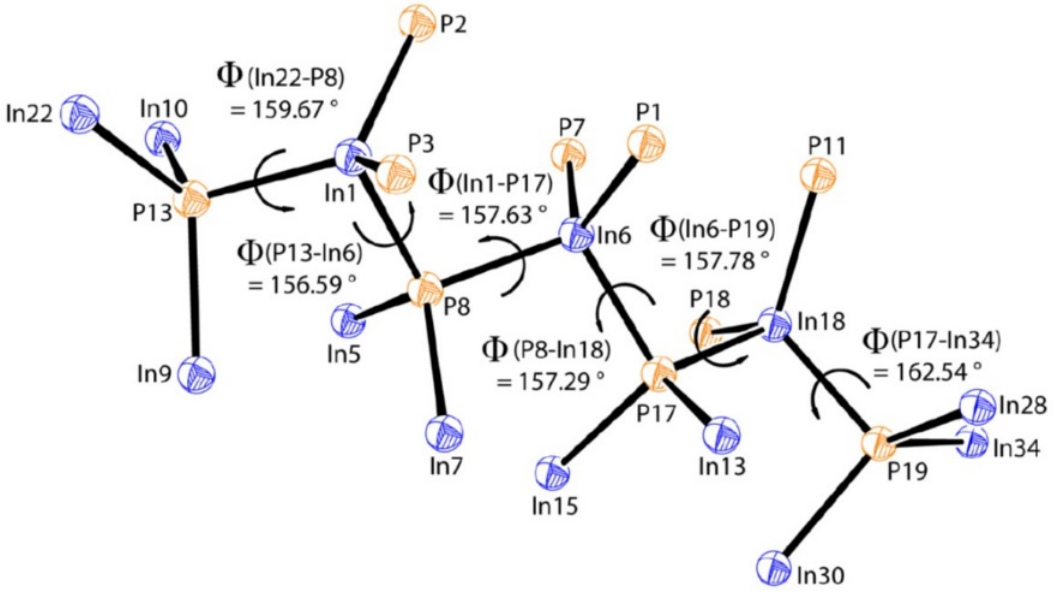

Figure 5.2 Dihedral angles between In and P atoms in the longest chain in $In_{37}P_{20}(O_2CCH_2C_6H_5)_{51}$. Color legend: indium = blue, phosphorus = orange. In6 is the central indium atom that is bisected by the C_2 axis of the $[In_{21}P_{20}]^{3+}$ core. All dihedral angles measure 160 ± 3 ° a clear deviation from the known crystalline phases of InP which are zincblende (ϕ = ±60° or ±180°) and wurtzite (ϕ = ±120°). Note, the subset of atoms depicted here as In1, In5, In7, In6, In15, In13, In18 is a unique subset of atoms of the cluster core in which no indium atom has a bond to an oxygen atom from surface carboxylates. These are the only indium atoms in the structure for which this is true.

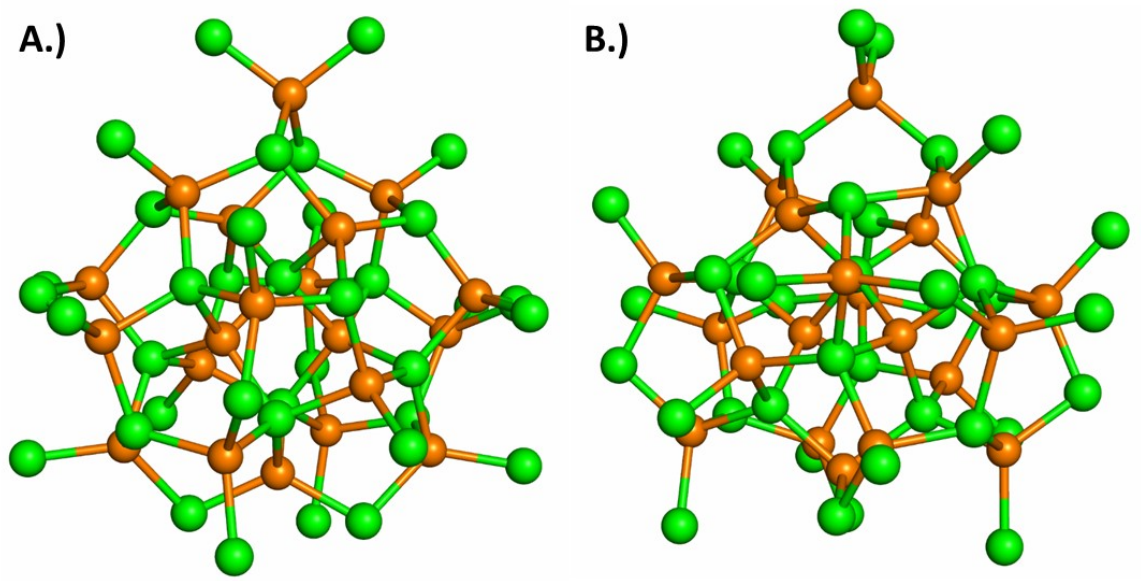

Figure 5.3 (A) Molecular geometry of the subset: $In_{37}P_{20}$. Color legend: indium = green, phosphorus = orange. This subset of atoms exhibits a pseudo C_2 symmetry in which two P atoms and one In atom lies along the principle rotation axis. (B) Shows the arrangement of $In_{37}P_{20}$ after rotation by 90° along the principle axis. Indium atoms bound to only a single phosphorus atom are considered "surface" indium atoms and by excluding these atoms from the structure of $In_{37}P_{20}$ we arrived at the cores structure of $[In_{21}P_{20}]^{3+}$ (See Figure 5.1). The phosphorus atom at the apex of the structure is unique in that is the only phosphorus atom bound to two surface indium atoms.

5.2.3 Structure of $In_{37}P_{20}(O_2CCH_2C_6H_5)_{51}$: a Densely Packed Ligand Set with Predominately Bridging Ligand Set

An accurate picture of the surface chemistry of InP nanoparticles is essential for understanding their optoelectronic properties and for designing methods to alter their surfaces post-synthetically, a crucial step for applications requiring high photoluminescence quantum yield or efficient charge extraction.[27,28,31–34] $In_{37}P_{20}(O_2CCH_2C_6H_5)_{51}$ is an In-rich nanoparticle that is

completely passivated by a phenylacetate ligand set with highly variable coordination modes (Figure 5.4 and Figure 5.5). Each surface indium atom is bound to at least two other indium atoms through bridging carboxylate ligands, and as such this ligand set is best described as entirely anionic in nature (i.e., X-type), with no neutral, datively bound ligands.[27] This stands in contrast to the prevailing model of QD surfaces wherein the dominant coordination modes are thought to be labile, neutral Lewis bases such as primary amines acting as two-electron donors (L-type) or neutral Lewis acids acting as two-electron acceptors (Z-type).[28] The complete structure has an overall spherical appearance with a dense ligand coverage (Figure 5.6). The complete structure exhibits a nearly spherical appearance with a dense ligand coverage. Retention of this tightly bound and dense ligand packing in solution is confirmed via NMR spectroscopy. A ^{1}H–^{1}H COSY spectrum revealed that the methylene protons on a common carbon atom are chemically inequivalent, separated by up to 1.3 ppm. This large difference in chemical shift may be indicative of both hindered rotations about the C–C bonds of the methylene linker and CH−π interactions with nearby aromatic rings (Figure 5.7). Similar interactions have been observed for phenylalanine residues in small proteins.[35]

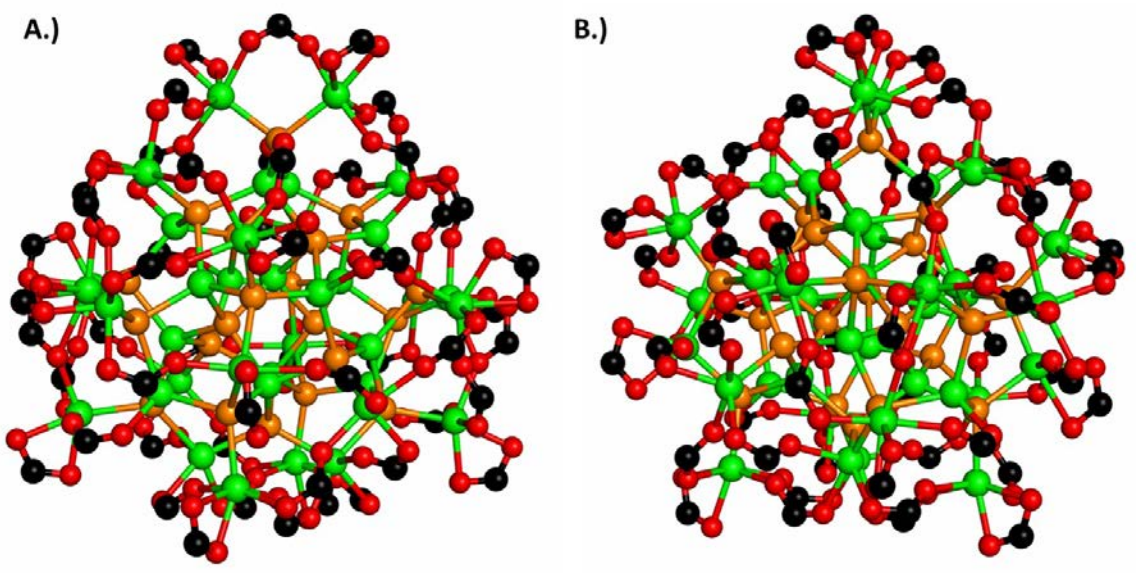

Figure 5.4 (A) Molecular geometry of the subset $In_{37}P_{20}(O_2C)_{51}$. Color legend: indium = green, phosphorus = orange, oxygen = red, carbon = black. (B) Shows the arrangement of $In_{37}P_{20}(O_2C)_{51}$ after rotation by 90° along the principle axis.

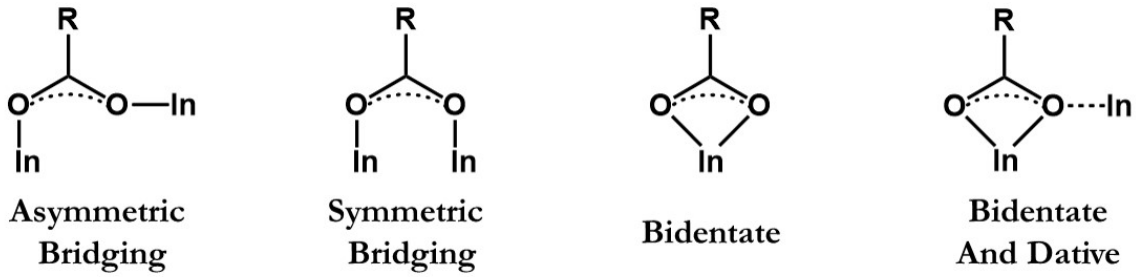

Figure 5.5 Schematic representation of all observed ligand binding modes for $In_{37}P_{20}(O_2CCH_2C_6H_5)_{51}$ arranged from most prominent to least prominent. All carboxylate binding modes are bidentate. Of the 51 phenylacetate ligands, 33 are identified as asymmetric bridging, 12 are identified as bidentate, 5 are identified as symmetric bridging, and 1 is identified as bidentate + dative.

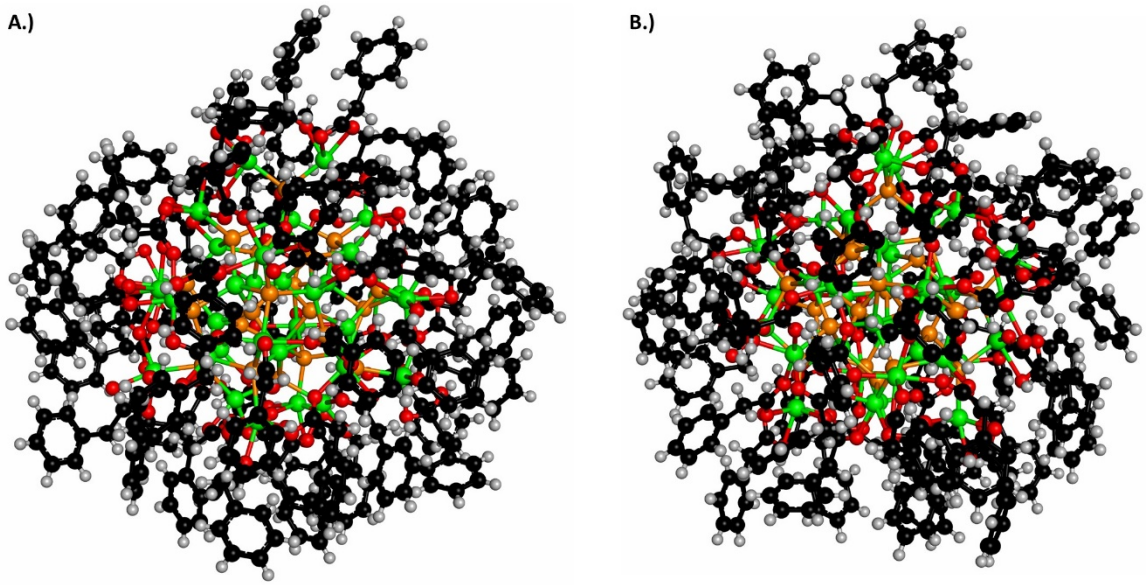

Figure 5.6 Molecular geometry of the complete structure of $In_{37}P_{20}(O_2CCH_2C_6H_5)_{51}$. Color legend: indium = green, phosphorus = orange, oxygen = red, carbon = black, hydrogen = gray. (B) Shows the arrangement of $In_{37}P_{20}(O_2CCH_2C_6H_5)_{51}$ after rotation by 90° along the principle axis. The overall appearance of the nanocluster is nearly spherical with dense ligand coverage.

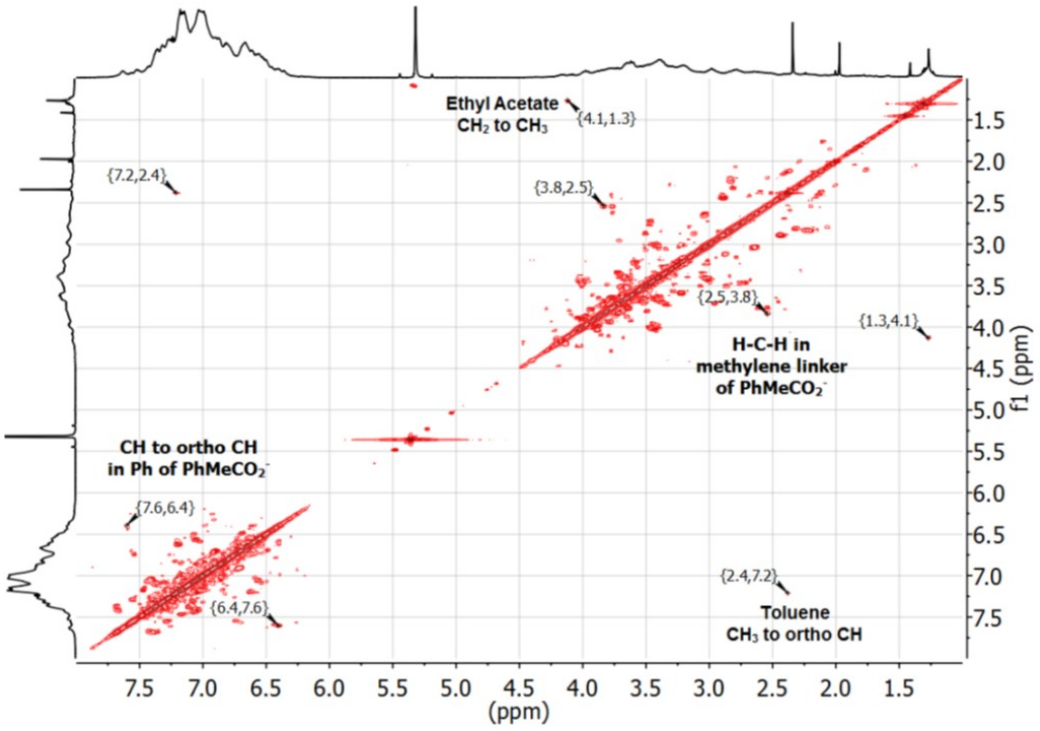

Figure 5.7 ^{1}H-^{1}H COSY NMR spectrum of InP $In_{37}P_{20}(O_2CCH_2C_6H_5)_{51}$ acquired at 700 MHz in CD_2Cl_2 at 298 K. Protons in the methylene region on each phenylacetate ligand are inequivalent indicative of hindered rotation and CH-π interactions.

5.2.4 Analysis of the Crystal Structure of the Sole Reaction Product of with $In_{37}P_{20}(O_2CCH_2C_6H_5)_{51}$ with a Single Equivalent of Water

We discovered that single crystals of $In_{37}P_{20}(O_2CCH_2C_6H_5)_{51}$ are sensitive to air exposure,[12] suggesting a chemical transformation of the particles under these conditions. When these crystals are exposed to air they begin to fracture within 30 min, and a change is observed in the dimensions of the unit cell. In a separate single-crystal XRD study on crystals exposed to moist air, we have identified a stoichiometric reaction with water wherein a single carboxylate ligand adopts a

monodentate binding motif with the resulting open coordination site filled by a water molecule (Figure 5.8). This structural change has minimal impact on the frontier orbitals of the cluster, and hence its electronic structure shows little change, as indicated by TDDFT calculations (Figure 5.9). Interestingly, the reaction with water is selective for a single indium site (likely due to small differences in the Lewis acidity of the indium sites). This result suggests that stoichiometric and site-specific ligand chemistry may be achieved at the surfaces of semiconductor QDs.

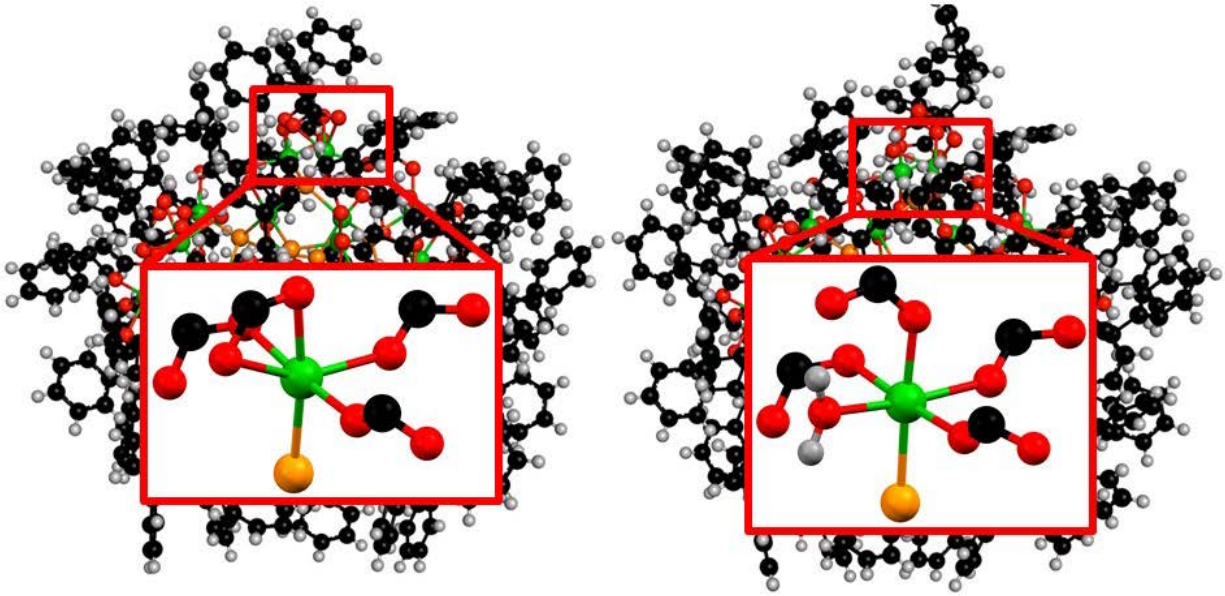

Figure 5.8 (A) Structure of the of $In_{37}P_{20}(O_2CCH_2C_6H_5)_{51}$ and (B) the reaction product of $In_{37}P_{20}(O_2CCH_2C_6H_5)_{51}$ with one equivalent of water including a zoom-in of the specific indium center (16) that has been transformed through coordination of water and a transition of a phenylacetate ligand from bidentate to monodentate.

To further illustrate the preference for complete saturation of the coordination sphere of the surface indium atoms (no "dangling bonds"), calculations were performed on a theoretical structure

where a single bidentate carboxylate ligand was altered to act as a monodentate ligand. This structure is identical to the structure observed on exposure to water, but with the water ligand removed. The calculations from this model reveal that while the HOMO and HOMO-1 remain relatively unperturbed, the LUMO has shifted such that the majority of the electron density is localized on the open coordination site of the under-coordinated indium atom (Figure 5.9). These calculations suggest that it is energetically favorable to saturate the coordination sphere of surface-bound In atoms and that the introduction of an open In coordination site (dangling bond) would manifest as a notable energetic separation of the HOMO-1–LUMO and HOMO–LUMO transitions, resulting in a more asymmetric peak shape in the absorption spectrum of the sample

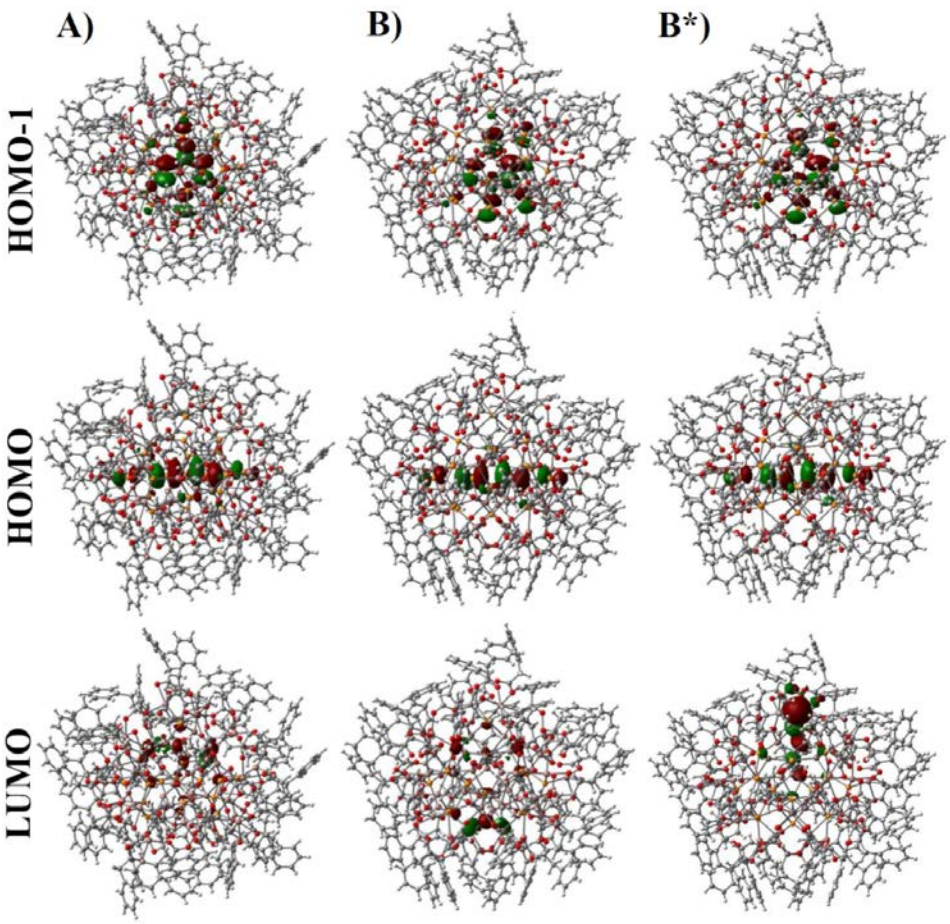

Figure 5.9 (A) HSE06/LANL2DZ molecular orbital (MO) diagrams of the occupied (HOMO-1 and HOMO) and unoccupied (LUMO) orbitals involved in the two brightest transitions calculated for the air-free crystal A $In_{37}P_{20}(O_2CCH_2C_6H_5)_{51}$ and (B) corresponding MOs in the air exposed crystal $In_{37}P_{20}(O_2CCH_2C_6H_5)_{51}$ (H_2O) and (B*) $In_{37}P_{20}(O_2CCH_2C_6H_5)_{51}$ (a theoretical structure where the datively bound H_2O from structure (B) is removed). The MOs were plotted with an isosurface value of 0.025. While the HOMO-1 and HOMO are fairly similar in each structure, the LUMO is drastically altered for the theoretical structure where a single indium atom has decreased its coordination number by one.

5.2.5 Electronic Structure and Optical Properties of $In_{37}P_{20}(O_2CCH_2C_6H_5)_{51}$

$In_{37}P_{20}(O_2CCH_2C_6H_5)_{51}$ shows an asymmetric peak shape in the UV-Vis spectrum for the lowest energy absorbance feature with maxima centered at 2.97 and 3.21 eV (Figure 5.10). TDDFT calculations predict this peak shape to be the result of a pair of energetically similar transitions, with the HOMO–LUMO transition assigned to the shoulder at 2.97 eV (418 nm) and the HOMO-1–LUMO transition assigned to the dominant peak at 3.21 eV (386 nm). These discrete electronic transitions, which are found at higher energies than in bulk InP (1.34 eV),[29] are typical of quantum-confined materials. For InP QDs, experimental data and theoretical predictions suggest that the size dependence of the band gap is best described by a $1/r$ relationship.[36–38] For a diameter of 1.3 nm, the $1/r$ model predicts a bandgap of 3.33 eV (372 nm),[37] which agrees favorably with our experimental observations.

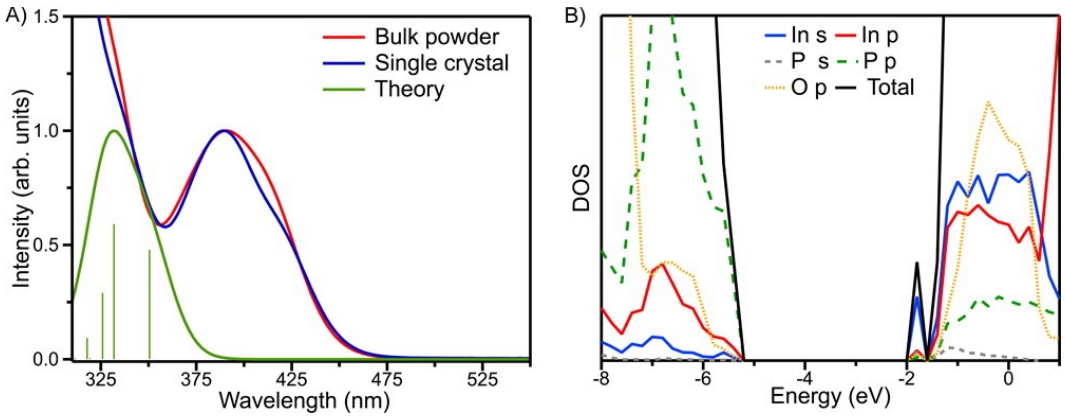

Figure 5.10 Optical spectra and density of states for $In_{37}P_{20}(O_2CCH_2C_6H_5)_{51}$. (A) Experimental (blue, single crystal; red, bulk powder) and TD-HSE06/LANL2DZ computed (green) spectra obtained from the first 10 individual optical transitions (green vertical lines) with a Gaussian smoothing function (width 0.12 eV). All intensities are normalized. (B) HSE06/LANL2DZ DOS and PDOS (see legend) diagram.

5.2.6 Analysis of Spectral Lineshape through a Combination of Time-Density Functional Theory

At room temperature the lowest energy electronic transitions in $In_{37}P_{20}(O_2CCH_2C_6H_5)_{51}$ are broad, with full widths at half-maximum of approximately 0.306 and 0.247 eV (Figure 5.11). Typically, such broad peaks are thought to arise as a result of sample inhomogeneity, and synthetic efforts in the QD community have been directed at minimizing spectral line width through minimizing particle size and shape deviations.[26,39–41] In the absence of broadening from ensemble effects, spectral line widths tend to increase with a corresponding decrease in particle size.[42,43]

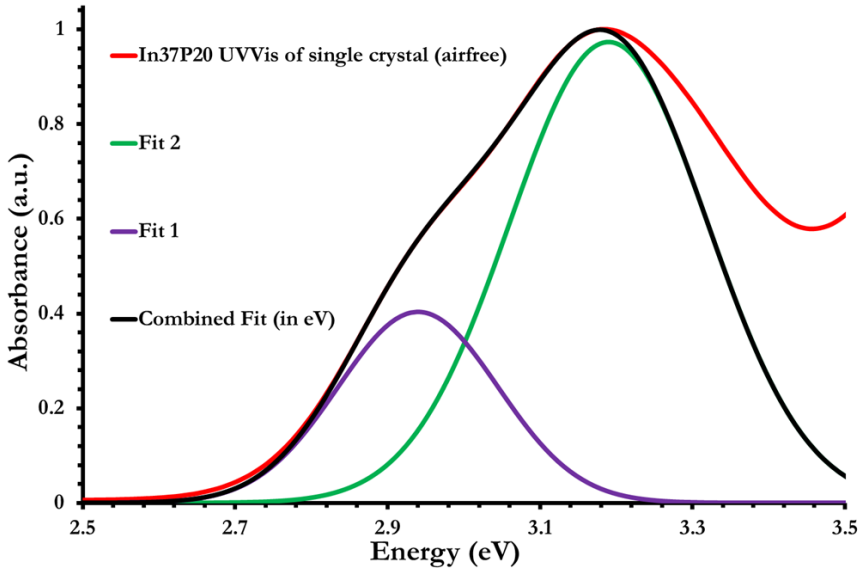

Figure 5.11 Gaussian fits for the first two features present in the absorption spectrum of $In_{37}P_{20}(O_2CCH_2C_6H_5)_{51}$ after normalizing to the HOMO-1 to LUMO transition. Fits were made using the equation: $f(x) = y + ae^{(\frac{-(x-b)^2}{2c^2})}$ with Fit 1 using the following values: y = 0.00, a = 0.4035, b = 2.94 eV, and c = 0.105 The values used for Fit 2 were: y = 0.00, a = 0.973, b = 3.19 eV, and c = 0.130 Full width at half max for each fit was calculated using the equation: $FWHM = 2\sqrt{2\ln(2)}c$ which gives the values of 0.247 eV for Fit 1 and 0.306 eV for Fit 2).

In order to qualitatively track precursor conversion during a synthesis of InP nanocrystals, several studies have monitored the total absorbance in the UV at a specified wavelength.[22,40,44] An inherent assumption in this technique is that the absorbance of the solution at the specified wavelength in the UV is indicative of the total amount of InP present in solution, regardless of particle size. Since we are able to obtain $In_{37}P_{20}(O_2CCH_2C_6H_5)_{51}$ with >99% purity by elemental analysis, we are now capable of determining the absorbance of $In_{37}P_{20}(O_2CCH_2C_6H_5)_{51}$ at various wavelengths and concentrations. This will allow us to determine the extinction coefficient of $In_{37}P_{20}(O_2CCH_2C_6H_5)_{51}$

and test the validity of the assumption that absorbance in the UV can be used to track InP concentration (Figure 5.12).

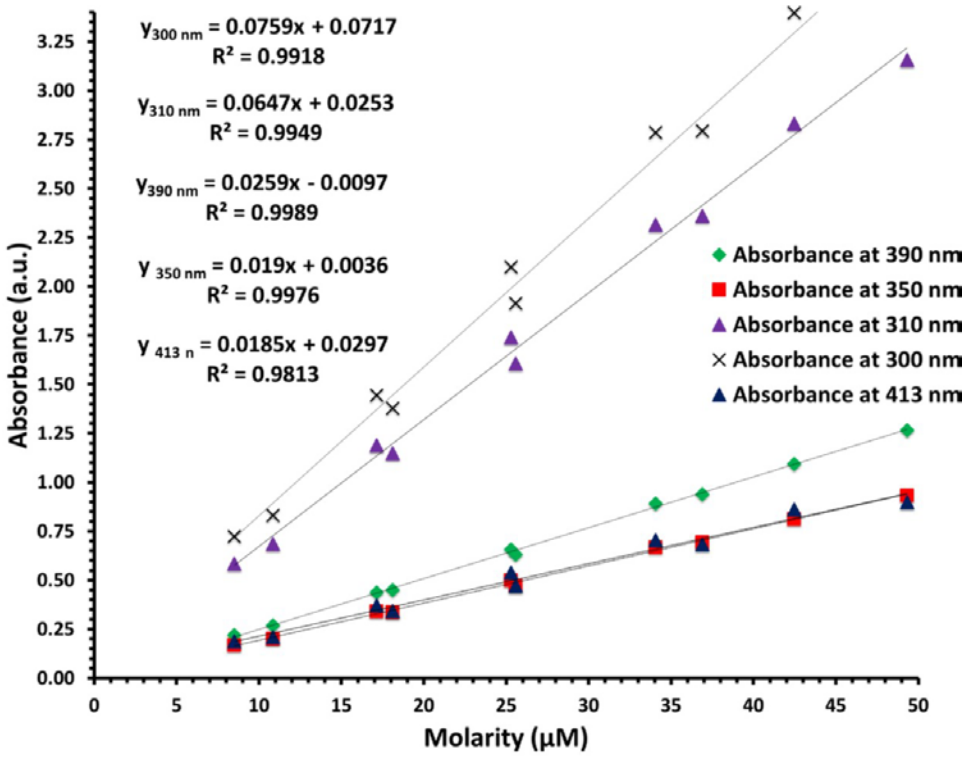

Figure 5.12 Plots of absorbance vs. concentration of $In_{37}P_{20}(O_2CCH_2C_6H_5)_{51}$ for 413 nm (blue triangle), 390 nm (green diamond), 350 nm (red square), 310 nm (purple triangle), and 300 nm (black cross) which give extinction coefficients of 18,500 L mol^{-1} cm^{-1}, 18, 800 L mol^{-1} cm^{-1}, 25,700 L mol^{-1} cm^{-1}, 64,300 L mol^{-1} cm^{-1}, and 75,500 L mol^{-1} cm^{-1} respectively. Solutions of $In_{37}P_{20}(O_2CCH_2C_6H_5)_{51}$ in toluene obey the Beer–Lambert law for these wavelengths at least up to 50 μM concentrations. 413 nm and 350 nm lie on either side of the most prominent electronic transition in the spectrum (located at 386 nm) of $In_{37}P_{20}(O_2CCH_2C_6H_5)_{51}$ illustrating that the extinction coefficient at these wavelengths is still dependent upon the quantum confinement effect.

Even though we have been able to prepare a homogeneous sample, we still observe a broader absorption line width than what has been reported for the intrinsic line width of nanocrystalline InP as well as for InP nanoclusters with a similar size.[12,45] We hypothesize that the major contributor to this line broadening is coupling with specific vibrational motions within the nanocrystal lattice that arises due to the localization of the frontier molecular orbitals of the particle (Figure 5.13). This hypothesis is supported by variable-temperature UV-Vis spectroscopy, which shows significant spectral line narrowing and enhanced resolution of the HOMO–LUMO transition into a distinct peak as the sample is cooled to 100 K (Figure 5.14).

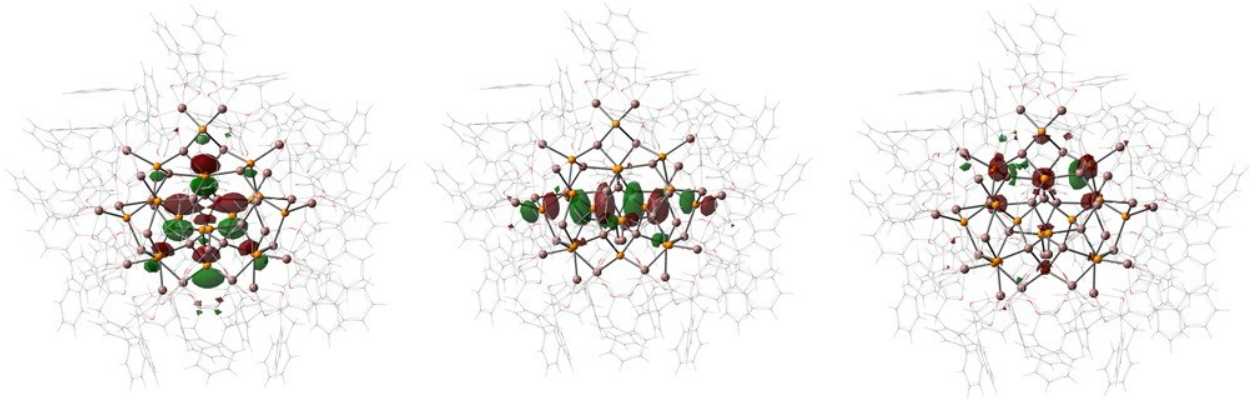

Figure 5.13 HSE06/LANL2DZ molecular orbital (MO) diagrams of the occupied (HOMO-1, left and HOMO, middle) and unoccupied (LUMO, right) orbitals involved in the lowest energy computed electronic transitions for $In_{37}P_{20}(O_2CCH_2C_6H_5)_{51}$. The MOs were plotted with an isosurface value of 0.025.

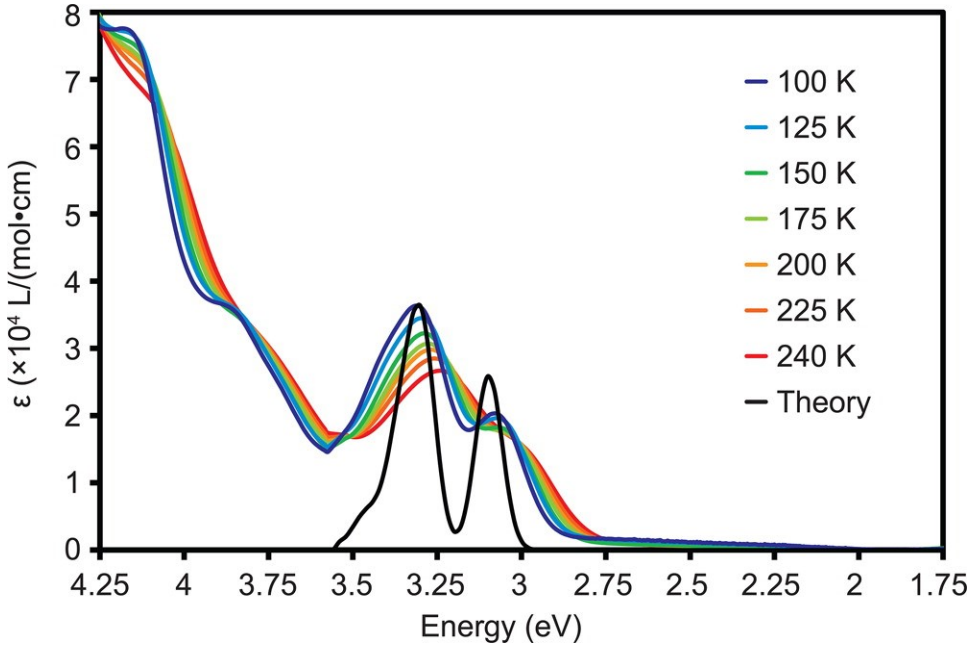

Figure 5.14 Experimental variable-temperature UV-Vis spectra of $In_{37}P_{20}(O_2CCH_2C_6H_5)_{51}$ in the solid state with a comparison to the TD-HSE06/LANL2DZ theoretical prediction obtained from the first 5 individual optical transitions smoothed by Gaussian functions (width 0.04 eV) and shifted and normalized to match the experimental peak maximum around 3.3 eV at 100 K.

$In_{37}P_{20}(O_2CCH_2C_6H_5)_{51}$ shows no appreciable photoluminescence at 298 K, consistent with observations of larger In-rich InP QDs, which typically exhibit photoluminescence quantum yields lower than 1%.[22,31] The primary non-radiative pathway proposed for InP nanocrystals is one where unpassivated surface atoms (dangling bonds) act as charge traps.[46] This is in line with observations that HF etching increases quantum yields up to 47% by passivation of In dangling bonds with F^- and of P dangling bonds with H^+.[47] Additionally, EPR measurements of ground-state and photoexcited colloidal InP support the presence of both electron and hole traps.[48] Given that $In_{37}P_{20}(O_2CCH_2C_6H_5)_{51}$ has neither unpassivated indium atoms nor phosphorus atoms at its surface, we hypothesize that the main energy loss pathway in this sample is through non-radiative vibrational relaxation due to motions within the crystal lattice.

5.2.6 Evidence that the Structure of $In_{37}P_{20}(O_2CR)_{51}$ is General to Alkylcarboxylates and Comparison to Phosphonate Ligated Clusters

We have previously shown that carboxylate-ligated InP MSCs exhibit a unique solution phase $^{31}P\{^1H\}$ spectrum (See Chapter 4 Figure 5.11). While these spectra are reproducible from batch to batch for a given carboxylate ligand, there are significant differences in $^{31}P\{^1H\}$ spectra of InP MSCs synthesized with different carboxylate ligands (Figure 5.15).

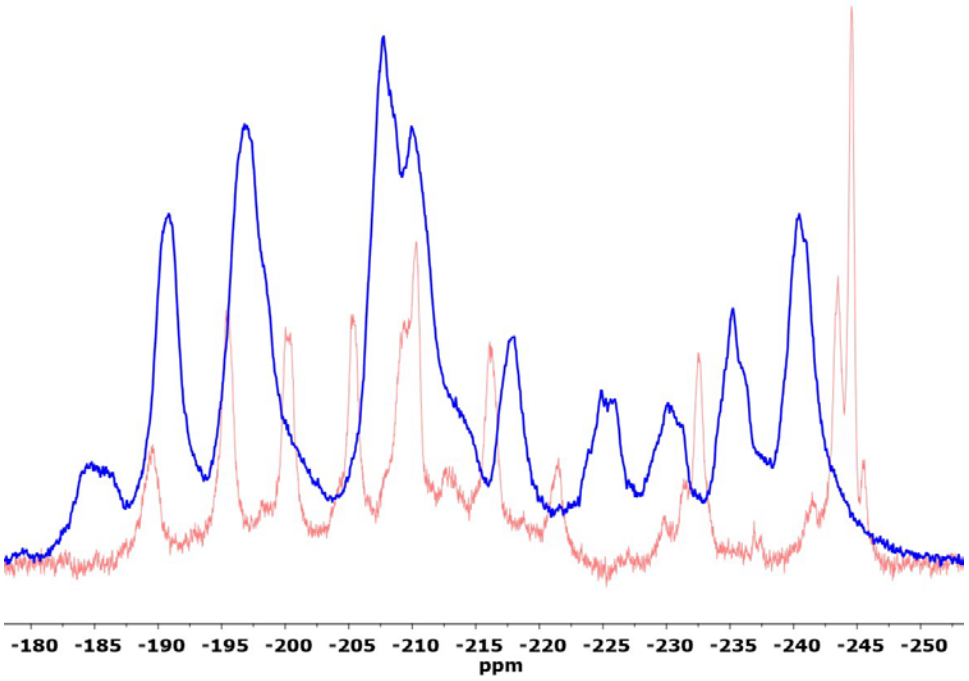

Figure 5.15 $^{31}P\{^1H\}$ NMR spectra of InP nanoclusters with either a phenylacetate ligand set (blue trace) or with an oleate ligand set (red trace) taken at 202.3 MHz in C_6D_6. While both spectra exhibit nine distinct peaks in approximately same region of their spectrum there are clear differences in individual peak positions and linewidths between the two spectra.

While there are significant differences in terms of peak position and linewidth between the $^{31}P\{^{1}H\}$ NMR spectra of InP nanoclusters with different carboxylate ligand sets it is known that $^{31}P\{^{1}H\}$ NMR is sensitive to small deviations in bond angles.[49,50] Additionally, the choice of ligand set will influence the hydrodynamic radius and the molecular weight of the nanocluster. This could in turn affect spectral linewidths in solution phase $^{31}P\{^{1}H\}$ NMR by altering the tumbling rate of the nanocluster. A similar effect has been observed for ^{1}H and ^{13}C NMR spectra of nanoparticles where a decrease in particle size coincided with an increase in spectral linewidths due to a decrease in the T_2 times from the change in tumbling rate.[38, 39] Given that the $^{31}P\{^{1}H\}$ NMR spectrum is not ligand independent, we turned to UV-Vis absorbance spectroscopy and PDF analysis of nanoclusters to determine if the molecular geometry observed for the subset $In_{37}P_{20}(O_2CR)_{51}$ in $In_{37}P_{20}(O_2CCH_2C_6H_5)_{51}$ is general for alky carboxylate ligand sets. We observed that UV-Vis spectra are nearly identical for single crystals of $In_{37}P_{20}(O_2CCH_2C_6H_5)_{51}$ and InP magic-size nanoclusters with a myristate ligand set (Figure 5.16). PDF analysis revealed that both $In_{37}P_{20}(O_2CCH_2C_6H_5)_{51}$ and InP myristate ligated clusters agree well with the molecular geometry solved by X-ray crystallography (Figures 5.17 and Figure 5.18). In contrast, InP phosphonate ligated clusters are predicted to be of a similar size based upon UV-Vis and PDF analysis but do not match the molecular geometry observed for $In_{37}P_{20}(O_2CCH_2C_6H_5)_{51}$ or an $In_{35}P_{20}$ tetrahedron that would be analogous to structures characterized by crystallography for CdSe clusters (See Chapter 4, Figures 4.7 and Figure 4.8 for UV-Vis absorbance spectra of InP clusters with phosphonate ligands).[8]

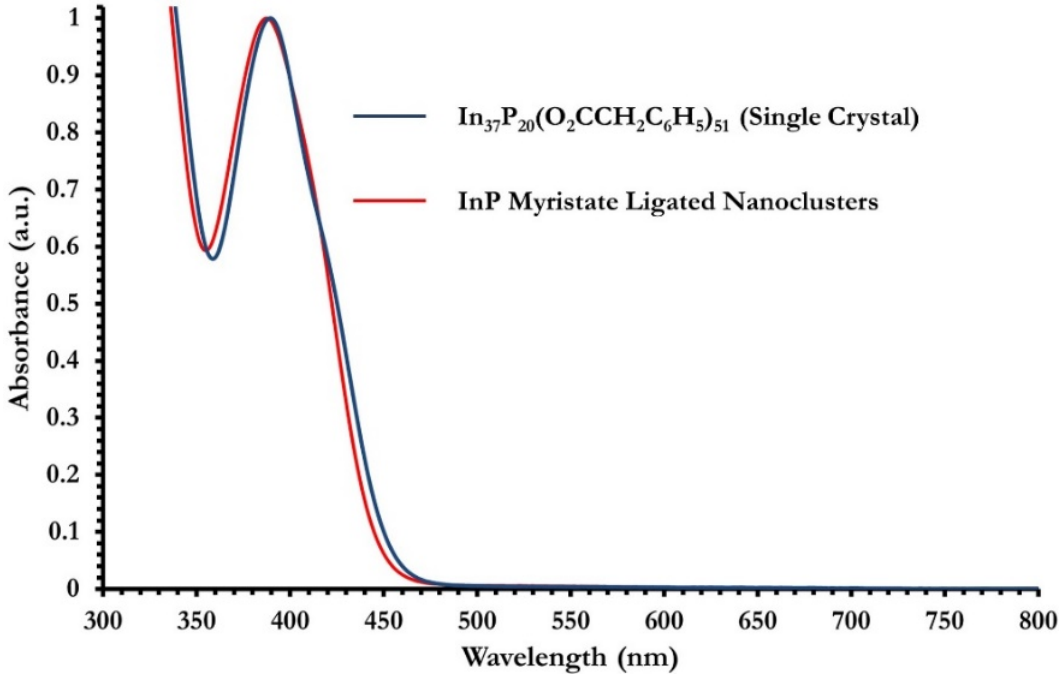

Figure 5.16 Normalized UV-Vis absorbance spectra of single crystals of $In_{37}P_{20}(O_2CCH_2C_6H_5)_{51}$ and a solution of InP myristate ligated nanoclusters. Both spectra match well with the spectrum predicted from the crystal structure of $In_{37}P_{20}(O_2CCH_2C_6H_5)_{51}$ by TDDFT (See Figure 5.10).

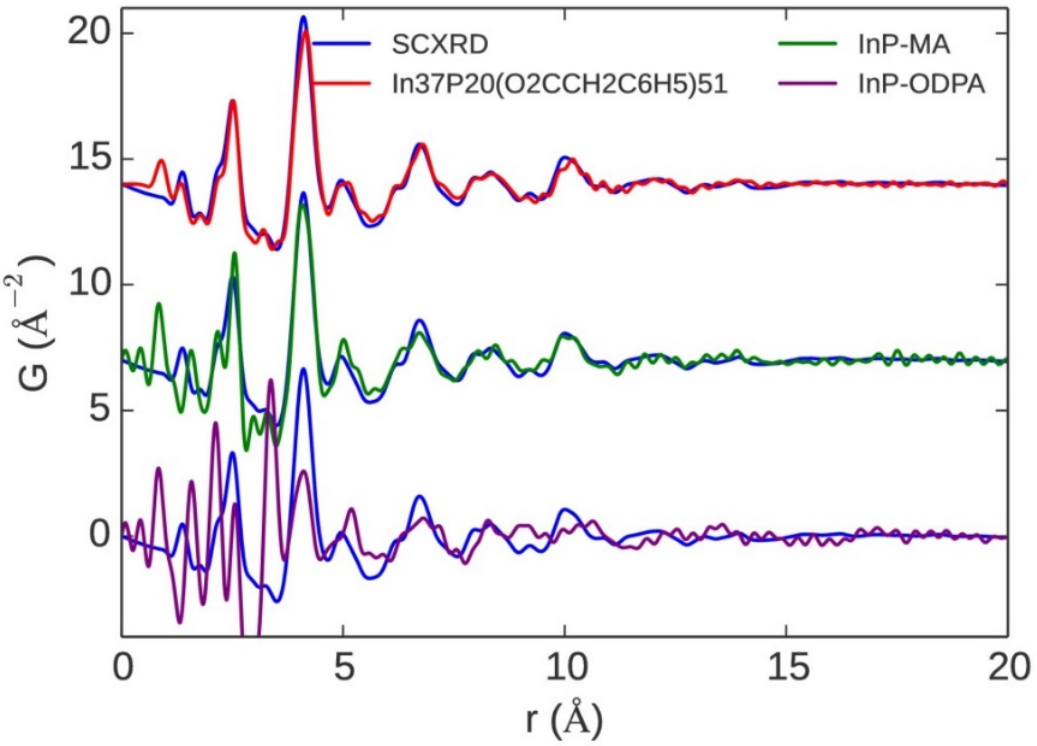

Figure 5.17 Comparison of PDF Analysis of $In_{37}P_{20}(O_2CCH_2C_6H_5)_{51}$, InP MA MSCs, and InP ODPA MSCs to the model obtained by single crystal X-ray diffraction (SCXRD) of $In_{37}P_{20}(O_2CCH_2C_6H_5)_{51}$. $In_{37}P_{20}(O_2CCH_2C_6H_5)_{51}$ and InP MA MSCs fit the SCXRD model well, but the InP ODPA do not.

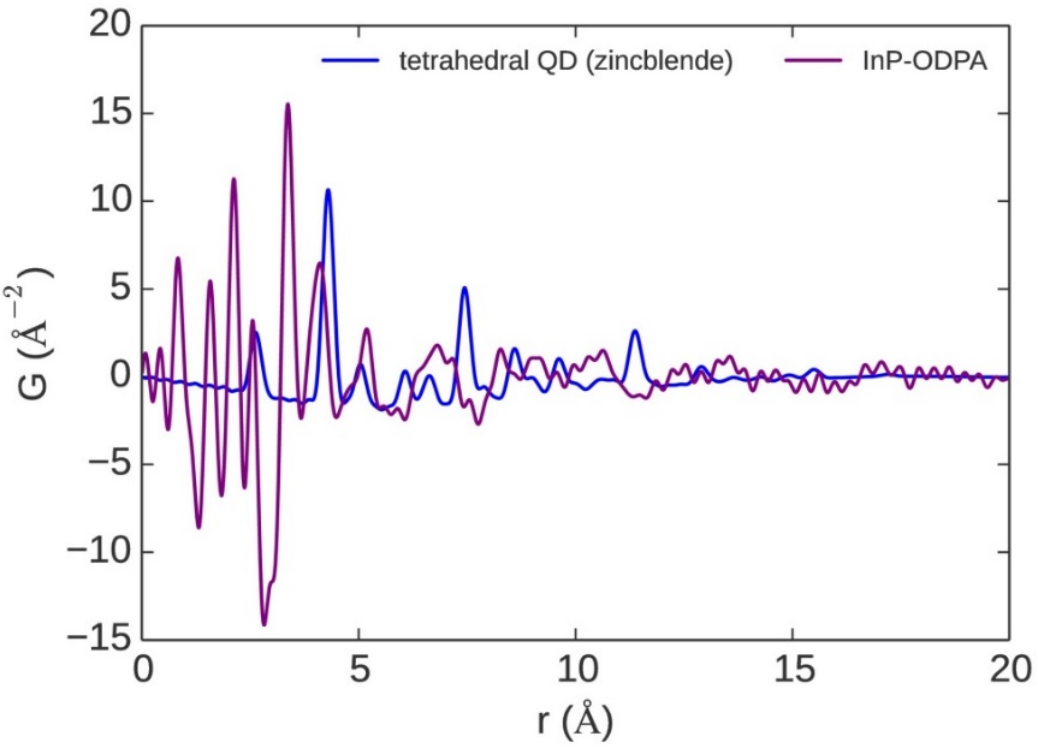

Figure 5.18 PDF analysis of a zincblende model of an $In_{35}P_{20}$ tetrahedron and InP clusters with a phosphonate ligand set. No improvement in the fit observed for the $In_{35}P_{20}$ tetrahedron model over the SCXRD model of $In_{37}P_{20}(O_2CCH_2C_6H_5)_{51}$.

5.2.7 Tentative Assignment of Solution Phase ^{31}P NMR Spectrum of $In_{37}P_{20}(O_2CR)_{51}$ by Consulting the Crystal Structure

UV-Vis absorbance spectroscopy and PDF analysis suggest that the molecular geometry of the subset $In_{37}P_{20}(O_2C)_{51}$ from the crystal structure of $In_{37}P_{20}(O_2CCH_2C_6H_5)_{51}$ should be general for alkyl carboxylate ligated MSCs. With this information and the crystal structure of $In_{37}P_{20}(O_2CCH_2C_6H_5)_{51}$, it should be feasible to give a tentative assignment to the $^{31}P\{^1H\}$ NMR of carboxylate ligated InP MSCs. The $^{31}P\{^1H\}$ NMR spectrum of the oleate ligated clusters is the most

straightforward to assign given that it has sharper peaks with better separation than the $^{31}P\{^{1}H\}$ NMR spectrum of $In_{37}P_{20}(O_2CCH_2C_6H_5)_{51}$. In order to determine the minimal delay time needed between pulses such that each ^{31}P environment would be represented quantitatively in the averaged spectra, an inversion recovery experiment was performed to determine T_1 times for ^{31}P in InP oleate clusters (Figure 5.19).

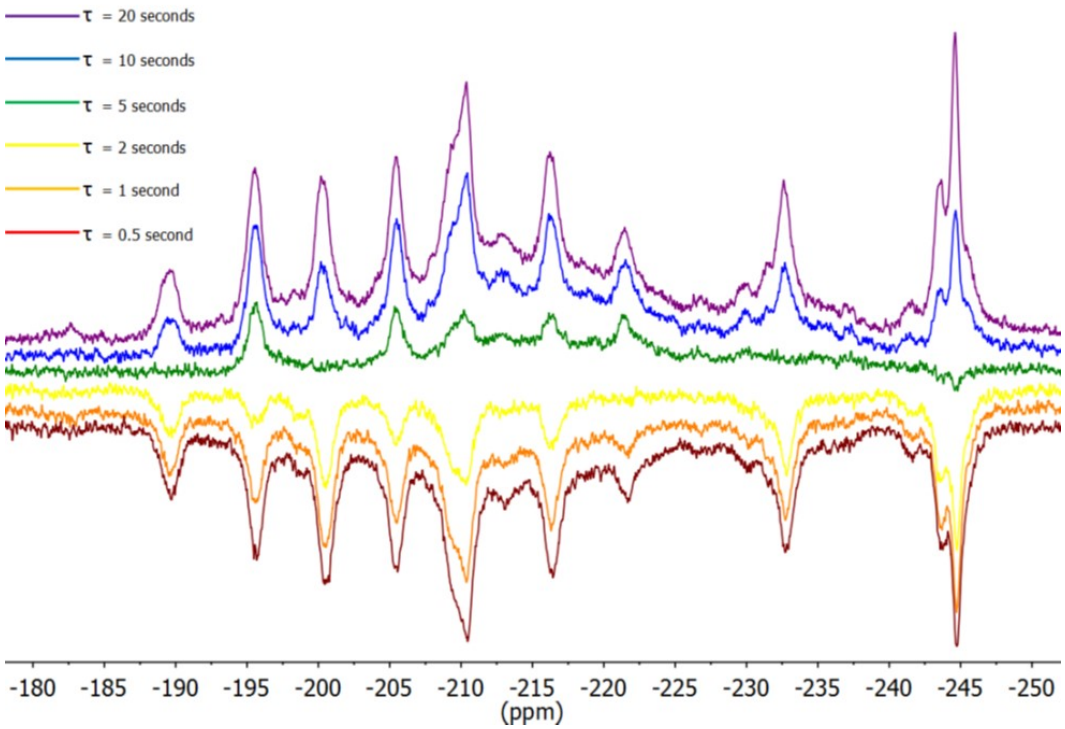

Figure 5.19 $^{31}P\{^{1}H\}$ NMR inversion recovery spectra of $In_{37}P_{20}(O_2C(CH_2)_7CH{=}CH(CH2)_7CH_3)_{51}$ with delays between of 0.5, 1, 2, 5, 10 and 20 s between the 180 and 90 ° pulses. All T1 times lie between about 0.7 and 8 seconds. Spectra were acquired at 202.4 MHz in C_6D_6.

After determining by the inversion recovery experiment that the minimal delay time between pulses should be about 40 seconds for integration of the ^{31}P resonances to be 99% accurate we

acquired such a quantitative spectrum (Figure 5.19). If the integral of the peak furthest downfield in the $^{31}P\{^{1}H\}$ NMR spectrum of $In_{37}P_{20}(O_2C(CH_2)_7CH=CH(CH_2)_7CH_3)_{51}$ is normalized to 1, then each other integration is within 0.1 of the integers of 1, 2, or 4 and sum to 19 which is consistent with the model of $In_{37}P_{20}(O_2C(CH_2)_7CH=CH(CH_2)_7CH_3)_{51}$ (Figure 5.20).

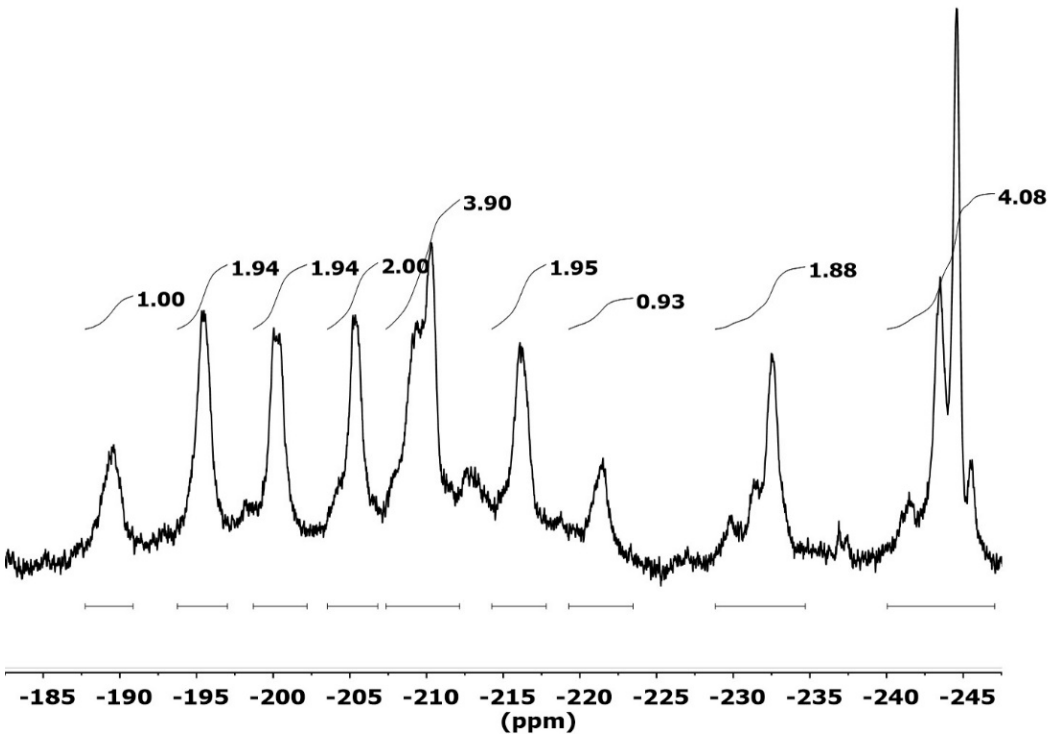

Figure 5.20 $^{31}P\{^{1}H\}$ NMR spectrum of $In_{37}P_{20}(O_2C(CH_2)_7CH=CH(CH2)_7CH_3)_{51}$ taken at 202.3 MHz in C_6D_6 with a delay of 42 seconds in between pulses.

There are only two ^{31}P environments that are unique in the crystal structure of $In_{37}P_{20}(O_2CCH_2C_6H_5)_{51}$, namely those that are bisected by the C_2 axis for the subset $In_{37}P_{20}$. The mostly likely candidates for these two ^{31}P environments are therefore the resonances at –189.5 and –221.5 ppm as these are the only two peaks that integrate to 1. These two peaks are separated in chemical

shift by a difference of 32 ppm. Given that all P atoms in the cluster are in a pseudo tetrahedral environment with four In–P bonds, in order to account for this difference in chemical shift we need to determine a relative measure of the shielding felt by each phosphorus atom in the cluster. In order to account for shielding, an analysis was performed where the bonding environment was analyzed by classifying each indium atom according to the number of In–P bonds it possessed (Table 5.1). The more In–P bonds an atom possessed, the more "core character" it was assigned. Indium atoms with more core character are assumed to be more electron donating than an indium atom with more surface character since oxygen is more electronegative than phosphorus. A phosphorus atom bound to such an indium will therefore experience greater shielding than a phosphorus atom bound to indium atoms that are more surface-like (electron withdrawing).

	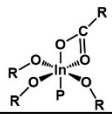	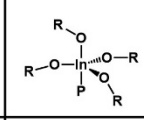	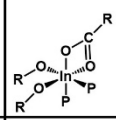	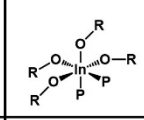	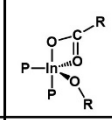	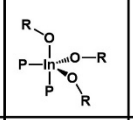	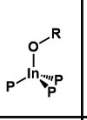	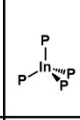
In-P Bond Count	1	1	2	2	2	2	3	4
In-O Bond Count	5	4	4	4	3	3	1	0
# of In Atoms in Cluster	8	2	2	6	2	2	8	7

Table 5.1 Description of the 1st coordination sphere for every indium atom in $In_{37}P_{20}(O_2CCH_2C_6H_5)_{51}$. Note that as the number of In–P bonds increases the number of In-O bonds decreases. This trend holds true for all indium atoms in the cluster (bottom row sums to all 37 indium atoms) and therefore the number of In–P bonds an indium center possess can be used as a back-of-the-envelope calculation of how electron donating or withdrawing that indium center is.

By applying this counting method to the two unique ^{31}P environments observed in $In_{37}P_{20}(O_2CCH_2C_6H_5)_{51}$, the phosphorus atom that is bound to two surface indium atoms (shown as the top atom in Figures 5.1) is predicted to be the most deshielded, and therefore the most downfield. This is consistent with the observation that one of the two peaks in the $^{31}P\{^1H\}$ NMR spectrum of $In_{37}P_{20}(O_2C(CH_2)_7CH=CH(CH_2)_7CH_3)_{51}$ that integrates to 1 is the peak that comes in most downfield. In contrast, the most shielded ^{31}P environments should be those closest to the core. There are only two phosphors atoms that are bound to indium centers that only exhibit In–P bonds. These two phosphorus atoms should appear most upfield, but the most upfield peak was previously assigned as a multiplet that integrated to about 4.1 which is not consistent with this assignment. If we treat this multiplet as two doublets we obtain integrations of about 1.9 and 2.2 which would now be consistent with assignment. The next furthest upfield resonances would be the other pair of phosphorus atoms bound to the central indium atom which is bisected by the C_2 axis for the $In_{37}P_{20}$ subset. The next furthest upfield resonance is predicted to be for the pair of phosphorus atoms that are located the shortest distance away from the single phosphorus atom predicted to be most downfield. The assignment of these last two pair of phosphorus may seem counterintuitive if one were attempting to assign ^{31}P atoms by their relative position in $In_{37}P_{20}(O_2CR)_{51}$. All other phosphorus nuclei in $In_{37}P_{20}(O_2CR)_{51}$ should experience approximately the same shielding according to this method and are indeed adjacent to each other by our assignment so far (Figure 5.21).

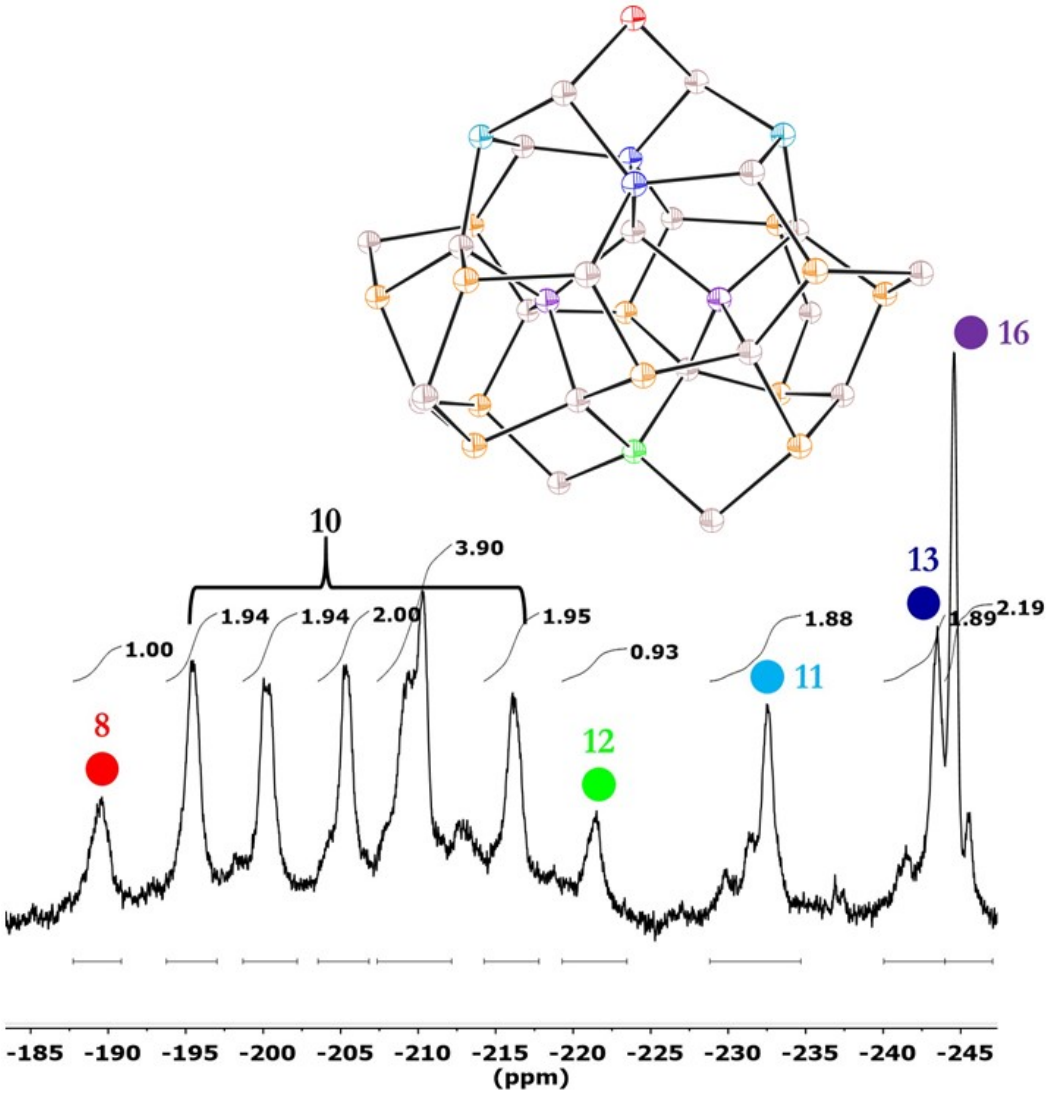

Figure 5.21 Assignment of $^{31}P\{^{1}H\}$ NMR spectrum of $In_{37}P_{20}(O_2C(CH_2)_7CH{=}CH(CH2)_7CH_3)_{51}$ so far based upon the crystal structure of $In_{37}P_{20}(O_2CCH_2C_6H_5)_{51}$, the C_2 symmetry of the $In_{37}P_{20}(O_2CR)_{51}$ atom subset, and the number of In–P bounds exhibited by each indium metal center. The colored numbers indicate the sum of all In–P bonds for each of the 4 indium atoms bound to that ^{31}P environment. The sum of all In–P bonds from each of the 4 indium atoms bound to each unassigned ^{31}P environment is 10. Gray ellipsoids are indium and orange ellipsoids are unassigned phosphorus atoms. See Figure 5.22 for labels of the assigned phosphorus atoms.

Six ^{31}P environments remain unassigned in the $^{31}P\{^{1}H\}$ NMR spectrum of $In_{37}P_{20}(O_2C(CH_2)_7CH=CH(CH2)_7CH_3)_{51}$ after accounting for the shielding experienced by each ^{31}P environment. While the number of In–P bonds an indium atom is relatively easy to visualize and can be used as a kind of back-of-the-envelope calculation of how electron withdrawing a given indium atom should be, a more in depth analysis will need to account for the number of In–O bonds at each indium center. Note that in Table 5.1 that an indium atom with 1 In–P bonds may have 4 or 5 In–O bonds and an In atom with 2 In–P bonds may have 3 or 2 In–O bonds. By carefully accounting for every In–O bond, we will be able to give a more precise assignment of the expected shielding at each phosphorus atom. Taking inventory of every oxygen atom bound to every indium atom allows for a tentative assignment of two more peaks (Table 5.2, Table 5.3, Table 5.4, Figures 5.21, and Figure 5.22).

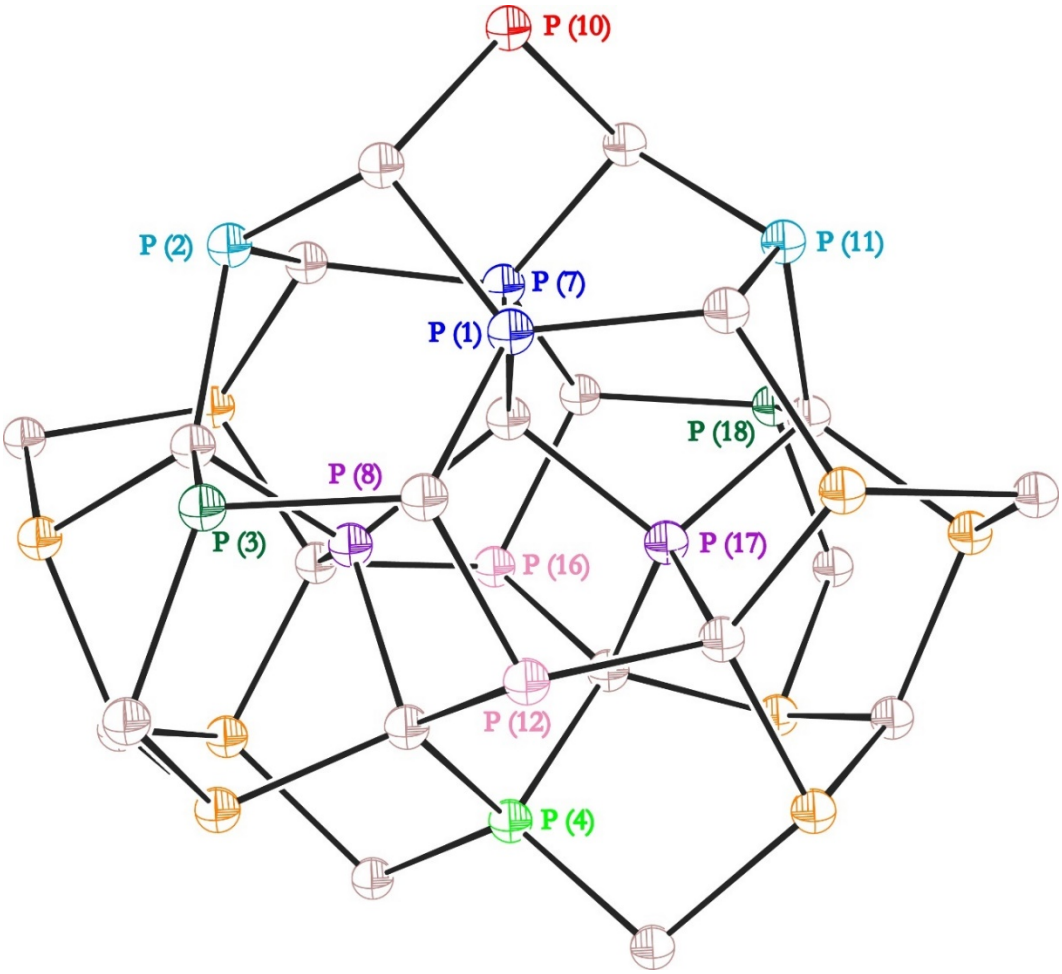

Figure 5.22 Diagram of every phosphorus atom for the subset $In_{21}P_{20}$. Phosphorus labels are the same as will be used in Table 5.2, Table 5.3, Table 5.4. Each phosphorus atom and its label (except for those which cannot be unanimously assigned in the ^{31}P NMR spectrum) are colored to match the Figure 5.22 for the final assignment of $^{31}P\{^{1}H\}$ NMR spectrum of $In_{37}P_{20}(O_2C(CH_2)_7CH{=}CH(CH2)_7CH_3)_{51}$.

Phosphorus Atom	Indium Atoms Bound to Phosphorus Atoms	Oxygen Atoms Bound to Those Indium Atoms
P(8) and P(17) (most upfield)	In(6) In(1) In(5) In(7) In(6) In(18) In(13) In(15)	None
P(7) and P(1) (2nd most upfield)	In(2) In(8) In(3) In(6) In(18) In(13) In(15)	O(71) O(70) O(53) O(13) O(38) O(59)
P(11) and P(2) (doublet 3rd most upfield)	In(21) In(3) In(18) In(12) In(25) In(14) In(1) In(2)	O(71) O(59) O(99) O(83) O(74) O(58) O(53) O(38) O(20) O(34) O(11) O(26)
P(4) (singlet 4th most upfield)	In(7) In(15) In(29) In(20)	O(66) O(31) O(75) O(48) O(29) O(22)
P(16) and P(12)	In(31) In(15) In(8) In(5) In(17) In(7) In(13) In(11)	O(13) O(21) O(16) O(24) O(18) O(70) O(76) O(68) O(40) O(62)
P(13) and P(19) (unassigned)	In(22) In(10) In(1) In(9) In(34) In(18) In(28) In(30)	O(12) O(1) O(10) (O2) O(63) O(51) O(9) O(96) O(19) O(46) O(73) O(78) O(89) O(77) O(85) O(90) O(87) O(84)
P(9) and P(14) (unassigned)	In(19) In(5) In(2) In(10) In(32) In(13) In(12) In(28)	O(38) O(12) O(1) O(10) O(2) O(17) O(3) O(5) O(6) O(14) O(71) O(73) O(78) O(89) O(61) O(92) O(81) O(82) O(69)
P(5) and P(20)	In(9) In(24) In(7) In(4) In(35) In(30) In(15) In(37)	O(63) O(65) O(50) O(39) O(47) O(101) O(95) O(102) O(67) O(93) O(88) O(15) O(94) O(46) O(30) O(23) O(28) O(27)
P(15) and P(6)	In(30) In(36) In(13) In(29) In(9) In(26) In(5) In(20)	O(46) O(66) O(31) O(75) O(91) O(79) O(77) O(45) O(80) O(48) O(29) O(22) O(63) O(4) O(2) O(7) O(8) O(64)
P(18) and P(3) (unassigned)	In(33) In(8) In(18) In(37) In(23) In(1) In(11) In(4)	O(70) O(25) O(41) O(42) O(54) O(52) O(101) O(95) O(102) O(67) O(93) O(88) O(15) O(94) O(13) O(57) O(55) O(56) O(86) O(60)
P(10) (least upfield)	In(16) In(27) In(14) In(3)	O(53) O(59) O(33) O(36) O(37) O(97) O(35) O(100) O(72) O(43) O(98) O(44)

Table 5.2 Inventory of every ^{31}P environment (1st column), each indium atom bound to those ^{31}P nuclei (2nd column), and every oxygen atom bound to those indium atoms (3rd column). ^{31}P that have previously been assigned are colored according to their assignment in Figure 5.19.

Phosphorus Atom	Total # of In-O Bonds	Total # of In-O Bonds per P	Chemical Shift (ppm)
P(8) and P(17) (most upfield)	0	0	-244.5
P(7) and P(1) (2nd most upfield)	6	3	-243.5
P(11) and P(2) (doublet 3rd most upfield)	12	6	-232.5
P(4) (singlet 4th most upfield)	6	6	-221.5
P(16) and P(12)	10	5	to be assigned
P(13) and P(19)	18	9	to be assigned
P(9) and P(14)	18	9	to be assigned
P(5) and P(20)	18	9	to be assigned
P(15) and P(6)	18	9	to be assigned
P(18) and P(3)	20	10	to be assigned
P(10) (least upfield)	12	12	-189.6

Table 5.3 Inventory of every ^{31}P environment (1st column) the total number of In–O bonds for every indium atom that ^{31}P environment is bound to (2nd column), and the total number of oxygen atoms bound to those indium atoms (3rd column). ^{31}P that have previously been assigned are colored according to their assignment in Figure 5.19. Based upon the total number of In–O bonds, P(18) and P(3) are likely to lie just upfield of P(10) and P(16) and P(12) are likely to be the peak just downfield of P(4) (Figure 5.22).

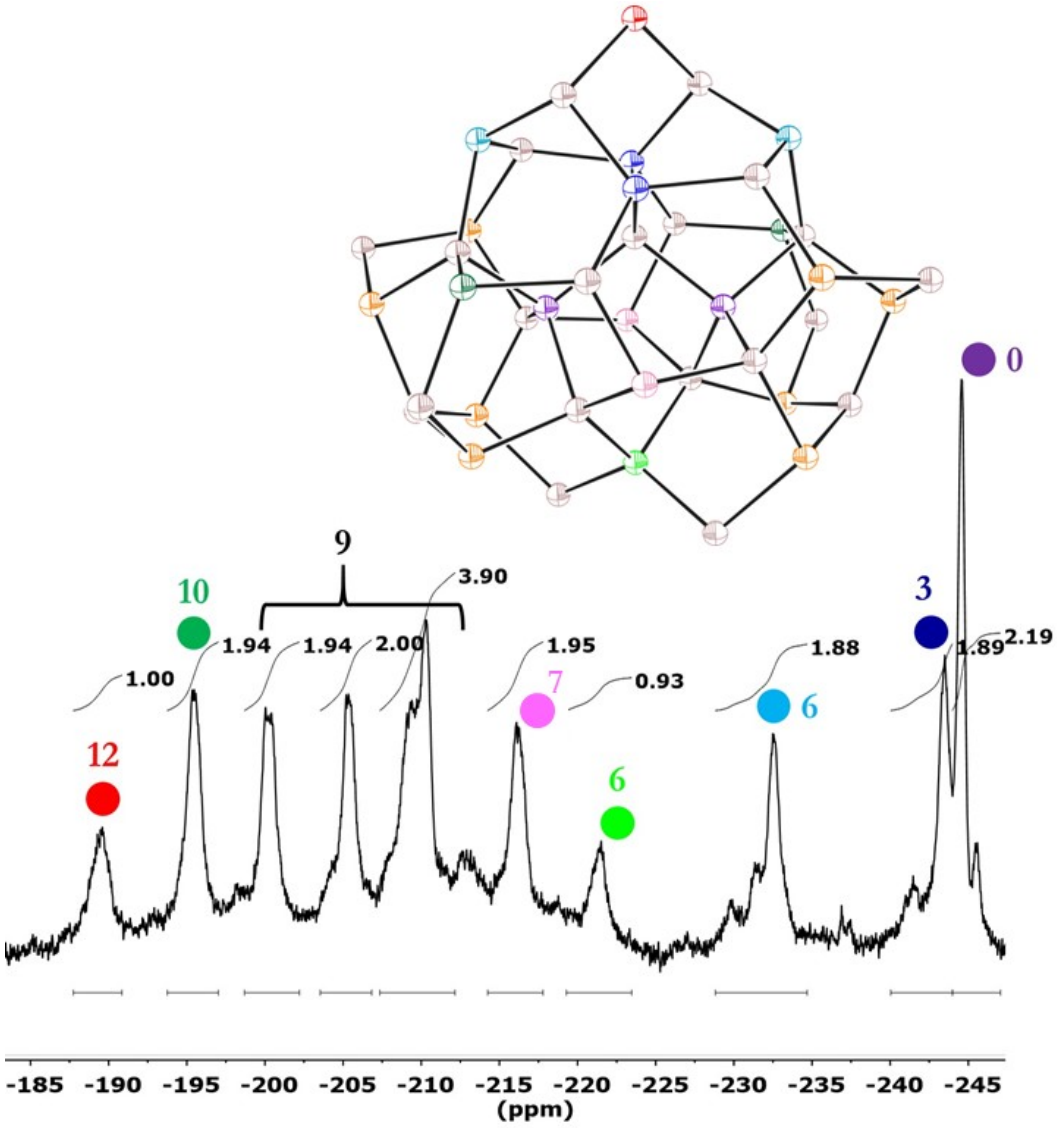

Figure 5.23 Assignment of $^{31}P\{^{1}H\}$ NMR spectrum of $In_{37}P_{20}(O_2C(CH_2)_7CH{=}CH(CH2)_7CH_3)_{51}$ based upon the crystal structure of $In_{37}P_{20}(O_2CCH_2C_6H_5)_{51}$, the C_2 symmetry of the $In_{37}P_{20}(O_2CR)_{51}$ atom subset, and the first coordination sphere of each indium metal center. The colored numbers indicate the sum of all In–O bonds for each of the 4 indium atoms bound to that ^{31}P environment. The sum of all In–O bonds from each of the 4 indium atoms bound to each unassigned ^{31}P environment is 9. Gray ellipsoids are indium and orange ellipsoids are unassigned phosphorus atoms.

Even after accounting for all oxygen atoms bound to each indium atom, four ^{31}P environments remain that are ambiguous for the shielding predicted by the crystal structure of $In_{37}P_{20}(O_2CCH_2C_6H_5)_{51}$. Since ^{31}P NMR is sensitive to bond angles, an account was also made of every In–P–In bond angle in the cluster (Table 6.4). Unfortunately, accounting for In–P–In bond angles is unable to resolve this ambiguity as the unassigned ^{31}P environments show only modest deviation from ideal tetrahedral geometry.

Phosphorus Atom	Chemical Shift (ppm)	Average bond angle	Maximum Bond Angle Deviation from 109.47122016	Deviation from tetrahedral
P(8) and P(17) (most upfield)	-244.5	109.3539583	5.97962016	0.117261827
P(7) and P(1) (2nd most upfield)	-243.5	108.141425	13.42037984	1.32979516
P(11) and P(2) (3rd most upfield)	-232.5	109.342125	6.44982016	0.12909516
P(4) (4th most upfield)	-221.5	109.0766	17.17047984	0.39462016
P(16) and P(12)	-216	109.2490417	8.93047984	0.222178493
P(13) and P(19) (unassigned)	to be assigned	109.2772	9.90037984	0.19402016
P(9) and P(14) (unassigned)	to be assigned	109.2499	11.33047984	0.22132016
P(5) and P(20) (unassigned)	to be assigned	108.9046167	14.13047984	0.566603493
P(15) and P(6) (unassigned)	to be assigned	109.0013917	14.44877984	0.469828493
P(18) and P(3) (2nd least upfield)	-195.5	109.3171167	7.60982016	0.154103493
P(10) (least upfield)	-189.6	109.4950333	5.27057984	0.023813173

Table 5.4 Account of deviation from tetrahedral geometry for all In–P–In bonds in the crystal structure of $In_{37}P_{20}(O_2CCH_2C_6H_5)_{51}$.

5.3 Conclusions

In conclusion, we have characterized the physical and electronic structure of an indium phosphide magic-size cluster, $In_{37}P_{20}(O_2CR)_{51}$, which is a key intermediate in the synthesis of InP quantum dots. Since this structure does not correspond to a known bulk phase or a magic number for a closed shell of valence electrons, it may be that the selectivity for and stability of this cluster can be attributed to the dense, interconnected network of supporting ligands passivating the particle surface. Not only does this result allow us insight into the structure of III-V QDs and nanocluster intermediates, it also leads us to propose several new structural principles to the field of semiconductor QDs. First, the cores of semiconductor nanocrystals need not be stoichiometric (neutral), as is seen for the $[In_{21}P_{20}]^{3+}$ fragment in $In_{37}P_{20}(O_2CR)_{51}$. Second, observations of differential ligand exchange on QDs need not be related to coordination at different facets, but rather may be due to the presence of different and often interlinked coordination networks.

As a consequence of this interconnected ligand set, which has predominately bridging binding modes and is free of any neutral, datively bound metal carboxylate complexes, ligand exchange reactions that displace $M(O_2CR)_x$ complexes are likely coupled with significant structural changes. In contrast, X and L-type ligand exchange reactions can be site specific, allowing for subtle changes to the surface coordination in a controlled manner, as is observed for the reaction of $In_{37}P_{20}(O_2CCH_2C_6H_5)_{51}$ with 1 equivalent of water. In addition, spectral line widths of ultrasmall quantum-confined semiconductors may be heavily influenced by lattice vibrations and thus remain broad even for monodisperse samples. Moreover, we hypothesize that the presence of dangling bonds would dramatically influence the electronic structure of these materials and would be readily identified by asymmetry or broadening in the optical spectra. UV-Vis absorbance spectra and PDF analysis of powdered samples suggest that the structure of $In_{37}P_{20}(O_2CR)_{51}$ is general for InP magic-size clusters with alkyl carboxylate ligand sets.

Using this information, we have been able to tentatively assign 7 of the 11 ^{31}P environments in the $^{31}P\{^{1}H\}$ NMR spectrum of $In_{37}P_{20}(O_2C(CH_2)_7CH{=}CH(CH2)_7CH_3)_{51}$. These assignments are consistent with the symmetry of the molecule, the relative number of phosphorus atoms for each ^{31}P environment, and the shielding expected at each phosphorus atom based upon the first coordination sphere of each indium atom in the cluster. This result suggests that specific phosphorus environments in phosphide nanoclusters of this size may be identified and quantified by solution phase ^{31}P NMR spectroscopy. This result will also prove useful in obtaining a better understanding the reactivity of $In_{37}P_{20}(O_2CR)_{51}$ with primary amines as will be discussed in Chapter 6.

5.4 Experimental

5.4.1 General Considerations

Indium acetate (99.99%), phenylacetic acid (99%), and oleic acid (90%) were purchased from Sigma-Aldrich and used without further purification. NMR solvents were purchased from Cambridge Isotope Laboratories. All solvents were dried over calcium hydride, distilled, and stored over 4 Å molecular sieves prior to use. $P(Si(CH_3)_3)_3$ was prepared according to literature procedures.[53] All manipulations were performed under an inert atmosphere of dry N_2 using standard Schlenk or glovebox techniques unless otherwise stated. Optical spectra were acquired on a Cary 5000 UV-Vis-NIR spectrophotometer from Agilent Technologies. NMR spectra were acquired on 300, 500, and 700 MHz Bruker Avance spectrometers.

5.4.2 Synthesis of $In_{37}P_{20}(O_2CC_6H_5)_{51}$

$In_{37}P_{20}(O_2CCH_2C_6H_5)_{51}$ was prepared by modification of a reported procedure for myristate-capped particles using $In(O_2CCH_3)_3$ (934 mg, 3.20 mmol) and phenylacetic acid (1.58 g, 11.6 mmol) in toluene (10 mL), and $P(Si(CH_3)_3)_3$ (465 μL, 1.60 mmol) in toluene (5 mL).[12] The workup procedure was modified from that of the particles with a myristate ligand set by substituting pentane for acetonitrile to selectively precipitate the particles (three cycles). $In_{37}P_{20}(O_2CCH_2C_6H_5)_{51}$ was isolated in 25% yield (238 mg, 0.02 mmol) based on $P(Si(CH_3)_3)_3$ as the limiting reagent.

5.4.3 Elemental Analysis of $In_{37}P_{20}(O_2CCH_2C_6H_5)_{51}$

Calculated C 41.67%, H 3.06%, N 0.00%; Actual C 41.872%, H 3.053%, N −0.227%

5.4.4 Extinction Coefficient of $In_{37}P_{20}(O_2CCH_2C_6H_5)_{51}$

75,900 L $mol^{-1}cm^{-1}$ (300 nm; Figure 5.12).

5.4.5 Crystallization Procedure

Under a nitrogen atmosphere $In_{37}P_{20}(O_2CCH_2C_6H_5)_{51}$ (200 mg) was dissolved in ethyl acetate (0.5 mL) and was filtered into a J. Young tube using a 1 mL syringe outfitted with a PFTE filter with a 0.45 μm pore size. Single crystals grew in the J. Young tube overnight at room temperature.

5.4.6 Single Crystal X-Ray Diffraction Methods

Two separate crystals were mounted with oil on a nylon loop and data was collected at –173 °C on a Bruker APEX II single crystal X-ray diffractometer using Mo radiation. Solvent analysis discovered two distinct voids filled with ethyl acetate; this contribution to the diffraction pattern was removed with SQUEEZE. With this size of molecule comes the possibility of disorder, which may have contributed to larger than expected positive as well as negative rest electron densities near the indium atoms, estimated to be about 5%. Some disorder of the aromatic groups was treated explicitly as some inter molecular 'squeezing' occurs. As a result of the large molecular size (11.7 kD) and strong scattering of the In–P cluster core, carbon atoms were weakly represented in the data, requiring DELU (In–O–C) and ISOR (O, C) restraints. In addition, the general geometry of the organic ligands was linked via SAME commands. The crystallographic data for the two structures have been deposited in the Cambridge Crystallographic Database under deposition numbers 1417965 and 1417966.

5.4.7 Low Temperature UV-Vis Spectroscopy

Low temperature absorption spectroscopy was performed using an optical flow cryostat mounted in an Agilent Cary 5000. The sample film was prepared by drop-casting $In_{37}P_{20}(O_2CCH_2C_6H_5)_{51}$ dissolved in toluene onto a quartz substrate and sandwiching the film with another quartz disk under a nitrogen atmosphere. The sample was quickly transferred to the flow cryostat under positive nitrogen pressure. The sample was cooled to 100 K by flowing cold nitrogen gas over the sample and the spectra were acquired during cooling.

5.4.8 Computational Methods

Computational studies were performed using the *Gaussian* electronic structure package.[54] The HSE06[55–57] range-separated hybrid DFT functional was used to perform the linear-response TDDFT absorption spectra. This method is appropriate for describing charge-transfer excitations and has been previously shown to correctly compute the InP quantum dot band gap.[37] TDDFT[58–60] was used to compute both the excitation energies and corresponding oscillator strengths of the first 10 electronic transitions. The LANL2DZ basis set is used in TDDFT studies, in which core electrons are replaced by an effective core potential, and only O (1s, 2s, 2p), C (1s, 2s, 2p), In (5s, 5p) and P (3s, 3p) atomic orbitals are described with explicit basis functions.[61–64] For all these calculations the air-free $In_{37}P_{20}(O_2CCH_2C_6H_5)_{51}$ crystallographic structure was used (namely crystal A).

Air exposed crystal structures were also analyzed. These structures arise from exposure of the crystals to humidity and mainly affect the coordination of one In atom on the surface of the cluster. Specifically, one carboxylate ligand adopts a monodentate binding motif with the resulting open coordination site filled by water datively binding. The water displays two hydrogen bonds to neighboring oxygen atoms, one being the non-bonding oxygen of the monodentate carboxylate and an oxygen of a neighboring ligand. The electronic properties of two air exposed crystal structures, crystal B, where we were able to resolve the electronic density of water, modeled as $In_{37}P_{20}(O_2CCH_2C_6H_5)_{51}(H_2O)$ and crystal B*, where the In atom on the surface has a dangling valence, modeled as $In_{37}P_{20}(O_2CCH_2C_6H_5)_{51}$ (crystal B without water) are computed.

5.5 References

(1) Lunt, R. R.; Osedach, T. P.; Brown, P. R.; Rowehl, J. A.; Bulović, V. *Advanced Materials* **2011**, *23* (48), 5712–5727.

(2) Shirasaki, Y.; Supran, G. J.; Bawendi, M. G.; Bulović, V. *Nature Photonics* **2012**, *7* (1), 13–23.

(3) Vossmeyer, T.; Reck, G.; Katsikas, L.; Haupt, E. T. K.; Schulz, B.; Weller, H. *Science* **1995**, *267* (5203), 1476–1479.

(4) Herron, N.; Calabrese, J. C.; Farneth, W. E.; Wang, Y. *Science* **1993**, *259* (5100), 1426–1428.

(5) Schnöckel, H. *Chemical Reviews* **2010**, *110* (7), 4125–4163.

(6) Corrigan, J. F.; DeGroot, M. W. In *The Chemistry of Nanomaterials*; Rao, C. N. R., Müller, A., Cheetham, A. K., Eds.; Wiley-VCH Verlag GmbH & Co. KGaA: Weinheim, FRG, 2005; pp 418–451.

(7) Brennan, J. G.; Siegrist, T.; Stuczynski, S. M.; Steigerwald, M. L. *Journal of the American Chemical Society* **1989**, *111* (26), 9240–9241.

(8) Beecher, A. N.; Yang, X.; Palmer, J. H.; LaGrassa, A. L.; Juhas, P.; Billinge, S. J. L.; Owen, J. S. *Journal of the American Chemical Society* **2014**, *136* (30), 10645–10653.

(9) Jadzinsky, P. D.; Calero, G.; Ackerson, C. J.; Bushnell, D. A.; Kornberg, R. D. *Science* **2007**, *318* (5849), 430–433.

(10) McBride, J. R.; Dukes, A. D.; Schreuder, M. A.; Rosenthal, S. J. *Chemical Physics Letters* **2010**, *498* (1–3), 1–9.

(11) Evans, C. M.; Guo, L.; Peterson, J. J.; Maccagnano-Zacher, S.; Krauss, T. D. *Nano Letters* **2008**, *8* (9), 2896–2899.

(12) Gary, D. C.; Terban, M. W.; Billinge, S. J. L.; Cossairt, B. M. *Chemistry of Materials* **2015**, *27* (4), 1432–1441.

(13) Kudera, S.; Zanella, M.; Giannini, C.; Rizzo, A.; Li, Y.; Gigli, G.; Cingolani, R.; Ciccarella, G.; Spahl, W.; Parak, W. J.; Manna, L. *Advanced Materials* **2007**, *19* (4), 548–552.

(14) Wang, Y.; Zhang, Y.; Wang, F.; Giblin, D. E.; Hoy, J.; Rohrs, H. W.; Loomis, R. A.; Buhro, W. E. *Chemistry of Materials* **2014**, *26* (7), 2233–2243.

(15) Yu, Q.; Liu, C.-Y. *The Journal of Physical Chemistry C* **2009**, *113* (29), 12766–12771.

(16) Zhang, J.; Rowland, C.; Liu, Y.; Xiong, H.; Kwon, S.; Shevchenko, E.; Schaller, R. D.; Prakapenka, V. B.; Tkachev, S.; Rajh, T. *Journal of the American Chemical Society* **2015**, *137* (2), 742–749.

(17) Kasuya, A.; Sivamohan, R.; Barnakov, Y. A.; Dmitruk, I. M.; Nirasawa, T.; Romanyuk, V. R.; Kumar, V.; Mamykin, S. V.; Tohji, K.; Jeyadevan, B.; Shinoda, K.; Kudo, T.; Terasaki, O.; Liu, Z.; Belosludov, R. V.; Sundararajan, V.; Kawazoe, Y. *Nat Mater* **2004**, *3* (2), 99–102.

(18) Chan, E. M.; Xu, C.; Mao, A. W.; Han, G.; Owen, J. S.; Cohen, B. E.; Milliron, D. J. *Nano Letters* **2010**, *10* (5), 1874–1885.

(19) Clark, M. D.; Kumar, S. K.; Owen, J. S.; Chan, E. M. *Nano Letters* **2011**, *11* (5), 1976–1980.

(20) Hendricks, M. P.; Campos, M. P.; Cleveland, G. T.; Jen-La Plante, I.; Owen, J. S. *Science* **2015**, *348* (6240), 1226–1230.

(21) Hendricks, M. P.; Cossairt, B. M.; Owen, J. S. *ACS Nano* **2012**, *6* (11), 10054–10062.

(22) Gary, D. C.; Glassy, B. A.; Cossairt, B. M. *Chemistry of Materials* **2014**, *26* (4), 1734–1744.

(23) Franke, D.; Harris, D. K.; Xie, L.; Jensen, K. F.; Bawendi, M. G. *Angewandte Chemie International Edition* **2015**, *54* (48), 14299–14303.

(24) Xie, R.; Li, Z.; Peng, X. *Journal of the American Chemical Society* **2009**, *131* (42), 15457–15466.

(25) Xie, R.; Peng, X. *Angewandte Chemie International Edition* **2008**, *47* (40), 7677–7680.

(26) Murray, C. B.; Kagan, C. R.; Bawendi, M. G. *Annual Review of Materials Science* **2000**, *30* (1), 545–610.

(27) Owen, J. *Science* **2015**, *347* (6222), 615–616.

(28) Owen, J. S.; Park, J.; Trudeau, P.-E.; Alivisatos, A. P. *Journal of the American Chemical Society* **2008**, *130* (37), 12279–12281.

(29) Adachi, S. *Properties of Group-IV, III-V and II-VI Semiconductors: Adachi/Properties of Group-IV, III-V and II-VI Semiconductors*; John Wiley & Sons, Ltd: Chichester, UK, 2005.

(30) Pyykkö, P.; Atsumi, M. *Chemistry - A European Journal* **2009**, *15* (1), 186–197.

(31) Cros-Gagneux, A.; Delpech, F.; Nayral, C.; Cornejo, A.; Coppel, Y.; Chaudret, B. *Journal of the American Chemical Society* **2010**, *132* (51), 18147–18157.

(32) Cossairt, B. M.; Owen, J. S. *Chemistry of Materials* **2011**, *23* (12), 3114–3119.

(33) Kovalenko, M. V.; Scheele, M.; Talapin, D. V. *Science* **2009**, *324* (5933), 1417–1420.

(34) Lan, X.; Masala, S.; Sargent, E. H. *Nat Mater* **2014**, *13* (3), 233–240.

(35) Jennings, W. B.; McCarthy, N. J. P.; Kelly, P.; Malone, J. F. *Organic & Biomolecular Chemistry* **2009**, *7* (24), 5156–5162.

(36) Micic, O. I.; Curtis, C. J.; Jones, K. M.; Sprague, J. R.; Nozik, A. J. *The Journal of Physical Chemistry* **1994**, *98* (19), 4966–4969.

(37) Cho, E.; Jang, H.; Lee, J.; Jang, E. *Nanotechnology* **2013**, *24* (21), 215201.

(38) Narayanaswamy, A.; Feiner, L. F.; Meijerink, A.; van der Zaag, P. J. *ACS Nano* **2009**, *3* (9), 2539–2546.

(39) Murray, C. B.; Norris, D. J.; Bawendi, M. G. *Journal of the American Chemical Society* **1993**, *115* (19), 8706–8715.

(40) Harris, D. K.; Bawendi, M. G. *Journal of the American Chemical Society* **2012**, *134* (50), 20211–20213.

(41) Chen, O.; Wei, H.; Maurice, A.; Bawendi, M.; Reiss, P. *MRS Bulletin* **2013**, *38* (9), 696–702.

(42) Norris, D. J.; Bawendi, M. G. *Physical Review B* **1996**, *53* (24), 16338–16346.

(43) Cui, J.; Beyler, A. P.; Coropceanu, I.; Cleary, L.; Avila, T. R.; Chen, Y.; Cordero, J. M.; Heathcote, S. L.; Harris, D. K.; Chen, O.; Cao, J.; Bawendi, M. G. *Nano Letters* **2016**, *16* (1), 289–296.

(44) Li, L.; Protière, M.; Reiss, P. *Chemistry of Materials* **2008**, *20* (8), 2621–2623.

(45) Chen, O.; Zhao, J.; Chauhan, V. P.; Cui, J.; Wong, C.; Harris, D. K.; Wei, H.; Han, H.-S.; Fukumura, D.; Jain, R. K.; Bawendi, M. G. *Nat Mater* **2013**, *12* (5), 445–451.

(46) Blackburn, J. L.; Ellingson, R. J.; Mićić, O. I.; Nozik, A. J. *The Journal of Physical Chemistry B* **2003**, *107* (1), 102–109.

(47) Adam, S.; Talapin, D. V.; Borchert, H.; Lobo, A.; McGinley, C.; de Castro, A. R. B.; Haase, M.; Weller, H.; Möller, T. *The Journal of Chemical Physics* **2005**, *123* (8), 84706.

(48) Mićić, O. I.; Nozik, A. J.; Lifshitz, E.; Rajh, T.; Poluektov, O. G.; Thurnauer, M. C. *The Journal of Physical Chemistry B* **2002**, *106* (17), 4390–4395.

(49) Gorenstein, D. G. *Journal of the American Chemical Society* **1975**, *97* (4), 898–900.

(50) Schnackerz, K. D.; Wahler, G.; Vincent, M. G.; Jansonius, J. N. *European Journal of Biochemistry* **1989**, *185* (3), 525–531.

(51) Sachleben, J. R.; Wooten, E. W.; Emsley, L.; Pines, A.; Colvin, V. L.; Alivisatos, A. P. *Chemical Physics Letters* **1992**, *198* (5), 431–436.

(52) Hostetler, M. J.; Wingate, J. E.; Zhong, C.-J.; Harris, J. E.; Vachet, R. W.; Clark, M. R.; Londono, J. D.; Green, S. J.; Stokes, J. J.; Wignall, G. D.; Glish, G. L.; Porter, M. D.; Evans, N. D.; Murray, R. W. *Langmuir* **1998**, *14* (1), 17–30.

(53) Gary, D. C.; Cossairt, B. M. *Chemistry of Materials* **2013**, *25* (12), 2463–2469.

(54) Frisch, M. J.; Trucks, G. W.; Schlegel, H. B.; Scuseria, G. E.; Robb, M. A.; Cheeseman, J. R.; Scalmani, G.; Barone, V.; Mennucci, B.; Petersson, G. A.; Nakatsuji, H.; Caricato, M.; Li, X.; Hratchian, H. P.; Izmaylov, A. F.; Bloino, J.; Zheng, G.; Sonnenberg, J. L.; Hada, M.; Ehara,

M.; Toyota, K.; Fukuda, R.; Hasegawa, J.; Ishida, M.; Nakajima, T.; Honda, Y.; Kitao, O.; Nakai, H.; Vreven, T.; Montgomery, J. A., Jr.; Peralta, J. E.; Ogliaro, F.; Bearpark, M.; Heyd, J. J.; Brothers, E.; Kudin, K. N.; Staroverov, V. N.; Kobayashi, R.; Normand, J.; Raghavachari, K.; Rendell, A.; Burant, J. C.; Iyengar, S. S.; Tomasi, J.; Cossi, M.; Rega, N.; Millam, N. J.; Klene, M.; Knox, J. E.; Cross, J. B.; Bakken, V.; Adamo, C.; Jaramillo, J.; Gomperts, R.; Stratmann, R. E.; Yazyev, O.; Austin, A. J.; Cammi, R.; Pomelli, C.; Ochterski, J. W.; Martin, R. L.; Morokuma, K.; Zakrzewski, V. G.; Voth, G. A.; Salvador, P.; Dannenberg, J. J.; Dapprich, S.; Daniels, A. D.; Farkas, O.; Foresman, J. B.; Ortiz, J. V.; Cioslowski, J.; Fox, D. J. *Gaussian 09*; Gaussian, Inc.: Wallingford, CT, 2009.

(55) Heyd, J.; Scuseria, G. E. *The Journal of Chemical Physics* **2004**, *121* (3), 1187.

(56) Heyd, J.; Scuseria, G. E.; Ernzerhof, M. *The Journal of Chemical Physics* **2003**, *118* (18), 8207.

(57) Vydrov, O. A.; Heyd, J.; Krukau, A. V.; Scuseria, G. E. *The Journal of Chemical Physics* **2006**, *125* (7), 74106.

(58) Casida, M. E.; Jamorski, C.; Casida, K. C.; Salahub, D. R. *The Journal of Chemical Physics* **1998**, *108* (11), 4439.

(59) Furche, F.; Ahlrichs, R. *The Journal of Chemical Physics* **2002**, *117* (16), 7433.

(60) Stratmann, R. E.; Scuseria, G. E.; Frisch, M. J. *The Journal of Chemical Physics* **1998**, *109* (19), 8218.

(61) *Methods of Electronic Structure Theory*; Schaefer, H. F., Ed.; Springer US: Boston, MA, 1977.

(62) Hay, P. J.; Wadt, W. R. *The Journal of Chemical Physics* **1985**, *82* (1), 270.

(63) Hay, P. J.; Wadt, W. R. *The Journal of Chemical Physics* **1985**, *82* (1), 299.

(64) Wadt, W. R.; Hay, P. J. *The Journal of Chemical Physics* **1985**, *82* (1), 284.

Chapter 6: Reaction of Primary Amines with $In_{37}P_{20}(O_2CR)_{51}$: ^{31}P, ^{19}F, ^{1}H, NMR and UV-Vis Spectroscopy Suggest Stoichiometric Binding Preceding Removal of $In(O_2CR)_3$

6.1 Introduction

Primary amines have been reported to play a variety of roles in colloidal syntheses of indium phosphide nanocrystals whose mechanisms are dependent on the choice of molecular precursors. Long chain primary amines are used as a coordinating solvent in syntheses that employ aminophosphines as a phosphorus precursor and indium halides as an indium precursor. [1–3] Syntheses that use these types of reagents as molecular precursors must undergo formal redox reactions in order to form InP since the phosphorus precursor is initially in the 3^+ oxidation state and is in the 3^- oxidation state in the end product. Recently, Tessier et al. proposed a mechanism for this reaction where aminophosphines disproportionate such that four equivalents of P^{3+} would yield three equivalents of P^{5+} and one equivalent of P^{3-}.[4] These syntheses produce InP tetrahedrons in which each face of the tetrahedron has the (111) facet exposed. The preference for the shape anisotropy in this systems was illuminated through computational analysis of the interaction of the ligand set with the exposed facet. The passivation of these In-rich surfaces was modeled using chloride and methylamine ligands. Calculations were performed for an indium rich (111) facet solely passivated by chlorides or methylamine. These calculations predicted that either ligand set by themselves would be unable to passivate all of the dangling electrons at the surface of the tetrahedron and therefore the two types of ligands are likely working in tandem. The lowest energy configuration was calculated to be for a system where three dangling electrons from four surface bound indium ions (each surface indium contributes 0.75 dangling electrons) were passivated by three electrons from three chloride ligands and two electrons from the lone pair of one methylamine ligand. In this way, each of the four indium atoms acquired the 1.25 electrons necessary for a complete valance shell.

Amine has been shown to play a several different roles when employing indium carboxylates and silylphosphines as molecular precursors to InP.[5] Protière et al. proposed a reaction scheme in which two equivalents of amine reacts with anhydride produced from the reaction of indium carboxylate and silylphosphine after In–P bond formation to give one equivalent of water and two equivalents of amide.[5] The water generated from this reaction would then go on to oxidize the surface of the InP nanocrystals, forming an In_2O_3 shell. This reaction scheme is consistent with the observations that inclusion of amine in the synthesis results in formation of an In_2O_3 shell by XRD and an increase in the photoluminescence quantum yield which is suggestive of a well-passivated InP core. An In_2O_3 shell increases photoluminescence quantum yield, but effectively halts the growth of the nanocrystals precluding growth from newly generated monomers which are necessary for size-focusing.[6] Xie et al. have claimed that amines act as activating agents for indium carboxylates by increasing their reactivity towards silylphosphines.[7] This hypothesis is consistent with the observation that the addition of a large excess of primary amine (222 equivalents relative to indium carboxylate) enabled the synthesis of high quality InP nanocrystals below 190 °C, which is approximately 10 °C lower in temperature than would otherwise be feasible. For this study, it is interesting to note that in addition to lowering the temperature necessary for nucleation and growth, amines also red-shifted the absorption peak of the nanocrystals relative to those synthesized in the absence of amine (λ_{max} = 720 nm vs 590 nm). This change in absorbance spectra is predicted to correspond to the nanocrystal volume increasing by a factor of about 7 (nanocrystal diameter change of 7.7 nm vs 3.6 nm with corresponding volume change of 236 nm^3 vs 32 nm^3).[8] At first glance, this result appears to contradict the claim by Protière et al. that amine should inhibit growth by formation of an In_2O_3 shell. This apparent discrepancy may be rectified by the difference in reaction temperature at which these two studies were carried out. At the lowered reaction temperatures reported by Xie et al., the condensation of amine and anhydride (or amine and free carboxylic acid) would likely take place at a slower rate

than precursor conversion and growth of InP based upon reported reaction kinetics of the direct amidation of carboxylic acids with primary amines at similar temperatures.[9]

Precursor conversion rates have indeed been shown to be affected by the presence of amine in the reaction solution. Allen et al. discovered that amine retards In–P bond formation from silylphosphines and indium carboxylates by monitoring the reaction by NMR spectroscopy. Based on these observations, a reaction mechanism in which amine competes with phosphine for coordination to indium prior to In–P bond formation via an S_N2 transition state was proposed.[10] This is a direct contradiction to the hypothesis by Xie et al. that amine activates indium carboxylates to assist in In–P bond formation.[7] In light of this new information, another explanation was needed to account for the observation that the addition of primary amines lowers the temperature necessary to synthesize high quality InP. Our group offered an explanation consistent with the observations of both Allen et al. and Xie et al.[11] We repeated the synthesis of InP reported by Xie et al. at a slightly lower temperature (110–160 °C) in the absence of primary amine. Under these reaction conditions, we obtained magic-size clusters of InP instead of the larger dynamic structures reported by Xie et al. Addition of primary amine to a solution of these clusters held at 160 °C was shown by UV-Vis absorbance spectroscopy to rapidly induce growth of InP through a continuum of sizes. By destabilizing magic-size clusters, which are kinetically persistent intermediates, amine can both inhibit precursor conversion as well as lower the temperature necessary for the nucleation of InP nanocrystals since these are distinct, temporally separate events in a two-step nucleation mechanism. Overall, the main effect of incorporating amine in syntheses that employ indium carboxylate and silylphosphine precursors is to assist in the growth of nanocrystals by destabilizing the nanocrystal surface in stark contrast to syntheses that employ indium halides and aminophosphines where amines play a critical role in passivating the nanocrystal surface.

In Chapter 5, we were able to determine the structure of the cluster ($In_{37}P_{20}(O_2CCH_2C_6H_5)_{51}$) with sub-angstrom resolution by x-ray crystallography and gave a tentative assignment to the solution phase ^{31}P NMR spectrum of $In_{37}P_{20}(O_2C(CH_2)_7CH{=}CH(CH_2)_7CH_3)_{51}$. This information has set the stage for a stoichiometric investigation of the reaction of primary amines with $In_{37}P_{20}(O_2CR)_{51}$ in hopes of determining the reaction scheme.

6.2 Results and Discussion

6.2.1 Removal of Surface Bound Indium Atoms from $In_{37}P_{20}(O_2CR)_{51}$ by Primary Amine Observed by Crystallography

Our observations that amine destabilized magic-size InP and the observation by Xie et al. that amine enabled the growth of larger sizes of InP than would otherwise be accessible suggest that amine directly interacts with the surface of InP to lower the barrier to growth. We have previously observed that the UV-Vis absorbance spectrum of InP clusters will redshift and broaden upon the addition of primary amine at room temperature (See Chapter 4, Figure 4.5).[11] We attributed this effect to a direct reaction with the cluster's surface rather than a result of a side reaction since the reaction was carried out with purified clusters and amine in an inert atmosphere. At the time, we were unable to add a stoichiometric amount of primary amine as we did not know the molecular weight of the cluster. Recently, we were able to determine the molecular formula of these clusters to be $In_{37}P_{20}(O_2CR)_{51}$ by substitution of the long chain carboxylates ($R = (CH_2)_{12}CH_3$) with a shorter chain carboxylate ($R = CH_2C_6H_5$) which enabled structural analysis by single crystal X-ray diffraction methods.[12] UV-Vis spectra as well as PDF analysis of powder XRD data suggests that carboxylate chain length does not affect the core structure of the cluster (See Chapter 5 Figure 5.16, Figure 5.17, and Figure 5.18). $In_{37}P_{20}(O_2CCH_2C_6H_5)_{51}$ can be isolated from the reaction of $P(Si(CH_3)_3)_3$ and $In(O_2CCH_2C_6H_5)_3$ and

purified to >99% purity by selective precipitation from toluene by addition of hexane (See Experimental of Chapter 5).

These results have set the stage for us to investigate the role of primary amines by adding stoichiometric equivalents of primary amines to $In_{37}P_{20}(O_2CCH_2C_6H_5)_{51}$ in order to determine the overall reaction scheme. Prior to performing such experiments, we were able to determine one of the reaction products of $In_{37}P_{20}(O_2CCH_2C_6H_5)_{51}$ and amine by X-ray crystallography. A large excess of primary amine (~100 equivalents) was added to $In_{37}P_{20}(O_2CCH_2C_6H_5)_{51}$ dissolved in ethyl acetate in an effort to obtain a single crystal by slow evaporation. From this solution a crystal of $In(O_2CH_2C_5H_6)_3(H_2NCH_2C_6H_5)_3$ was obtained (Figure 6.1). In this structure, indium exhibits an octahedral geometry in which every datively bound benzylamine is trans to a phenylacetate ligand These results demonstrate that amine is capable of liberating one or more of the sixteen surface bound indium atoms from $In_{37}P_{20}(O_2CCH_2C_6H_5)_{51}$, even at room temperature. In light of this discovery, we chose to employ 4-fluorobenzylamine ($H_2NCH_2C_6H_4F$) for stoichiometric additions to $In_{37}P_{20}(O_2CCH_2C_6H_5)_{51}$ in hopes of being able to track the formation of any molecular intermediates such as $In(O_2CH_2C_5H_6)_3(H_2NCH_2C_6H_4F)_3$ by ^{19}F NMR.

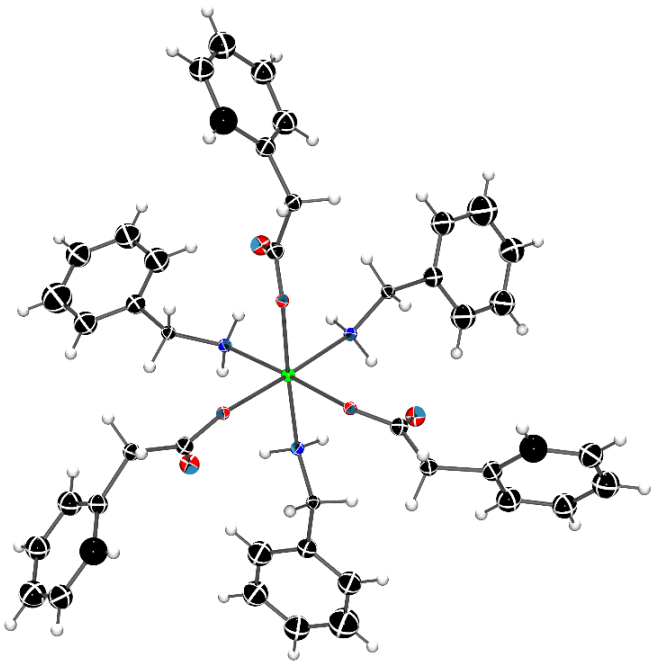

Figure 6.1 Crystal structure of $In(O_2CCH_2C_6H_5)_3(H_2NCH_2C_6H_5)_3$ with thermal ellipsoids at 50% probability level obtained by addition of 108 equivalents of $H_2NCH_2C_6H_5$ to $In_{37}P_{20}(O_2CCH_2C_6H_5)_{51}$. Unit cell contains three $In(O_2CCH_2C_6H_5)_3(H_2NCH_2C_6H_5)_3$ molecules. Only one $In(O_2CCH_2C_6H_5)_3(H_2NCH_2C_6H_5)_3$ is depicted here for clarity.

6.2.2 Titration of Removal of $In_{37}P_{20}(O_2CCH_2C_6H_5)_{51}$ by Primary Amine with Concurrent ^{31}P, ^{19}F, and ^{1}H NMR Spectroscopy

^{31}P NMR spectra were acquired after the addition of 1, 3, 6, 12, 24, 48, 100, and 200 equivalents of $H_2NCH_2C_6H_4F$ to $In_{37}P_{20}(O_2CCH_2C_6H_5)_{51}$ (Figure 6.2). Addition of primary amine in multiples of three should coincide with removing additional surface bound indium assuming indium is removed in the form of $In(O_2CCH_2C_6H_5)_3(H_2NCH_2C_6H_5)_3$, and 48 would be the maximum amount needed to remove every surface bound indium in the form of $In(O_2CCH_2C_6H_5)_3(H_2NCH_2C_6H_5)_3$. After the

addition of 48 equivalents of benzylamine, 100 and 200 equivalents of $H_2NCH_2C_6H_4F$ were chosen to investigate the effects of an excess of amine.

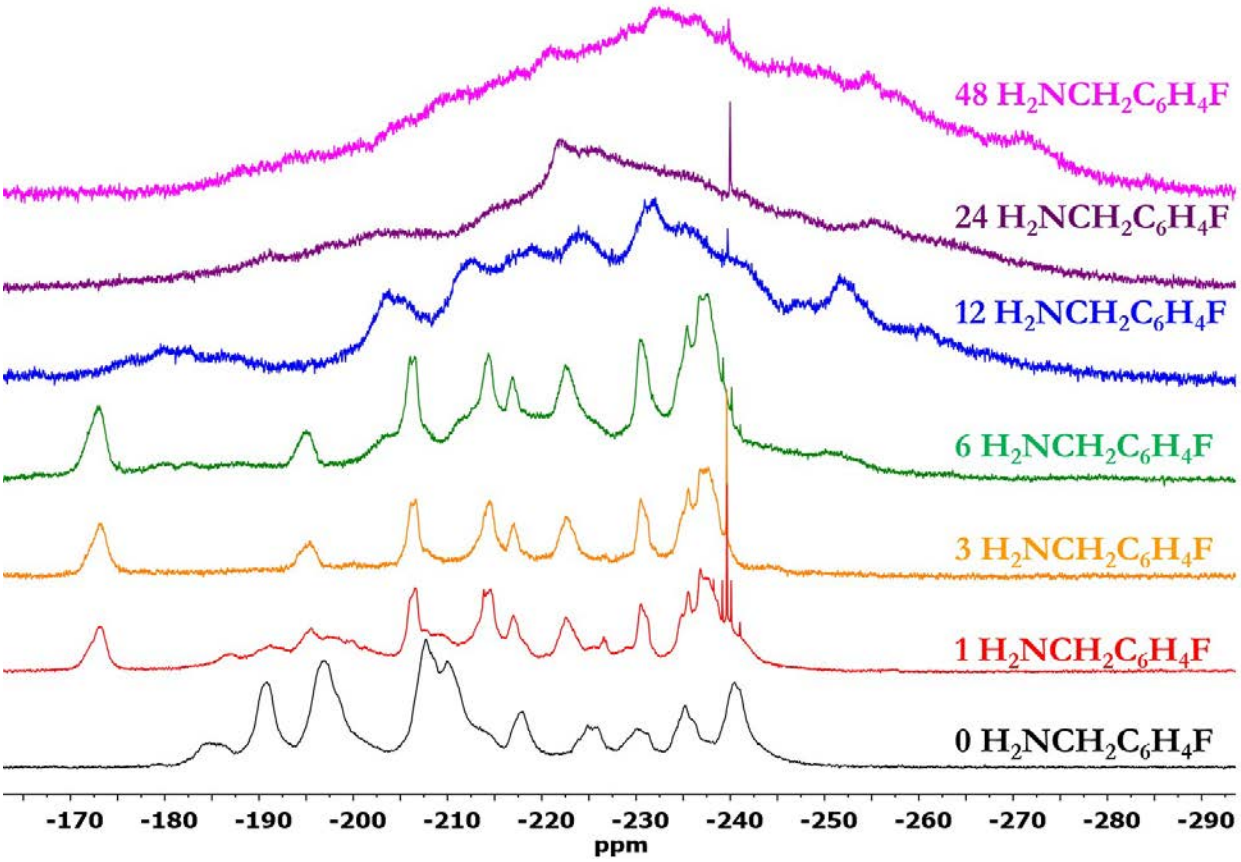

Figure 6.2 ^{31}P NMR of $In_{37}P_{20}(O_2CCH_2C_6H_5)_{51}$ after addition of 0, 1, 3, 6, 12, 24, and 48 equivalents of $H_2NCH_2C_6H_4F$ acquired at 202.3 MHz in CD_2Cl_2. The sharp peaks coming in near –240 ppm area are PH_3 gas. PH_3 was not observed in other experiments and its presence here was likely due to decomposition of $In_{37}P_{20}(O_2CCH_2C_6H_5)_{51}$ from a small amount of an acidic impurity inadvertently introduced to the sample. The PH_3 gas integrates to <1% of the ^{31}P nuclei and should not have a large effect on the investigation of primary amines.

From the ^{31}P NMR spectra, we see a clear stoichiometric reaction from the addition of one equivalent of 4-flurobenzylamine in that every peak has shifted relative to the spectrum of the untreated particles. In Chapter 5, the $^{31}P\{^{1}H\}$ NMR of $In_{37}P_{20}(O_2C(CH_2)_7CH{=}CH(CH_2)_7CH_3)_{51}$ was assigned for 7 of the 11 ^{31}P environments (Chapter 5, Figure 5.20). From this assignment, we learned that the ^{31}P environment that comes in furthest downfield is most likely the unique phosphorus atom which was bound to two surface indium atoms in the crystal structure of $In_{37}P_{20}(O_2CCH_2C_6H_5)_{51}$. We now see that after addition of one equivalent of $H_2NCH_2C_6H_4F$, a new peak has appeared with a chemical shift that is ~12 ppm more downfield than any peak observed in the spectrum of the clusters prior to addition of amine. This suggests that the phosphorus atom bound to two surface indiums (See Chapter 5 Figure 5.3) is the ^{31}P environment most affected by the addition of primary amine to $In_{37}P_{20}(O_2CCH_2C_6H_5)_{51}$. Further support for this hypothesis comes from the site-selective stoichiometric reaction we have observed between $In_{37}P_{20}(O_2CCH_2C_6H_5)_{51}$ and water at one of the two indium sites bound to this same phosphorus atom (Chapter 5, Figure 5.8).[12] These data suggest that the initial reaction of $In_{37}P_{20}(O_2CCH_2C_6H_5)_{51}$ with one equivalent of primary amine is analogous to the reaction observed with water in that amine datively binds to one of the two indium atoms at the surface that share a common phosphorus atom.

^{19}F NMR was taken of the same solution of $In_{37}P_{20}(O_2CCH_2C_6H_5)_{51}$ with 17 equivalents of α,α,α-trifluorotoluene ($C_6H_4CF_3$) as an internal standard (Figure 6.3). All of the ^{19}F nuclei are accounted for throughout these additions within experimental error according the relative integration of the $H_2NCH_2C_6H_4F$ peaks to $C_6H_4CF_3$. Upon addition of a single equivalent of $H_2NCH_2C_6H_4F$ to $In_{37}P_{20}(O_2CCH_2C_6H_5)_{51}$, three main peaks are observed in the ^{19}F spectrum at –114.3 ppm, –115.1 ppm, and –115.3 ppm. We attribute these peaks to $H_2NCH_2C_6H_4F$ binding to the surface of the $In_{37}P_{20}(O_2CCH_2C_6H_5)_{51}$. This initial reaction goes to completion in terms of the consumption of $H_2NCH_2C_6H_4F$ since we observe no free $H_2NCH_2C_6H_4F$ (singlet at –118.3 ppm). Up to the addition

of 6 equivalents of $H_2NCH_2C_6H_4F$, the ^{19}F spectra can be explained in terms of $H_2NCH_2C_6H_4F$ exhibiting three predominant coordination modes to the surface of $In_{37}P_{20}(O_2CCH_2C_6H_5)_{51}$ though the relative amounts of each type evolve during the course of the titration up to this point. After 12 equivalents of $H_2NCH_2C_6H_4F$ are added to the solution, all of the peaks assigned to the initial binding modes of $H_2NCH_2C_6H_4F$ have been lost and a broad singlet has grown in around –115.5 ppm. This is likely due to amine liberating surface bound indium from $In_{37}P_{20}(O_2CCH_2C_6H_5)_{51}$ in the form of $In(O_2CCH_2C_6H_5)_3(H_2NCH_2C_6H_5)_3$. This would be consistent with the ^{31}P NMR spectra assuming that initial binding of $H_2NCH_2C_6H_4F$ and subsequent removal of surface indium atoms induce a structural rearrangement of $In_{37}P_{20}(O_2CCH_2C_6H_5)_{51}$. Upon further additions of $H_2NCH_2C_6H_4F$, the broad peak attributed to liberated $In(O_2CCH_2C_6H_5)_3(H_2NCH_2C_6H_5)_3$ continues to grow in, sharpen, and shift upfield toward free $H_2NCH_2C_6H_4F$. Since we see no other peaks in the ^{19}F NMR spectra, we attribute this single resonance to $H_2NCH_2C_6H_4F$ in equilibrium between datively binding to indium at the surface of the resultant InP cluster or to $In(O_2CCH_2C_6H_5)_3(H_2NCH_2C_6H_5)_3$ and freely diffusing in solution.

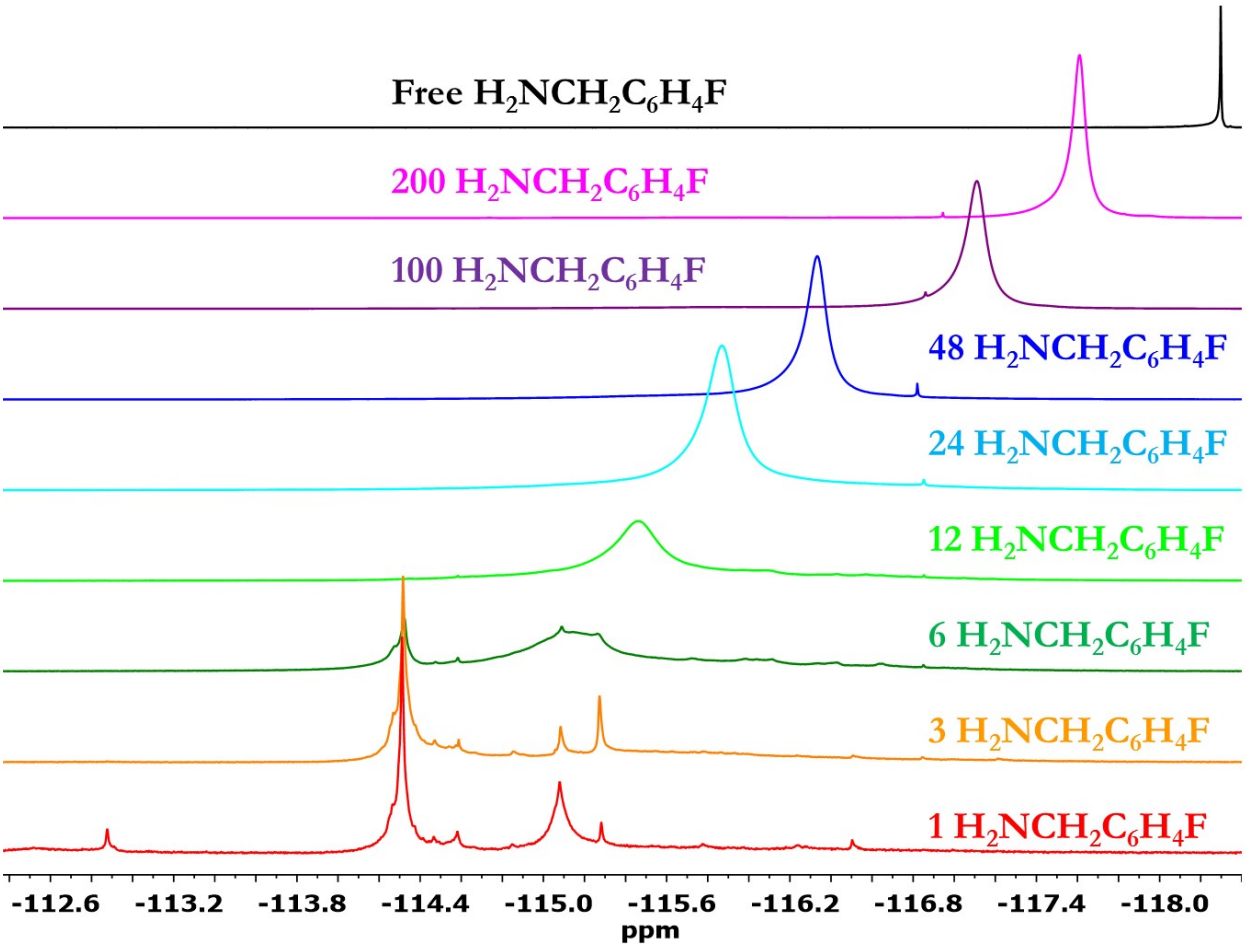

Figure 6.3 ^{19}F NMR spectra of stoichiometric additions of $H_2NCH_2C_6H_4F$ to a solution of $In_{37}P_{20}(O_2CCH_2C_6H_5)_{51}$ carried out at 469MHz in CD_2Cl_2 with 48 equivalents of α,α,α-trifluorotoluene as an internal standard (singlet at –64 ppm not shown in the figure). Spectra have been normalized for total area for ease of viewing. Numbers at the right indicate the total amount of ^{19}F nuclei for each spectrum obtained by integrating relative to the internal standard.

^1H NMR of the titration of $In_{37}P_{20}(O_2CCH_2C_6H_5)_{51}$ with $H_2NCH_2C_6H_4F$ exhibits significant line sharpening during the course of the titration in both the alkyl and aromatic regions of the spectrum (Figure 6.4). We previously saw by a ^1H–^1H COSY experiment that the methylene protons of specific

carboxylate ligands of $In_{37}P_{20}(O_2CCH_2C_6H_5)_{51}$ are magnetically inequivalent suggestive of hindered rotation due to a densely packed ligand set (Chapter 5, Figure 5.7). Upon addition of 12 equivalents of $H_2NCH_2C_6H_4F$, we no longer observe an array of peaks spanning from about 2 to 4 ppm for the methylene protons of $In_{37}P_{20}(O_2CCH_2C_6H_5)_{51}$ and instead observe two broad peaks grow in around 3.5 and 3.4 ppm. This suggests that upon removal of surface bound indium, the resultant cluster is no longer so densely ligated as to prevent rotation about the C–C bond of the carbonyl carbon and methylene carbon of the carboxylate ligands. N–H protons are not observed during the course of this titration, likely due to line broadening associated with hydrogen bonding to carboxylate ligands of $In_{37}P_{20}(O_2CCH_2C_6H_5)_{51}$.

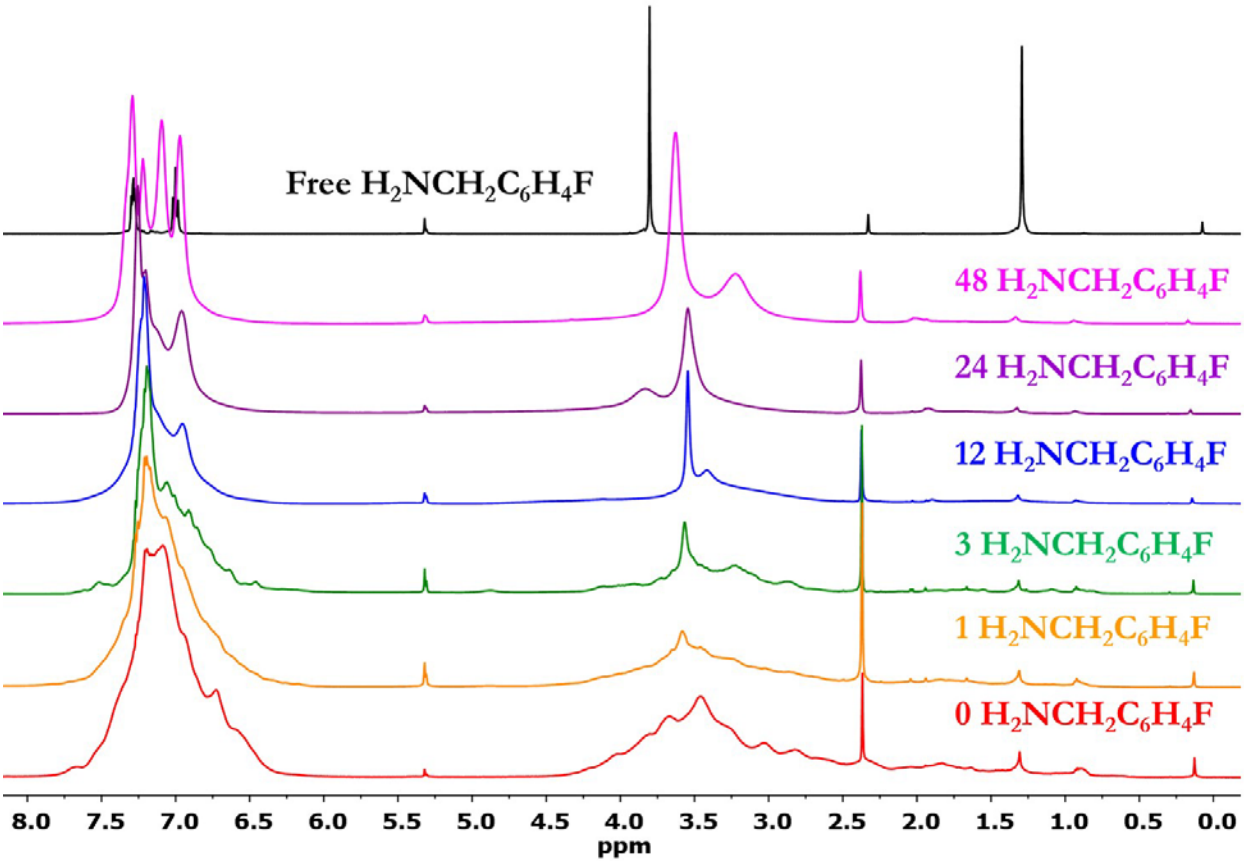

Figure 6.4 ^{1}H NMR spectrum of the titration of $In_{37}P_{20}(O_2CCH_2C_6H_5)_{51}$ with $H_2NCH_2C_6H_4F$ ($C_6H_4CF_3$ was omitted for this titration) taken at 500 MHz in CD_2Cl_2 spectra have been normalized to maximum peak intensity. Peaks are observed to sharpen both in the alkyl and in aromatic regions of the spectra during the course of the titration. After 12 equivalents of amine have been added, there are two distinct broad peaks in the observed in the region from 3.0 ppm and 4.0 ppm which can be attributed to Unlike the methylene protons of $H_2NCH_2C_6H_4F$, the N–H protons of $H_2NCH_2C_6H_4F$ (1.3 ppm) are not observed during the course of the titration probably due line broadening from hydrogen bonding with carboxylate ligands. The peak at 2.3 ppm is the CH_3 peak from a small amount of residual toluene.

6.2.3 UV-Vis Spectra of Titrations of $In_{37}P_{20}(O_2CR)_{51}$ with Primary Amine Analogous to NMR Experiments

UV-Vis spectra were also acquired for an analogous titration of $In_{37}P_{20}(O_2CCH_2C_6H_5)_{51}$ with $H_2NCH_2C_6H_4F$ carried out under inert atmosphere (Figure 6.5). In contrast to the ^{31}P and ^{19}F NMR spectra, the UV-Vis absorbance spectra of $In_{37}P_{20}(O_2CCH_2C_6H_5)_{51}$ exhibits a continuous shift where the main peak at 386 nm is lost after a single equivalent of $H_2NCH_2C_6H_4F$ has been added, and a new peak at 404 nm grows in up to the addition of 24 equivalents of $H_2NCH_2C_6H_4F$. Little change is observed in the UV-Vis spectra upon further addition of $H_2NCH_2C_6H_4F$. While a significant change in core structure was implicated between the additions of 6 and 12 equivalents of $H_2NCH_2C_6H_4F$ by the ^{31}P NMR of this titration (Figure 6.2), this abrupt change is not reflected in the UV-Vis absorbance spectra, demonstrating that UV-Vis is not necessarily sensitive to such changes. This is consistent with the lowest energy electronic transitions primarily reporting on the extent of quantum confinement in the cluster, which we do not expect to dramatically change on removal of one or two indium atoms.

The crystal structure of $In(O_2CCH_2C_6H_5)_3(H_2NCH_2C_6H_5)_3$ suggests that three equivalent of primary amine are necessary to remove one equivalent of $In(O_2CR)_3$ from the surface of $In_{37}P_{20}(O_2CCH_2C_6H_5)_{51}$. ^{19}F NMR and ^{31}P NMR spectra for the addition of 1, 3, and 6 equivalents of $H_2NCH_2C_6H_4F$ suggest that all 16 surface indium remain for up to 6 additions of primary amine as one equivalent of $H_2NCH_2C_6H_4F$ should be insufficient to liberate $In(O_2CCH_2C_6)_3$ and no new peaks are observed after addition of one equivalent. The addition of 12 equivalents of $H_2NCH_2C_6H_4F$ marks the final structural change observed by ^{31}P NMR. At this point and onward in the titration, ^{19}F NMR shows only a single broad peak that continues to shift towards free $H_2NCH_2C_6H_4F$. These results suggest that there are no more sites on the cluster for which amine can tightly bind after the removal of indium upon addition of 12 equivalents of primary amine. Since every indium atom has at least one

In–P bond, removal of a surface bound indium must coincide with the development of phosphorus dangling bond or structural rearrangement to passivate phosphorus. A phosphorus dangling bond should introduce a mid-gap state that would be readily observed by UV-Vis, but we observe no change in the position of the LEET by UV-Vis after the addition of 12 equivalents of $H_2NCH_2C_6H_4F$. Additionally, no abrupt changes are observed in the ^{31}P NMR after addition of 12 equivalents. These results suggest that the reaction of $H_2NCH_2C_6H_4F$ with $In_{37}P_{20}(O_2CCH_2C_6H_5)_{51}$ is complete when either one, or both of the surface bound indium atoms which are bound to a common phosphorus atom are removed from the cluster. Further removal of surface bound indium after addition of 12 equivalents of $H_2NCH_2C_6H_4F$ would likely have been observed by an abrupt change in either the ^{19}F or ^{31}P NMR spectra or by UV-Vis spectroscopy.

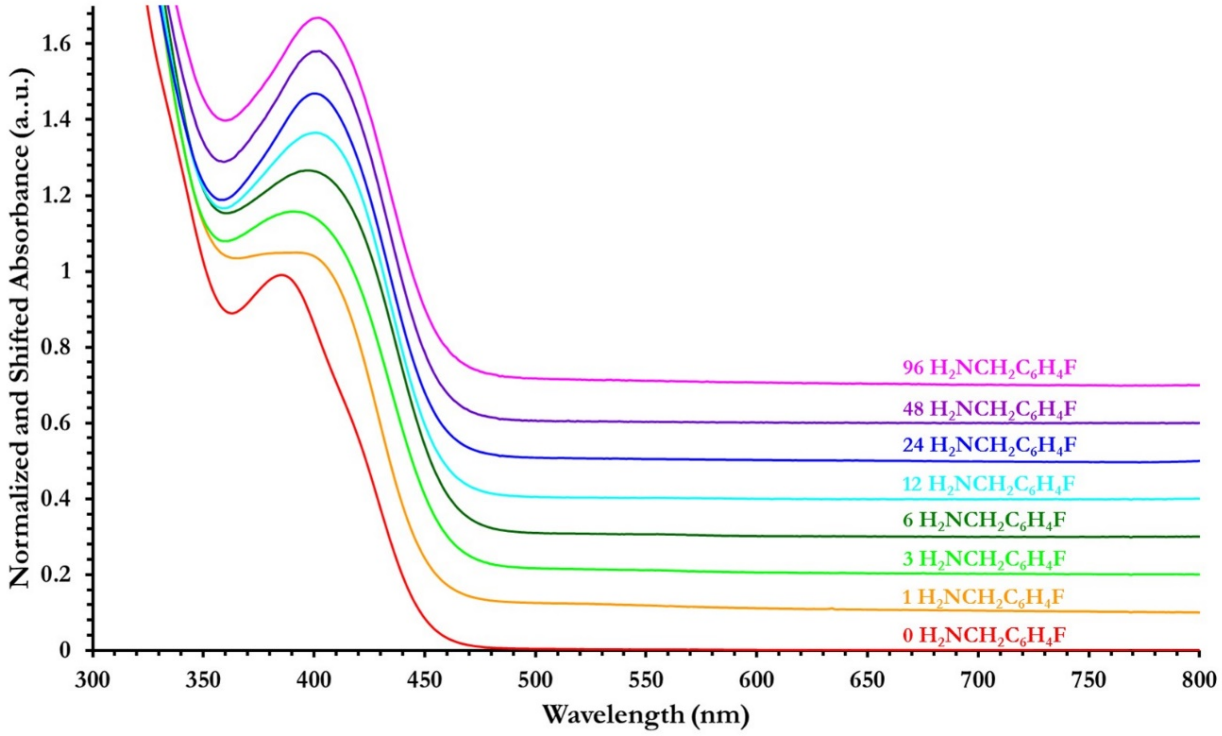

Figure 6.5 UV-Vis spectra of $In_{37}P_{20}(O_2CCH_2C_6H_5)_{51}$ after the addition of 0, 1, 3, 6, 12, 24, 48, and 96 equivalents of $H_2NCH_2C_6H_4F$. Unlike ^{31}P and ^{19}F NMR spectra, the UV-Vis spectra acquired during the course of the titration show only a smooth transition where the initial peaks at 386 nm is lost and a new peak at 404 nm grows in over the course of the titration.

6.2.4 Synthesis and Characterization of $In_{37}P_{20}(O_2CCH_2C_6H_4F)_{51}$

While the titrations carried out with $H_2NCH_2C_6H_4F$ were enlightening in terms of the structural and optical changes exhibited by $In_{37}P_{20}(O_2CCH_2C_6H_5)_{51}$ upon addition of primary amine, we have still been unable to propose a complete reaction scheme. In hopes of gaining further insight into this reaction, we modified the synthesis of $In_{37}P_{20}(O_2CCH_2C_6H_5)_{51}$ by substituting 4-fluorophenylacetic acid ($HO_2CCH_2C_6H_4F$) for phenylacetic acid ($HO_2CCH_2C_6H_5$) in order to obtain $In_{37}P_{20}(O_2CCH_2C_6H_4F)_{51}$. The similarity of both UV-Vis and ^{31}P NMR spectra between

$In_{37}P_{20}(O_2CCH_2C_6H_5)_{51}$ and the new cluster obtained with $HO_2CCH_2C_6H_4F$ suggested that we were successful in synthesizing $In_{37}P_{20}(O_2CCH_2C_6H_4F)_{51}$ (Figures 6.6 and Figure 6.7). With $In_{37}P_{20}(O_2CCH_2C_6H_4F)_{51}$ in hand, we set out to monitor the titration of $In_{37}P_{20}(O_2CCH_2C_6H_4F)_{51}$ with benzylamine ($H_2NCH_2C_6H_5$). We predicted that these experiments would be analogous to the previous titrations with the exception that the ^{19}F NMR would now provide new information about the native carboxylate ligand set of the cluster instead of the amine titrant throughout the course of the reaction.

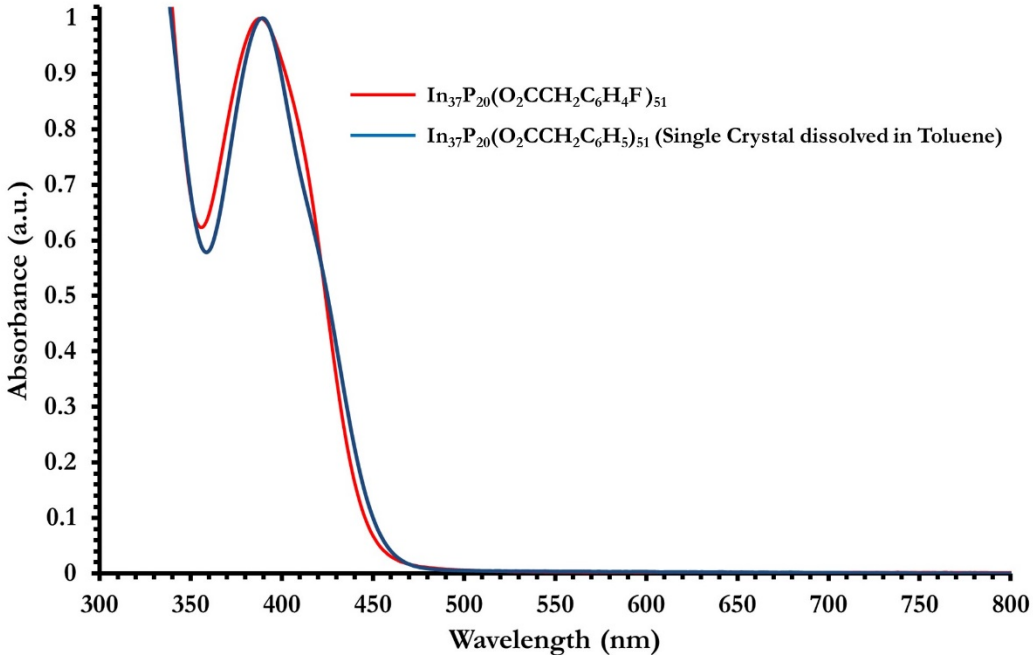

Figure 6.6 Normalized UV-Vis spectra of $In_{37}P_{20}(O_2CCH_2C_6H_5)_{51}$ obtained by dissolving a diffraction quality single crystal in toluene (blue trace) and a timed aliquot from the synthesis of $In_{37}P_{20}(O_2CCH_2C_6H_4F)_{51}$ (red trace).

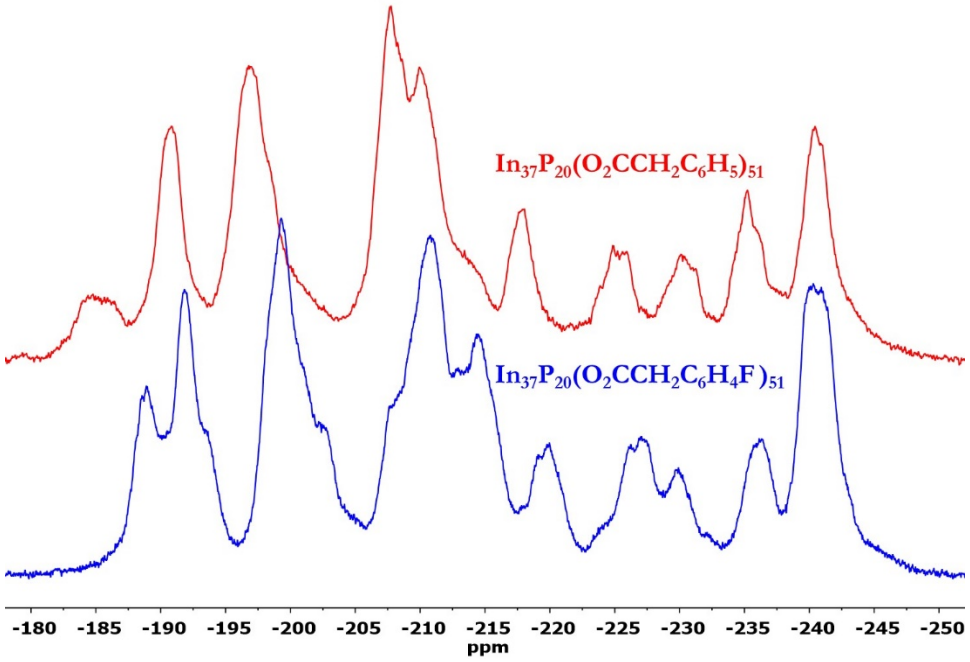

Figure 6.7 $^{31}P\{^{1}H\}$ NMR of $In_{37}P_{20}(O_2CCH_2C_6H_5)_{51}$ (red trace) and the InP cluster presumed to be $In_{37}P_{20}(O_2CCH_2C_6H_4F)_{51}$ (blue trace) both spectra were acquired at 202.3 MHz in CD_2Cl_2. While the spectra are not identical, it is a closer match than $In_{37}P_{20}(O_2CCH_2C_6H_5)_{51}$ and $In_{37}P_{20}(O_2C(CH_2)_7CH{=}CH(CH_2)_7CH_3)_{51}$ for which PDF analysis predicted the same core structure (See Chapter 5 Figure 5.17).

6.2.5 Titration of Removal of $In_{37}P_{20}(O_2CCH_2C_6H_4F)_{51}$ by Primary Amine with Concurrent ^{31}P, ^{19}F, and ^{1}H NMR Spectroscopy

^{19}F NMR spectra were collected for the titration of $In_{37}P_{20}(O_2CCH_2C_6H_4F)_{51}$ with 0, 1, and 3 equivalents of $H_2NCH_2C_6H_5$. For the ^{19}F NMR spectra, we observed a change from several broad resonances for the untreated cluster to a spectrum with several sharper resonances embedded within a series of broader peaks (Figure 5.8). Since the structure of $In_{37}P_{20}(O_2CCR)_{51}$ consists of ligand

binding modes that are exclusively bidentate or bridging, binding of amine at the surface of $In_{37}P_{20}(O_2CCR)_{51}$ would likely either shift a carboxylate ligand to a monodentate binding mode as was observed in the hydrated structure of $In_{37}P_{20}(O_2CCH_2C_6H_5)_{51}(H_2O)$ (See Chapter 5, Figure 5.8), or remove a surface bound indium atom as was observed for addition of 100 equivalents of $H_2NCH_2C_6H_5$ to $In_{37}P_{20}(O_2CCR)_{51}$ (Figure 6.1). One peak in particular, at –116.6 ppm had a linewidth suggestive of a freely diffusing molecular species.

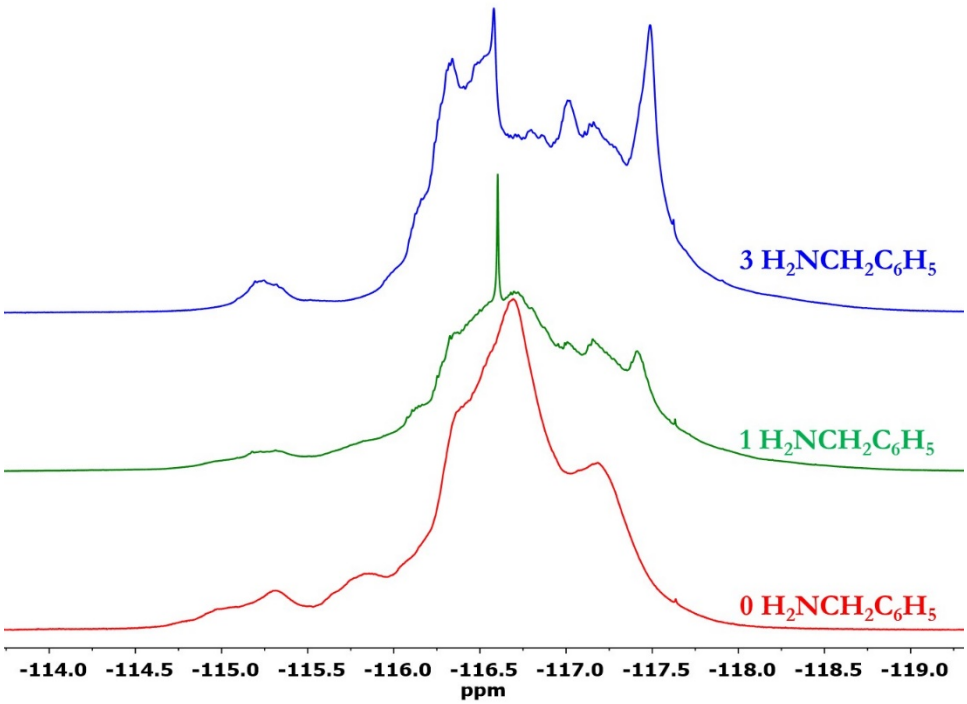

Figure 6.8 ^{19}F NMR of the titration of $In_{37}P_{20}(O_2CCH_2C_6H_4F)_{51}$ with 0 (red trace), 1 (green trace), and 3 (blue trace) equivalents of $H_2NCH_2C_6H_5$. Sharper peaks are observed growing in upon further addition of $H_2NCH_2C_6H_5$, possibly suggestive of greater freedom of motion for the carboxylate ligands upon dative binding of amine.

6.2.6 The Role of Free Carboxylic Acid in Promoting Removal of Surface Bound Indium Carboxylates by Primary Amines

Upon addition of 3 equivalents of $H_2NCH_2C_6H_5$, a large amount of precipitate collected in the NMR tube overnight, impeding further investigation by ^{19}F NMR spectroscopy. A single crystal X-ray diffraction structure obtained from the precipitate revealed $In(O_2CCH_2C_6H_4F)_4(H_3NCH_2C_6H_5)$ (Figure 6.9).

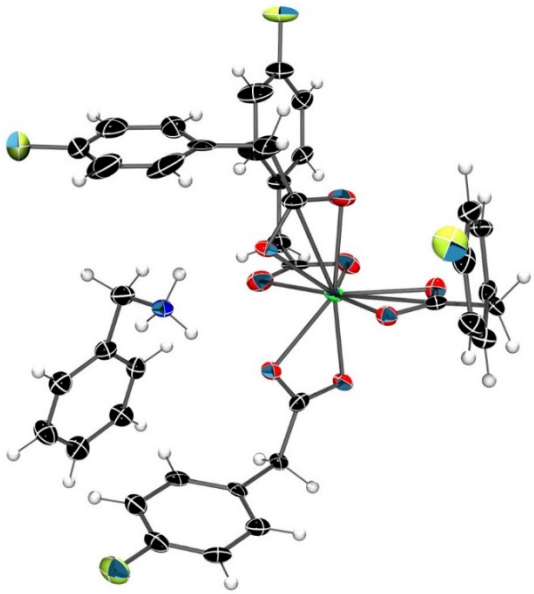

Figure 6.9 Crystal structure of $In(O_2CCH_2C_6H_4F)_4(H_3NCH_2C_6H_5)$ with thermal ellipsoids at 50% probability obtained by addition of 3 equivalents of $H_2NCH_2C_6H_5$ to $In_{37}P_{20}(O_2CCH_2C_6H_4F)_{51}$. Unit cell contains two additional CD_2Cl_2 and one toluene molecule omitted for clarity.

The presence of an extra carboxylate ligand on indium and an ammonium counterion suggests that the sample purification for $In_{37}P_{20}(O_2CCH_2C_6H_4F)_{51}$, unlike that for $In_{37}P_{20}(O_2CCH_2C_6H_5)_{51}$, was inadequate to completely remove excess carboxylic acid. The UV-Vis spectrum of the supernatant

from the NMR tube shows a blue shift in the spectrum from the untreated cluster. The difference in the UV-Vis spectra between $In_{37}P_{20}(O_2CCH_2C_6H_4F)_{51}$ and $In_{37}P_{20}(O_2CCH_2C_6H_5)_{51}$ after addition of 3 equivalents of primary amine suggests a fundamentally different reaction occurred (Figure 6.10).

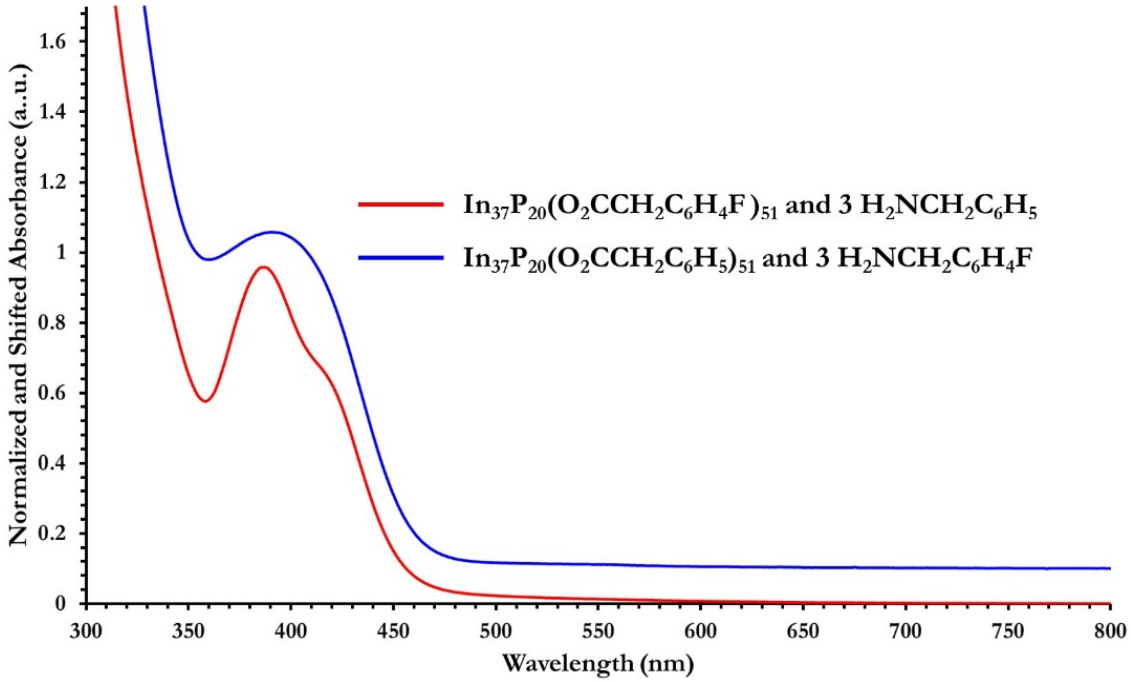

Figure 6.10 Normalized UV-Vis spectra of $In_{37}P_{20}(O_2CCH_2C_6H_5)_{51}$ after the addition of three equivalents of $H_2NCH_2C_6H_4F$ (blue trace) and of $In_{37}P_{20}(O_2CCH_2C_6H_4F)_{51}$ after three equivalents of $H_2NCH_2C_6H_5$ (red trace). While $In_{37}P_{20}(O_2CCH_2C_6H_5)_{51}$ red shifted and broadened upon exposure to primary amine, the primary peak of the $In_{37}P_{20}(O_2CCH_2C_6H_4F)_{51}$ sample blue shifted while the LEET red shifted.

Given the difference in the UV-Vis spectra and crystal structures obtained for the indium complexes liberated from InP clusters between the two samples, free $HO_2CCH_2C_6H_4F$ may assist amine in removal of surface bound indium by an alternate reaction pathway to the one observed for $In_{37}P_{20}(O_2CCH_2C_6H_5)_{51}$ and amine alone. In order to test this hypothesis, 50 equivalents of $H_2NCH_2C_6H_4F$ was added to $In_{37}P_{20}(O_2CCH_2C_6H_5)_{51}$ to fully remove at indium carboxylate from

$In_{37}P_{20}(O_2CCH_2C_6H_5)_{51}$ followed by addition of 100 equivalents of $HO_2CCH_2C_6H_5$ in an attempt to remove the datively bound amine from the cluster by the formation the ammonium carboxylate salt $[O_2CCH_2C_6H_5][H_3NCH_2C_6H_4F]$ (Figure 6.11). The UV-Vis spectrum exhibits alternating blue and red shifts with alternating additions of carboxylic acid and amine respectively. This change is not reflected in the ^{31}P NMR where addition of carboxylic acid is unable to restore the multiple, narrow peaks observed for $In_{37}P_{20}(O_2CCH_2C_6H_5)_{51}$ prior to any treatment (Figure 6.15). This is further evidence that UV-Vis spectroscopy is sensitive to specific binding modes of indium at the surface of the particle and changes in optical spectra alone are not sufficient evidence to infer a change in core structure for InP clusters. Since $H_2NCH_2C_6H_4F$ was chosen for this control experiment, we were able to confirm that amine remains datively bound to the cluster even after addition of $HO_2CCH_2C_6H_5$ (Figure 6.12). The peak width observed for the single $H_2NCH_2C_6H_4F$ resonance in the ^{19}F NMR spectrum is considerably greater than any of the peaks observed during the titration of $In_{37}P_{20}(O_2CCH_2C_6H_5)_{51}$ in the absence of $HO_2CCH_2C_6H_5$. This may indicate that more surface bound indium sites are susceptible to $H_2NCH_2C_6H_4F$ binding from the combined addition of $HO_2CCH_2C_6H_5$ and $H_2NCH_2C_6H_4F$ than from $H_2NCH_2C_6H_4F$ alone. This is important to note when designing a synthesis of InP QDs as most syntheses that employ amine as an additive do so in the presence of excess carboxylic acids.[5,7,13,14]

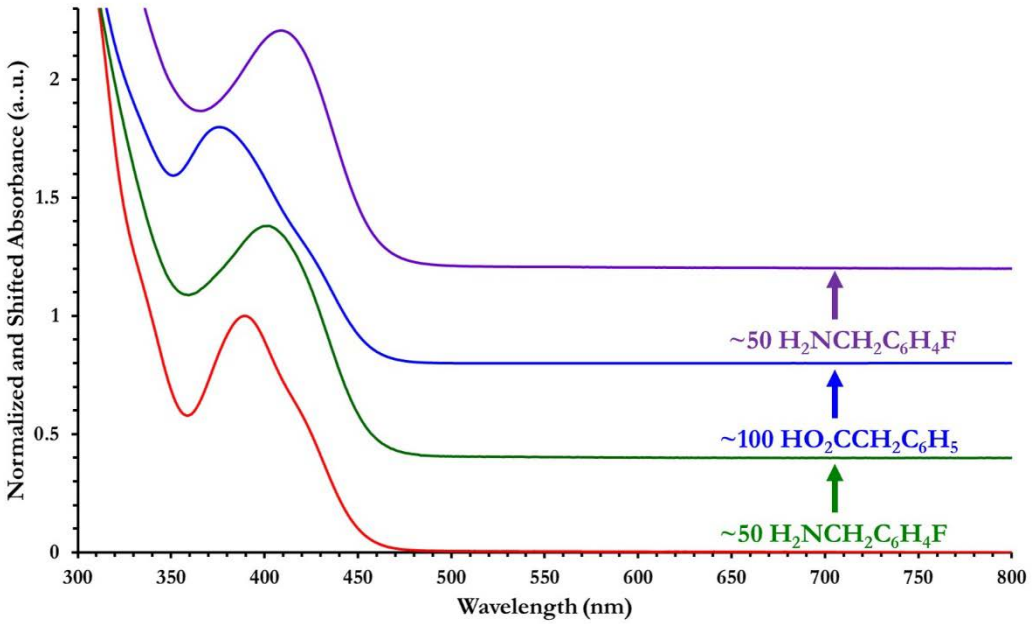

Figure 6.11 UV-Vis spectra of $In_{37}P_{20}(O_2CCH_2C_6H_5)_{51}$ (red spectrum) after addition of 50 equivalents of $H_2NCH_2C_6H_4F$ (green spectrum), subsequent addition of 100 equivalents of $HO_2CCH_2C_6H_5$, and finally a second addition of 50 equivalents of $H_2NCH_2C_6H_4F$.

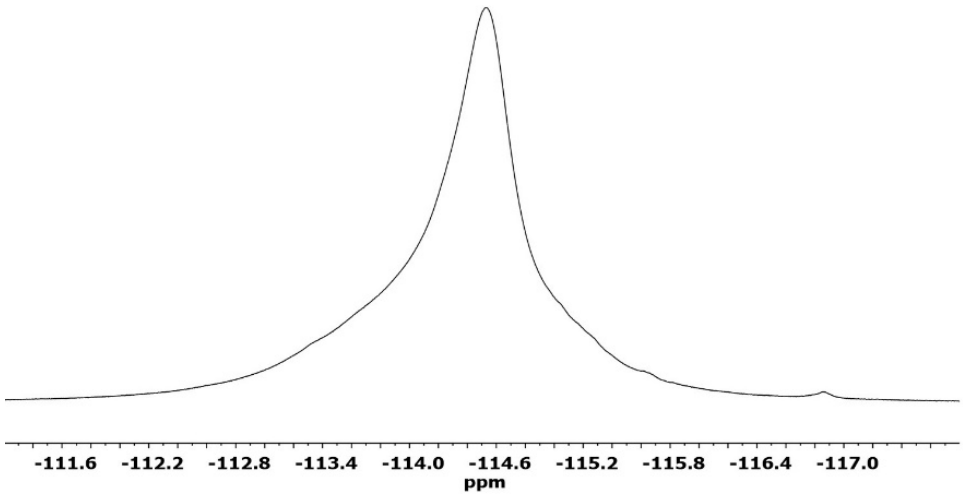

Figure 6.12 ^{19}F NMR spectra of $In_{37}P_{20}(O_2CCH_2C_6H_5)_{51}$ after addition of 50 equivalents of $H_2NCH_2C_6H_4F$ followed by 100 equivalents of $HO_2CCH_2C_6H_5$ carried out at 469MHz in CD_2Cl_2. The linewidth of this peak is approximately 4 times greater than any peak observed during the titration of $In_{37}P_{20}(O_2CCH_2C_6H_5)_{51}$ with $HO_2CCH_2C_6H_5$ (Note that the range of chemical shits the same between Figure 6.3 and Figure 6.12. This may indicate that $HO_2CCH_2C_6H_5$ and $H_2NCH_2C_6H_4F$ together are able to react with more indium atoms of $In_{37}P_{20}(O_2CCH_2C_6H_5)_{51}$ than $H_2NCH_2C_6H_4F$ is alone and the increase in linewidth of this spectrum is due to an increase in binding modes of $H_2NCH_2C_6H_4F$.

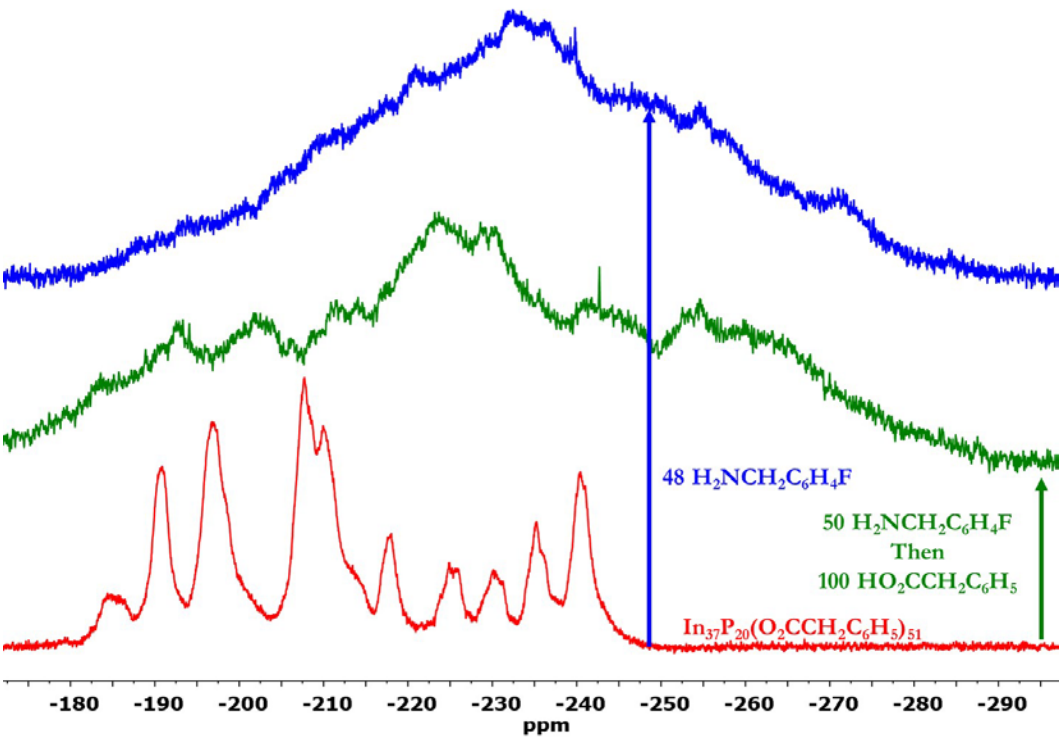

Figure 6.13 ^{31}P NMR spectra of $In_{37}P_{20}(O_2CCH_2C_6H_5)_{51}$ (red spectrum) and the resultant spectra from either the addition of 48 equivalents of $H_2NCH_2C_6H_4F$ (blue spectrum) or the addition of 50 equivalents of $H_2NCH_2C_6H_4F$ followed by addition of 100 equivalents of $HO_2CCH_2C_6H_5$ (green spectrum). Spectra were acquired at 203 MHz in CD_2Cl_2 (blue and red spectra) or ethyl acetate (green spectrum).

6.3 Conclusions

We can conclude from these data that the observed changes in the optical spectra are primarily a result of amine coordination and its impact on the energies of the frontier molecular orbitals of the cluster which are predicted to be highly localized on specific indium atoms (See Chapter 5, Figure 5.12). In contrast, we have gained insight into the reaction products, structural rearrangement of $In_{37}P_{20}(O_2CR)_{51}$, and reaction stoichiometry from ^{19}F and ^{31}P NMR and X-ray crystallography. Based

on the cumulative data, our current hypothesis for the chemical transformation occurring in this reaction is shown in Scheme 6.1.

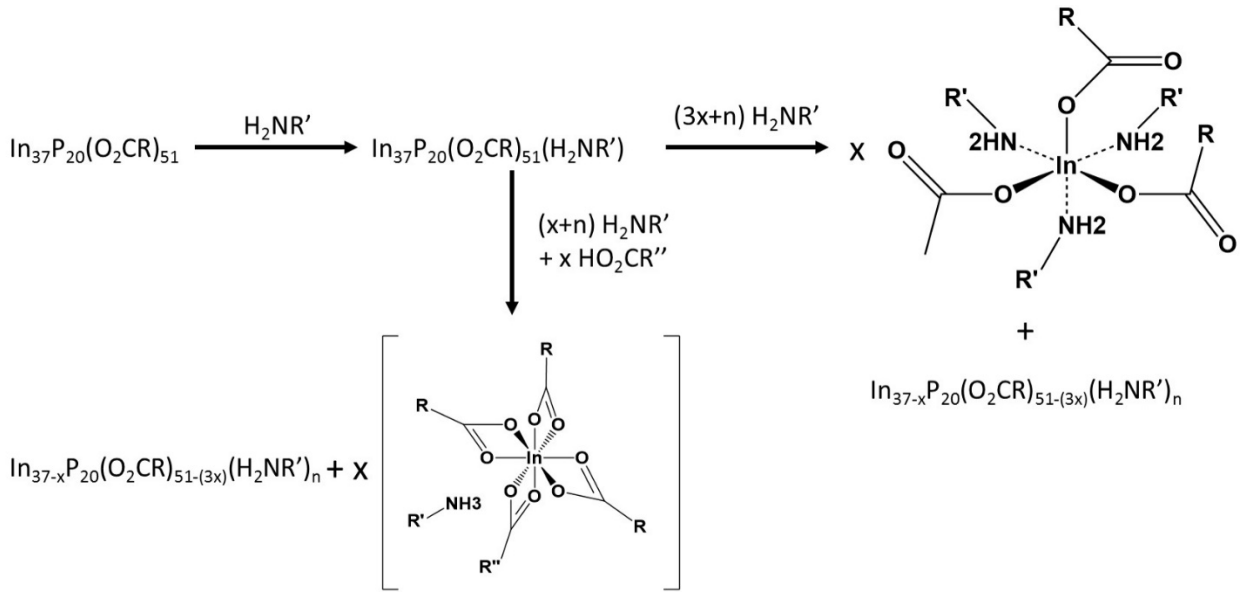

Scheme 6.1 Proposed reaction scheme between $In_{37}P_{20}(O_2CR)_{51}$ and primary amine. First amine binds to $In_{37}P_{20}(O_2CR)_{51}$ with a concurrent change in core structure as observed by ^{31}P NMR. This new cluster is tentatively labeled as $In_{37}P_{20}(O_2CR)_{51}(H_2NR')$ since one equivalent of H_2NR' is sufficient to observe the structural change by ^{31}P NMR. Upon additional equivalents of H_2NR', indium is removed from the surface of the cluster to form $In_{37-x}P_{20}(O_2CR)_{51-(3x)}(H_2NR')_n$ where x is the number of indium carboxylate species removed. Three amines are predicted to be necessary to remove indium carboxylate from the surface of the cluster in the absence of HO_2CR" while only one of each is predicted to be necessary in the presence of free HO_2CR". Based on ^{19}F, ^{31}P, and UV-Vis absorbance spectroscopy, the value of x is predicted to be either 1 or 2. The number of H_2NR' that remain bound to the cluster after the removal of indium is given by the subscript n.

This project is part of an ongoing investigation and future experiments will be aimed at discerning the differences in the reaction scheme when incorporating both free carboxylic acids and amines as opposed to employing amines in an acid free environment. Experiments will also be performed to assess the potential of employing amine treated clusters as precursors to InP nanocrystals.

6.4 Experimental

6.4.1 General Considerations

Indium acetate (99.99%), phenylacetic acid (99%), and oleic acid (90%) were purchased from Sigma-Aldrich and used without further purification. NMR solvents were purchased from Cambridge Isotope Laboratories. Benzylamine (99%) and 4-fluorobenzylamine (97%) were purchased from Sigma Aldrich and dried over calcium hydride, distilled, and stored over 4 Å molecular sieves prior to use. All solvents were dried over calcium hydride, distilled, and stored over 4 Å molecular sieves prior to use. $P(Si(CH_3)_3)_3$ was prepared according to literature procedures.[15] All manipulations were performed under an inert atmosphere of dry N_2 using standard Schlenk or glovebox techniques unless otherwise stated. Optical spectra were acquired on a Cary 5000 UV-Vis-NIR spectrophotometer from Agilent Technologies. NMR spectra were acquired on 499, and 500 MHz Bruker Avance spectrometers.

6.4.2 Synthesis of $In_{37}P_{20}(O_2CCH_2C_6H_5)_{51}$

$In_{37}P_{20}(O_2CCH_2C_6H_5)_{51}$ was prepared by modification of a reported procedure for myristate-capped particles using $In(O_2CCH_3)_3$ (934 mg, 3.20 mmol) and phenylacetic acid (1.58 g, 11.6 mmol)

in toluene (10 mL), and $P(Si(CH_3)_3)_3$ (465 μL, 1.60 mmol) in toluene (5 mL).[11] The workup procedure was modified from that of the particles with a myristate ligand set by substituting pentane for acetonitrile to selectively precipitate the particles (three cycles). $In_{37}P_{20}(O_2CCH_2C_6H_5)_{51}$ was isolated in 25% yield (238 mg, 0.02 mmol) based on $P(Si(CH_3)_3)_3$ as the limiting reagent.

6.4.3 Synthesis of $In_{37}P_{20}(O_2CCH_2C_6H_4F)_{51}$

$In_{37}P_{20}(O_2CCH_2C_6H_4F)_{51}$ was prepared by modification of the synthesis procedure for $In_{37}P_{20}(O_2CCH_2C_6H_5)_{51}$ was prepared by modification (*vide supra*) by substituting an equimolar amount of 4-fluorophenylacetic acid for phenylacetic acid.

6.4.4 Crystallization Procedure for $In(O_2CCH_2C_6H_5)_3(H_2NCH_2C_6H_5)_3$

Under a nitrogen atmosphere $In_{37}P_{20}(O_2CCH_2C_6H_5)_{51}$ (100 mg) was dissolved in ethyl acetate (1 mL) and was filtered into a scintillation vial using a 1 mL syringe outfitted with a PFTE filter with a 0.45 μm pore size. Small, white needles were found in the scintillation vial after about one week at room temperature.

6.4.5 Crystallization Procedure for $In(O_2CCH_2C_6H_4F)_4(H_3NCH_2C_6H_5)$

In a nitrogen filled glovebox, $In_{37}P_{20}(O_2CCH_2C_6H_5)_{51}$ (117mg) was weighed directly into a J. Young NMR tube. CD_2Cl_2 (0.5 mL) was then added to the J. Young tube. $H_2NCH_2C_6H_5$ was added (3 μL) and a yellow precipitate was observed in the NMR tube the next day. The precipitate was redissolved by adding ~2 mL of toluene to the J. Young tube, sealing the tube, bringing the tube out

of the glovebox, and then sonicating the tube for an hour at 60 °C. The tube was then allowed to slowly come to room temperature. Small, yellow needles were found amongst the precipitate the following day.

6.4.6 All X-ray Crystallography Measurements and Analysis

Single Crystal X-Ray Diffraction Methods for $In(O_2CCH_2C_6H_5)_3(H_2NCH_2C_6H_5)_3$

A colorless needle, measuring 0.19 x 0.03 x 0.03 mm^3 was mounted on a loop with oil. Data was collected at -173° C on a Bruker APEX II single crystal X-ray diffractometer, Mo-radiation.

Single Crystal X-Ray Diffraction Methods for $In(O_2CCH_2C_6H_4F)_4(H_3NCH_2C_6H_5)$

A yellow prism, measuring 0.18 x 0.03 x 0.03 mm^3 was mounted on a loop with oil. Data was collected at -173° C on a Bruker APEX II single crystal X-ray diffractometer, Mo-radiation.

6.4.7 Titration of $In_{37}P_{20}(O_2CCH_2C_6H_5)_{51}$ with $H_2NCH_2C_6H_4F$ for ^{19}F, ^{31}P, and ^1H NMR

$In_{37}P_{20}(O_2CCH_2C_6H_5)_{51}$ (107 mg) was weighed directly into a J. Young tube in a nitrogen filled glovebox using weight paper as a funnel. CD_2Cl_2 (0.5 mL) was added to the J. Young tube. α, α, α trifluorotoluene (17 μL) was added to the tube as an internal standard for ^{19}F NMR. For each addition of $H_2NCH_2C_6H_4F$, 1μL of $H_2NCH_2C_6H_4F$ was added with a microliter syringe. ^{31}P, ^{19}F, and ^1H NMR were acquired between each addition of $H_2NCH_2C_6H_4F$.

6.4.8 Titration of $In_{37}P_{20}(O_2CCH_2C_6H_4F)_{51}$ with $H_2NCH_2C_6H_5$ for ^{19}F, ^{31}P, and ^1H NMR

$In_{37}P_{20}(O_2CCH_2C_6H_4F)_{51}$ (117 mg) was weighed directly into a J. Young tube in a nitrogen filled glovebox using weight paper as a funnel. CD_2Cl_2 (0.5 mL) was added to the J. Young tube. α, α, α trifluorotoluene (17 μL) was added to the tube as an internal standard for ^{19}F NMR. For each addition of $H_2NCH_2C_6H_5$, 1μL of $H_2NCH_2C_6H_5$ was added with a microliter syringe. ^{31}P, ^{19}F, and ^1H NMR were acquired between each addition of $H_2NCH_2C_6H_5$.

6.4.9 Titration of $In_{37}P_{20}(O_2CCH_2C_6H_5)_{51}$ with $H_2NCH_2C_6H_4F$ for UV-Vis

$In_{37}P_{20}(O_2CCH_2C_6H_5)_{51}$ (31 mg) was weighed out into a 100 mL volumetric flask in a nitrogen filled glovebox and toluene was added to the flask to dissolve $In_{37}P_{20}(O_2CCH_2C_6H_5)_{51}$ and dilute to the mark. A microliter syringe was used to add 26.6 μL of $H_2NCH_2C_6H_4F$ to a 5 mL volumetric flask. Toluene was added to the 5 mL flask and filled to the mark. For each spectrum, a 500 μL syringe was used to measure out 1 mL of $In_{37}P_{20}(O_2CCH_2C_6H_5)_{51}$ stock solution into a cuvette to which 10 μL of the $H_2NCH_2C_6H_4F$ stock solution was added for every equivalent of $H_2NCH_2C_6H_4F$ intended for the final solution. The cuvette was sealed with a screw cap and electrical tape and brought out of the glovebox and the spectrum was acquired.

6.5 References

(1) Kim, K.; Yoo, D.; Choi, H.; Tamang, S.; Ko, J.-H.; Kim, S.; Kim, Y.-H.; Jeong, S. *Angewandte Chemie International Edition* **2016**, *55* (11), 3714–3718.

(2) Song, W.-S.; Lee, H.-S.; Lee, J. C.; Jang, D. S.; Choi, Y.; Choi, M.; Yang, H. *Journal of Nanoparticle Research* **2013**, *15* (6).

(3) Tessier, M. D.; Dupont, D.; De Nolf, K.; De Roo, J.; Hens, Z. *Chemistry of Materials* **2015**, *27* (13), 4893–4898.

(4) Tessier, M. D.; De Nolf, K.; Dupont, D.; Sinnaeve, D.; De Roo, J.; Hens, Z. *Journal of the American Chemical Society* **2016**, *138* (18), 5923–5929.

(5) Protiere, M.; Reiss, P. *Chemical Communications* **2007**, No. 23, 2417–2419.

(6) Sugimoto, T. *Advances in Colloid and Interface Science* **1987**, *28*, 65–108.

(7) Xie, R.; Battaglia, D.; Peng, X. *Journal of the American Chemical Society* **2007**, *129* (50), 15432–15433.

(8) Cho, E.; Jang, H.; Lee, J.; Jang, E. *Nanotechnology* **2013**, *24* (21), 215201.

(9) Gooßen, L. J.; Ohlmann, D. M.; Lange, P. P. *Synthesis* **2008**, *2009* (1), 160–164.

(10) Allen, P. M.; Walker, B. J.; Bawendi, M. G. *Angewandte Chemie International Edition* **2010**, *49* (4), 760–762.

(11) Gary, D. C.; Terban, M. W.; Billinge, S. J. L.; Cossairt, B. M. *Chemistry of Materials* **2015**, *27* (4), 1432–1441.

(12) Gary, D. C.; Flowers, S. E.; Kaminsky, W.; Petrone, A.; Li, X.; Cossairt, B. M. *Journal of the American Chemical Society* **2016**, *138* (5), 1510–1513.

(13) Lim, K.; Jang, H. S.; Woo, K. *Nanotechnology* **2012**, *23* (48), 485609.

(14) Xu, S.; Ziegler, J.; Nann, T. *Journal of Materials Chemistry* **2008**, *18* (23), 2653–2656.

(15) Gary, D. C.; Cossairt, B. M. *Chemistry of Materials* **2013**, *25* (12), 2463–2469.